

Study of Invisible Mode Nucleon Decay in the SNO+ Detector



John M. G. Walker

University of Liverpool

A thesis submitted for the degree of

Doctor of Philosophy

July 2016

Abstract

SNO+ is a large volume liquid scintillator experiment and is a refurbishment of the SNO detector. 780 tonnes of ultra-pure scintillator will be housed inside a 12 m diameter, 5.5 cm thick, acrylic vessel and observed by ~ 9300 photomultiplier tubes.

The primary purpose of the experiment is to search for neutrinoless double-beta decay ($0\nu\beta\beta$) of ^{130}Te , although it has a broad physics program. Prior to deployment of liquid scintillator the detector will be filled with light water to perform calibrations as well as to enable water phase physics analyses. One such analysis will be to search for “invisible” mode nucleon decay, in which very little or no energy is deposited in the detector by decay products. This thesis predicts that with three months of data taking SNO+ will set a new limit of $\tau > 1.5 \times 10^{30}$ years for the lifetime of the proton, and $\tau > 1.3 \times 10^{30}$ years for the neutron, to decay via an invisible mode.

To facilitate this analysis, the development of an energy estimator for the water phase is outlined which uses a detector energy response function. An obstacle for SNO+, both during the water and scintillator phases, will be the large instrumental background (non-radiative events caused by the detector) expected. The expected backgrounds are described, as well as cuts developed for their removal by SNO. The loss of signal events due to these cuts is estimated for the water and scintillator phases of the experiment. The residual background is estimated by developing an instrumental background generator.

Acknowledgements

I would like to start my acknowledgments with an apology to any reader of this thesis who has contributed to my life, both as a PhD student and in general, and finds themselves not named here. The necessary thank yous would constitute a thesis on their own. Thank you. Yes, you.

Large thanks must go to my supervisor Neil McCauley for his patience and enthusiasm, his insights have been invaluable in completing this thesis. I am a better physicist for it and certainly more knowledgeable about “The Albion”.

Special thanks must also go to Robert Stainforth whose friendship throughout our PhDs has made the experience immeasurably better. It has also been a pleasure to work and play with the rest of the SNO+ UK students, particular mentions to Ashley, Evelina, Stefanie, James, Chris and Jack.

To all the Liverpool students, you have been thoroughly enjoyable to work alongside, and more often wonderfully distracting. Further thanks to the rest of the department for the friendly and supportive environment.

I would like to recognise the support I have received completing the material in this thesis from Matt Mottram on energy reconstruction, Robert Knapik on instrumental backgrounds, and Ian Coulter on nucleon decay.

An enormous thank you to my parents without whose love and support throughout my life I could not be where I am, both in physics and in general. I would also like to express my gratitude to Sarah for supporting me on this journey, from London to Liverpool and Sudbury.

Finally, my gratitude to the Science and Technology Facilities Council, without whom none of this would be possible.

Statement of Originality

The work presented in this thesis is the work of the author, except as noted here and where the work of others has been cited.

The energy reconstruction algorithms described in Chapter 4 build on work completed by various SNO collaboration members. In particular the development of RSP by Ryan MacLellan, which has been adapted for a light water filled SNO+ detector by this author.

Instrumental backgrounds were observed and identified by the SNO collaboration. The data cleaning and higher level cuts, described in Chapter 5, were then developed by the data cleaning working group. A sacrifice and contamination study was performed for SNO using calibration data. The sacrifice study presented here was performed using Monte Carlo, which was not attempted by SNO. Simulation of the “flasher” type instrumental background was developed by this author and used to estimate contamination independently of the SNO method.

A limit for invisible mode nucleon decay was set by the SNO experiment using heavy water, and is the basis for the analysis presented in Chapter 6. Using light water will reduce the background allowing an improved limit setting potential.

Contents

1	Neutrinos	1
1.1	A Brief History of the Neutrino	1
1.1.1	The missing neutrino	1
1.1.2	The ν_e discovery	2
1.1.3	ν_μ and lepton family	3
1.1.4	The ν_τ discovery	4
1.2	Neutrinos in the Standard Model	4
1.3	Neutrino Interactions	7
1.3.1	Neutrino-electron interactions	7
1.3.2	Hadron decays	9
1.3.3	Neutrino-nucleon scattering	9
1.4	Neutrino Sources	10
1.4.1	Solar Neutrinos	11
1.4.2	Accelerator	15
1.4.3	Reactor	15
1.4.4	Geological	15
1.4.5	Atmospheric	16
1.4.6	Cosmological	16
1.4.7	Supernovae	17
1.4.8	Cosmic neutrinos	18
1.5	Neutrino Detection	19
1.5.1	Radiochemical Detectors	19
1.5.2	Tracking Detectors	19
1.5.3	Water Cherenkov Detectors	19
1.5.4	Scintillation Detectors	20
1.6	Beyond the Standard Model	21
1.6.1	Neutrino Anomalies	21
1.6.1.1	Solar Neutrinos	21
1.6.1.2	Atmospheric Neutrinos	22
1.6.2	Solution to the Solar and Atmospheric Neutrino Problems	22

1.6.3	Neutrino Flavour Oscillations	25
1.6.3.1	Neutrino Oscillations in Matter	29
1.7	Neutrino Mass	34
1.7.1	Dirac masses	36
1.7.2	Majorana Masses	36
1.7.3	Electron Neutrino Mass	38
1.7.4	Neutrinoless Double β Decay	39
2	The SNO+ Experiment	43
2.1	SNOLAB	43
2.2	The Detector	43
2.3	Electronics and detector readout	44
2.4	Calibration	46
2.5	Monte Carlo	48
2.6	Scintillation	48
2.7	Backgrounds	49
2.7.1	^{238}U Chain	50
2.7.2	^{232}Th Chain	53
2.7.3	Internal ^{40}K , ^{39}Ar , and ^{85}Kr Backgrounds	54
2.7.4	Cosmogenically Induced Backgrounds	54
2.7.5	(α, n) Backgrounds	55
2.7.6	Pile-Up Backgrounds	55
2.7.7	External Backgrounds	55
2.8	Physics Program	56
2.8.1	Neutrinoless Double Beta Decay	57
3	Refurbishing the SNO Detector	61
3.1	Scintillator Plant	61
3.2	Water Plant	65
3.3	Hold-down Ropes	65
3.4	Optical Fibre Calibration System	66
3.5	PMT Repair	68
3.6	Electronics	72
3.7	Cover Gas	75
3.8	Universal Interface	76
3.9	Summary	76
4	Energy Reconstruction	79
4.1	SNO+ Energy Response	79
4.1.1	Cherenkov Radiation	80

4.1.2	Attenuation and Scattering	81
4.1.3	Fresnel Transmission Probability	83
4.1.4	PMT Efficiency	84
4.1.5	Response Model	85
4.2	Prompt Lookup Method	86
4.2.1	The scaling factor	86
4.2.1.1	Light water	87
4.2.1.2	Scintillator	87
4.2.2	Prompt hits to energy map	89
4.2.2.1	Light water	89
4.2.2.2	Scintillator	91
4.2.3	Comments	91
4.3	RSP Method	92
4.3.1	The Response Function	93
4.3.1.1	Light Path	94
4.3.1.2	Cherenkov Angular Distribution	94
4.3.1.3	Solid Angle	95
4.3.1.4	Fresnel Transmission Probability	97
4.3.1.5	PMT Efficiency	97
4.3.1.6	Attenuation and Scattering	97
4.3.1.7	Summary of the SNO+ RSP Detector Response	98
4.3.2	The RSP Algorithm	99
4.3.2.1	Multi-photoelectron Correction	101
4.3.2.2	Energy Calibration Function	102
4.3.3	Comments	103
4.4	Estimator performance	105
4.4.1	Light water	105
4.4.2	Scintillator	107
4.5	Summary	113
5	Instrumental Backgrounds	119
5.1	Causes of Instrumental Backgrounds	121
5.1.1	Flashers	121
5.1.2	Other causes	122
5.2	Pre-reconstruction cuts	123
5.2.1	Crate Isotropy	124
5.2.2	Flasher Geometry Cut	125
5.2.3	Neck Cut	125
5.2.4	Junk Cut	125
5.2.5	Q Cluster	125

5.2.6	Q v T	126
5.2.7	Q v Nhit	126
5.2.8	ITC Time Spread	126
5.2.9	Fitterless Timespread	127
5.2.10	CAEN cuts	127
5.3	Post-reconstruction cuts	128
5.3.1	Isotropy	128
5.3.2	ITR	128
5.4	Sacrifice	130
5.4.1	Light water	131
5.4.2	Liquid scintillator	134
5.5	Developing a Flasher Generator	135
5.6	Contamination from flashers	144
5.6.1	Light water	145
5.6.2	Scintillator	148
5.6.3	Summary	156
6	Nucleon Decay	159
6.1	Possible decay modes	159
6.2	Invisible decay modes	161
6.3	Expected signal	163
6.4	Backgrounds	165
6.4.1	External Backgrounds	166
6.4.1.1	Acrylic Vessel, Hold-down Ropes, and Hold-up Ropes .	167
6.4.1.2	Water Shielding and PMTs	168
6.4.2	Solar Neutrinos	169
6.4.3	Reactor Anti-Neutrinos	171
6.4.4	Instrumental background	173
6.4.5	Summary	175
6.5	Limit setting	178
6.5.1	Simple Poisson method	178
6.5.2	Feldman-Cousins method	182
6.5.3	Profile Likelihood method	186
6.6	Summary	188
7	Conclusions	193
Bibliography		197

Chapter 1

Neutrinos

This chapter is devoted to the current status of neutrino theory. It is discussed how the neutrino fits into the *Standard Model* (SM) including how the neutrino interacts with matter. These interactions are set in a practical context through discussion on how the neutrino may be produced and subsequently detected.

There has been much excitement over the last several decades regarding the observed behaviour of neutrinos that does not fit with the Standard Model description. Such behaviour is known as being *beyond the Standard Model* (BSM). This behaviour was explained by neutrino flavour oscillations, for which Takaaki Kajita and Arthur McDonald were awarded the Nobel Prize in 2015. The evidence for these oscillations, and the theory that explains them, is described.

Finally, Dirac and Majorana neutrinos are described. It is explained how if neutrinos are Majorana, a framework exists to explain the lightness of the neutrino mass (see-saw mechanism) as well as the matter-antimatter asymmetry in the universe (leptogenesis). Neutrinoless double β decay is a hypothesised rare process that if discovered would provide experimental evidence that the neutrino is Majorana.

1.1 A Brief History of the Neutrino

Here it is described how our current understanding of neutrinos emerged, starting with the evidence for a new particle through to the discovery of three neutrino species. For a more complete description see Reference [1].

1.1.1 The missing neutrino

In 1896 Henri Becquerel discovered, by “accident” that without application of external energy, some chemical elements were naturally radioactive, leaving marks on photographic plates [2]. One year subsequently J. J. Thomson discovered the electron through investigating the properties of cathode rays (later revealed to be β -rays) [3].

Analysis of this natural radioactivity continued through the early 1900s, revealing three distinctly identifiable types of radiation, labelled α , β , and γ :

- α -rays were easily absorbed, hard to bend, and positively charged.
- β -rays were harder to absorb, more easily bent, and negatively charged.
- γ -rays were even harder to absorb, and did not bend under a magnetic field so were neutrally charged.

The α -ray and γ -ray spectra were shown to be discrete, and it was anticipated that the same was true for β -rays. However, in 1914 James Chadwick presented definitive evidence for a continuous β -ray spectrum [4]. The explanation for this was unknown. The energy of the electron should be equal to the mass difference of the parent and daughter nuclei, so a continuous spectrum would break energy conservation. It took over 15 years to agree that the β -ray spectrum really was continuous [5, 6].

Niels Bohr suggested that energy may not be conserved for processes involving nuclear electrons [7]. The alternative explanation, which turned out to be correct, was the existence of a new particle so β -decay was not completely analogous to α and γ emission.

In his 1930 letter addressed to the Tubingen conference's "Radioactive Ladies and Gentlemen" Wolfgang Pauli postulated the existence of a neutral, weakly interacting "neutron". Chadwick discovered what we call today the neutron [8], and the Pauli particle was renamed by Enrico Fermi the "neutrino". In 1934 Fermi went further by formulating his theory for β -decay [9],¹

$$\frac{G_F}{\sqrt{2}}(\bar{n}\Gamma_{NP})(\bar{\nu}_e\Gamma_{LE}) + h.c. \quad (1.1)$$

Under this theory the β -decay process can be written $n \rightarrow p + e^- + \bar{\nu}_e$, with the neutrino denoted ν_e . Fermi theory further allowed neutrinos to be detected from the process $\bar{\nu}_e + p \rightarrow e^+ + n$.

1.1.2 The ν_e discovery

In the 1950s Frederick Reines and Clyde Cowan tried to detect anti-neutrinos via the $\bar{\nu}_e + p \rightarrow e^+ + n$ process. After initially considering an atomic bomb explosion as a source, they decided to use the anti-neutrinos produced by the Savannah River nuclear reactor site instead [10]. The positron produced annihilates in liquid scintillator to produce two photons ($e^+ + e^- \rightarrow \gamma + \gamma$), the total energy deposited is related to the positron energy. The neutron produced is captured shortly thereafter, resulting in the emission of γ -rays with well-defined energy. In 1956 they telegrammed Pauli to inform him of the discovery.

Up to about this time it was believed that parity was conserved i.e. the particle was the same regardless of a spatial translation. However in 1956 T. D. Lee and C.

¹Modern notation.

N. Yang hypothesised that parity could be violated in weak processes [11]. This was experimentally confirmed for β -decay by Wu et al [12]. The $V - A$ (or $\gamma_\mu(1 - \gamma_5)$) theoretical framework for this was formulated by R. P. Feynman and M. Gell-Mann [13], and E. C. G. Sudarshan and R. E. Marshak [14]. In this theory the neutrino has total spin $\frac{1}{2}$ which, projected in the direction of motion, gives the handedness, or helicity. If the spin projection is $+\frac{1}{2}$ the neutrino is right-handed, and if the spin projection is $-\frac{1}{2}$ the neutrino is left-handed.

The neutrino helicity was determined by M. Goldhaber, L. Grodzins and A. W. Sunyar in 1958 [15]. They measured electron capture in the reaction $e^- + {}^{152}\text{Eu} \rightarrow {}^{152}\text{Sm}^* + \nu_e$ and the subsequent decay ${}^{152}\text{Sm}^* \rightarrow {}^{152}\text{Sm} + \gamma$. The polarity of the photon, through conservation of angular momentum, is correlated to the neutrino helicity, so by measuring the photon they were able to show that the neutrino is purely left-handed. Correspondingly the anti-neutrino is purely right-handed.

At the same time as the Reines Cowan experiment, Ray Davis was attempting to measure an alternative channel for anti-neutrino detection, $\bar{\nu}_e + {}^{37}\text{Cl} \rightarrow e^- + {}^{37}\text{Ar}$ [16]. The process did not occur at a measurable rate. This was because lepton number was not conserved, a concept that was introduced in 1953 by E. J. Konopinski and H. M. Mahmoud [17]. Electrons, e^- , and neutrinos, ν_e , are assigned lepton number $L = 1$, while their anti-particles were assigned lepton number $L = -1$. The process Davis was investigating would violate lepton number by two.

1.1.3 ν_μ and lepton family

While the aforementioned studies into neutrino properties were ongoing, several other discoveries were being made. Using cosmic ray experiments, the discovery of what are now known as muons, μ^\pm , were made in 1937 [18, 19]. These were initially confused with the pion, π^\pm , although this was resolved when pions were also detected from cosmic rays in 1947 [20]. It was established that the pion decayed via [1],

$$\pi^+ \rightarrow \mu^+ + \nu_\mu, \quad (1.2)$$

but it was unclear whether or not this *muon neutrino*, ν_μ was different to ν_e .

Efforts to establish whether ν_e and ν_μ are indeed different particles were led by L. Lederman, J. Steinberger and M. Schwartz at the Brookhaven National Laboratory [21]. To obtain a ν_μ source they developed the first neutrino beam. This was achieved by colliding protons with a target at sufficient energy to create a flux of pions, which then decay into muons and neutrinos. So by aiming the pion beam at a beam-dump in front of the detector, to absorb charged leptons and hadrons, the detector would be traversed by mostly muon type neutrinos. Some beam contamination was expected from muon and kaon decays to both muon and electron type neutrinos. The experiment was to see whether muon neutrinos could produce both muons and electrons in the detector.

Specifically they were trying to observe the following processes:

$$\nu_\mu + n \rightarrow p + \mu^-, \quad (1.3)$$

$$\bar{\nu}_\mu + p \rightarrow n + \mu^+, \quad (1.4)$$

$$\nu_\mu + n \rightarrow p + e^-, \quad (1.5)$$

$$\bar{\nu}_\mu + p \rightarrow n + e^+. \quad (1.6)$$

In 1962 they reported that, overwhelmingly, the muon final state was observed. The small instance of electron production could be explained by beam contamination. This demonstrated the existence of a second neutrino, ν_μ , and a lepton family conservation law was established.

1.1.4 The ν_τ discovery

A third charged lepton, τ , was discovered by Martin Perl at SLAC in 1975 [22], for which he was awarded the Nobel Prize in 1995 (along with Reines for detecting the neutrino). It was assumed that it must be associated with a new undiscovered neutrino.

The existence of a third neutrino flavour was first indirectly tested with the ALEPH detector at LEP by measuring the decay width of the Z boson [23]. By assuming the Z boson decays with comparable probability into each allowed fermionic state, it was possible to set a limit on the number of $\nu_l \bar{\nu}_l$ final states. The number of non-sterile light neutrino flavours, with mass less than $m_Z/2$, was consistent with three. There could still exist, however, sterile or heavier neutrinos.

Existence of three neutrinos is further supported by calculating the abundance of primeval light elements, in particular ${}^4\text{He}$ [24]. This is because the number of neutrino types affects the energy density and therefore rate of primordial nucleosynthesis, determining the composition of elements in the universe.

The eventual discovery of ν_τ was made by the DONUT experiment in 2000 [25]. They were looking for the charged current interaction,

$$\nu_\tau + X \rightarrow \tau^- + Y. \quad (1.7)$$

Similarly to the Brookhaven experiment they aimed a beam of protons at a target. This time a ν_τ source was created from the decays of charmed mesons ($D_S^- \rightarrow \tau^- + \bar{\nu}_\tau$), and the subsequent decay of the τ to a ν_τ . The beam was incident on an emulsion target, which was used to identify tracks with a kink as the τ decays within 2 mm to a single charged daughter.

1.2 Neutrinos in the Standard Model

The neutrino is the lightest massive elementary particle. It is described by the Standard Model, the theory of the interactions between all known fundamental particles. These

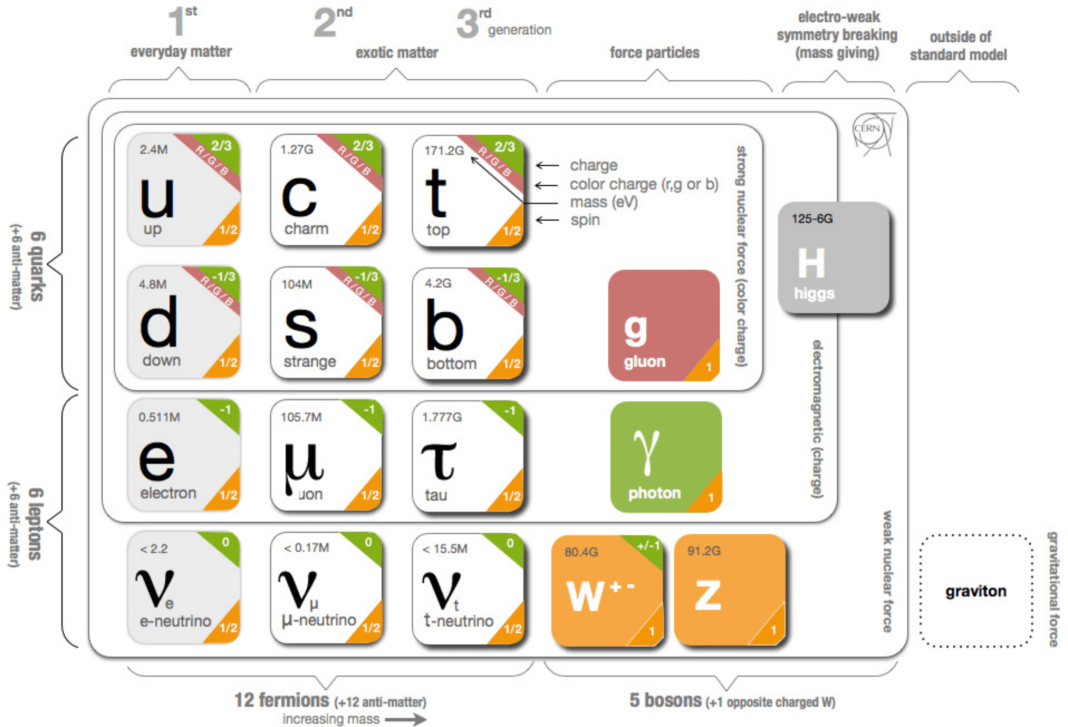


Figure 1.1: Elementary particles described in the Standard Model: three generations of the fermions (quarks and leptons), four force mediating gauge bosons, and the Higgs boson [27].

include 12 matter particles (fermions), four force mediating gauge bosons, and the Higgs boson. Figure 1.1 details these particles. The bosons propagate the electroweak and strong forces. They have integer spin and obey Bose-Einstein statistics. The fermions have $\frac{1}{2}$ integer spin and obey Fermi-Dirac statistics. The strong force is mediated by the gluon, electromagnetic (EM) force by the photon, and the weak force by the W^\pm and Z^0 bosons. The 12 fermions consist of six quarks and three negatively charged leptons (flavours e , μ and τ) with associated neutral neutrinos. Each fermion has an antiparticle with opposite charge. The charged leptons interact via the EM and weak force, while neutrinos only interact via the weak force. As the weak force is propagated by massive bosons, weak cross-sections are $\sim 10^{-11}$ times smaller than EM cross-sections [26]. Consequently neutrino interaction cross-sections are very small.

The Lagrangian for the Standard Model is the sum of the electroweak, Higgs, Yukawa and QCD Lagrangians,

$$\mathcal{L}_{SM} = \mathcal{L}_{EW} + \mathcal{L}_H + \mathcal{L}_Y + \mathcal{L}_{QCD}. \quad (1.8)$$

The quantum field theory Lagrangian above, describing the Standard Model, is invariant under local symmetry transformations of gauge groups $U(1)_{EM}$, $SU(2)_{isospin}$ and $SU(3)_{colour}$. Each group represents one of the three forces: electromagnetic; weak and strong respectively. $SU(2) \times U(1)$ has been unified into a single electroweak theory

which describes electromagnetic and weak interactions within one system.

The leptonic charged current weak interaction Lagrangian is [28],

$$\mathcal{L}_{I,L}^{(CC)} = -\frac{g}{2\sqrt{2}} \left(j_{W,L}^\rho W_\rho + j_{W,L}^\rho {}^\dagger W_\rho {}^\dagger \right), \quad (1.9)$$

and the neutrino part of the leptonic neutral current weak interaction Lagrangian is,

$$\mathcal{L}_{I,\nu}^{(NC)} = -\frac{g}{2\cos\theta_W} j_{Z,\nu}^\rho Z_\rho. \quad (1.10)$$

Standard neutrino interactions are described by the leptonic charged weak current,

$$j_{W,L}^\rho = 2 \sum_{\alpha=e,\mu,\tau} \overline{\nu_{\alpha L}} \gamma^\rho l_{\alpha L} = \sum_{\alpha=e,\mu,\tau} \overline{\nu_\alpha} \gamma^\rho (1 - \gamma^5) l_\alpha, \quad (1.11)$$

and the neutrino part of the leptonic neutral weak current,

$$j_{Z,\nu}^\rho = \sum_{\alpha=e,\mu,\tau} \overline{\nu_{\alpha L}} \gamma^\rho \nu_{\alpha L} = \frac{1}{2} \sum_{\alpha=e,\mu,\tau} \overline{\nu_\alpha} \gamma^\rho (1 - \gamma^5) \nu_\alpha. \quad (1.12)$$

Under electroweak theory neutrinos form a $SU(2)_L$ weak isospin doublet with the leptons,

$$\begin{pmatrix} \nu_{\alpha L} \\ \alpha_L \end{pmatrix}, \quad (1.13)$$

where $\alpha = e, \mu, \tau$. The subscript L indicates that the elements of the group have left-handed chirality, where chiral states are eigenfunctions of the γ^5 matrix.

Neutrinos form left-handed Weyl spinors and anti-neutrinos form right-handed Weyl spinors,

$$\nu_L \equiv P_L \nu, \quad \nu_R \equiv P_R \nu, \quad (1.14)$$

where the chirality projection operators are,

$$P_L = \frac{1 - \gamma^5}{2}, \quad P_R = \frac{1 + \gamma^5}{2}. \quad (1.15)$$

Helicity is the projection of a particle's spin on its momentum. The operator is,

$$\hat{h} = \frac{\boldsymbol{\sigma} \cdot \mathbf{p}}{|\mathbf{p}|}, \quad (1.16)$$

which has eigenvalues, $\hat{h} = \mp 1$, for neutrinos and anti-neutrinos respectively.

For relativistic particles chirality and helicity are highly correlated. For a left-handed neutrino the positive helicity state is suppressed by a factor of $\approx m/E$, the reverse is true for the right-handed anti-neutrino. Consequently a massless neutrino would have a negative helicity and spin antiparallel to momentum. The massless anti-neutrino would have a positive helicity and spin parallel to momentum.

The Standard Model has been very successful as a theory and survived considerable experimental testing. It predicted the existence of W and Z bosons before they had

been observed and their mass to better than 2% accuracy, as well as the existence of the Higgs boson.

Despite the excellent agreement of the Standard Model to experimental results, there are a number of issues which it does not resolve. For instance, while it provides an excellent framework for describing the strong, weak, and EM forces, it does not extend to describing gravity. It is also not a true unification of the electroweak and strong forces. The Standard Model does not provide an explanation for the existence of dark matter as there is no weakly interacting massive particle.

The Standard Model describes neutrinos as being massless, however through the observation of neutrino oscillations, when a neutrino is created as one flavour and observed at a time later as another flavour, we know that neutrino mass eigenstates must be non-zero and different. Other consequences are that CP violation may occur in the lepton sector, and that neutrinos may be their own antiparticles.

1.3 Neutrino Interactions

The interactions of neutrinos are described in the Standard Model by Equations 1.9-1.12. These interactions are of two types, neutral current (NC) and charged current (CC). In NC interactions, two neutrinos of the same identity couple to the Z^0 boson. The two neutrinos will, however, have different four-momenta. The CC interaction couples a neutrino, $\nu_l(\bar{\nu}_l)$, and a charged lepton, l^\pm , with a W^\pm boson. Neutrinos can be detected through their CC and NC interactions with matter. This section outlines these processes, greater detail can be found in Reference [28].

1.3.1 Neutrino-electron interactions

There are three types of neutrino-electron interaction: elastic scattering, quasi-elastic scattering and neutrino-anti-neutrino pair production. They are among the simplest of neutrino interactions with matter.

During the elastic scattering process low energy neutrinos of all flavours interact with electrons,

$$\nu_\alpha(\bar{\nu}_\alpha) + e^- \rightarrow \nu_\alpha(\bar{\nu}_\alpha) + e^- . \quad (1.17)$$

Feynman diagrams for this process are shown in Figures 1.2 and 1.3.

The quasi-elastic scattering process, also known as *inverse muon decay*, is represented by the following equation,

$$\nu_\mu + e^- \rightarrow \nu_e + \mu^- . \quad (1.18)$$

Here muon neutrinos with sufficient energy ($\gtrsim 10.9$ GeV) interact with electrons to produce muons. See Figure 1.4 for a Feynman diagram.

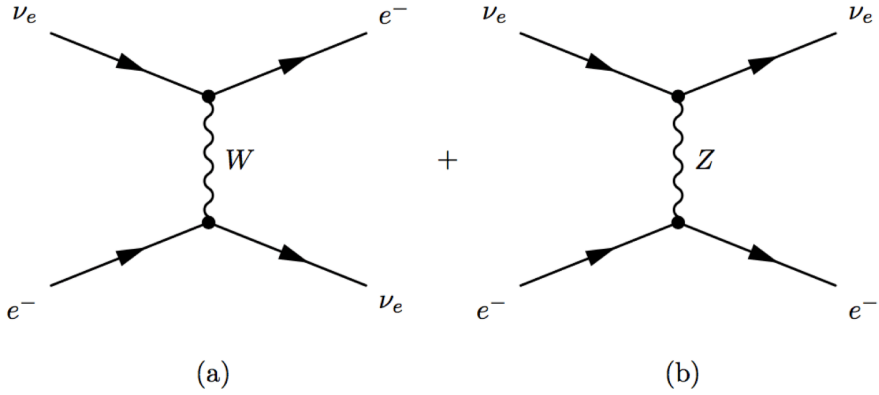


Figure 1.2: Feynman diagrams for the CC (a) and NC (b) elastic scattering process $\nu_\alpha + e^- \rightarrow \nu_\alpha + e^-$ [28].

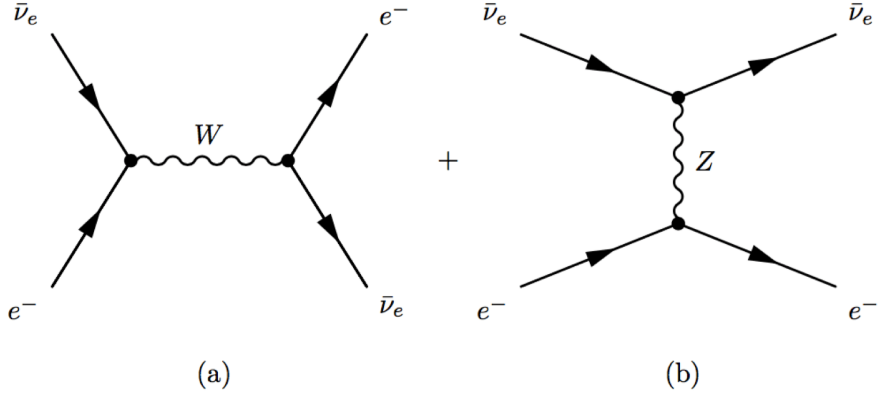


Figure 1.3: Feynman diagrams for the CC (a) and NC (b) elastic scattering process $\bar{\nu}_\alpha + e^- \rightarrow \bar{\nu}_\alpha + e^-$ [28].

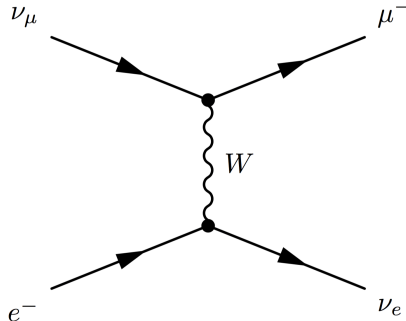


Figure 1.4: Feynman diagram for the CC quasi-elastic scattering process $\nu_\mu + e^- \rightarrow \nu_e + \mu^-$ [28].

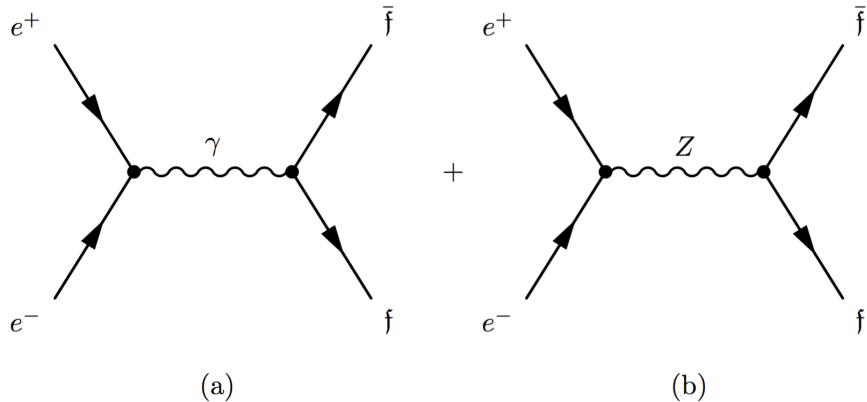


Figure 1.5: Feynman diagrams for fermion-anti-fermion pair production through (a) photon exchange and (b) Z-boson exchange [28].

A further neutrino-electron interaction involves electrons and positrons producing neutrino-anti-neutrino pairs,

$$e^+ + e^- \rightarrow \nu + \bar{\nu}. \quad (1.19)$$

Figure 1.5 shows this process for a general fermion-anti-fermion pair. This is the process that was used in the LEP experiments, as described in Section 1.1.4, to determine the number of neutrino species.

1.3.2 Hadron decays

Neutrinos and anti-neutrinos are produced through charged pion decay,

$$\pi^\pm \rightarrow l^\pm + \nu_l (\bar{\nu}_l), \quad (1.20)$$

where $l = e$ or μ . The decay to muonic products is the dominant process by a factor of $\sim 10^4$. This is a common and important process because charged pions are produced during a number of hadronic interactions, for example cosmic rays colliding with the atmosphere or at particle accelerators. Charged kaons, which decay analogously to pions, can also be created in high energy hadron collisions.

Another important hadronic decay involving neutrinos is neutron decay, or β decay,

$$n \rightarrow p + e^- + \bar{\nu}_e. \quad (1.21)$$

During neutron decay a d quark transitions to a u quark, see Figure 1.6 for a Feynman diagram.

1.3.3 Neutrino-nucleon scattering

Neutrinos can also interact with nucleons through three types of interaction: elastic scattering (NC), quasi-elastic scattering (CC), and deep inelastic scattering (both CC and NC).

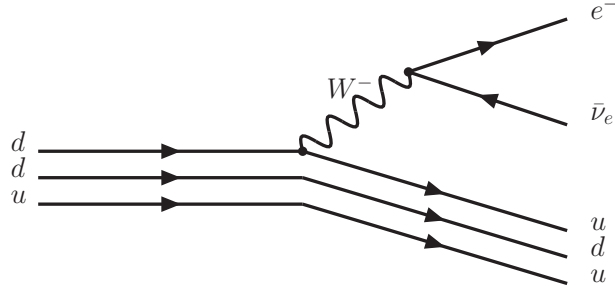


Figure 1.6: A Feynman diagram for the neutron decay process $n \rightarrow p + e^- + \bar{\nu}_e$.

The process for the elastic scattering neutral current interaction of neutrinos and anti-neutrinos is,

$$\nu_l(\bar{\nu}_l) + N \rightarrow \nu_l(\bar{\nu}_l) + N, \quad (1.22)$$

where $N = p, n$.

The quasi-elastic scattering charged current interactions of neutrinos and anti-neutrinos with nucleons are described by,

$$\nu_l + n \rightarrow p + l^-, \quad (1.23)$$

$$\bar{\nu}_l + p \rightarrow n + l^+, \quad (1.24)$$

where $l = e, \mu, \tau$. The case where the outgoing lepton is a positron is known as *inverse neutron* or *inverse β decay* and is the process used to detect reactor anti-neutrinos.

A neutrino in the ~ 1 GeV energy range can excite the target nucleon to a resonant state. The baryonic resonance (Δ, N^*) can decay to a variety of mesonic final states, for example a nucleon and a pion [29].

The deep inelastic scattering (DIS) process is the dominant CC neutrino-nucleon interaction for the energy range $E_\nu \gg m_N$. With enough energy the neutrino interacts with individual quarks rather than the nucleon as a whole, resulting in a hadronic shower [29]. The process is described by,

$$\nu_l(\bar{\nu}_l) + N \rightarrow l^\mp + X, \quad (1.25)$$

where $l = e, \mu, \tau$, $N = p, n$ and X is any final hadronic product.

High energy neutrino- and anti-neutrino-nucleon interactions can also occur through the NC DIS process,

$$\nu_l(\bar{\nu}_l) + N \rightarrow \nu_l(\bar{\nu}_l) + X, \quad (1.26)$$

where $N = p, n$ and X is the final hadronic product.

1.4 Neutrino Sources

Neutrinos are some of the most abundant particles in the universe. Our detection and understanding of them may improve our knowledge of a broad range of physics

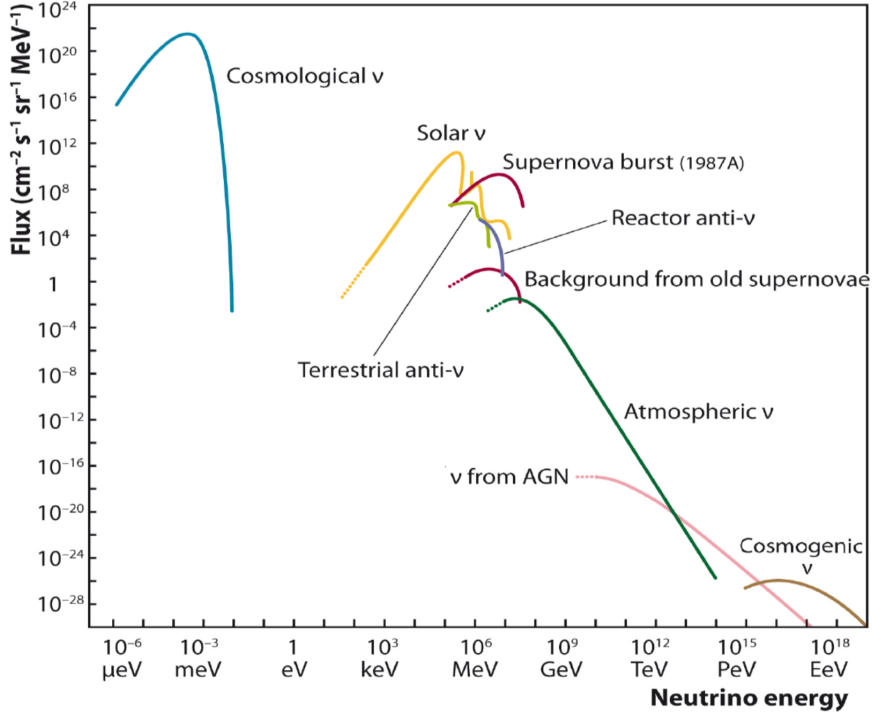


Figure 1.7: Neutrino flux at the Earth’s surface [30].

processes. Figure 1.7 shows a plot of the neutrino flux at the Earth’s surface from a variety of different sources.

1.4.1 Solar Neutrinos

The sun generates its energy from thermonuclear fusion reactions. There are two fusion chains, pp and CNO, which form the Standard Solar Model (SSM). These thermonuclear reactions release energy in the form of photons and pure electron neutrinos. The weakly interacting neutrinos pass undisturbed from the solar core into space [28]. John Bahcall, who pioneered the SSM, realised that these neutrinos could be used to test our understanding of solar fusion processes.

The pp chain, which generates 98.4% of the solar neutrino flux, begins as two protons fuse to form a deuterium (heavy hydrogen) nucleus as well as a positron and electron neutrino (**pp** neutrino) [31]. An alternative reaction involving two protons and an electron also forms a deuterium nucleus and electron neutrino (**pep** neutrino), although this is 250 times less likely. The next step in the reaction chain is for the deuterium nucleus to fuse with another proton to form a ${}^3\text{He}$ nucleus.

85% of the time the ${}^3\text{He}$ nucleus will fuse with another, forming a ${}^4\text{He}$ nucleus and two protons, completing the ppI cycle. Once every 5 million completions of the pp chain the ${}^3\text{He}$ nucleus will fuse with another proton, forming a ${}^4\text{He}$ nucleus and an electron neutrino (**hep** neutrino). 15% of the time the ${}^3\text{He}$ nucleus fuses with a ${}^4\text{He}$ nucleus to

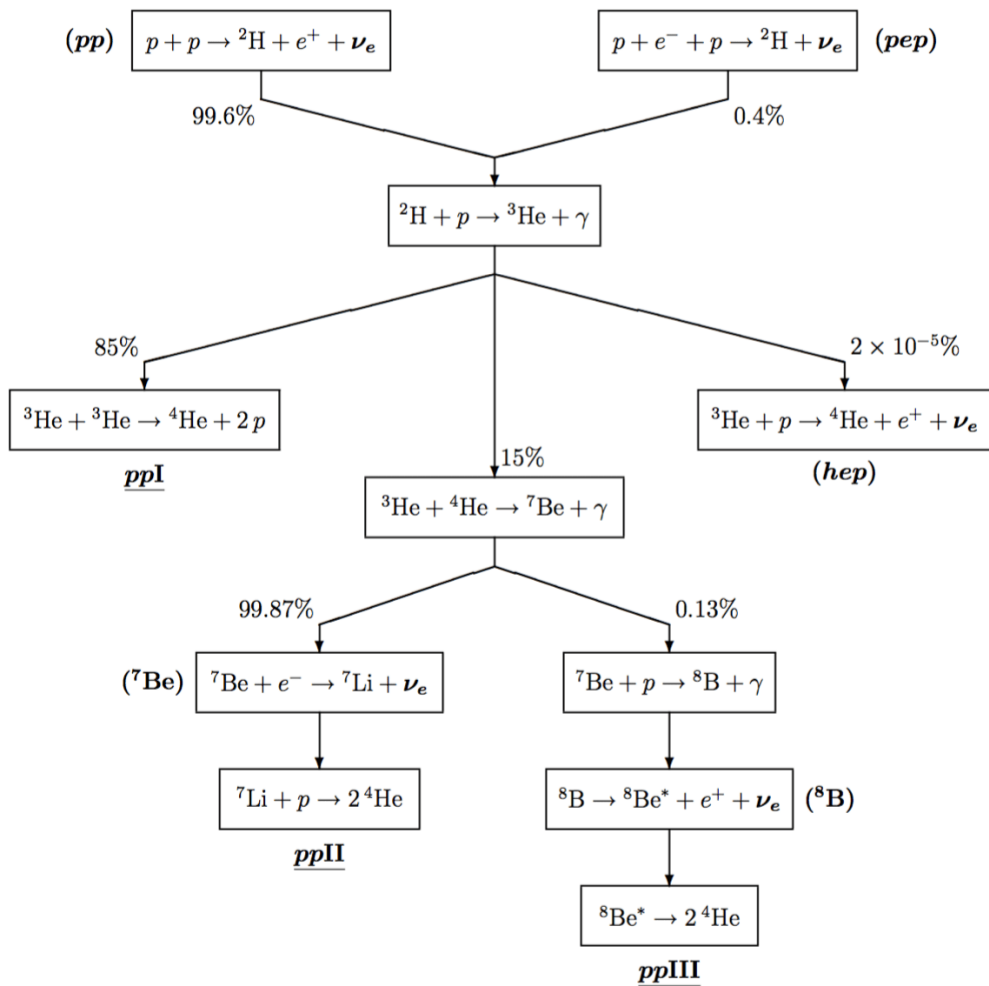


Figure 1.8: The *pp* cycle [28].

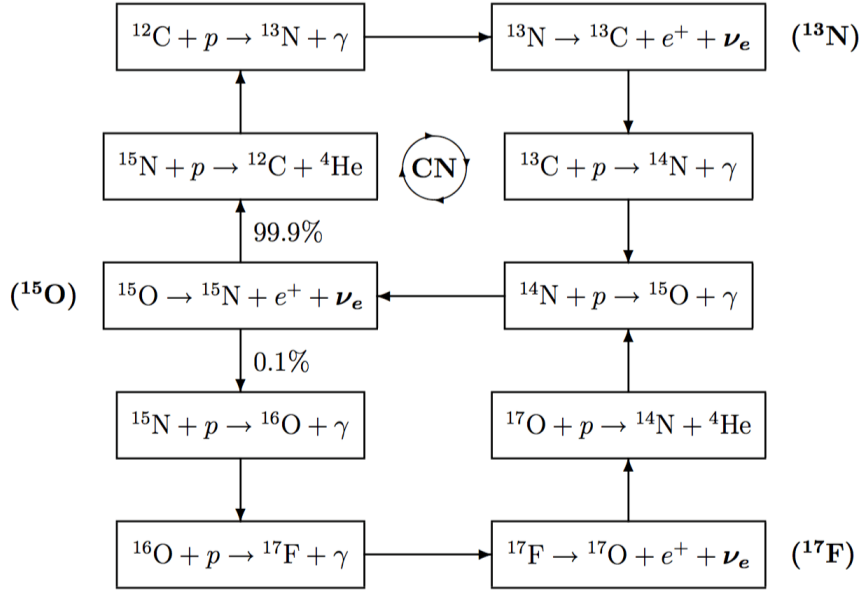


Figure 1.9: The CNO cycle [28].

create a ^7Be nucleus.

The ^7Be nucleus then absorbs an electron and transmutes into a ^7Li nucleus and an electron neutrino (^7Be neutrino). The ^7Li nucleus fuses with another proton, forming two ^4He nuclei, completing the ppII cycle. Approximately once every 5000 completions of the pp chain, rather than absorbing an electron the ^7Be nucleus instead fuses with another proton, forming a ^8B nucleus. The ^8B nucleus then decays into two ^4He nuclei, emitting an electron neutrino (^8B neutrino) and completing the ppIII cycle. See Figure 1.8.

The other fusion chain, called the Carbon-Nitrogen-Oxygen (CNO) cycle, is responsible for 1.6% of the solar neutrino flux. See Figure 1.9. Three neutrinos are produced: ^{15}O and ^{17}Fe neutrinos are less than 1.7 MeV, and the ^{13}N neutrino is less than 1.2 MeV.

The predicted solar flux from the pp and CNO cycles can be seen in Figure 1.10. Most of the flux is from pp neutrinos, however only gallium experiments are sensitive to some of these. Chlorine experiments can only see part of the ^7Be neutrino spectra, while water Cherenkov experiments are only sensitive to ^8B and hep neutrinos. The hep spectrum is dominated by ^8B except for very high energies.

The total solar flux is about $6 \times 10^{10} \text{ cm}^{-2}\text{s}^{-1}$ [28] and is the dominant source of neutrinos on Earth.

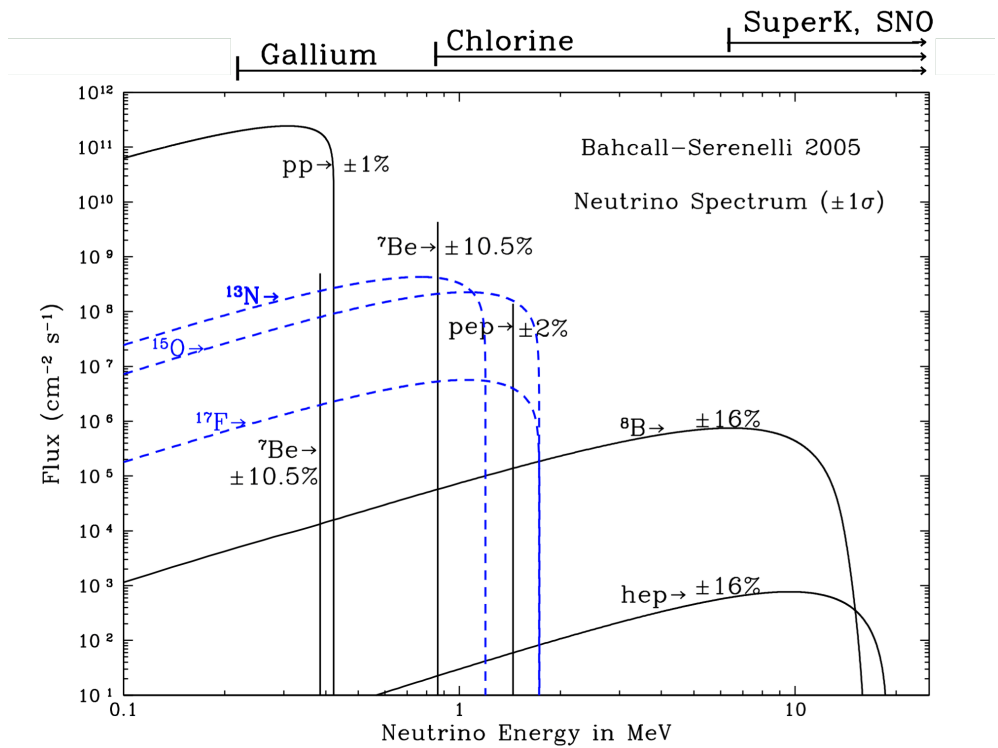


Figure 1.10: Energy spectra of the pp chain and CNO cycle solar neutrino flux predicted by the BS05(OP) SSM. For the continuous sources the differential flux is in $\text{cm}^{-2}\text{s}^{-1}\text{MeV}^{-1}$ units, while the units for the discrete sources is $\text{cm}^{-2}\text{s}^{-1}$. The percentages represent the uncertainties. The energy ranges probed by different experiment types are shown. Adapted from [32].

1.4.2 Accelerator

For many desired measurements it is necessary to produce our own neutrinos. This is done by accelerating protons with a synchrotron and firing them at a fixed target, creating pions and kaons. A magnetic field focusses the mesons with the correct charge into a beam. The beam then enters a decay tunnel where the mesons decay, mostly to muons and muon neutrinos [28],

$$\pi, K \rightarrow \mu^+ + \nu_\mu. \quad (1.27)$$

The muons decay via $\mu^+ \rightarrow e^+ + \bar{\nu}_\mu + \nu_e$, contaminating the beam, but most of these muons and undecayed mesons are absorbed by shielding at the end of the tunnel. The detector is located further down the beam line.

1.4.3 Reactor

Nuclear reactors are a plentiful source of $\bar{\nu}_e$ anti-neutrinos, produced during β decays from the decay chains of unstable fissioning isotopes. The majority of the nuclear fission in a reactor is from the isotopes ^{235}U ($\approx 56\%$), ^{239}Pu ($\approx 30\%$), ^{238}U ($\approx 8\%$), and ^{241}Pu ($\approx 6\%$) [28].

The $\bar{\nu}_e$ output is approximately $2 \times 10^{20} \text{ s}^{-1}$ per GW of thermal power, with a typical reactor producing 3 GW of thermal power. However, these neutrinos are emitted isotropically, and the flux falls as the inverse square of the distance from the reactor.

Reactor $\bar{\nu}_e$ anti-neutrinos interact via the inverse β decay reaction,

$$\bar{\nu}_e + p \rightarrow e^+ + n. \quad (1.28)$$

The threshold for the energy of the neutrino to enable this reaction is 1.8 MeV, and can be observed from the positron and subsequent neutron capture. See Figure 1.11 for the expected $\bar{\nu}_e$ flux and interactions in a detector. SNO+ will be able to measure anti-neutrinos from surrounding reactors.

1.4.4 Geological

Unstable radioactive isotopes inside the earth (mostly ^{238}U , ^{232}Th and ^{40}K) β decay to produce $\bar{\nu}_e$ geo-neutrinos [34].

These decays are a major generator of geothermal heat, the specific output dependent on the quantity of radioactive material inside Earth. Data is hard to come by beyond the Earth's crust, but measurements of geo-neutrinos provide a method of probing deep inside the Earth's interior.

SNO+ is sensitive to geo-neutrinos from the ^{238}U and ^{232}Th chains. Geo-neutrinos from ^{40}K decays are below the 1.8 MeV threshold needed for inverse beta decay.

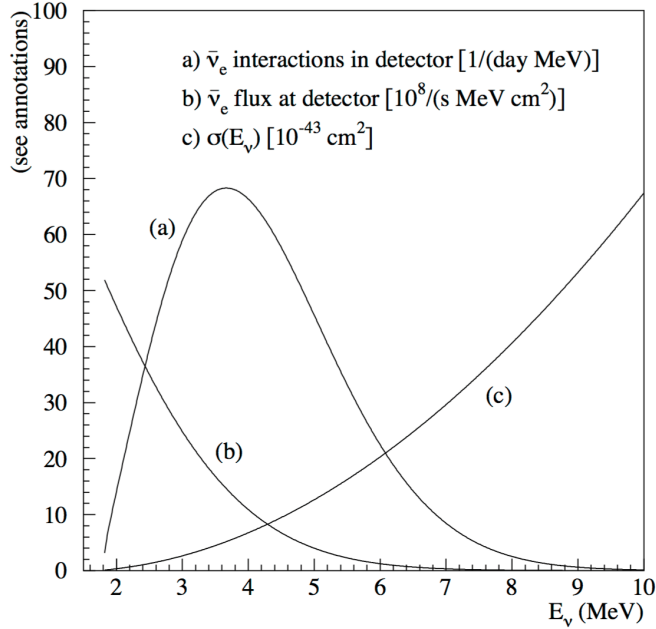


Figure 1.11: Reactor $\bar{\nu}_e$ flux, inverse beta decay, and interaction spectrum [33].

1.4.5 Atmospheric

Primary cosmic rays from space are constantly colliding with the Earth's atmosphere. These primary cosmic rays are mostly protons, with a small constituent of alpha particles and other heavier nuclei [28]. The flux spectrum for primary cosmic rays peaks in the GeV region and decreases at higher energies according to a power law. As these primary cosmic rays collide with nuclei in the atmosphere, they generate a hadronic shower of *secondary* cosmic rays. These hadrons include pions which decay to create atmospheric neutrinos (see Figure 1.12). The decay chains for this reaction are:

$$\pi^+ \rightarrow \mu^+ + \nu_\mu, \quad \mu^+ \rightarrow e^+ + \nu_e + \bar{\nu}_\mu. \quad (1.29)$$

$$\pi^- \rightarrow \mu^- + \bar{\nu}_\mu, \quad \mu^- \rightarrow e^- + \bar{\nu}_e + \nu_\mu. \quad (1.30)$$

1.4.6 Cosmological

Cosmological, or *relic*, neutrinos were created during the early evolution of the universe. When the universe was hot enough (above 10^{10} K), neutrinos were in thermal equilibrium with photons through reactions such as $\gamma + \gamma \leftrightarrow \nu + \bar{\nu}$ [35]. As the universe expanded and the temperature dropped below this point the neutrinos decoupled from the rest of the universe, known as the neutrino *freeze out*. These neutrinos continued to cool as the universe expanded. Models suggest they currently have energy $\sim 10^{-4}$ eV and a number density $\approx 56 \text{ cm}^{-3}$ [35]. As their low energy is well below the electron mass they only interact very rarely via NC interactions. Consequently they are

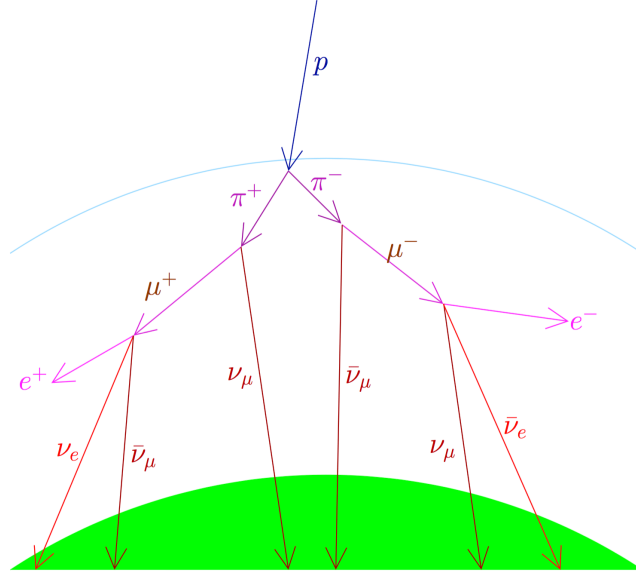


Figure 1.12: Cosmic ray interactions creating atmospheric neutrinos [28].

very hard to detect, but if they were information may be revealed about the early universe, analogously to the detection of the relic photons comprising the cosmic microwave background (CMB).

1.4.7 Supernovae

Supernovae explosions are powerful events that end the lives of stars. They eject mass into space with energy $\sim 10^{51}$ erg [28]. Some of these supernovae produce neutron stars or black holes.

The most common neutrino producing supernovae are caused by iron core collapse [36]. They also have the most well defined predictions for neutrino emission fluxes. A star is stable against its own gravity because of nuclear fusion from H to He. As H becomes depleted in the core the star contracts, raising the temperature and density. Fusion then occurs by three He nuclei fusing into a C nucleus. As the He is exhausted the star contracts further and progresses to the fusion of heavier nuclei until the star has a dense iron core. It is energetically unfavourable for iron nuclei to undergo nuclear fusion. The core then collapses under gravity and, heated by the compression, the iron nuclei separate into individual nucleons [35]. Electrons are then captured on the free protons, converting most of them into neutrons and releasing a *neutronisation burst* of $\bar{\nu}_e$ s, via the reaction,

$$e^- + p \rightarrow n + \bar{\nu}_e. \quad (1.31)$$

When the collapsed neutron core reaches sufficient density, a shock wave ejects matter out of the star, causing the visible explosion. Approximately 99% of the energy released by supernovae is in the form of neutrinos. The neutrinos are produced in

flavour blind processes such as $\gamma + \gamma \rightarrow \nu_\alpha + \bar{\nu}_\alpha$, so all six neutrino species make an approximately equal contribution to the energy output.

Over the last millennium many supernovae have been observed both by the naked eye and, in more recent centuries, by telescope. The most recently observed local supernova, SN1987A, occurred on 23rd February 1987 in the Large Magellanic Cloud (a satellite galaxy of the milky way). It was the first to be observed by the naked eye since Kepler in 1604, and is the only supernova to have been observed with neutrino detectors. Kamiokande-II [37], IMB [38], Baksan [39], and LSD [40] were all operational at the time of the event, although only sensitive to $\bar{\nu}_{eS}$ via inverse beta decay. They observed an unusual number of events of energy ~ 10 MeV within a time window of 10 s, except LSD which measured its 5 hours earlier and so is usually excluded from analysis [28]. These neutrinos were detected hours before the optical discovery of SN1987A. In total 24 neutrinos were observed.

Since the vast majority of supernovae are extra-galactic, a flux superposing all sources is expected. The flux is approximately isotropic with some anisotropy due to closer and more powerful supernovae. This is known as the diffuse supernovae neutrino background (DSNB). The DSNB has a small flux and is yet to be detected [41].

SNO+ will be sensitive to local supernova neutrinos, should a galactic supernova event occur during the operational period.

1.4.8 Cosmic neutrinos

Cosmic rays as high as 10^{20} eV are known to exist. For highest energy cosmic rays the sources and composition are not known. The flux above $\sim 3 \times 10^{18}$ eV is most likely dominated by extra-Galactic sources of ultra-high energy (UHE) protons.

UHE neutrinos are thought to be produced by collisions of UHE protons with photons or mesons in the radiation field of their sources. This result in pions which decay to UHE neutrinos. The detection of UHE neutrinos may provide information for models of proton acceleration mechanisms, for example gamma-ray bursts (GRBs) or active galactic nuclei (AGN) jets [42].

Another mechanism for the production of UHE neutrinos is UHE protons interacting with CMB photons. This results in a theoretical upper limit on the spectrum of cosmic rays, known as the Greisen-Zatsepin-Kuzmin (GZK) limit, and produces GZK neutrinos.

UHE neutrinos have small fluxes and broad energy ranges, they require very large neutrino telescopes to detect them. IceCUBE has observed extra-terrestrial neutrinos up to ~ 2 PeV [43].

1.5 Neutrino Detection

1.5.1 Radiochemical Detectors

Radiochemical detectors are used to detect neutrino interactions via the inverse β decay process. The detector is then flushed to collect the resultant daughter nuclei, $\mathcal{N}(A, Z + 1)$, in order to count them. The daughters must be unstable and decay with a short half-life, but not too short that they decay immediately in the detector. This method gives the number of interactions in the detector, but no other information about the interaction. The radiochemical detection method was famously used by the Homestake experiment [16], which used chlorine, and the GALLEX/GNO [44, 45] and SAGE [46] gallium experiments.

1.5.2 Tracking Detectors

There are a number of different ways to design a tracking detector, but they all have good event position, direction and energy reconstruction. One design is the “club sandwich” in which passive layers, for the neutrino to interact with, alternate with active layers, which detect the charged particles. There are many candidates for the active medium, such as the emulsion plates used by the DONUT experiment [25] as described in Section 1.1.4. Alternatively, rather than having separate passive and active layers, if the active medium is dense enough it can be segmented, such as in the NO ν A experiment [47].

A further possibility is the Time Projection Chamber (TPC) in which free electrons created by particle interactions are drifted and measured. The drift time and measured position of the drifted electron enables the path of the particle to be reconstructed, as well as the energy from the signal amplitude. In this way a large volume experiment with good reconstruction can be done at relatively low cost. Liquid argon has been chosen as the interaction medium for the next generation experiment DUNE [48].

1.5.3 Water Cherenkov Detectors

When a charged particle travels through a medium faster than the speed of light in said medium ($n\beta > 1$), a cone of Cherenkov photons are radiated [49]. Here n is the refractive index of the water and $\beta = v/c$ is the relativistic velocity of the particle. A popular material used for detectors taking advantage of this process is water. The cone has an angle of

$$\cos \theta_c = \frac{1}{n\beta} \quad (1.32)$$

relative to the direction of travel of the particle, and the rate of energy loss for the charged particle is given by [50],

$$\frac{dE}{dx} = \left(\frac{e}{c}\right)^2 \int_{n\beta>1} \left[1 - \left(\frac{1}{n\beta}\right)\right] \omega d\omega, \quad (1.33)$$

where e is the electron charge and x is a coordinate along the track. The integral over the photon frequency, ω , is such that the Cherenkov emission condition ($n\beta > 1$) is met. The energy lost by an ionising particle tends to be dominated by ionisation, rather than Cherenkov emission, which will define the distance travelled above the Cherenkov threshold.

From Equation 1.33 can be derived the photon emission spectrum [28],

$$\frac{dN}{d\lambda dx} = 2\pi\alpha \left[1 - \left(\frac{1}{n\beta} \right)^2 \right] \lambda^{-2}, \quad (1.34)$$

where α is the fine structure constant, N is the number of photons, λ is the wavelength.

Water has a refractive index of $n \simeq 1.33$, resulting in an angle $\theta_c \simeq 41^\circ$. As the charged particle loses energy and goes beneath the Cherenkov threshold it stops radiating photons. By detecting the Cherenkov photons, the position, direction and energy of the charged particle can be determined. Electrons can be distinguished from muons because they have a fuzzier ring due to electron scattering [31]. However identification of particles with similar signatures, for example muons and pions, is not possible. Famous examples of water Cherenkov detectors are Super-Kamiokande [51] and SNO [52]. SNO+ will have an initial water phase which will therefore observe Cherenkov events.

1.5.4 Scintillation Detectors

As a charged particle traverses a volume of scintillator its energy is absorbed and emitted as light. The wavelength of the photons emitted by the scintillator depends on the specific material's characteristic spectrum. There are a number of different materials which scintillate, including inorganic crystals (such as lead tungstate used by CMS [53]), organic plastics (such as extruded polystyrene used by SciBooNE [54]), and organic liquids (such as mineral oil used by MiniBooNE [55]).

In a detector the volume of scintillator is surrounded by photodetectors. Using the timing of the signals from the photodetectors, position reconstruction may be possible, but direction reconstruction is poor because the light is emitted isotropically. However, if the scintillator is segmented, such as for NO ν A, direction is possible. One advantage of scintillator over water Cherenkov detectors is the improvement in energy reconstruction because of the greater number of photons produced. Famous examples of scintillator neutrino experiments are MiniBooNE [55] and KamLAND [56].

The acrylic vessel in SNO+ will be filled with the organic liquid scintillator linear alkyl benzene (LAB) after an initial water phase. LAB (and indeed scintillator in general) has a lower energy threshold than water, so SNO+ will be able to observe lower energy physics than SNO.

1.6 Beyond the Standard Model

As more was discovered about neutrinos, a number of anomalies with Standard Model predictions were observed. This section outlines some of the unusual behaviour of neutrinos that necessitates modification of the SM.

1.6.1 Neutrino Anomalies

1.6.1.1 Solar Neutrinos

In the 1960s Raymond Davis set about detecting solar neutrinos using his Homestake experiment, located in the Homestake mine in South Dakota. This deep underground location was chosen to reduce cosmogenic backgrounds. Homestake was a radiochemical experiment, the theory for which is described in Section 1.5.1. Davis used 615 tons of dry cleaning fluid, containing chlorine, as the interaction medium.

Solar electron neutrinos were observing using inverse β decay with chlorine atoms,



The tank of fluid was flushed periodically to extract the argon atoms. About 16 argon atoms were measured every other month, compared to about 30 produced, due to an extraction efficiency of about 90% and the decay of some atoms prior to extraction [28]. Homestake measured the solar neutrino flux over a period of about 30 years. Davis, alongside Masatoshi Koshiba, won the 2002 Physics Nobel Prize for detecting extra-terrestrial neutrinos.

SAGE and GALLEX started taking data in 1990 and 1991 respectively. They were also radiochemical experiments, but used gallium to observe solar electron neutrinos through the inverse β decay process,



The Kamiokande detector, a large water Cherenkov experiment intended to search for nucleon decay, turned on in 1985. Kamiokande was also able to measure solar neutrinos via elastic neutrino-electron scattering, $\nu_e + e^- \rightarrow \nu_e + e^-$.

While all these experiments observed solar electron neutrinos, they complemented each other because of their different detection techniques. The chlorine and gallium experiments could only measure the event rate, but had a lower energy threshold, gallium particularly so. Kamiokande was only sensitive to the higher energy ${}^8\text{B}$ neutrinos, but could measure their energies, and using direction reconstruction could make cuts based on the position of the Sun. See Figure 1.10 for the different experiment's energy thresholds.

All the above experiments measured a neutrino flux that was below theoretical predictions, this was known as the *solar neutrino problem*. The deficit in the solar

Total Rates: Standard Model vs. Experiment

Bahcall–Pinsonneault 2000

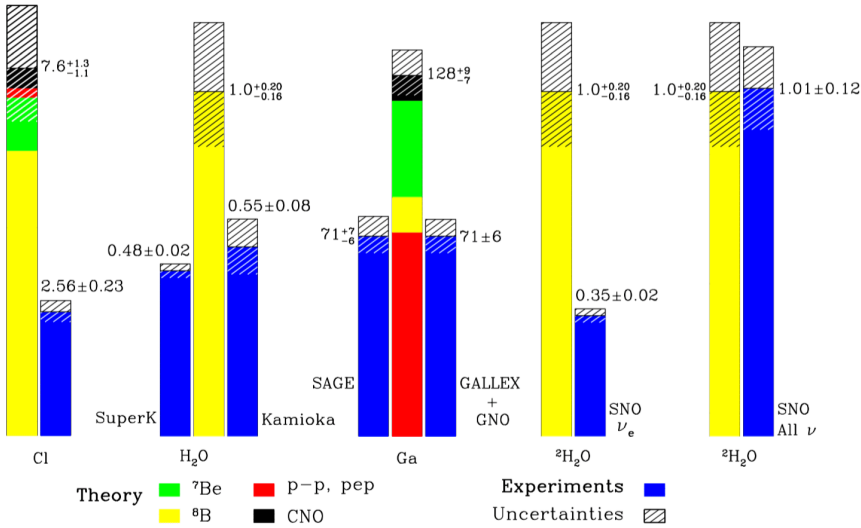


Figure 1.13: Comparisons between the predicted flux from the Standard Solar Model and the total observed flux for the different solar neutrino counting experiments. The experiments are Homestake, Super-Kamiokande, Kamiokande, SAGE, GALLEX, and SNO. Cross hatching shows the 1σ uncertainties [1].

neutrino flux for each experiment, compared to theoretical predictions, can be seen in Figure 1.13.

1.6.1.2 Atmospheric Neutrinos

In the 1980s precise measurements of the atmospheric neutrino flux were attempted. The processes by which atmospheric neutrinos are created are described in Section 1.4.5. Twice as many atmospheric muon flavour neutrinos than atmospheric electron flavour neutrinos are expected at the Earth’s surface. This ratio increases as the neutrino energy increases because higher energy muons are less likely to decay in flight. NUSEX [57], Fréjus [58], Soudan 2 [59], MACRO [60], Kamiokande [61], and IMB [62] were all able to measure atmospheric neutrinos.

NUSEX and Fréjus did not observe an anomaly, but each of the other experiments demonstrated a lower ν_μ to ν_e flux ratio than was theoretically predicted. However, the Kamiokande experiment, with its direction reconstruction capability, showed that the ν_μ to ν_e flux ratio was larger for neutrinos coming from above than below [63].

1.6.2 Solution to the Solar and Atmospheric Neutrino Problems

The study of helioseismology, the measurement of the propagation of acoustic waves from the Sun provides additional evidence for the accuracy of the SSM, as the relative

abundance of different elements in the Sun's core affects the propagation of these waves. A deficit in neutrinos produced in the Sun could not therefore explain the atmospheric neutrino anomaly [64].

One hypothesis was that as a neutrino, produced with one particular flavour, propagates, there is a probability of it being detected as another flavour. This would account for the lower ν_e rates for solar experiments and the lower ν_μ rates for atmospheric experiments.

New experiments were built in order to address this question. Super-Kamiokande (SK) was an improved and larger version of its predecessor. SK showed that atmospheric ν_μ neutrinos were disappearing, and that the disappearance rate depended on neutrino energy and distance travelled (inferred from the zenith angle) [51]. Figure 1.14 shows the measured angular and energy dependence of the atmospheric ν_μ flux. SK also confirmed the solar ν_e deficit observed by Kamiokande.

Homestake and the other radiochemical experiments were only sensitive to ν_e solar neutrinos. This is because solar neutrino energies (less than ≈ 30 MeV) are insufficient to produce μs or τs . The Sudbury Neutrino Observatory (SNO) was built in order to make a flavour independent measurement of the ^8B neutrino flux [65], and thus demonstrate flavour change. This was done by using heavy water as the target material. Heavy water contains deuterium, rather than hydrogen, which contains a proton and a neutron in its nuclei. Deuterium has a 2.2 MeV threshold to be broken apart via NC DIS, so ^8B neutrinos have sufficient energy whatever their flavour.

The different processes SNO was able to detect were:

- Charged-current (CC) interaction,

$$\nu_e + {}^2\text{H} \rightarrow p + p + e^- . \quad (1.37)$$

This channel was observed by measuring the outgoing electron and can only measure the flux of the electron neutrinos, $\phi(\nu_e)$.

- Elastic scattering (ES) interaction,

$$\nu_\alpha + e^- \rightarrow \nu_\alpha + e^- . \quad (1.38)$$

The outgoing electron was observed and distinguished from the CC produced electrons by its kinematics. The ν_e s can interact via the CC or NC processes, however $\nu_{\mu,\tau}$ neutrinos can only interact via the NC process. This interaction measured the combined neutrino flux, $\phi(\nu_e) + 0.15(\phi(\nu_\mu) + \phi(\nu_\tau))$.

- Neutral current (NC) interaction:

$$\nu_\alpha + {}^2\text{H} \rightarrow n + p + \nu_\alpha . \quad (1.39)$$

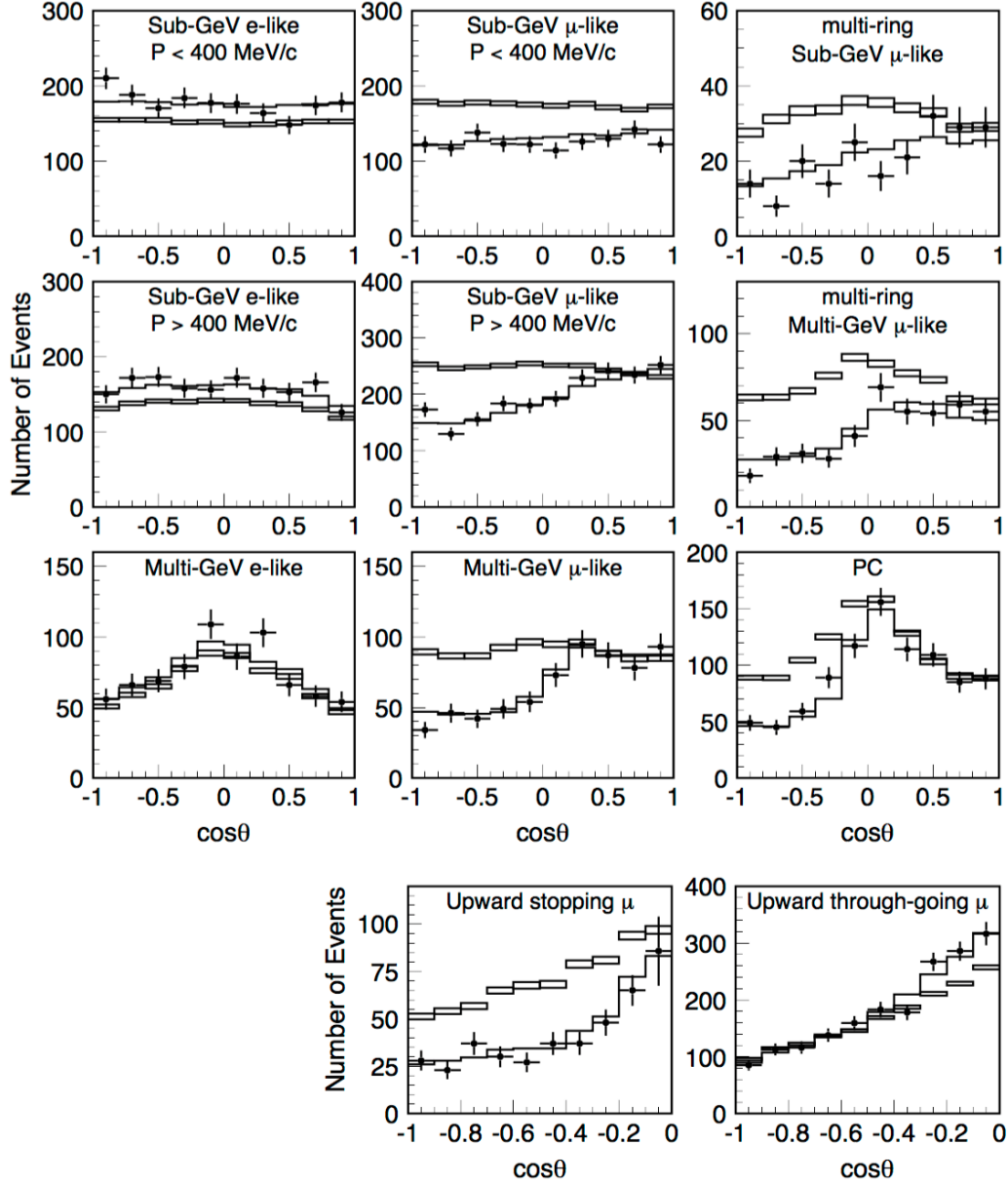


Figure 1.14: Zenith angle distribution for SK events. The points show the data, box histograms show the non-oscillated Monte Carlo events (heights representing the statistical error) and the lines show the best-fit expectations for $\nu_\mu \leftrightarrow \nu_\tau$ oscillations with $\sin^2 2\theta = 1.00$ and $\Delta m^2 = 2.1 \times 10^{-3} \text{ eV}^2$ [51].

This channel was observed by measuring photons from neutron capture. During Phase I of SNO neutrons were captured on deuterons, emitting a single 6.25 MeV γ ray. The secondary Compton electrons and e^+e^- pairs produced then created Cherenkov light, detectable by the PMTs. For Phase II (the salt phase) 2×10^3 kg of NaCl was added because ^{35}Cl nuclei have a larger capture cross-section. They also release 8.6 MeV across multiple γ rays, thus increasing neutron event identification. For Phase III an array of proportional counters were added which detected neutrons via the reaction $^3\text{He} + n \rightarrow ^3\text{H} + p$ [66]. The NC interaction is equally sensitive to all neutrino flavours and so measures the total flux, $\phi(\nu_e) + \phi(\nu_\mu) + \phi(\nu_\tau)$.

Figure 1.13 shows that the total flux for all three neutrino species observed by SNO was approximately three times larger than $\phi(\nu_e)$. The total flux also matches closely the prediction from the standard solar model (SSM). The results of the SNO neutrino flavour transformation analysis is represented by the $\nu_{\mu,\tau}$ flux versus the ν_e flux in Figure 1.15. It can be seen that there is good agreement with the total flux from the SSM. This established that the electron neutrinos produced in the Sun were oscillating into muon or tau-type neutrinos on their way to Earth.

Further evidence for the oscillation solution came from the KamLAND detector located in the Kamioka mine in Japan [67]. KamLAND used a 13 m diameter transparent nylon balloon filled with 1 kton liquid scintillator, surrounded by 1325 17-inch PMTs. Its primary purpose was to observe the oscillation of $\bar{\nu}_e$ s emitted by nuclear reactors. The $\bar{\nu}_e$ flux was dominated by a few powerful reactors at an average distance of ~ 180 km.

KamLAND observed anti-neutrinos through the inverse beta decay interaction, $\bar{\nu}_e + p \rightarrow n + e^+$. Ionisation from the positron would result in a prompt signal from scintillation light. Subsequently a 2.2 MeV γ ray would be emitted by neutron capture. This delayed coincidence distinguished the $\bar{\nu}_e$ signal from non-anti-neutrino backgrounds. An energy threshold of 2.6 MeV was applied to reduce the geo-neutrino background. After applying cuts, the ratio of observed flux was $0.611 \pm 0.085(\text{stat}) \pm 0.041(\text{syst})$ compared to the expectation from the no oscillation scenario. The expected prompt positron spectrum with no oscillation, as well as the KamLAND data and a best fit under a two-neutrino flavour oscillation scenario, is shown in Figure 1.16.

1.6.3 Neutrino Flavour Oscillations

Neutrino oscillation is a quantum mechanical process, by which a neutrino can be created as one flavour and observed some time and distance later as a different flavour. The observation of this flavour change implies a non-zero neutrino mass and is described by the mixing of three neutrino mass eigenstates ν_1, ν_2, ν_3 . A neutrino state $|\nu_\alpha\rangle$, of

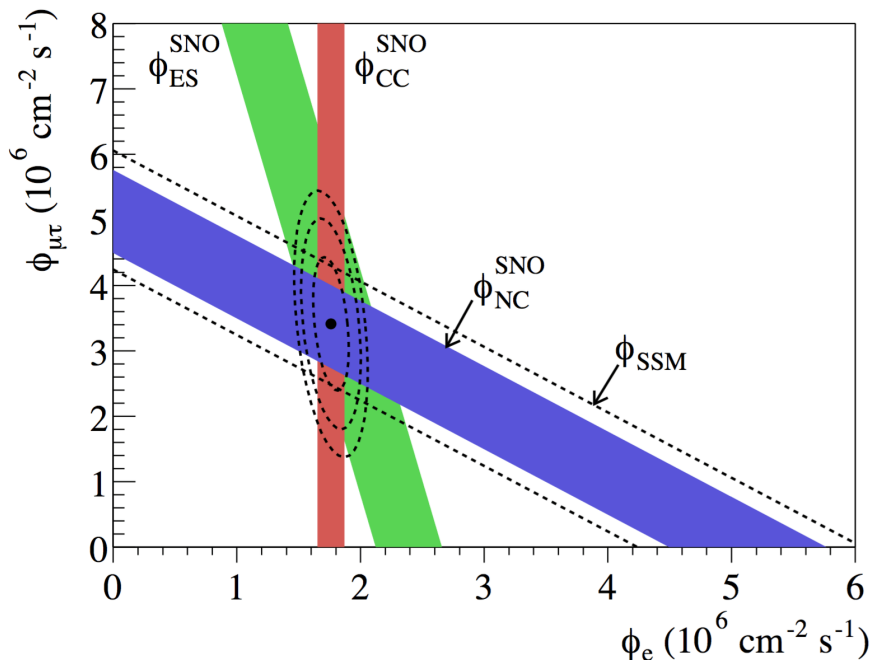


Figure 1.15: Flux of muon or tau-type ${}^8\text{B}$ neutrinos, $\phi(\nu_{\mu,\tau})$, versus the ν_e flux, $\phi(\nu_e)$, deduced from the three interactions measured by SNO. The dashed diagonal lines show the total ${}^8\text{B}$ flux predicted by the SSM, and the blue band is the NC measurement. The intercepts with the axis represent the $\pm 1\sigma$ errors. The bands intersect at the fitted values for $\phi(\nu_e)$ and $\phi(\nu_{\mu,\tau})$, demonstrating that the three interaction measurements are consistent with neutrino flavour oscillations [65].

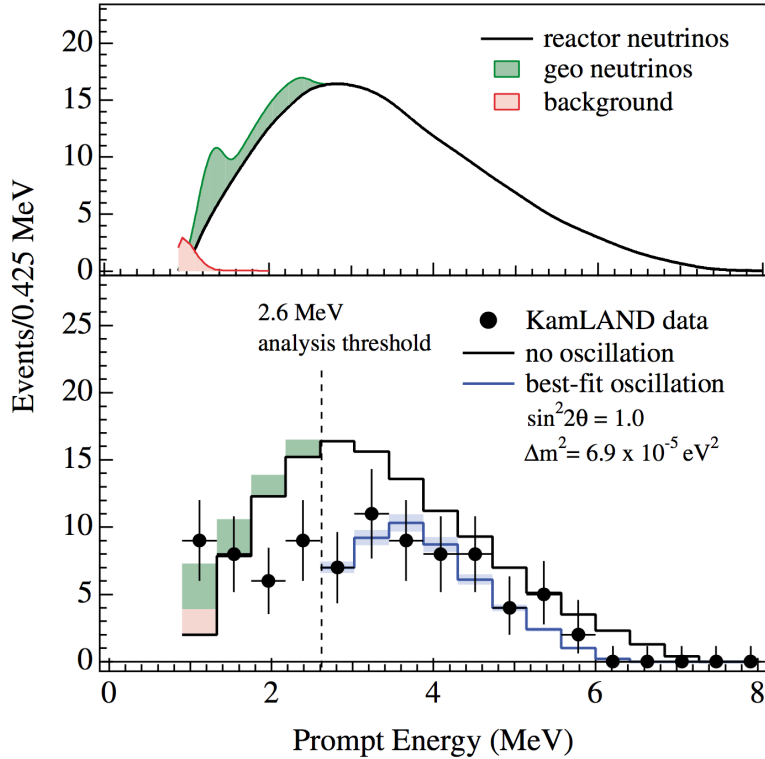


Figure 1.16: Upper panel: Expected $\bar{\nu}_e$ energy spectrum from reactors, geo-neutrinos, and background. Lower panel: Expected prompt positron spectrum with no oscillation, as well as the KamLAND data and a best fit under a two-neutrino flavour oscillation scenario. The shaded bands represent the systematic error for the best-fit spectrum [67].

flavour $\alpha = e, \mu, \tau$, can be written

$$|\nu_\alpha\rangle = \sum_i U_{\alpha i}^* |\nu_i\rangle, \quad (1.40)$$

where U , called the *Pontecorvo-Maki-Nakagawa-Sakata* (PMNS) matrix, is the unitary 3×3 leptonic mixing matrix,

$$U = \begin{pmatrix} U_{e1} & U_{e2} & U_{e3} \\ U_{\mu 1} & U_{\mu 2} & U_{\mu 3} \\ U_{\tau 1} & U_{\tau 2} & U_{\tau 3} \end{pmatrix}. \quad (1.41)$$

Equivalently, the equation for anti-neutrinos is,

$$|\bar{\nu}_\alpha\rangle = \sum_i U_{\alpha i} |\bar{\nu}_i\rangle. \quad (1.42)$$

The PMNS matrix can be written in terms of three mixing angles, θ_{ij} , and a complex phase, δ , related to the CP asymmetry of the lepton sector,

$$U = \begin{pmatrix} 1 & 0 & 0 \\ 0 & c_{23} & s_{23} \\ 0 & -s_{23} & c_{23} \end{pmatrix} \begin{pmatrix} c_{13} & 0 & s_{13}e^{-i\delta} \\ 0 & 1 & 0 \\ -s_{13}e^{i\delta} & 0 & c_{13} \end{pmatrix} \begin{pmatrix} c_{12} & s_{12} & 0 \\ -s_{12} & c_{12} & 0 \\ 0 & 0 & 1 \end{pmatrix}, \quad (1.43)$$

where $c_{ij} = \cos \theta_{ij}$ and $s_{ij} = \sin \theta_{ij}$. Multiplied out the PMNS matrix is expressed,

$$U = \begin{pmatrix} c_{12}c_{13} & s_{12}c_{13} & s_{13}e^{-i\delta} \\ -s_{12}c_{23} - c_{12}s_{23}s_{13}e^{i\delta} & c_{12}c_{23} - s_{12}s_{13}s_{23}e^{i\delta} & c_{13}s_{23} \\ s_{12}s_{23} - c_{12}s_{13}c_{23}e^{i\delta} & -c_{12}s_{23} - s_{12}s_{13}c_{23}e^{i\delta} & c_{13}c_{23} \end{pmatrix}. \quad (1.44)$$

The first matrix is the *solar* or *12-sector*, the second matrix is the *13-sector*, and the third matrix is the *atmospheric* or *23-sector*.

To determine the amplitude of the mixing from one state to another, one must consider the propagation of mass eigenstates,

$$A_{\nu_\alpha \rightarrow \nu_\beta}(t) \equiv \langle \nu_\beta | \nu_\alpha(t) \rangle = \sum_k U_{\alpha k}^* U_{\beta k} e^{-iE_k t}. \quad (1.45)$$

The oscillation probability is then given as,

$$P_{\nu_\alpha \rightarrow \nu_\beta}(t) = |A_{\nu_\alpha \rightarrow \nu_\beta}(t)|^2 = \sum_{k,j} U_{\alpha k}^* U_{\beta k} U_{\alpha j} U_{\beta j}^* e^{-i(E_k - E_j)t}. \quad (1.46)$$

For ultra-relativistic neutrinos the energy difference can be written,

$$E_k - E_j \approx \frac{\Delta m_{kj}^2}{2E}, \quad (1.47)$$

where $\Delta m_{kj}^2 = m_j^2 - m_k^2$ is the *squared mass difference* of the mass eigenstates. These mass splittings are related by,

$$\Delta m_{12}^2 + \Delta m_{23}^2 + \Delta m_{31}^2 = 0, \quad (1.48)$$

and thus only two are independent. As neutrinos travel at almost the speed of light it is also possible to let $t = L$, the distance travelled. The oscillation probability can then be written,

$$P_{\nu_\alpha \rightarrow \nu_\beta}(t) = \delta_{\alpha\beta} - 4 \sum_{k>j} \Re[U_{\alpha k}^* U_{\beta k} U_{\alpha j} U_{\beta j}^*] \sin^2 \left(\frac{\Delta m_{k,j}^2 L}{4E} \right) \\ \pm 2 \sum_{k>j} \Im[U_{\alpha k}^* U_{\beta k} U_{\alpha j} U_{\beta j}^*] \sin \left(\frac{\Delta m_{k,j}^2 L}{2E} \right). \quad (1.49)$$

Equation 1.49 gives the probability of *transition* if $\alpha \neq \beta$, and the probability of *survival* if $\alpha = \beta$. One can see that for a non-zero oscillation probability at least one neutrino mass eigenstate must be non-zero and they cannot be the same. Therefore, the observance of neutrino flavour oscillations demonstrated that neutrinos are massive, contradicting SM predictions.

The minus sign in Equation 1.49 is for anti-neutrinos. The oscillation probability for neutrinos and anti-neutrinos is equivalent if $\delta = 0$ and CP is conserved.

The experimental choice of L , E and the neutrino species determines sensitivity to parameters m , θ and δ .

As it turned out, θ_{12} and Δm_{12}^2 are sensitive to solar neutrinos, although they cannot be extracted directly from a two-flavour oscillation analysis because of the matter effect (see Section 1.6.3.1). Parameters θ_{23} and Δm_{23}^2 are sensitive to atmospheric neutrinos. As a result sometimes Δm_{12}^2 referred to as Δm_{sol}^2 and Δm_{23}^2 is called Δm_{atm}^2 . The results from solar and atmospheric oscillation analyses showed that $0 < \Delta m_{\text{sol}}^2 \ll |\Delta m_{\text{atm}}^2|$, which implies that $\Delta m_{13}^2 \approx \Delta m_{23}^2$.

The neutrino mass eigenstates can be ordered arbitrarily, by convention they are chosen such that Δm_{12}^2 is positive ($m_1 < m_2$). However the sign of Δm_{23}^2 is not known. There are two ordering schemes, the *normal hierarchy* (NH) and the *inverted hierarchy* (IH). In the NH the lightest mass is m_1 and the ordering is such that $m_1 < m_2 \ll m_3$. In the IH the lightest mass is m_3 and the ordering is such that $m_3 \ll m_1 < m_2$. The two neutrino mass hierarchy scenarios are represented in Figure 1.17.

The most up to date values for the oscillation parameters are given in Table 1.1.

1.6.3.1 Neutrino Oscillations in Matter

In 1978, L. Wolfenstein [68] proposed that neutrinos propagating in matter are subject to coherent forward elastic scattering, giving them an additional potential which modifies their mixing.

A neutrino of any flavour can interact with matter via a NC process by exchanging a Z boson with an electron, proton or neutron. Assuming that the matter the neutrino travels through is electrically neutral, the contributions to coherent forward scattering from electrons and protons cancels out. Thus the potential is proportional to the number

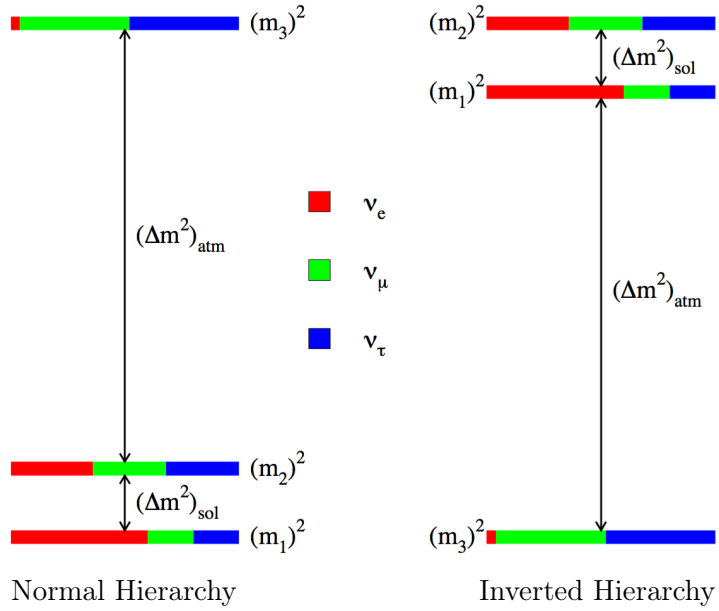


Figure 1.17: A representation of the two mass hierarchy schemes. The colour coding represents the fraction, $|U_{\alpha i}|^2$, of each mass eigenstate represented by each neutrino flavour [1].

Parameter	Best-fit ($\pm 1\sigma$)
$\Delta m_{12}^2 [10^{-5}\text{eV}^2]$	7.53 ± 0.18
$\Delta m_{23}^2 [10^{-3}\text{eV}^2]$, NH	2.44 ± 0.06
$\Delta m_{23}^2 [10^{-3}\text{eV}^2]$, IH	2.52 ± 0.07
$\sin^2(2\theta_{12})$	0.846 ± 0.021
$\sin^2(2\theta_{13})$	$(9.3 \pm 0.8) \times 10^{-2}$
$\sin^2(2\theta_{23})$, NH	$0.999^{+0.001}_{-0.018}$
$\sin^2(2\theta_{23})$, IH	$1.000^{+0.000}_{-0.017}$

Table 1.1: The most up to date three-neutrino mixing scheme parameters for both normal (NH) and inverted (IH) hierarchy scenarios [26].

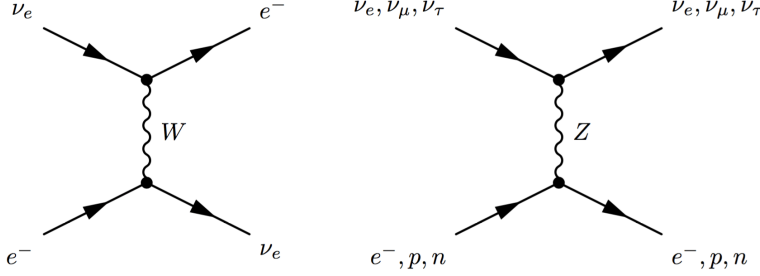


Figure 1.18: Feynman diagrams of the coherent forward elastic scattering processes that generate the CC potential V_{CC} and the NC potential V_{NC} [28].

of neutrons per unit volume, N_n , and is given by [69],

$$V_{NC} = \mp \frac{\sqrt{2}}{2} G_F N_n, \quad (1.50)$$

where the positive sign is for $\bar{\nu}_e$.

Electron neutrinos propagating through matter can interact with electrons via a CC process in which they exchange a W boson. This gives them an additional interaction potential V_{CC} . The interaction potential is proportional to the Fermi coupling constant, G_F , and the number of electrons per unit volume, N_e , and is given by [69],

$$V_{CC} = \pm \sqrt{2} G_F N_e, \quad (1.51)$$

where the positive sign is for ν_e and the negative for $\bar{\nu}_e$. The total potential is therefore given by,

$$V_\alpha = V_{CC} \delta_{\alpha e} + V_{NC} = \sqrt{2} G_F \left(N_e \delta_{\alpha e} - \frac{1}{2} N_n \right). \quad (1.52)$$

Feynman diagrams for the CC and NC processes are shown in Figure 1.18.

The matter potential is described as being analogous to a medium's index of refraction [28]. Neutrinos are affected as they leave the Sun due to the high matter density they pass through. The same effect is experienced on Earth as well, as atmospheric and accelerator produced neutrinos may have to travel long distances through Earth.

The aforementioned observation of neutrino oscillations implies that neutrinos are also mixing when travelling through matter. Neutrino flavour oscillation can be described by the Schrödinger time-evolution equation,

$$i \frac{\partial}{\partial t} |\nu_\alpha(t)\rangle = \mathcal{H} |\nu_\alpha(t)\rangle, \quad (1.53)$$

where \mathcal{H} is the Hamiltonian. The Hamiltonian is the sum of a vacuum component, \mathcal{H}_0 , and potential energy component from matter interactions, \mathcal{H}_m ,

$$\mathcal{H} = \mathcal{H}_0 + \mathcal{H}_m. \quad (1.54)$$

The neutrino mass states are eigenstates of the vacuum Hamiltonian and the neutrino flavour states are eigenstates of the matter Hamiltonian such that,

$$\mathcal{H}_0|\nu_k\rangle = E_k|\nu_k\rangle, \quad (1.55)$$

$$\mathcal{H}_m|\nu_\alpha\rangle = V_\alpha|\nu_\alpha\rangle. \quad (1.56)$$

The amplitude of the $\nu_\alpha \rightarrow \nu_\beta$ transition is $\psi_{\alpha\beta}(t) = \langle \nu_\beta | \nu_\alpha \rangle$, and thus the time evolution of flavour change amplitude is,

$$i \frac{d}{dt} \psi_{\alpha\beta}(t) = \sum_\eta \left(\sum_k U_{\beta k} E_k U_{\eta k}^* + \delta_{\beta\eta} V_\beta \right) \psi_{\alpha\eta}(t). \quad (1.57)$$

By making relativistic approximations the evolution in space becomes,

$$\begin{aligned} i \frac{d}{dL} \psi_{\alpha\beta}(L) &= \left(p + \frac{m_1^2}{2E} + V_{NC} \right) \psi_{\alpha\beta}(L) \\ &\quad + \sum_\eta \left(\sum_k U_{\beta k} \frac{\Delta m_{k1}^2}{2E} U_{\eta k}^* + \delta_{\beta e} \delta_{\eta e} V_{CC} \right) \psi_{\alpha\eta}(L). \end{aligned} \quad (1.58)$$

The first term in this expression is common for all flavours. It can be eliminated by a phase shift which doesn't affect the flavour change probability. Only the second term in the expression is relevant and can be written in matrix form as,

$$i \frac{d}{dL} \Psi_\alpha = \frac{1}{2E} \left(U \mathcal{M}^2 U^\dagger + \mathcal{A} \right) \Psi_\alpha, \quad (1.59)$$

where,

$$\Psi_\alpha = \begin{pmatrix} \psi_{\alpha e} \\ \psi_{\alpha \mu} \\ \psi_{\alpha \tau} \end{pmatrix}, \quad \mathcal{M}^2 = \begin{pmatrix} 0 & 0 & 0 \\ 0 & \Delta m_{12}^2 & 0 \\ 0 & 0 & \Delta m_{13}^2 \end{pmatrix}, \quad \mathcal{A} = \begin{pmatrix} A_{CC} & 0 & 0 \\ 0 & 0 & 0 \\ 0 & 0 & 0 \end{pmatrix}, \quad (1.60)$$

and,

$$A_{CC} \equiv 2E V_{CC} = \pm 2\sqrt{2} E G_F N_e. \quad (1.61)$$

For simplicity, the following considers two-neutrino species mixing. Making a suitable transformation the evolution Equation 1.59 can become,

$$i \frac{d}{dL} \begin{pmatrix} \psi_{ee} \\ \psi_{e\mu} \end{pmatrix} = \frac{1}{4E} \begin{pmatrix} -\Delta m_M^2 \cos 2\theta_M & \Delta m_M^2 \sin 2\theta_M \\ \Delta m_M^2 \sin 2\theta_M & \Delta m_M^2 \cos 2\theta_M \end{pmatrix} \begin{pmatrix} \psi_{ee} \\ \psi_{e\mu} \end{pmatrix}, \quad (1.62)$$

where θ_M is an effective matter mixing angle obeying the following relations,

$$\cos 2\theta_M = \frac{\Delta m^2 \cos 2\theta - A_{CC}}{\Delta m_M^2}, \text{ and } \sin 2\theta_M = \frac{\Delta m^2 \sin 2\theta}{\Delta m_M^2}, \quad (1.63)$$

and the effective squared mass difference is given by,

$$\Delta m_M^2 = \sqrt{(\Delta m^2 \cos 2\theta - A_{CC})^2 + (\Delta m^2 \sin 2\theta)^2}. \quad (1.64)$$

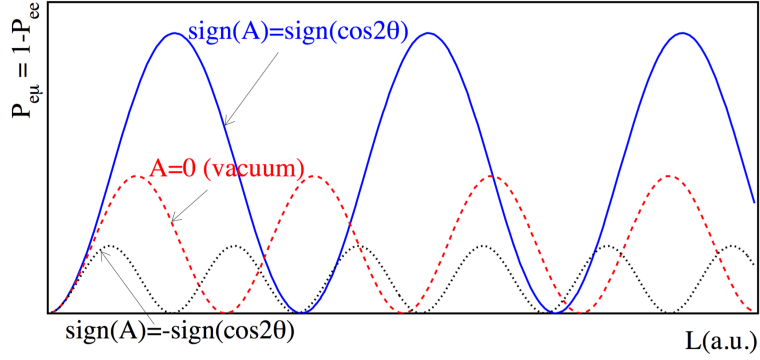


Figure 1.19: Flavour transition probability as a function of L in vacuum and matter for neutrinos (blue) and anti-neutrinos (black) [1].

Assuming a constant matter density ($d\theta_M/dx = 0$), this leads to the transition probability,

$$P_{\nu_e \rightarrow \nu_\mu}(L) = \sin^2 2\theta_M \sin^2 \left(\frac{\Delta m_M^2 L}{4E} \right), \quad (1.65)$$

which has the same structure as two-neutrino flavour change probability in a vacuum. It can be seen that for small L matter effects are not important. For many shorter baseline oscillation experiments they do not need to be accounted for.

This demonstrates that neutrinos and anti-neutrinos will oscillate differently under the presence of matter, because of its electron rather than positron composition. Figure 1.19 shows the transition probability $P_{\nu_e \rightarrow \nu_\mu}$ in vacuum and matter. For neutrinos, when the sign of A_{CC} agrees, there is an enhancement of the transition amplitude, $\sin^2 2\theta_M > \sin^2 2\theta$. It can also be seen that the oscillation length increases in matter. The opposite is true in the case of anti-neutrinos.

The oscillation enhancement is optimal when $A_{CC} = \Delta m^2 \cos 2\theta$, the *MSW resonance condition*, named after Mikheyev, Smirnov, and Wolfenstein. In this instance, mixing in matter is maximal ($\theta_M = \pi/4$). The corresponding resonant electron density is,

$$N_e^R = \frac{\Delta m^2 \cos 2\theta}{2E\sqrt{2}G_F}. \quad (1.66)$$

If the matter density is not constant it is necessary to take the effect of $d\theta_M/dx$ into account. Figure 1.20 shows how θ_M and Δm_M^2 behave as they cross resonance for $\Delta m^2 = 7 \times 10^{-6} \text{ eV}^2$, $\sin^2 2\theta = 10^{-3}$. For a neutrino created in the centre of the Sun, where $N_e \gg N_e^R$, the mixing angle is nearly $\pi/2$ and neutrinos are produced as almost pure ν_2 . The neutrino then propagates through lower density regions and crosses resonance where the squared-mass splitting is minimal. The adiabaticity condition is met if the density changes slowly enough, in which case the neutrino remains ν_2 and enters the vacuum as $\nu_2 = \sin \theta \nu_e + \cos \theta \nu_\mu$. If the mixing angle is small there is almost total $\nu_e \rightarrow \nu_\mu$ conversion. If the resonance is not crossed adiabatically then transitions occur

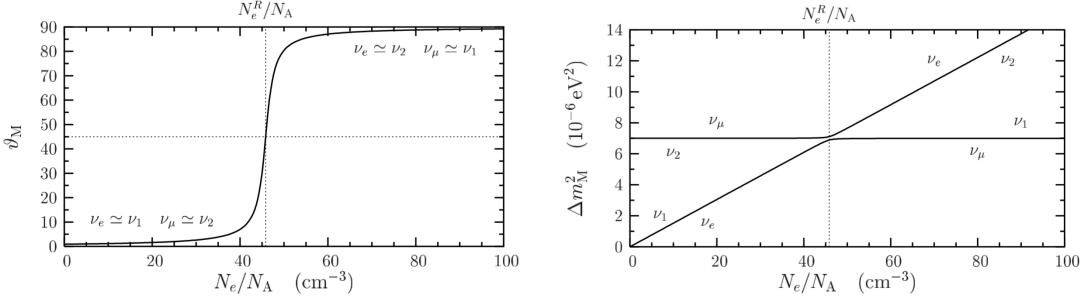


Figure 1.20: Left: The effective mixing angle, θ_M , as a function of electron number density, N_e , divided by the Avogadro number, N_A . Right: The effective squared-mass difference. Both plots assume $\Delta m^2 = 7 \times 10^{-6} \text{ eV}^2$ and $\sin^2 2\theta = 10^{-3}$ [70].

in the resonance region and the neutrino emerges into vacuum as a mixture of ν_2 and ν_1 [70].

Figure 1.21a shows the regions of the $\tan^2 \theta$ - Δm^2 plane allowed by the different models for neutrino propagation out of the Sun using the first 128.5 and 177.9 days of day and night live-time, respectively, recorded by the SNO D₂O phase. There is the Small Mixing Angle (SMA) with resonant enhancement from the MSW effect, the Large Mixing Angle (LMA) with large mixing angle and Δm^2 , the LOW region with large mixing angle and low Δm^2 , as well as the Quasi-Vacuum-Oscillations (QVO) and VACuum Oscillations (VAC) which have small matter effects and most oscillation occurs in the vacuum [70]. The LMA solution is now preferred as can be seen in Figure 1.21b, a combined analysis of the SNO and KamLAND data.

Figure 1.22 shows the electron neutrino survival probability as a function of energy for the LMA solution. In the lower energy region vacuum oscillation effects dominate, and in the higher energy region the matter effect dominates. Fitted to neutrino data the transition from vacuum to matter oscillation domination occurs around 2 MeV [1].

1.7 Neutrino Mass

As we have seen, neutrinos do in fact have a mass, however, this property is not predicted by the SM. Neutrinos cannot interact with the Higgs boson if they are described by a purely left-handed component. Another method of mass generation is necessary and two are described here: Dirac and Majorana mass generation mechanisms.

It will be shown that if neutrinos are Majorana particles it is possible to explain why their masses are so small. The *see-saw mechanism* could suppress the neutrino mass by an undiscovered high energy scale. Searching for neutrinoless double β decay may help determine the true nature of the neutrino.

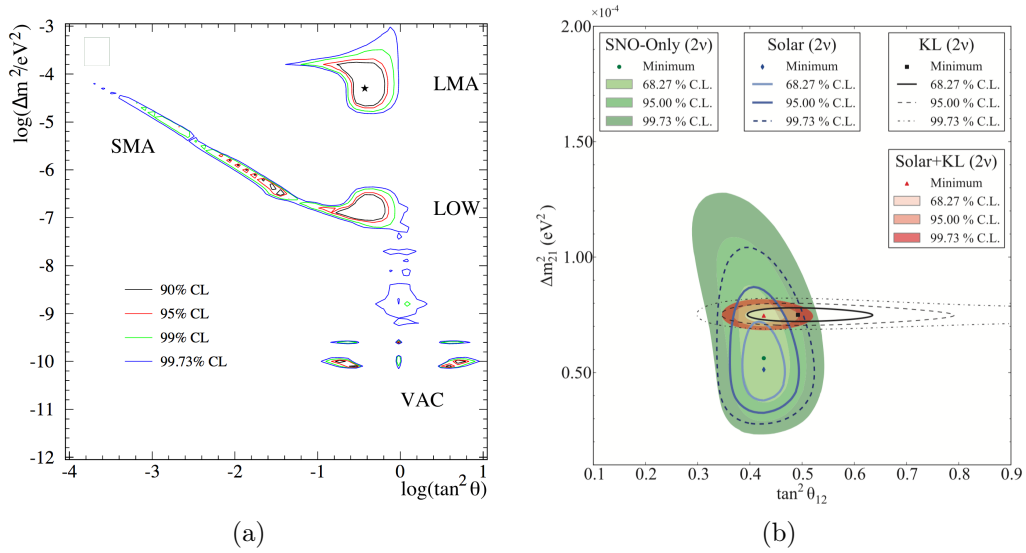


Figure 1.21: (a) Regions of the $\tan^2 \theta$ - Δm^2 plane allowed by the different models for neutrino propagation out of the Sun using the first 128.5 and 177.9 days of day and night live-time, respectively, recorded by the SNO D₂O phase [71]. (b) Two neutrino flavour oscillation analysis contour using KamLAND results and data from all phases of SNO [66].

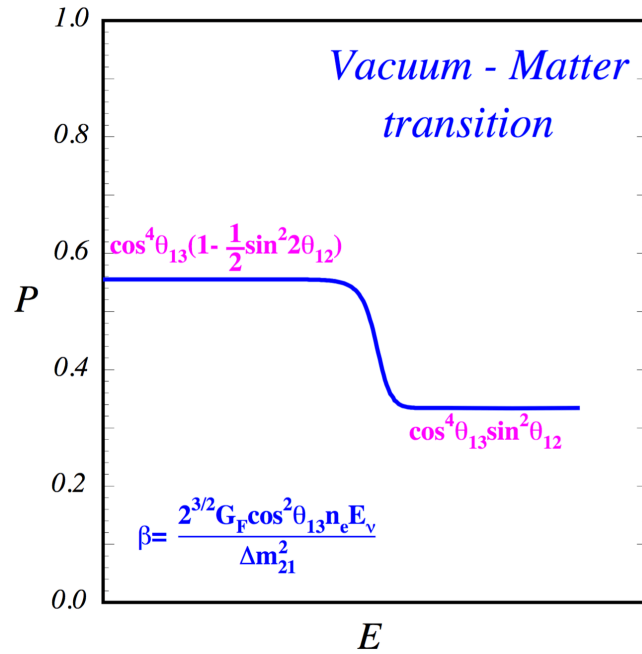


Figure 1.22: LMA solution for electron neutrino survival probability as a function of energy for neutrinos arriving at Earth [72].

1.7.1 Dirac masses

The SM Lagrangian for neutrinos as free Dirac fermions is,

$$\mathcal{L}_D = \bar{\nu} (i\gamma^\mu \partial_\mu - m_D) \nu, \quad (1.67)$$

where the Dirac spinor, ν , can be considered a superposition of the left and right-handed chiral states,

$$\nu = \nu_L + \nu_R = P_L \nu + P_R \nu. \quad (1.68)$$

The mass term of the Lagrangian then takes the form,

$$\mathcal{L}_{\text{mass}}^D = -m_D \bar{\nu} \nu = -m_D \bar{\nu}_L \nu_R + m_D \bar{\nu}_R \nu_L = -m_D \bar{\nu}_L \nu_R + \text{H.c.} \quad (1.69)$$

This implies that for a non-zero Dirac mass, the particle must have both left and right-handed chiral states. Neutrinos in the SM, however, are purely left-handed and therefore cannot have a mass. This can be resolved by the existence of a sterile right-handed neutrino, which has not been discovered because it doesn't couple to the weak interaction. The Dirac neutrino would be represented by a four component spinor, containing left- and right-handed neutrinos and left- and right-handed anti-neutrinos. This is known as the *minimal SM extension*.

1.7.2 Majorana Masses

In 1937 E. Majorana proposed an alternative mechanism for giving mass to the neutrino, a neutral fermion. He allowed the neutrino to still be described by a two component spinor by defining a coupling between a right-handed fermion and its charge conjugate,

$$\nu_R = C \bar{\nu}_L^T, \quad (1.70)$$

where $C = i\gamma^2\gamma^0$ is the charge conjugate operator. The Majorana field then becomes,

$$\nu = \nu_L + \nu_L^C, \quad (1.71)$$

where the charge conjugate field is defined as $\nu_L^C = C \bar{\nu}_L^T$. In this way he was able to rewrite the Dirac equation purely in terms of the left-handed, ν_L . The mass term of the Majorana Lagrangian is then,

$$\mathcal{L}_{\text{mass}}^L = \frac{m_L}{2} \bar{\nu}_L \nu_L^C + \text{H.c.} \quad (1.72)$$

The factor of $1/2$ accounts for the identicalness of the hermitian conjugate.

If neutrinos are Dirac particles the lepton number is conserved, however for Majorana neutrinos this is not the case. The Majorana Lagrangian couples neutrinos ($L = +1$) to anti-neutrinos ($L = -1$), and so cannot conserve lepton number. Processes involving Majorana neutrinos generally violate lepton conservation by $\Delta L = \pm 2$.

Unfortunately this Majorana Lagrangian mass term cannot exist in the SM. The coupling $\overline{\nu_L} \nu_L^C$ has the third component of weak isospin, $I_3 = 1$, and hypercharge, $Y = -2$, but the SM has no corresponding weak isospin triplet with $Y = 2$. More is needed to be done before Majorana neutrinos can have a mass.

It is not known that the right-handed chiral field ν_R exists, but supposing it does, a Majorana Lagrangian for ν_R can also be written,

$$\mathcal{L}_{\text{mass}}^R = \frac{m_R}{2} \overline{\nu_R} \nu_R^C + \text{H.c.}, \quad (1.73)$$

and the a total Dirac-Majorana neutrino mass term is,

$$\mathcal{L}_{\text{mass}}^{\text{D+M}} = \mathcal{L}_{\text{mass}}^D + \mathcal{L}_{\text{mass}}^L + \mathcal{L}_{\text{mass}}^R. \quad (1.74)$$

The Dirac-Majorana mass term can be rewritten in matrix form as,

$$\mathcal{L}_{\text{mass}}^{\text{D+M}} = \frac{1}{2} \begin{pmatrix} \overline{\nu_L^C} & \overline{\nu_R} \end{pmatrix} \begin{pmatrix} m_L & m_D \\ m_D & m_R \end{pmatrix} \begin{pmatrix} \nu_L \\ \nu_R^C \end{pmatrix} + \text{H.c.} \quad (1.75)$$

The chiral fields, ν_L and ν_R^C , described by Equation 1.75 do not have definite mass because of the off-diagonal Dirac masses. By applying a suitable unitary transformation, U , such that,

$$\begin{pmatrix} \nu_L \\ \nu_R^C \end{pmatrix} = U \begin{pmatrix} \nu_{1,L} \\ \nu_{2,L} \end{pmatrix}, \quad (1.76)$$

the mass matrix becomes,

$$U^T M U = \begin{pmatrix} m_1 & 0 \\ 0 & m_2 \end{pmatrix} \quad (1.77)$$

where the mass eigenvalues are expressed,

$$m_{1,2} = \frac{1}{2} \left[(m_L + m_R) \mp \sqrt{(m_L - m_R)^2 + 4m_D^2} \right]. \quad (1.78)$$

The most interesting choices of parameter values are,

$$m_D \ll m_R, \quad m_L = 0. \quad (1.79)$$

The choice of $m_L = 0$ is natural because, as explained above, a left-handed Majorana mass term cannot exist. In this case the masses become,

$$m_1 = \frac{m_D^2}{m_R} \quad \text{and} \quad m_2 = m_R \left(1 + \frac{m_D^2}{m_R^2} \right) \approx m_R. \quad (1.80)$$

This is known as the *see-saw mechanism*, because it results in a neutrino, ν_2 , with a very heavy mass, and a very light neutrino, ν_1 , suppressed by a factor of $1/m_R$.

The mixing angle,

$$\tan 2\theta = 2 \frac{m_D}{m_R} \ll 1, \quad (1.81)$$

is very small, which means that ν_1 is mostly the left-handed active neutrino, ν_L , while ν_2 is mostly the right-handed sterile, ν_R .

This mechanism has the potential to explain why the neutrino mass is so small, because, if the mass for the heavy sterile is very large then the left-handed Majorana mass is very small. Majorana neutrinos could also explain a matter dominated universe. In the theory of *leptogenesis*, if the Sakharov conditions² are met, heavy neutrinos in the early universe could decay to left-handed and right-handed neutrinos as well as Higgs decaying to quarks. Majorana neutrinos violate lepton number so more left-handed neutrinos could be created than right-handed neutrinos. The quantum number, $B - L$, is thought to be conserved, so if L is violated B is correspondingly violated resulting in more left-handed quarks. Missing antimatter could therefore be explained from CP violation in the neutrino sector.

Extending the one-generational case given above to three generations results in a modification to the PMNS matrix. The matrix given in Equation 1.43 transforms to,

$$U \rightarrow UD(\alpha_1, \alpha_2), \quad (1.82)$$

where $D(\alpha_1, \alpha_2) = \text{diag}(1, e^{i\alpha_1}, e^{i\alpha_2})$, and $\alpha_{1,2}$ are the Majorana phases.

1.7.3 Electron Neutrino Mass

Limits on the neutrino mass were set by observing decays of pions at rest at the PSI experiment [74], as well as observing tau decays at the ALEPH experiment [75]. However much more stringent limits have been set by measuring the single β decay of tritium.

Electron neutrino mass can be directly measured from β decay [28],

$$\mathcal{N}(A, Z) \rightarrow \mathcal{N}(A, Z + 1) + e^- + \bar{\nu}_e, \quad (1.83)$$

where A is the mass and Z is the atomic number of the nucleus.

The non-zero neutrino mass reduces the maximum energy of the electron, therefore precision measurements of the energy spectrum enable a determination of the neutrino mass. The β decay energy spectrum is given by [76],

$$\begin{aligned} \frac{dN}{dE_e} \approx & \frac{G_F^2}{2\pi^3} \cos^2 \theta_C |\mathcal{M}|^2 F(E, Z) p_e (E_e + m_e c^2) (E_0 - E_e) \\ & \times \sqrt{(E_0 - E_e)^2 - \sum_i |U_{ei}|^2 m_i^2}, \end{aligned} \quad (1.84)$$

where G_F is the Fermi constant, θ_C is the Cabibbo angle for the transition of a down quark into an up quark, \mathcal{M} is the nuclear matrix element, $F(E, Z)$ is the Fermi function

²Sakharov conditions[73]:

1. At least one baryon-number violating process.
2. C and CP-violation.
3. Interactions outside of thermal equilibrium.

describing the electromagnetic reaction between the produced electron and the final state nucleus, p_e is the electron momentum, E_e is the electron energy, m_e is the electron mass, and E_0 is the endpoint energy assuming zero neutrino mass so $(E_0 - E_e)$ is the total energy of the neutrino. The expression $\sum_i |U_{ei}|^2 m_i^2 \equiv m_{\nu_e}^2$ is the effective electron neutrino mass.

The current best limits on the electron neutrino mass were obtained from the Mainz ($m_{\nu_e} < 2.3$ eV) [77] and Troitzk ($m_{\nu_e} < 2.5$ eV) [78] experiments at the 95% confidence level. These experiments observed tritium (${}^3\text{H}$) β decay. These limits will soon be superseded by the KATRIN experiment which has a sensitivity of approximately 0.2 eV [79].

1.7.4 Neutrinoless Double β Decay

One method for determining if neutrinos are Majorana particles is to search for *neutrinoless double β decay* ($0\nu\beta\beta$).

For some isotopes single β decay is energetically forbidden because the mass of the daughter isotope plus an electron would be more than the parent,

$$m(A, Z) < m(A, Z + 1) + m_e. \quad (1.85)$$

These isotopes may decay via double β decay,

$$\mathcal{N}(A, Z) \rightarrow \mathcal{N}(A, Z + 2) + 2e^- + 2\bar{\nu}_e, \quad (1.86)$$

provided the mass of $\mathcal{N}(A, Z + 2)$ plus two electrons is less than the mass of the parent.

Double β decay is a second order weak interaction process [28], so decay rates are typically low, usually of the order of $T \gtrsim 10^{19}$ years. Isotopes undergoing this process usually have a low natural abundance. A selection of double β decay transitions, with a Q-value of at least 2 MeV is listed in Table 1.2, compiled from references [28, 80].

If the neutrino is a Majorana particle then it is possible that neutrinoless double β decay (Figure 1.23) could occur. In this process, as with 2ν double β decay, two neutrons decay to protons, or at the fundamental level two down quarks transition to two up quarks. However, in this case, the right-handed $\bar{\nu}_e$ emitted from one decay is absorbed by the other as a left-handed ν_e . This can only occur if the neutrino and the anti-neutrino are the same particle. Neutrinoless double β decay breaks lepton number and chirality conservation.

The energy spectrum for the two electrons created during neutrinoless double β decay is a delta function at the transition energy. This is known as the *Q-value*,

$$E(e_1^-) + E(e_2^-) \approx Q \equiv M_i - M_f \quad (1.87)$$

The energy spectrum (Figure 1.24) for 2ν double β decay is continuous, with an end point at the $0\nu\beta\beta$ energy, owing to the missing energies of the neutrinos.

$\beta\beta$ decay	Q-value [keV]	Nat. abund. [%]	$T_{1/2}^{2\nu}$ [y]
$^{48}\text{Ca} \rightarrow ^{48}\text{Ti}$	4272 ± 4	0.187	$4.2_{-1.3}^{+3.3} \times 10^{19}$
$^{76}\text{Ge} \rightarrow ^{76}\text{Se}$	2039.006 ± 0.050	7.8	$(1.8 \pm 0.1) \times 10^{21}$
$^{82}\text{Se} \rightarrow ^{82}\text{Kr}$	2995.1 ± 2.0	9.2	$(8.3 \pm 1.2) \times 10^{19}$
$^{96}\text{Zr} \rightarrow ^{96}\text{Mo}$	3350.4 ± 2.9	2.8	$2.1_{-0.4}^{+0.8} \times 10^{19}$
$^{100}\text{Mo} \rightarrow ^{100}\text{Ru}$	3034 ± 6	9.6	$6.8_{-0.9}^{+0.8} \times 10^{18}$
$^{110}\text{Pd} \rightarrow ^{110}\text{Cd}$	2000 ± 11	11.8	$> 6.0 \times 10^{16}$
$^{116}\text{Cd} \rightarrow ^{116}\text{Sn}$	2805.0 ± 3.8	7.5	$2.6_{-0.4}^{+0.7} \times 10^{19}$
$^{124}\text{Sn} \rightarrow ^{124}\text{Te}$	2287.0 ± 1.5	5.64	$> 1.0 \times 10^{17}$
$^{130}\text{Te} \rightarrow ^{130}\text{Xe}$	2528.8 ± 1.3	34.5	$(7.9 \pm 1.0) \times 10^{20}$
$^{136}\text{Xe} \rightarrow ^{136}\text{Ba}$	2468 ± 7	8.9	$> 8.1 \times 10^{20} (90\%)$
$^{150}\text{Nd} \rightarrow ^{150}\text{Sm}$	3367.5 ± 2.2	5.6	$(6.8 \pm 0.8) \times 10^{18}$

Table 1.2: A selection of double β decay processes with Q-values above 2 MeV, their natural abundances, and half-lives [28, 80].

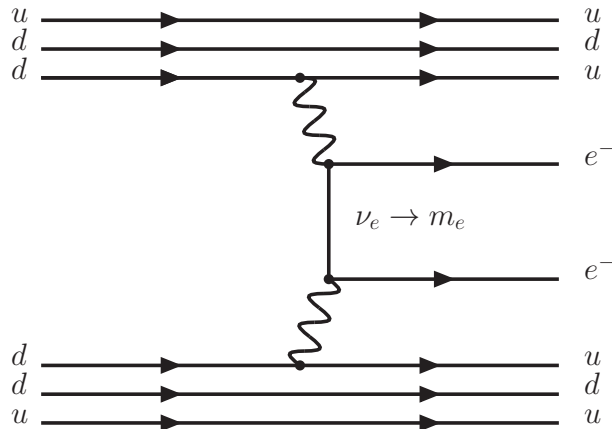


Figure 1.23: Feynman diagram of the neutrinoless double β decay process.

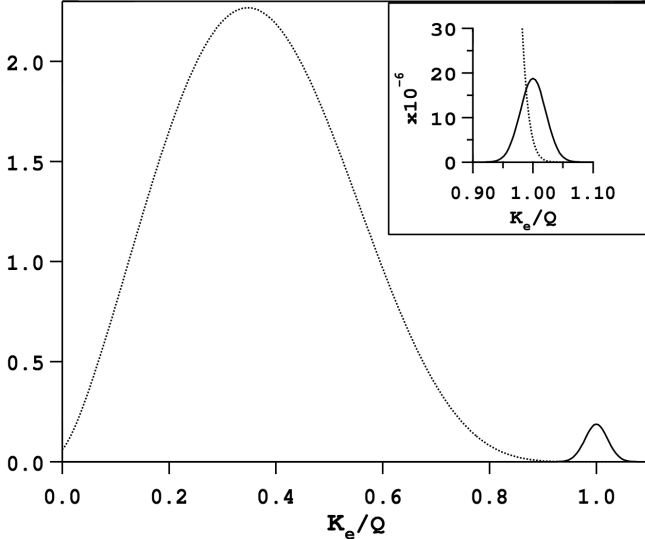


Figure 1.24: Energy spectra for the sum of the electrons, K_e , produced by $2\nu\beta\beta$ (dotted line) and $0\nu\beta\beta$ (solid line). The $2\nu\beta\beta$ spectrum has been normalised to 1 and the $0\nu\beta\beta$ spectrum is normalised to 10^{-2} (10^{-6} in the inset). All spectra have been convolved with a resolution of 5% [81].

The half-life of neutrinoless double β decay is expressed as,

$$T_{0\nu}^{-1} = G^{0\nu} |M^{0\nu}|^2 |m_{ee}|^2, \quad (1.88)$$

where $G^{0\nu}$ denotes the phase-space factor determining how many electrons have the correct energy and momenta for involvement in the process, $M^{0\nu}$ is a nuclear matrix element describing the decays, and m_{ee} is the effective Majorana mass, a coherent sum of the neutrino mass states,

$$|m_{ee}| = \left| \sum_i U_{ei}^2 m_i \right|, \quad (1.89)$$

where U_{ei} are elements of the PMNS matrix and m_i are the masses of the eigenstates.

The rate of neutrinoless double β decay is suppressed by a factor of $1/E_0^2$ where E_0 is the typical energy release for double β decay (~ 1 MeV). Consequently, compared to $2\nu\beta\beta$ decay, $0\nu\beta\beta$ decay is a rare process.

Through measuring the rate of neutrinoless double beta decay, an estimate for the absolute neutrino mass could be obtained because the effective Majorana mass, m_{ee} , is proportional to the square root of the half-life. The possible values of m_{ee} depend on whether there are two light and one heavy or one heavy and two light neutrino mass eigenstates, the two mass hierarchy scenarios described in Section 1.6.3. Therefore the value of m_{ee} may also tell us whether the hierarchy is normal or inverted. Figure 1.25 shows the bounds on the effective Majorana mass and the lightest neutrino mass for the normal and inverted hierarchy scenarios. To date, fruitless searches for $0\nu\beta\beta$ decay have put an upper limit on the effective Majorana neutrino mass.

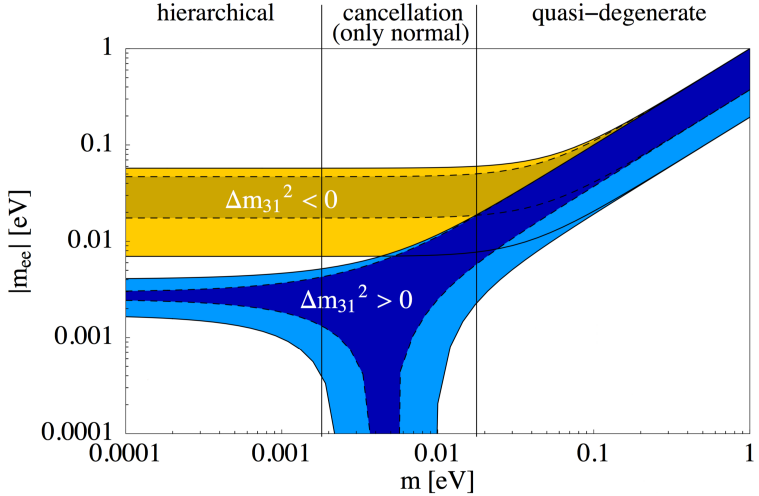


Figure 1.25: Bounds on the effective Majorana mass and the lightest neutrino mass at the 90% confidence level for the normal (blue) and inverted (yellow) hierarchy scenarios. The two scenarios overlay in the degenerate region. The darker region assumes negligible error on the current oscillation parameters. Adapted from [82].

The coefficients of the effective Majorana neutrino are U_{ei}^2 , rather than $|U_{ei}|^2$. Cancellations are therefore possible and so the effective Majorana mass may be smaller than the lightest neutrino mass, m_i . The effective Majorana mass does provide a lower limit on the heaviest neutrino mass.

Chapter 2

The SNO+ Experiment

2.1 SNOLAB

Located 2092 m underground at Vale’s Creighton nickel mine in Sudbury, Canada, is the SNOLAB research facility. It was originally built for the Sudbury Neutrino Observatory (SNO) experiment, but has since expanded to house a number of different sub-atomic physics experiments.

The laboratory comprises 5000 m² clean space at better than Class 2000 levels [83], and is the deepest clean room facility in the world. The rock overburden of 5890 ± 94 m water equivalent (m.w.e.) shields against cosmic muons. This shielding attenuates cosmic rays by a factor of 50 million to one cosmic ray muon per 3.4 m² per day [84].

2.2 The Detector

SNO+ is a large volume liquid scintillator experiment and is a refurbishment of the SNO detector. 780 tonnes of ultra-pure scintillator will be housed inside a 12 m diameter, 5.5 cm thick, acrylic vessel (AV) [84]. This will produce significantly more light than was created through the Cherenkov process in the heavy water used for SNO. As such, SNO+ will be sensitive to lower energies and will have a better energy resolution. A cylindrical neck 1.5 m in diameter inside, and 6.8 m high, allows access to the AV from the deck to fill and introduce calibration sources.

The AV will be surrounded by an approximately 8.9 m radius geodesic support structure (PSUP) holding ~ 9300 photomultiplier tubes (PMTs). The PMTs are the original 8” Hamamatsu R1408s that were used for SNO and sit inside a reflective collar (known as the “concentrator”) to increase the solid angle coverage to about 54% [36]. The whole experiment is contained within a barrel shaped cavity that is 22 m wide and 34 m high [85]. The cavity was lined with concrete and 8 mm of Urylon to waterproof the cavity and decrease radioactive contamination from the rocks. The volume between the AV and PSUP, and rest of the cavity, will be filled with 7000 tonnes of ultra-pure water (UPW) to shield the experiment from radioactivity from the rocks and PMT

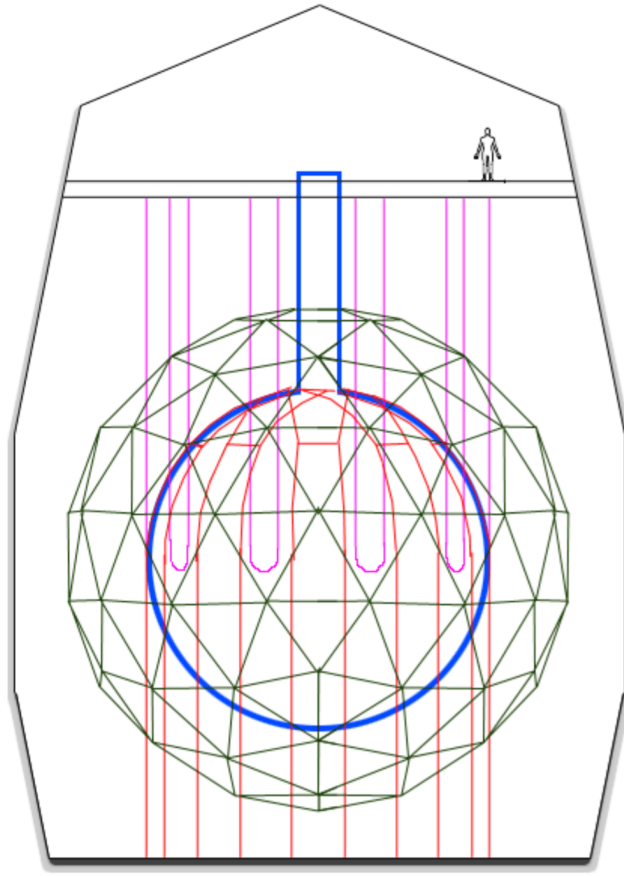


Figure 2.1: Diagram of the SNO+ detector showing the ~ 18 m geodesic PMT support structure (green), housing a 12 m diameter acrylic vessel (blue). The AV is suspended by a system of high purity ropes (purple) and held down by a rope net (red). The AV and PSUP are contained in a volume of ultra-pure water [85].

array.

Ten hold-up rope loops made from 19 mm thick very high purity polyethylene fibre (Tensylon) keep the AV suspended inside the PSUP. As the liquid scintillator will be less dense than water a new system of hold-down ropes has also been installed and anchored to the cavity floor. These are made from 38 mm thick Tensylon. See Figure 2.1 for an illustration of the SNO+ detector set-up.

2.3 Electronics and detector readout

With the use of scintillator as the material filling the AV, the light yield will increase significantly. Consequently the detector will be sensitive to lower energy events, resulting in an increase in signal frequency. A greater number of background events are also expected. Correspondingly the detector electronics have been upgraded to cope with the bandwidth increase [84]. The following section details how the detector electronics

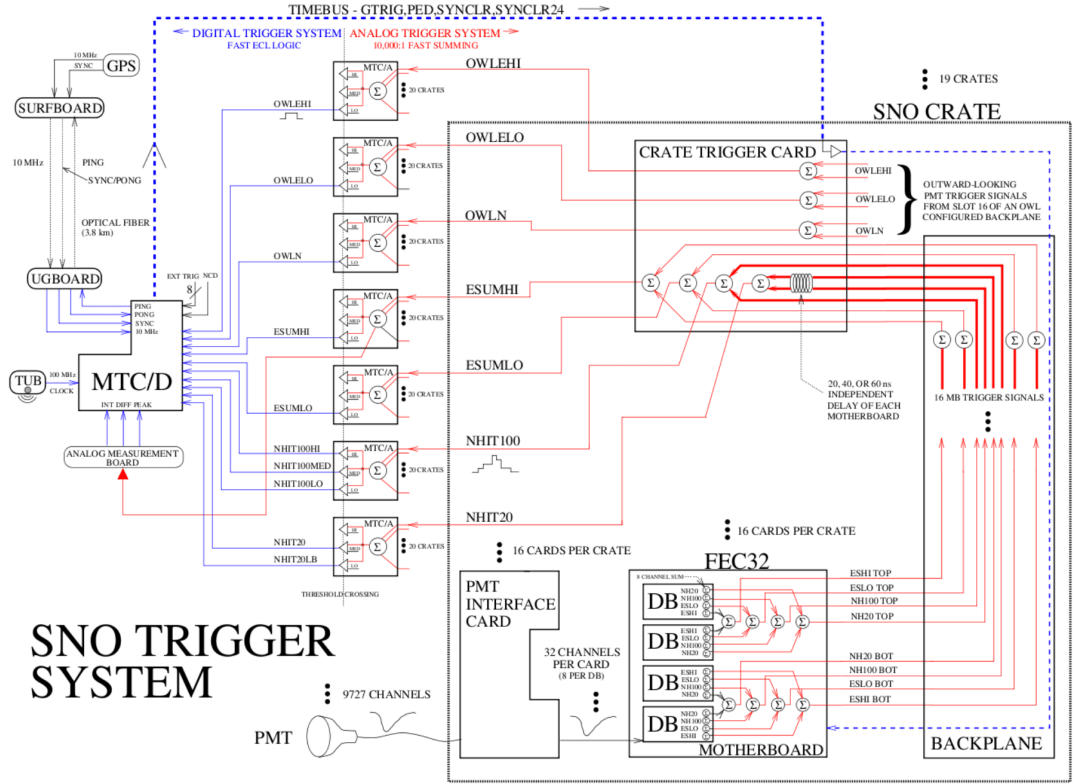


Figure 2.2: A block diagram of the SNO trigger system [86] which has been refurbished for SNO+. The XL3 boards which read out the charge and time information to the DAQ are not shown, and the MTC/A cards are replaced by MTC/A+.

work, including these upgrades. A diagram of the SNO+ electronics flow is given in Figure 2.2.

A pulse is produced by a PMT, either due to a photoelectron or noise, the charge and time of which is recorded by the electronics. First the pulse travels along 35 m of coaxial cable, which is grouped into bundles of eight. The bundles are connected to a Paddle Card which connects to a PMT Interface Card (PMTIC), four Paddle Cards per PMTIC. Each PMTIC therefore has 32 channels assigned to individual PMTs. Each PMTIC plugs into a Front End Card (FEC). The four groups of eight channels, corresponding to the Paddle Cards, are passed to their own DaughterBoard (DB) [87].

The DB checks the signal for each channel against a threshold voltage. If the threshold is crossed a high gain and low gain integration of the pulse across two time windows is performed. “QHS” is the charge integration at high gain with short integration time, “QHL” has high gain and long integration time so includes late light from scattering and reflections, and “QLX” has low gain and long integration time. As the discriminator threshold is passed, a “TAC” (time to amplitude conversion) voltage is produced which begins decreasing approximately linearly. The voltage that the TAC has fallen to when it is read out determines the PMT hit time. Two trigger pulses are created, one is 100 ns

long (NHIT100), the other 20 ns (NHIT20) [87].

There are 16 FECs per crate and each crate has a Crate Trigger Card (CTC). The FECs pass the NHIT100, NHIT20, and a copy of the PMT pulse (ESUM) to the CTC. The CTC then sums the trigger signal by type [87].

There are 19 crates in total, so 19 CTCs, which are connected to seven Master Trigger Cards / Analogue (MTC/A+). These perform an analogue sum of the trigger signals from the CTCs. A single trigger signal for each trigger type for the whole detector is then passed by the Analogue Crate Interface Card (ANALCIC) to the Master Trigger Card / Digital (MTC/D) which checks if the trigger signals are above their respective thresholds. If they are, a Global Trigger (GT) is issued [87].

Each crate also has an XL3 (new for SNO+) card. If a GT is issued the XL3 reads out the TAC, QHS, QHL, and QLX values, as ethernet packets, to the Data Acquisition System (DAQ) and Event Builder [87]. The trigger window is 400 ns long, if a GT is not issued within this window, the TAC resets and the PMT hit is not associated with an event. There is dead time of 30-50 ns between trigger windows [84].

2.4 Calibration

Calibration of the detector is required to understand how it will respond to an event and improve the accuracy of position, direction and energy reconstruction. The observables for SNO+ are the integrated charge of a PMT pulse, and the time said pulse crosses the discriminator threshold. The integrated charge measurement must be corrected for variations in the PMT gain, as well as differences in light collection efficiencies as a function of incident angle and wavelength. The time that the PMT pulse crosses the discriminator threshold must be corrected for channel dependent offsets and the discriminator time walk effect [88].

The SNO+ experiment will be calibrated using both optical and radioactive sources. An optical source used for SNO, which will be redeployed for SNO+, is a light diffusing sphere known as the “laserball”. The laserball uses a nitrogen dye laser, scattered using glass bubbles [89], to create an isotropic source of light at different wavelengths [90]. This enables an absolute efficiency measurement of each PMT [88].

Radioactive sources producing betas, gammas, alphas, and neutrons, will also be used. These sources will be used to verify the energy scale, measure the energy resolution, response linearity and systematic uncertainties. They will also be used to determine the efficiency of the reconstructed energy, position, and direction values [88].

Table 2.1 lists the radioactive sources, ranging from 0.1 to 6 MeV, considered for use by SNO+. The sources will be stored in a sealed “glove box” to prevent contamination of the experiment. The internal calibration sources (including the laserball) can be attached to an umbilical and moved by a rope system to locate the sources at different positions in the detector. They will be positioned by detecting and triangulating an

Source	Radiation	Energy [MeV]
AmBe	n, γ	2.2, 4.4 (γ)
^{60}Co	γ	2.5 (sum)
^{57}Co	γ	0.122
^{24}Na	γ	4.1 (sum)
^{48}Sc	γ	3.3 (sum)
^{16}N	γ	6.1
$^{220}\text{Rn}/^{222}\text{Rn}$	α, β, γ	various

Table 2.1: Radioactive calibration sources considered for use by the SNO+ experiment [84].

LED, attached to the source, with a system of under water cameras. This allows the position to be measured to less than 1 cm accuracy [90]. A PMT located inside the source triggers when a decay has occurred; alternatively a delayed coincidence decay can be used for some sources.

Sources of internal background radiation can also be used, enabling continuous calibration during data taking. Decays from the ^{238}U chain that can be used are ^{210}Po - α , ^{14}C - β , and delayed ^{214}Bi -Po coincidences. The ^{212}Bi -Po coincidence from the ^{232}Th chain can also be used, as well as muon followers [84].

New for SNO+ is an external optical calibration system consisting of optical fibres, attached to the PSUP at various positions, directing light into the detector. The radio-purity requirement of the SNO+ scintillator is higher than for the SNO D₂O; the new system is intended to replace regular deployment of calibration sources to reduce the risk of radioactive contamination.

The external calibration system is called the Embedded LED/Laser Light Injection Entity (ELLIE) system, and as the name suggests, uses light from fast pulsing LEDs or lasers. It provides *in-situ* measurements of optical properties (scattering and attenuation) of the detector materials, measurements of the PMT response (time and gain), and allows for continuous calibration as the detector operates [90]. PMT timing offsets and discriminator time walk information is provided by TELLIE which has 91 injection points, covering all inward facing PMTs [85]. SMELLIE measures the angular and wavelength dependent scattering of light in the detector. It has four injection points, each with three differently oriented fibres. The fibres can be connected to lasers with different wavelengths [85]. The AMELLIE system measures the wavelength dependent absorption as well as the optical degradation of the scintillator. It has four injection points, each with two differently oriented fibres, and can also be connected to lasers with different wavelengths [85].

2.5 Monte Carlo

SNO+ RAT (Reactor Analysis Tool) is the Monte Carlo (MC) simulation software package developed for the SNO+ experiment. It is developed in the C++ language and interfaces with the GEANT4 simulation libraries. Simulated data is stored in the ROOT format.

The geometry of the detector has been implemented, and includes a detailed geometry of the SNO+ PMTs [91]. The data acquisition and trigger system has also been simulated. Particle generators have been developed to simulate events studied as part of the SNO+ physics program, as well as the expected background radiation [84].

Version 6.1.0 of SNO+ RAT has been used for the work presented in this thesis. Any modifications to SNO+ RAT, necessary for the analysis presented, has been built on this version.

2.6 Scintillation

The bulk component of the SNO+ scintillator cocktail is the aromatic hydrocarbon, linear alkylbenzene (LAB), which is a solvent [84]. The chemical formula for LAB is $C_6H_5C_{12}H_{25}$ [92]. LAB is efficiently excited by charged particles passing through it, and de-excites by emitting photons with a peak of ≈ 300 nm [90].

LAB was chosen because it is compatible with acrylic, unlike pseudocumene which was used in the KamLAND and Borexino detectors [93]. It has the further benefits that it is stable and can dissolve heavy metals (e.g. tellurium) with good stability. It is produced with high purity by the manufacturer, Cepsa, at their plant in Becancour, Quebec. The relatively short distance it therefore has to travel (less than 900 km) helps reduce cosmogenic activation. LAB has a high light yield and responds linearly to the energy of the traversing particle. It has long attenuation and scattering lengths, and maintains these properties with dissolved tellurium [84]. Additionally LAB has a high flash point (140°C compared to pseudocumene's 38°C) and is environmentally safe [93].

LAB is highly absorbing at 300 nm, so without a fluor would reabsorb the emitted photons [90]. The LAB will therefore be doped with a concentration of 2 g/L 2,5-diphenyloxazole (PPO) [84]. PPO collects the excitation of the LAB molecules via dipole interactions and also emits that energy as photons [94]. The photons emitted by PPO are shifted to a wavelength region in which LAB and PPO are less absorbing. The fraction of photons which make an undisturbed journey from the scintillation point to a PMT is therefore increased [85].

Charged particles traversing the detector excite electrons in the LAB molecules. These excited electrons can only be excited to singlet states as the triplet state is forbidden by spin. It is possible, however, that some triplet states may occur by crossing from a singlet to a triplet state. Charged particles may also ionise the LAB molecules, in

which case both singlet and triplet states may be produced as the molecule recombines with an electron [92].

Light particles primarily excite the LAB molecules by interacting via elastic collisions, therefore resulting in a greater proportion of singlet states. Heavy particles are more likely to ionise the LAB molecules, resulting in a greater proportion of triplet states. These ionised molecules sometimes de-excite excited molecules non-radiatively, reducing the light output. This process is known as *ionisation quenching* [92].

Singlet states de-excite, producing photons via *fluorescence*. These photons have an exponentially decaying intensity spectrum as a function of time, with a lifetime of $\sim 10^{-9}$ s. Triplet electron states produce photons by *phosphorescence* or *delayed fluorescence*. Phosphorescence photons are created as the triplet states de-excite directly to ground and have a longer lifetime ($\sim 10^{-4}$ s) and longer wavelengths. Delayed fluorescence photons are produced by electrons which acquire enough thermal energy to jump from the triplet to the singlet state, and then de-excite via fluorescence. The photons therefore have the same wavelength spectrum as fluorescence photons but a non-exponential spectrum [92]. The different properties of the types of luminescence enables alpha-beta particle discrimination.

A few mg/L of a secondary shifter in the scintillator cocktail captures photons emitted by the fluor and re-emits them at longer wavelengths, where there is even lower absorption and a higher PMT quantum efficiency (see Figure 4.5) [94]. Two different secondary wavelength shifters are under consideration, perylene and bis-MSB. Perylene would shift the LAB-PPO emission peak (350-380 nm) to $\sim 450\text{-}480$ nm, and have a predicted light yield of 300 triggered PMT hits (N_{hits}) per MeV. Bis-MSB would shift the emission peak to $\sim 390\text{-}430$ nm, and have a predicted light yield of 200 N_{hits} per MeV. The final decision will depend on the timing properties, light yield and scattering length of the complete cocktail mixture [84].

For the $0\nu\beta\beta$ phase of the experiment, tellurium will be loaded into the liquid scintillator mixture. The process involves dissolving telluric acid Te(OH)_6 into water and adding a surfactant [84]. The inclusion of tellurium in the scintillator mixture retains the low absorption in the sensitivity region of the PMTs.

2.7 Backgrounds

There are a number of different background interactions which occur inside the SNO+ detector. Internal backgrounds are caused by impurities (mostly ^{238}U and ^{232}Th radio-isotopes) in the water or scintillator inside the AV. External backgrounds are also caused by impurities in the detector, from the AV outwards, including the hold-down and hold-up ropes, external water and the PMTs. Each detector component has its own level of impurity. Although external interactions occur outside the target volume they may reconstruct inside it, either because of mis-reconstruction or the particle has propagated

inside the target. Isotopes may also be created inside the target volume by cosmogenic interactions.

Measurements of the background levels may be made *in-situ* by performing analyses on the energy spectrum. *Ex-situ* assays are also useful but may not be sufficiently sensitive at the required purity levels for SNO+ [95]. Backgrounds must be understood to obtain the most accurate measurement possible, and minimised for the best signal observance ability. As well as achieving the highest possible purity levels, Monte Carlo studies may also be used to develop background rejection techniques.

All phases of the experiment have background electrons from elastically scattered ^8B solar neutrinos. In the water phase these may be reduced using a direction cut, but the isotropic nature of scintillation light means this will not be possible during scintillator phases. The $2\nu\beta\beta$ decays of ^{130}Te are also a background to $0\nu\beta\beta$ decay due to the energy resolution of SNO+. This background may not be reduced. The following sections detail the backgrounds expected due to radioactive impurities, and rejection techniques that will be employed.

2.7.1 ^{238}U Chain

Uranium-238 (^{238}U) is a naturally occurring radioisotope, with a half-life of 4.47×10^9 years [95]. A variety of different particles are emitted during the chain of daughter decays, some with an energy in the same region of interest (ROI) as physics signal, or causing pile-up. Figure 2.3 shows the part of the decay chain most relevant to SNO+. Daughter isotopes ^{214}Bi , ^{210}Tl , and ^{210}Bi are the most concerning [84].

The target levels of ^{238}U in LAB-PPO scintillator is 1.6×10^{-17} g/g, based on what was achieved by the Borexino experiment [96]. Similar purity levels are anticipated for the water phase. With the addition of tellurium and a surfactant to the LAB-PPO the purity levels will decrease, but a target of 2.5×10^{-15} g/g will be maintained (see Table 2.2) [84].

Occurring towards the end of the ^{238}U chain is ^{214}Bi . It has a half-life of 19.9 mins and decays 99.979% of the time by beta-gamma emission to ^{214}Po with a Q-value of 3.27 MeV. This acts as a background to $0\nu\beta\beta$, and nucleon decay in the water phase, because of the energy resolution.

The ^{214}Bi daughter, ^{214}Po has a half-life of $164 \mu\text{s}$ and alpha-decays with a Q-value of 7.83 MeV. This decay is usually separated from the preceding beta-decay by a time greater than the event window so will be recorded as two separate events. In the scintillator and Te-loaded phases the alpha may be identified so the decays can be cut. The tagging algorithm looks for events sufficiently close in time, with similar positions. The alpha energy will be quenched to ~ 0.8 MeV electron equivalent energy, and has an alpha characteristic hit time distribution. The tagged events can be used to determine the levels of ^{214}Bi in the detector. Due to the secular equilibrium with ^{214}Pb , ^{218}Po , and

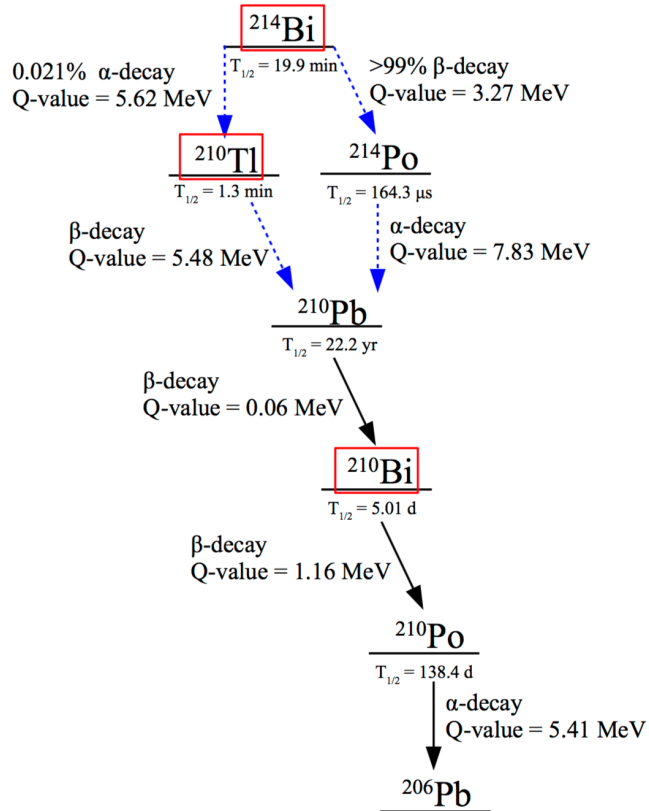


Figure 2.3: The portion of the ^{238}U decay chain most relevant to SNO+, including their Q-values, half-lives, and decay modes. The nuclides of most concern (^{214}Bi , ^{210}Tl , and ^{210}Bi) are highlighted in red. The α - β and β - α decays used for coincidence tagging have blue arrows [84].

Source	Target [g/g]	Decays/yr
<i>Internal H₂O, water phase</i>		
²³⁸ U chain	3.5×10^{-14}	1.2×10^7
²³² Th chain	3.5×10^{-15}	4.1×10^5
<i>LAB-PPO, pure scintillator phase</i>		
²³⁸ U chain	1.6×10^{-17}	4900
²³² Th chain	6.8×10^{-18}	700
²¹⁰ Bi	-	7.6×10^8 ^a
²¹⁰ Po	-	7.8×10^8 ^a
<i>0.3% Te-loaded scintillator, Te phase</i>		
²³⁸ U chain	2.5×10^{-15}	7.6×10^5
²³² Th chain	2.8×10^{-16}	2.8×10^4
²¹⁰ Bi	-	7.9×10^9 ^b
²¹⁰ Po	-	9.5×10^9 ^b

^aExpected number of events in the first year after 9 months of water phase

^bExpected number of events in the first year after 9 months of water phase, followed by 6 months of pure scintillator phase

Table 2.2: Target levels and expected decay rates of internal backgrounds from the ²³⁸U and ²³²Th chains. Secular equilibrium is expected to be broken for ²¹⁰Bi and ²¹⁰Po due to radon contamination [84].

²²²Rn their levels can be calculated also [95]. On rare occasions the beta-alphas may fall in the same event window and be misidentified as a single event. The distortion in the time distribution may be used in these instances to reduce their background in the $0\nu\beta\beta$ ROI [84].

In 0.021% of instances ²¹⁴Bi alpha-decays instead to ²¹⁰Tl, which then beta-decays to ²¹⁰Pb with a half-life of 1.3 mins and a Q-value of 5.5 MeV. This is less important than the aforementioned beta-alpha decays because of the small branching fraction, but can be tagged and removed similarly using alpha-beta coincidence [84].

Further down the ²³⁸U chain is the daughter, ²¹⁰Pb, with a half-life of 22 years and which decays to ²¹⁰Bi. ²¹⁰Bi then beta-decays to ²¹⁰Po with a half-life of 5.0 days and a Q-value of 1.16 MeV. ²¹⁰Bi decays are a direct background to CNO solar neutrinos in the LAB-PPO phase [95]. ²¹⁰Po alpha-decays with a half-life of 138.4 days, and a Q-value of 5.41 MeV which is quenched to ~ 0.5 MeV electron equivalent energy. This acts as a background to beta-alpha and alpha-beta delayed coincidences, which may result in mis-tagging and signal sacrifice. The alphas may also interact with scintillator molecules, producing neutrons (see Section 2.7.5) [84].

There may be a disequilibrium in the ²³⁸U chain at ²²²Rn if the scintillator or water is exposed to air, particularly given the radon richness of the mine air. Radon daughters can also implant into materials they come into contact with (including the AV), where they decay to ²¹⁰Pb. ²¹⁰Pb and its daughters may then leach into the scintillator or

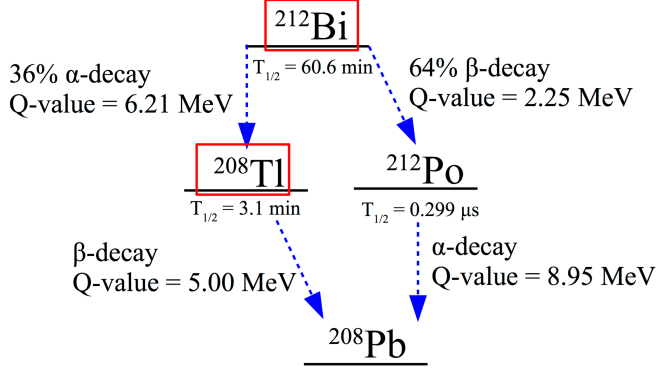


Figure 2.4: The portion of the ^{232}Th decay chain most relevant to SNO+, including their Q-values, half-lives, and decay modes. The nuclides of most concern (^{212}Bi and ^{208}Tl) are highlighted in red. The α - β and β - α decays used for coincidence tagging have blue arrows [84].

water. A cover gas system of cold dense nitrogen (see Section 3.7) is in place to minimise the exposure to lab air and reduce radon ingress. ^{222}Rn has a relatively short half-life of 3.82 days, so doesn't last long in the detector, but can manifest as a long term higher concentration of ^{210}Pb [95].

2.7.2 ^{232}Th Chain

Thorium-232 (^{232}Th), which has a half-life of 1.4×10^{10} years, is also a radio-isotope naturally occurring in liquid scintillator and water [95]. As with ^{238}U , it has daughter decays which are backgrounds to SNO+ physics searches, and cause pile-up. Figure 2.4 shows the part of the decay chain most relevant to SNO+. Daughter isotopes ^{212}Bi , and ^{208}Tl are the most problematic [84].

The target level of ^{232}Th in LAB-PPO scintillator is 6.8×10^{-18} g/g (see Table 2.2), based on what was achieved by the Borexino experiment [96]. Similar purity levels are anticipated for the water phase. A target of 2.8×10^{-16} g/g will be maintained with the addition of tellurium and a surfactant to the LAB-PPO [84].

Isotope ^{212}Bi (half-life of 60.6 min) beta-decays 64% of the time to ^{212}Po with a Q-value of 2.25 MeV. ^{212}Po has a half-life of 299 ns and alpha decays with a Q-value of 8.95 MeV. The problematic ^{212}Bi decay may be minimised by tagging the events using the beta-alpha delayed coincidence. This event tagging may also be used to obtain the ^{232}Th concentration. Almost 45% of the ^{212}Bi and ^{212}Po decays occur in the same trigger window and may be rejected using the PMT timing distribution [84].

In 36% of instances ^{212}Bi alpha decays to ^{208}Tl with a Q-value of 6.21 MeV. ^{208}Tl , which occurs near the end of the decay chain, has a half-life of 3.0 min and beta decays to ^{208}Pb with a Q-value of 5.00 MeV [84]. The decay of ^{208}Tl is problematic for double beta and nucleon decays, but alpha-beta delayed coincidence tagging may be used to

reduce the background in scintillator.

2.7.3 Internal ${}^{40}K$, ${}^{39}Ar$, and ${}^{85}Kr$ Backgrounds

Potassium-40 (${}^{40}K$) is a naturally occurring isotope with an abundance of 0.0117%. It has a half-life of 1.248×10^9 yr and decays with a beta component and a gamma peak at 1.46 MeV. This background falls in the *pep* solar neutrino window but has a distinctive spectrum which can be separated from signal using a fit to the energy spectrum.

The cosmogenic activation of stable ${}^{40}Ar$ produces ${}^{39}Ar$. It has a half-life of 269 yr and beta decays with a Q-value of 0.585 MeV. ${}^{85}Kr$ is released into the atmosphere by nuclear fission, whose non-negligible quantity in the air is a phenomenon of the nuclear age. ${}^{85}Kr$ has a half-life of 10.8 yr and beta-decays with a Q-value of 0.687 MeV. Both isotopes could create pile-up if significant quantities were present in the LAB. This background can be reduced by minimising contact with air and thoroughly degassing [95].

2.7.4 Cosmogenically Induced Backgrounds

Radioactive isotopes are produced in the detector by energetic cosmic rays interacting with stable elements. This will occur in the scintillator during transit, and in the detector during operation although this rate is reduced to less than three muons per hour due to the depth of the SNO+ experiment. The following isotopes have half-lives greater than one second: ${}^{16}N$ ($T_{1/2} = 7.13$ s), ${}^{11}C$ ($T_{1/2} = 20$ min), ${}^{10}C$ ($T_{1/2} = 19.3$ s), ${}^{11}Be$ ($T_{1/2} = 13.8$ s), and 7Be ($T_{1/2} = 53.3$ d) [95]. Most of these may be removed by vetoing events within a few minutes of a muon event, leaving just 7Be and ${}^{11}C$ [84].

Beryllium-7 (7Be) is produced as energetic neutrons, created during the spallation process, interact with ${}^{12}C$ nuclei [95]. It decays by electron capture with a 0.48 MeV gamma. Over 99% of 7Be created in the scintillator above ground can be removed by the scintillator purification plant [84]. The remaining 7Be , and isotope produced in the detector, may be calculated and constrained by signal extraction analyses [95].

Carbon-11 (${}^{11}C$) is produced by muon interactions with carbon nuclei and has a Q-value of 1.98 MeV. The estimated event rate is $(1.14 \pm 0.21) \times 10^3$ decays/kt/yr during operation, extrapolated from KamLAND data and the higher rock overburden of SNO+ [97]. This background may be reduced using a position cut around the muon track [95], as well as coincidence tagging and electron-positron discrimination [84].

Carbon-14 (${}^{14}C$) is produced in scintillator by cosmogenic activation of ${}^{14}N$ [95]. It has a half-life of 5700 yr and a Q-value of 0.16 MeV. Most of the activation occurred when the oil, used to produce the scintillator, was underground in oil fields. Activation in the SNO+ detector has a negligible contribution. A decay rate of a few hundred Hz is expected, which acts as a background to low energy *pp* neutrinos and may contribute to pile-up [84].

Spallation may also occur on the tellurium while stored on surface, however this may be reduced to a negligible level during the purification process [98].

2.7.5 (α,n) Backgrounds

The dominant source of α particles in the scintillator is from ^{210}Po . The alphas produce neutrons most prominently by interacting with the naturally occurring isotope ^{13}C through the (α,n) reaction, $\alpha + ^{13}\text{C} \rightarrow ^{16}\text{O} + n$ [84].

The neutrons scatter from protons during the thermalisation process. The nuclear recoils of these protons results in the emission of scintillation light. The prompt signal of an (α,n) reaction is from the energy lost by the α before the interaction, scintillation from the nuclear recoils, and from the de-excitation of excited isotopes. This prompt signal is a background for $0\nu\beta\beta$ decay and anti-neutrino measurements.

A late signal is produced in $> 90\%$ of cases when the thermalised neutron is captured by a hydrogen atom, emitting a 2.22 MeV gamma. In the other cases it is either captured on tellurium or carbon, producing a 0.6 MeV gamma and a 4.95 MeV gamma respectively. The prompt and delayed signal can be used to reject (α,n) events using a delayed coincidence technique [84].

2.7.6 Pile-Up Backgrounds

When at least two interactions happen in same event window this is known as *pile-up*. The event may be mis-identified as a single event with an energy equivalent to the sum of the individual energies. The interactions may be signal or background, which means background events may mis-identify as signal or remove signal from the ROI. Pile-up is of particular importance when the event rate is above hundreds of Hz, such as for the ^{14}C , ^{210}Bi , or ^{210}Po isotopes described in Sections 2.7.1 and 2.7.4. Distortions in the timing profile of these events may be used to reduce these backgrounds [84].

2.7.7 External Backgrounds

External backgrounds are radioactive decays occurring from the inner AV and beyond, which either propagate inside the AV or mis-reconstruct inside. These decays may occur in the acrylic, the ropes, external water, or the PMT array. The expected decay rates for each detector component are given in Table 2.3.

Most decay products are attenuated before they enter the AV, however higher energy gammas and betas are of concern. These are mainly from ^{214}Bi (^{238}U chain), ^{208}Tl (^{232}Th chain), or ^{40}K . By fiducialising the volume most external decays may be removed. The background may be further reduced using the differences in PMT hit times to events occurring inside the fiducial volume. In-situ analysis during the water and scintillator phases will constrain the number of background events [95].

Source	Measured levels	Decays/yr
Internal ropes	^{214}Bi : $(2.8 \pm 5.4) \times 10^{-10} \text{g}_U/\text{g}$ [99]	4966
	^{208}Tl : $< 2.0 \times 10^{-10} \text{g}_{Th}/\text{g}$ [99]	< 418
Hold-down ropes	^{214}Bi : $(4.7 \pm 3.2) \times 10^{-11} \text{g}_U/\text{g}$ [99]	4.06×10^6
	^{208}Tl : $(2.27 \pm 1.13) \times 10^{-10} \text{g}_{Th}/\text{g}$ [99]	2.32×10^6
Hold-up ropes	^{214}Bi : $(4.7 \pm 3.2) \times 10^{-11} \text{g}_U/\text{g}$ [99]	8.34×10^5
	^{208}Tl : $(2.27 \pm 1.13) \times 10^{-10} \text{g}_{Th}/\text{g}$ [99]	4.78×10^5
Water Shielding	^{214}Bi : $2.1 \times 10^{-13} \text{g}_U/\text{g}$ [100]	1.32×10^8
	^{208}Tl : $5.2 \times 10^{-14} \text{g}_{Th}/\text{g}$ [100]	3.92×10^6
Acrylic Vessel	^{214}Bi : $< 1.1 \times 10^{-12} \text{g}_U/\text{g}$ ^a [52]	1.28×10^7
	^{208}Tl : $< 1.1 \times 10^{-12} \text{g}_{Th}/\text{g}$ ^a [52]	1.50×10^6
Acrylic Vessel External Dust ^b	^{214}Bi : $(1.1 \pm 0.1) \times 10^{-6} \text{g}_U/\text{g}$ [84]	7.8×10^5
	^{208}Tl : $(5.6 \pm 0.5) \times 10^{-6} \text{g}_{Th}/\text{g}$ [84]	4.6×10^5
Acrylic Vessel Internal Dust	^{214}Bi : $(1.1 \pm 0.1) \times 10^{-6} \text{g}_U/\text{g}$ [84]	4.15×10^4
	^{208}Tl : $(5.6 \pm 0.5) \times 10^{-6} \text{g}_{Th}/\text{g}$ [84]	2.48×10^4
PMTs	^{214}Bi : $100 \times 10^{-6} \text{g}_U/\text{PMT}$ [52]	3.7×10^{11}
	^{208}Tl : $100 \times 10^{-6} \text{g}_{Th}/\text{PMT}$ [52]	4.4×10^{10}

^aAssumed $1.0 \times 10^{-12} \text{g/g}$

^bThe bottom hemisphere is assumed to be at target level while the top hemisphere is uncleaned

Table 2.3: Measured levels and expected rates of external backgrounds from the ^{238}U and ^{232}Th chains [84].

2.8 Physics Program

SNO+ has a broad physics program, across the different phases of the experiment. The water phase of the experiment can be used for exotic physics searches with unprecedented sensitivity, including axion-like particles and nucleon decay (see Chapter 6).

Prior to isotope deployment, the liquid scintillator can be used to investigate low energy solar neutrinos, including *pep* and CNO neutrinos. *pep* neutrinos are mono-energetic (1.44 MeV), and should be well observable. Their theoretical flux uncertainty is relatively small (1.2%), due to the constraint of solar luminosity [84]. A precise measurement will probe the MSW effect, and their survival probability is sensitive to non-standard interactions [101]. A measurement of the CNO neutrino flux may help explain the solar metallicity problem. The inferred distribution of heavy elements in the Sun may be compared to recent helioseismology results which suggest the metallicity is $\approx 30\%$ lower than Standard Solar Model predictions [84].

The Pickering, Darlington, and Bruce reactors, which contribute most of the anti-neutrino flux for SNO+, have longer baselines than is typical for KamLAND [101]. The spectral features of oscillations are therefore shifted to higher energies, helping to constrain the oscillation parameters [102].

The measurement of geo-neutrinos may aid our understanding of the heat production

inside Earth. KamLand, located near a mid-ocean ridge, has previously observed these neutrinos [103]. The lower reactor background of SNO+, and the well understood geology should yield an improved measurement [101], as well as providing a measurement for the continental crust.

SNO+ will also be on-line during all phases of operation to detect a galactic supernova, and will join the SuperNova Early Warning system (SNEWS) [104]. The primary physics goal, however, is to search for neutrinoless double beta decay in ^{130}Te loaded scintillator.

2.8.1 Neutrinoless Double Beta Decay

Majorana neutrinos and the motivation to search for neutrinoless double β decay are described in sections 1.7.2 and 1.7.4 respectively. The SNO+ experiment will search for $0\nu\beta\beta$ decay using the ^{130}Te isotope.

The ^{130}Te isotope was chosen because it has a high natural abundance of 34.1%, meaning that several tonnes can be loaded without enrichment. Compared to the other $0\nu\beta\beta$ isotopes, ^{130}Te has a relatively high Q-value of 2527.518 ± 0.012 keV, and one of the longest $2\nu\beta\beta$ decay half-lives of $(7.0 \pm 0.9(\text{stat}) \pm 1.1(\text{syst})) \times 10^{20}$ years. This is important given the ~ 100 keV energy resolution of liquid scintillator experiments [105]. Using the innovative loading technique, developed for SNO+, a loading of 0.3% natural tellurium (by mass) has been proven to be stable for a period of over two years. Up to 5% (by mass) of natural tellurium may be loaded whilst maintaining good absorption, scattering and light yield properties [84].

SNO+ benefits from being able to deploy a large quantity of isotope into the detector volume, and to easily and affordably scale this loading [84]. The isotope could also be changed in the future if desirable. Although SNO+ does not have the energy resolution of alternative detector designs, it is able to fit the energy spectrum using the large statistical sample of events [105]. SNO+ is able to measure the backgrounds before and after the deployment of isotope, making it possible to identify and remove contamination. The tellurium and scintillator can be removed and repurified if the background levels are too high. The detector response can also be measured without isotope deployment. As described in sections 2.6 and 2.7 some backgrounds can be tagged and removed by particle discrimination or coincidences. Water shielding and the deep underground location reduce backgrounds, and external backgrounds can be further reduced by fiducialising the detector envelope [84].

A stacked plot of the expected energy spectrum for all backgrounds in the region of $0\nu\beta\beta$ over five years of data taking is shown in Figure 2.5. A hypothetical signal is shown for a Majorana mass of $m_{\beta\beta} = 200$ meV, which corresponds to a half-life of $T_{1/2}^{0\nu\beta\beta} \sim 1 \times 10^{25}$ yr using the IBM-2 nuclear matrix element [106]. Events are for a fiducial volume of 3.5 m, 0.3% natural tellurium loading and 200 $N_{\text{hits}}/\text{MeV}$ light

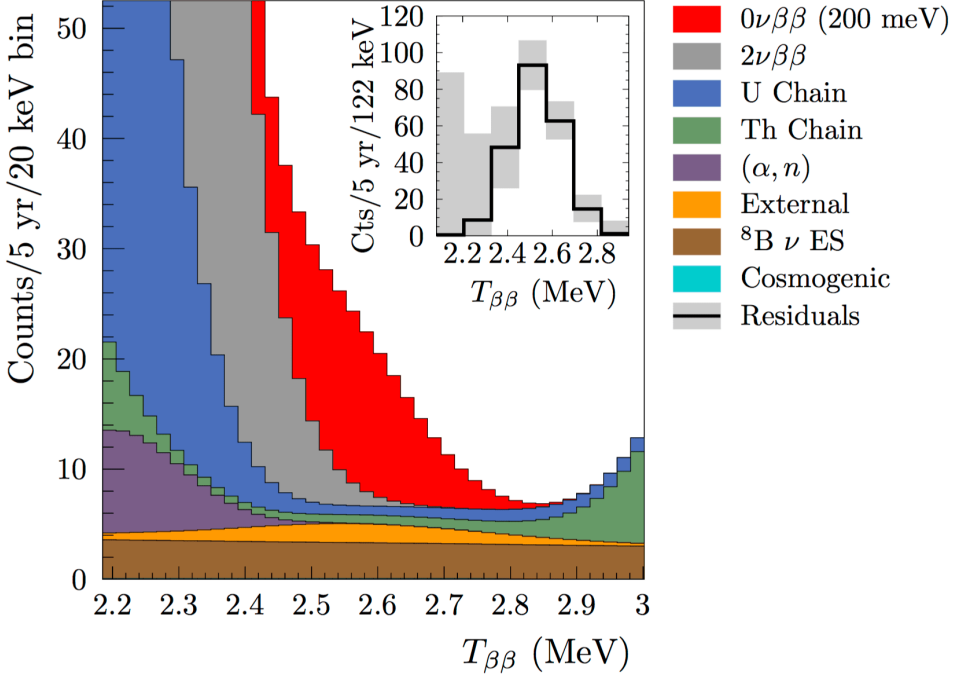


Figure 2.5: A stacked plot of the expected energy spectrum for all backgrounds in the region of $0\nu\beta\beta$ over five years of data taking. A hypothetical signal is shown for a Majorana mass of $m_{\beta\beta} = 200$ meV. Events are for a fiducial volume of 3.5 m, 0.3% natural tellurium loading and 200 $N_{\text{hits}}/\text{MeV}$ light yield. The effective kinetic energy is denoted $T_{\beta\beta}$ [84].

yield. A rejection is assumed of $> 99.99\%$ for $^{214}\text{Bi-Po}$ and $> 98\%$ for $^{212}\text{Bi-Po}$ [84]. The dominant background is $2\nu\beta\beta$ decay because of the energy resolution. Another significant background is the flat elastically scattered ^8B solar neutrinos, which cannot be reduced by a direction cut due to the isotropic nature of scintillation.

The number of $0\nu\beta\beta$ decays that are expected to be observed by the SNO+ detector is given by,

$$S = \epsilon N_{130} \ln 2 \frac{t}{T_{1/2}^{0\nu\beta\beta}}, \quad (2.1)$$

where ϵ is the signal detection efficiency, N_{130} is the number of ^{130}Te atoms in the fiducial volume, and t is the live-time [84].

Phase I of the SNO+ experiment, which will see a loading of 0.3% (by mass) of natural tellurium, is planned for 2017. This equates to nearly 800 kg of ^{130}Te . Assuming that the observed number of events in the ROI is equal to the expected background, with a 20% fiducial volume cut, and five years of live-time, sensitivity calculations set a lower limit on the half-life of $T_{1/2}^{0\nu\beta\beta} > 9 \times 10^{25}$ yr at 90% CL, or $T_{1/2}^{0\nu\beta\beta} > 4.8 \times 10^{25}$ yr at 3σ level. This corresponds to an effective Majorana mass of $m_{\beta\beta} = 55\text{-}133$ meV, using a phase space factor of $G = 3.69 \times 10^{-14} \text{yr}^{-1}$ [107] and $g_A = 1.269$. The range

is due to different nuclear matrix element calculation methods [84]. This is just above the sensitivity necessary to exclude a portion of the inverted hierarchy phase space.

With higher loadings it will be possible to probe the inverted mass hierarchy. For Phase II of SNO+, the natural tellurium loading is planned to be increased to 3% (by mass). The light yield at this loading is $150 N_{\text{hits}}/\text{MeV}$ with perylene used as a wavelength shifter. Replacement of the PMTs to high quantum efficiency tubes, and improvements to the concentrators would increase the light collection by factor of ~ 3 , compensating for the diminished photon output. This would improve the sensitivity to an effective Majorana mass of $m_{\beta\beta} = 19\text{-}46 \text{ meV}$ with a lower limit on the half-life of $T_{1/2}^{0\nu\beta\beta} > 7 \times 10^{26} \text{ yr}$ at 90% CL [84].

Chapter 3

Refurbishing the SNO Detector

The SNO detector has been repurposed for the SNO+ experiment, helping to lower the cost and construction time. SNO was designed to contain heavy water in the AV, had different physics goals, and experienced some degradation of the PMTs and trigger system over time. Consequently various upgrades and repairs have been necessary for the refurbishment process.

A plant has been constructed underground to process and purify the LAB-PPO, as well as improvements to the water plant. Hold-down ropes have been installed to counteract the buoyancy of a scintillator filled AV. An LED/laser system has been installed to calibrate the PMT and electronics response as well as monitor the detector optical properties. Upgrades have been made to the electronics system to cope with increased bandwidth and provide additional functionality, as well as repairs to both the trigger system and PMTs. A closed system of dense nitrogen gas has been installed to reduce radon ingress, as well as an interface to allow, amongst other purposes, water and scintillator to flow in and out of the AV. This chapter details this work, focussing on tasks that were contributed to by this author.

3.1 Scintillator Plant

This author was involved with the installation of many of the vessels and pumps for a scintillator processing plant, designed to purify LAB and PPO, mix them into scintillator, load with ^{130}Te , and repurify processed scintillator. A photograph taken during a vessel installation can be seen in Figure 3.1.

The plant uses the same techniques, and has similar cleanliness expectations to the Borexino and KamLAND experiments (see Table 2.2). Approximately $\sim 10^{-17}$ g/gLAB is anticipated for ^{238}U and $\sim 10^{-18}$ g/gLAB for ^{232}Th . This results in 13 counts per day from U and two per day from Th.

Design and construction of the plant was highly challenging due to its underground location. There are tight constraints on space and a complicated geometry of the excavated cavity. Strict hazard controls are also required when heating a combustible fluid



Figure 3.1: A photograph of the author taken during the installation of a vessel in the scintillator processing plant.

in an underground laboratory.

The plant's processes include multi-stage dual-stream distillation to separately purify LAB and PPO before their combination into scintillator. The scintillator is then purified by column water extraction to remove K, Pb, Bi, Th and Ra heavy metals. Steam/N₂ then further purifies the scintillator by removing Rn, Ar, Kr, O₂ gases and residual water. Functional metal scavengers then remove heavy metals remaining in the scintillator.

Scintillator in the detector can be recirculated in order to repurify and perform *ex-situ* radio-assaying. The repurification is done in quasi-batch mode using temperature regulation to minimise the mixing of repurified scintillator. Repurification turnover is within 100 hours, less than the half-lives of ²²⁴Ra and ²²²Rn. A detailed description of the plant can be found in [108, 109]; the following is an overview of its processes.

Figure 3.2 is a simplified flow diagram of the LAB and PPO distillation process. LAB is first vaporised in a boiler and fed into the mid-point of a distillation tower. The six-stage tower (32 in diameter × 13 ft 7 in height) vacuum distills the LAB at 55 Torr. There is separation due to the different boiling points of the impurities. A liquid level of concentrated impurities remains at the bottom of the tower and can be extracted through a bottom flow. Purified LAB flows out of the top of the column and is condensed. A fraction of the purified product, called the reflux, is sub-cooled and fed back into the top of the distillation column. Distillation is effective at removing the radioactive heavy metals Ra, Th, Po, Pb, Bi, K, as well as partially oxidised organic molecules from oxygen exposure, which all have lower volatility than pure LAB. Remov-

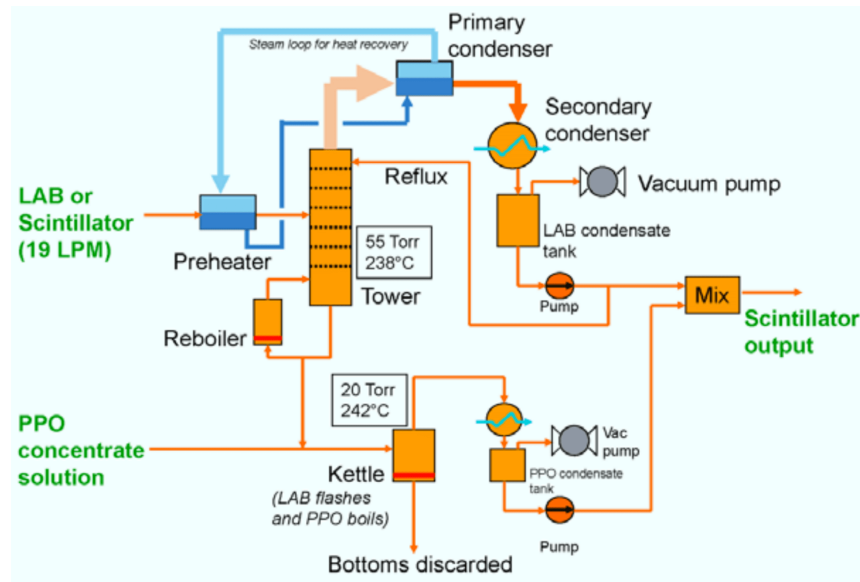


Figure 3.2: A flow diagram of the SNO+ distillation system. The distillation tower is used for vacuum distillation of LAB, while the kettle flash distills a concentrated solution of PPO in LAB. The tower can also distill scintillator for the recovery and purification of PPO [108].

ing oxidised molecules improves the optical transmission of the scintillator, increasing the light collection and therefore improving the energy resolution.

If scintillator is fed into the tower then PPO is concentrated at the bottom, which can be fed through to the PPO distillation process for repurification. PPO is also purified by distillation. It is first dissolved into LAB in a concentrated solution so it can be fed into the distillation kettle as a liquid. The LAB then flash distills, while the PPO boils, and the two are then recombined forming a solution in a condenser. Impurities are discarded from the bottom of the kettle. The purified LAB and PPO are then mixed together to form scintillator.

The scintillator then goes on to a solvent-solvent extraction phase, in which two immiscible solvents are mixed and allowed to separate. When water is the extract solvent the process is called water extraction. The process works because water is significantly more soluble than LAB. Figure 3.3 is a simplified flow diagram of the water-extraction scintillator purification process.

The plant uses a 30 in diameter \times 18 ft 4 in height ScheibelTM column. LAB enters the bottom of the column and moves upwards due to pressure from a driving pump. The water enters at the top and flows downwards against the flow of LAB due to its higher density. The column has a 22-stage rotating impeller stack and baffle plates to mechanically mix the water and scintillator. Scintillator at the top, above the water feed can be extracted from the column, as can water at the bottom below the LAB input. Spent water is then processed to clean it before its return to the UPW plant.

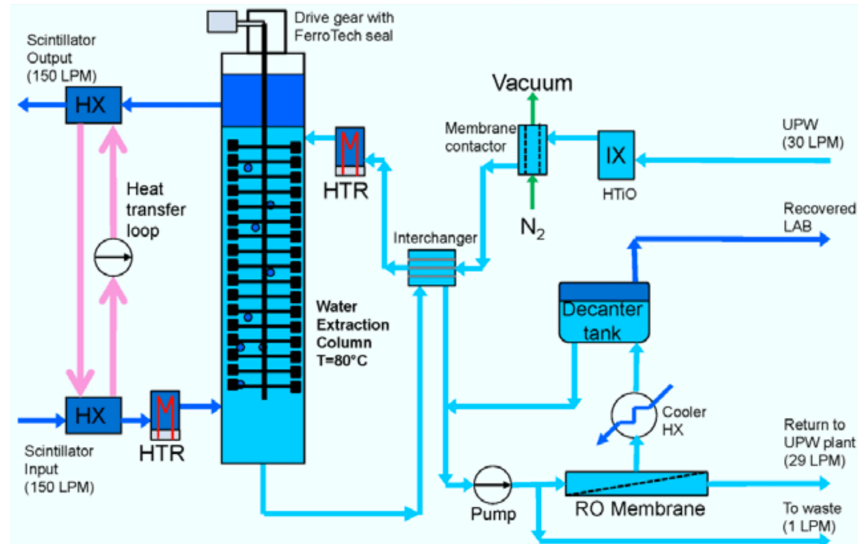


Figure 3.3: A flow diagram of the SNO+ water-extraction scintillator purification process [108].

Water extraction is effective at removing the ionic heavy metals U, Th, Ra, K, and Pb, as well as ultra-fine suspended particles. The extraction column can also be used to recover Te from scintillator.

Water extraction must then be followed by a gas stripping process to remove residual water, which can cause increased scattering and opaqueness. Similarly to water extraction, gas stripping is also a counter-current process, in which impurities more volatile than scintillator are converted from liquid to vapour and extracted. The scintillator is input into the top of a 24 in diameter \times 22 ft 8 in height column with 19 elements of Koch-Glitsch FlexiPac high surface area and density SS316L packing. Gas is fed into the bottom of the column and flows up through the packing, while the scintillator flows down. Both nitrogen and steam are used as stripping gasses, due to the impracticalities of shipping large quantities of nitrogen underground. The steam is super-heated so it is dry under vacuum at 100°C. Figure 3.4 is a simplified flow diagram of the gas stripping system. As well as residual water, gas stripping removes the radioactive impurities Rn, Ar, Kr, and the optical purity degrading oxygen. This technique has a 95% efficiency at removing Rn.

A metal scavenger is used to further remove metal contamination, and is a complementary process to water extraction. QuadraSil-AP™ is a commercially available scavenger selected for the SNO+ scintillator process plant. It has an amino propyl functional group on a 50 μ m mesh silica gel, and is effective at removing Pb and Ra. Metal contaminants can be recovered and *ex-situ* radioactive assayed for their ²²⁴Rn and ²²⁶Rn levels. The scavenger can be regenerated using HCl acid

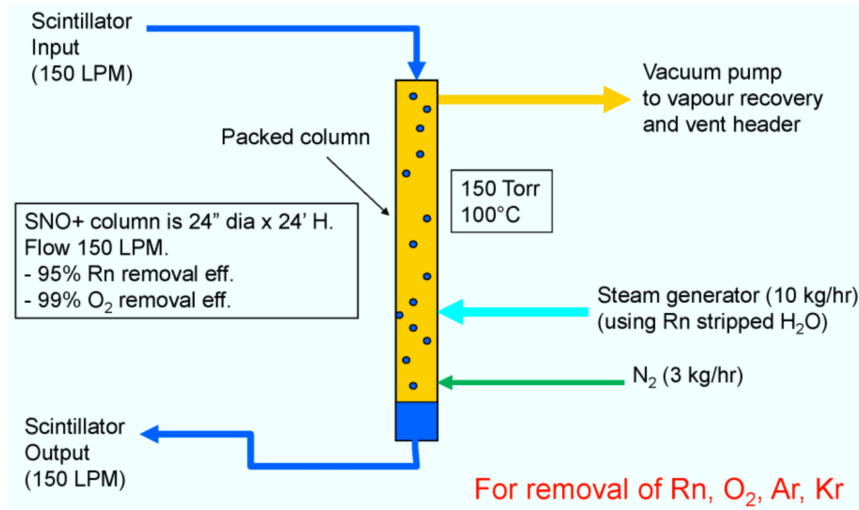


Figure 3.4: A flow diagram of the SNO+ gas stripping scintillator purification system. The stripping gas is a combination of nitrogen (3 kg/h) and super-heated steam (10 kg/h) [108].

3.2 Water Plant

The SNO+ light water purification plant is based on the plant used for SNO [110]. It takes water from main Vale INCO supply which is first passed through pre-treatment stages of filtration and chemical additives. The water then enters a purification and degassing loop. UV lamps are used to break apart organic compounds into an ionic form which is removable by ion exchange columns. A degasser then extracts radon and oxygen with high efficiency, followed by another UV steriliser which acts as a biological steriliser. Finally a $1\ \mu\text{m}$ filter bank removes particulates. The water then flows into the AV or cavity. The water can subsequently be extracted for repurification and degassing.

The SNO water plant has been upgraded for SNO+ to improve its performance. Components that were used for the purification of D₂O for SNO are now used to improve the purity of the SNO+ light water. For example, the D₂O high-flow skid was installed in order to use the HTiO columns for radium removal [111].

3.3 Hold-down Ropes

LAB-PPO has lower density ($\rho = 0.86\ \text{g/cm}^3$ at $T = 12^\circ\text{C}$) relative to light water. Consequently the AV will be buoyant and so a new rope system is required to hold it down. A network of high purity polyethylene fibre (Tensylon) ropes of 38 mm diameter are looped over the AV and anchored to the cavity floor. A visualisation of the rope system can be seen in Figure 3.5 and a photograph taken from below the AV can be seen in Figure 3.6. The original hold-up ropes have been replaced with new 19 mm Tensylon to reduce internal radioactivity. The full rope system has been simulated in

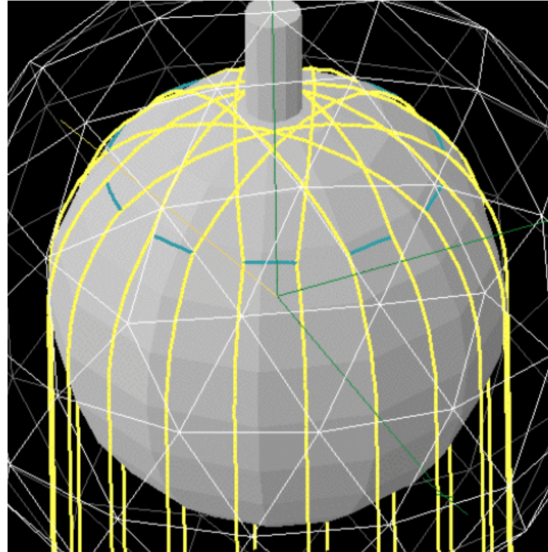


Figure 3.5: Visualisation of the hold-down rope system which compensates for the buoyancy of the AV due to the lower density of scintillator than water [84].

RAT so that the effect of shadowing on the PMTs can be estimated.

3.4 Optical Fibre Calibration System

The external optical calibration system, known as ELLIE, uses light from fast pulsing LEDs or lasers to provide *in-situ* measurements of the detector's optical properties and PMT response. A discussion of the purpose and benefits of the ELLIE optical fibre calibration system can be found in Section 2.4.

The TELLIE system has 91 injection points, one for each of the 92 nodes on the geodesic sphere of PMTs (except node 1 where the neck is located). Figure 3.7 is a flat map representation of the geodesic sphere, showing the number for each node. Each node is attached to a group of PMT hex cells (the structure housing an individual PMT), which can be of size seven or nineteen hex cells. A fibre is installed onto the outer-facing side of one of these hex cells.

The hex cells have rivet holes to attach to each other. These holes are unused for the hex cell faces on the outside of the group. The LED/laser fibres are designed to be fixed to fibre plates that can be mounted by rivets to the existing holes in the hex cells. Figure 3.8 shows the mounting position for TELLIE fibre plates.

A plastic skirting was attached to the outer facing cells for SNO, to restrict external light entering the detector. This must be removed to attach the fibre plate and then replaced afterwards. The same size rivets used to attach the fibre plates were holding the plastic skirting. The rivets hold well, so the existing ones must be destroyed.

Before installing, the fibres were tested by shining an LED through one end and

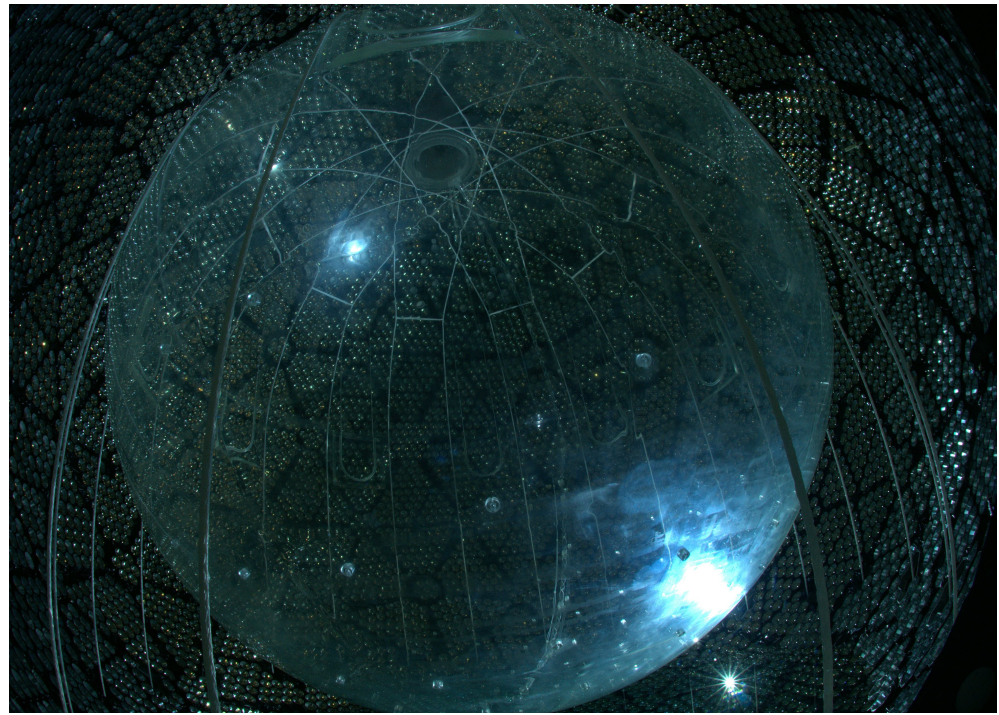


Figure 3.6: A photograph taken from below the acrylic vessel, showing the hold-down rope system [112].

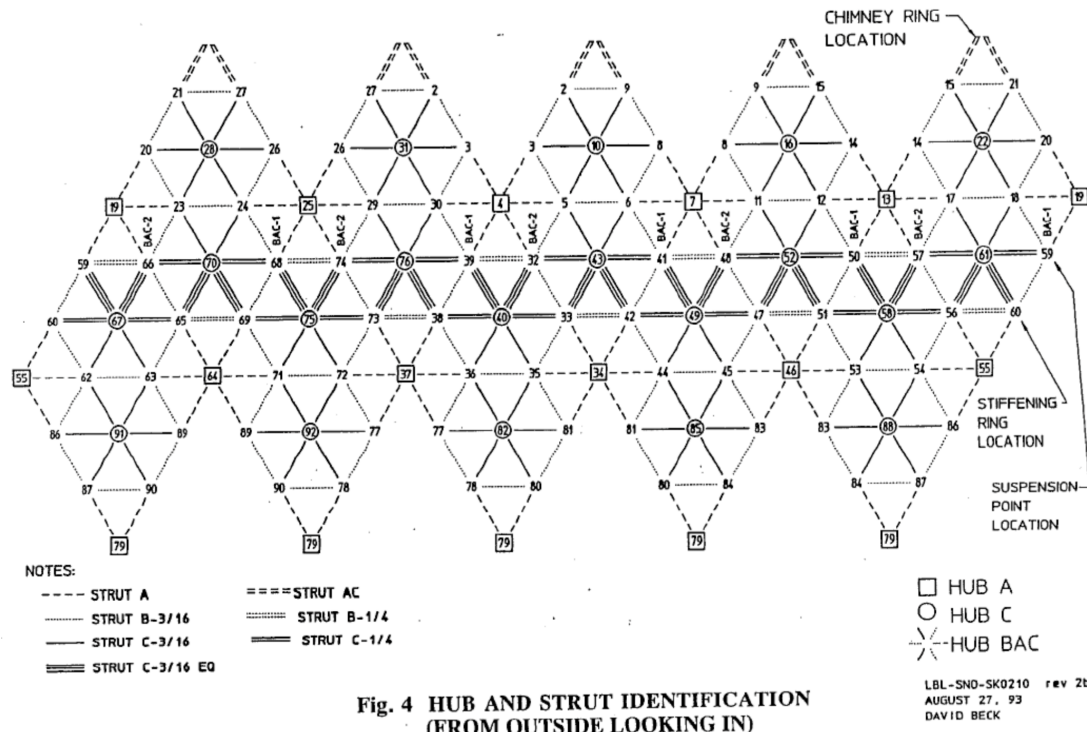


Figure 3.7: Flat map view of the detector with node panel numbering [113].

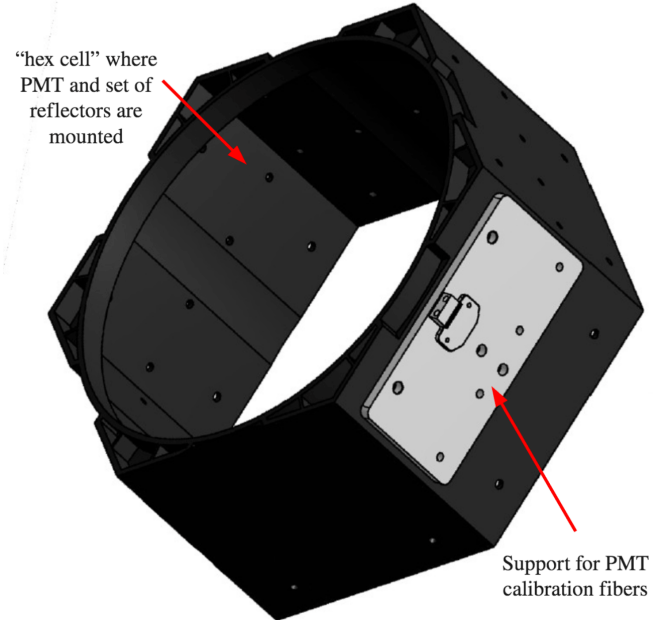


Figure 3.8: Mounting position for a TELLIE fibre plate [88].

recording the output at the other end with a lux meter. The hex cell that the fibre plate was mounted to was recorded to know the fibre position and direction with better than 1% error.

There are eight bundles of optical fibre cables, which contain all the optical fibres necessary for the ELLIE system and some spares. The wet ends for the fibres have been lowered into the cavity from the deck area. The PMT nodes in the flat map projection of Figure 3.7 are in nine horizontal rows. The fibres for the lower four node rows were installed from the cavity floor in March 2012 using bundles one and two [114]. This included thirty-six TELLIE fibres and two for SMELLIE. The next three rows of nodes are to be installed from a boat, reachable as the water level rises. The first of the three was installed in November 2014 using bundle three. Twelve TELLIE fibres were installed and two sets of AMELLIE fibres. The next two rows will be installed when the water level is higher using bundles four and five respectively, and bundle eight for any nodes for which the bundles do not have enough fibres. Fibres for the top two rows of nodes were installed from the top of the PSUP in October 2014 using bundle six. This author is pictured installing one of these TELLIE fibres in Figure 3.9. Bundle seven consists of spare fibres, should any be damaged during installation.

3.5 PMT Repair

SNO+ uses the original 8 inch Hamamatsu R1408 PMTs from the SNO experiment. Over the course of SNO, and the intervening period, approximately 800 PMTs have



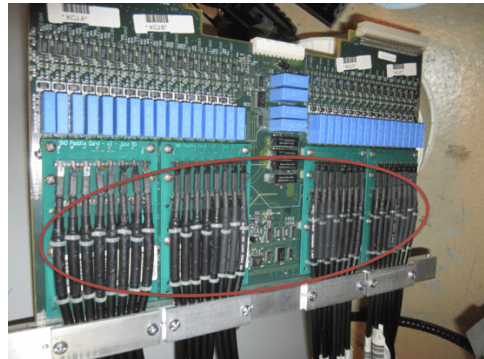
Figure 3.9: Photographs of a TELLIE plate being installed from the top of the PSUP.

stopped functioning correctly [115]. This reduction in PMT coverage of the detector, and correspondingly the light collection efficiency, lowers the energy resolution. Repairing all 800 faulty tubes would improve the energy resolution by approximately 9% relative to the state at the end of SNO. This decreases the background in the signal ROI from $2\nu\beta\beta$ decay, thus improving the signal detection capability.

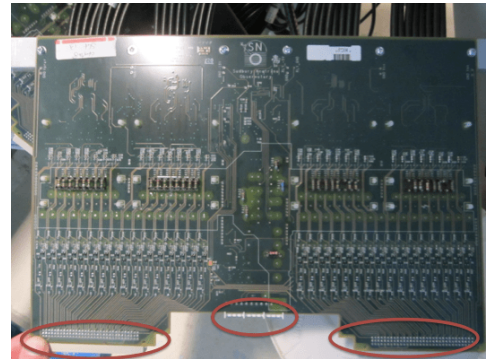
The ill-functioning PMTs were identified from their low occupancies and unusual base currents. Diagnostic tests could be performed from deck, without removing PMTs from the detector, by examining the PMTICs. Figure 3.10 shows a PMTIC, which connects the dry ends of the PMT cables to the electronics system. Measurements can be made of the resistance and capacitance across the PMT, as well as looking for shorts and incorrect resistances and capacitances on the PMTICs themselves. If there are no issues with the PMTIC channel, then it suggests that the PMT is faulty and should be pulled from the detector for testing.

PMTs on the bottom of the detector were accessed by lift from the cavity floor while the cavity was dry. Climbing on top of the PSUP could be used to access PMTs on the top of the detector. In this instance the worker would wear a safety harness attached to a fall arrest system. PMTs close to the equator of the detector can be accessed by boat as the cavity is filled with water. Photographs of this author replacing PMTs by boat can be seen in Figure 3.11.

The replaced and repaired PMTs must have similar operating voltages to be compatible with the voltage supplied by the electronics system. For PMTs towards the top and bottom of the PSUP there was time to remove a PMT, repair it and then return it to the same location. The PMTs that are accessed by boat, however, can only be accessed for the relatively short period when the water level is close to the PMT. These PMTs are replaced with a spare PMT that has a similar operating voltage.

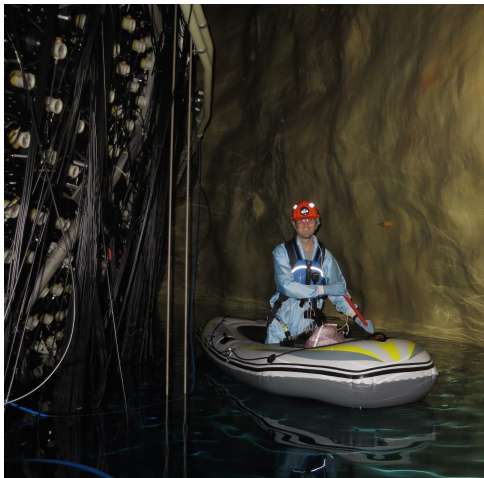


(a)



(b)

Figure 3.10: (a) The front face of a PMTIC, which connects the PMT cables (circled) to the electronics system. (b) The rear face of a PMTIC. The position of the connectors to the backplane and corresponding FEC are circled.



(a)



(b)

Figure 3.11: Boating in cavity (a) to access PMTs due to be replaced (b).

Faulty PMTs are brought to surface for testing and repair. The procedure for which is detailed in [115, 116]. The first stage of testing is to check the resistance and capacitance, expected to be $17.1\text{ M}\Omega$ and 9 nF respectively. The PMT is then placed in a dark box and tested for quality of signal, pulse rate, and breakdown while ramping to the operational voltage. PMTs that function correctly during these tests are likely to be failing in the detector for a different reason, for example a water leak in the PMT cable. These PMTs are recorded so that further inspections can be carried out to determine the cause.

If testing finds that the PMT is at fault it is most likely to be because of a short in the base electronics. The base circuit board should therefore be replaced. To do this the base must first be disassembled by removing the heat shrink collar and plastic hub. There is a silicone gel inside, providing protection to the electronics against water, that must be cleaned off. It can be pulled away from the faulty circuit board by hand, which can then be desoldered and removed. The remaining silicone gel around the PMT and hub is scooped off and further cleaned with solvents before being rinsed with isopropyl alcohol.

New capacitors are soldered to a fresh circuit board, and the board in turn soldered to the PMT pins. The high voltage (HV) connector is replaced if necessary, and attached to the circuit board. Figure 3.12a shows a PMT with a new circuit board and HV connector attached. The PMT is then tested again in the dark box. A second circuit board is attached and retested if it fails. If the PMT is still not functioning the PMT is assumed to have an internal fault, in which case it cannot be repaired. This is the case for approximately 10% of the PMTs.

A newly functioning PMT is cleaned with isopropyl alcohol and reassembled. The PMT hub is placed back over the base, taking care of the fragile HV connection as it is fed back through its port. It is then tested to ensure the connection has not been damaged. If working, a heat shrink collar bonds the PMT to its hub using a heat activated glue. This is a delicate process because the application of heat can deform the plastic hub. A motorised wheel is used to keep the PMT rotating and ensure an even application of heat. The inside of the hub is then cleaned with solvent, rinsed with isopropyl alcohol and dried. A conformal coating is poured inside of the hub, shaken to give a complete covering, including the electronics, and dried. This protects the circuitry from moisture and chemicals that could result in failure. The PMT hub is then filled with two-component silicone gel, providing further protection for the electronics circuitry against water. The silicone gel is degassed in a vacuum chamber and left to stand overnight. The hub filling port is topped up with silicone gel and plugged with a cap, ensuring there is no air space remaining underneath. The silicone is allowed to set before the cap is fixed in place and sealed with a heat shrink collar and heat activated glue. Figure 3.12b shows a fully repaired and resealed PMT. Finally the PMT is cleaned

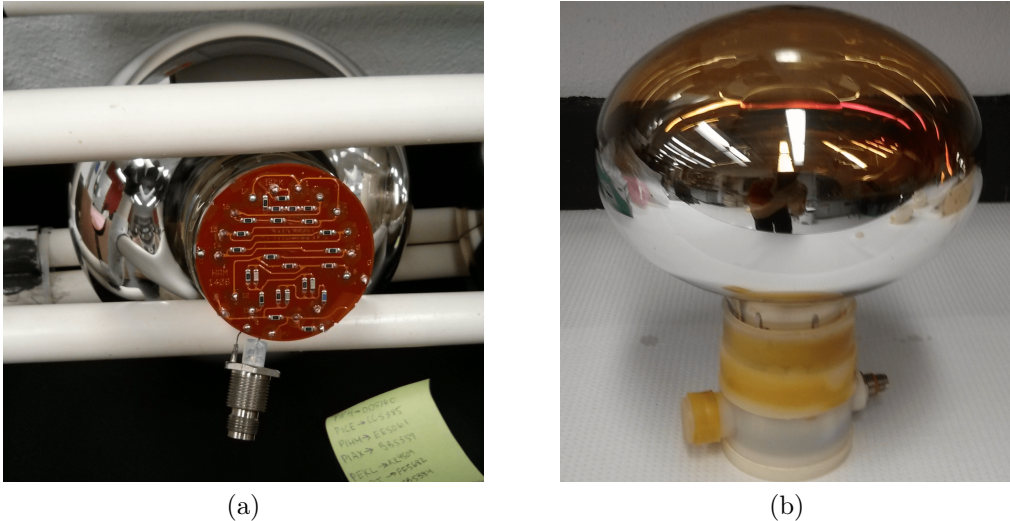


Figure 3.12: Exposed base circuitry of a PMT in repair (a) and a fully repaired and resealed tube (b) [115].

before being sealed in an airtight bag and transported back underground.

So far approximately 362 repaired PMTs have been installed [117], improving the light collection efficiency by $\approx 4\%$. A further 142 PMTs have been repaired and are ready to be installed in the detector [118] on future boating outings.

3.6 Electronics

Most of the SNO detector electronics can be reused for SNO+, which is beneficial because it is well understood and known to be reliable. However, during the course of its lifetime there has been some degradation requiring repair. There were also some upgrades necessary to cope with the data rate requirements of SNO+, as well as to provide some desirable functionality.

A build-up of low impedance dirt has accumulated on the electronics circuitry over time. This results in the electronics short circuiting, and the failure of many of the channels. The cause is thought to be sulphur in the lab air. The dirt, known as “dark matter”, needs to be cleaned off the circuit boards in order to fix the affected channels and reduce the probability of future failures [86].

The dark matter build-up was cleaned off the circuit boards by soaking them in a purpose-made commercially produced detergent for 30 minutes. The dark matter could then be gently brushed off. UPW was used to wash off the detergent before drying the boards [119]. Figure 3.13 is a photograph of dark matter that has been removed from electronics circuitry.

Several resistors on the PMTICs, motherboards, and daughterboards had a history of breaking during SNO. One in particular, on the PMTICs, would blow up with par-

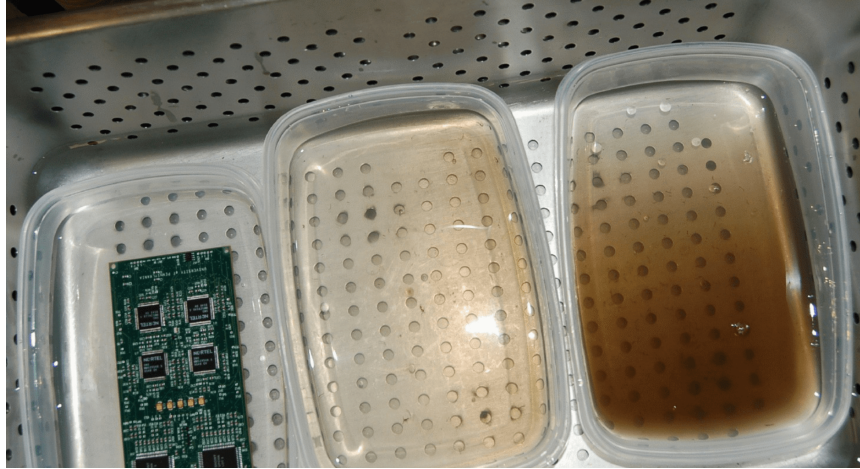


Figure 3.13: Photograph of dark matter being removed from the electronics circuitry [119].

ticularly violent consequences and short the board to ground. These have all been replaced for higher tolerance models. Two resistors to be replaced per channel on each daughterboard was especially time intensive, in total approximately 24,000 resistors were replaced [119].

Boards with replaced resistors could then be debugged for further problems. Common issues were with the voltage control circuitry, or a blown counting chip on a daughter or motherboard. Figure 3.14 is a photograph of a FEC with daughterboards attached, removed from its crate for debugging.

The original backplanes were replaced during the operation of SNO in order to reduce the crate noise rate [120]. This enabled the channel and trigger thresholds to be lowered and represented a significant improvement in the rates of certain types of instrumental background (false events caused by the detector electronics). During the commissioning of the electronics for SNO+ it was observed that the capacitors had a tendency to break down, dramatically, and catch fire. It was decided that all the backplane capacitors should be replaced for higher tolerance versions to prevent damage to the electronics. Figure 3.15 shows the damage caused by capacitor break down and this author soldering new components in place. Approximately 200 capacitors were replaced, a challenging process on a vertical surface.

The light yield will increase dramatically for SNO+, compared to SNO, and the photon hits will occur with a broader time distribution. For this reason the trigger signal integration time should be increased from ≈ 420 ns to $\approx 1\ \mu\text{s}$ (the longest time possible without hardware changes) and the long and short integration times should be retuned to match the scintillation time profile [120].

SNO+ will also have a much higher event rate than SNO, as some backgrounds have event rates of order hundreds of Hz. Data was read out one crate at a time for

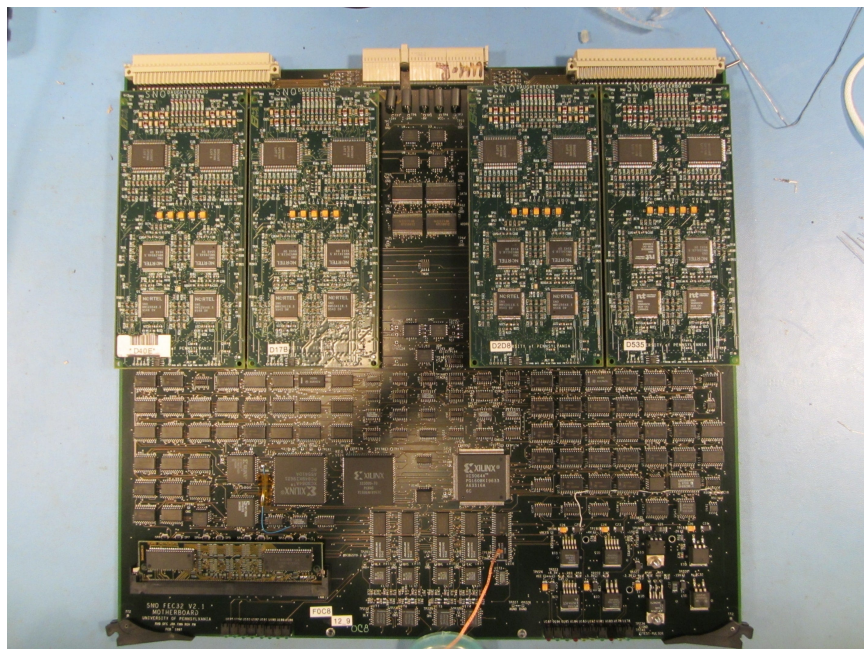


Figure 3.14: Photograph of motherboard.

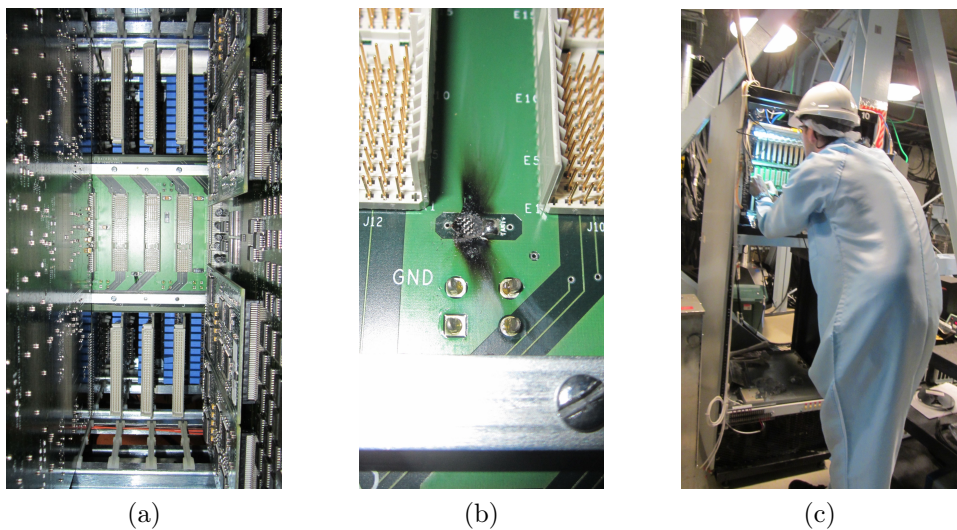


Figure 3.15: A backplane seen through the gap created by removing three FECs (a), a zoomed in shot of the damage caused by the blown capacitor (b), and this author replacing all capacitors on a crate (c).

SNO, with a bandwidth of 2 Mbit/s. This was sufficient for the normal running rate of 16 kBit/s for SNO, but will not be sufficient for the increased data rate of SNO+. The new XL3 modules designed for SNO+ read the data out in parallel. They have a 13 Mbit/s limit for each crate resulting in a 250 Mbit/s limit for the whole experiment, and should reduce noise by replacing detector-wide memory addressing [86].

An issue for SNO was that the current-based summation of trigger signals by the MTC/A boards ran up to about 50% of their 1 Watt power limit. There were some instances where a problem with the electronics caused a sustained current pushing the summation above this limit. This damaged the final summing node on the MTC/A which would require replacement [86].

The MTC/A+ boards, designed for SNO+, use operational amplifiers rather than transistors, and thus perform voltage-based rather than current-based sums. By discarding excess current the MTC/A+ can cope with the increased occupancy expected for SNO+. The trigger logic is also implemented using a Complex Programmable Logic Device (CPLD) rather than the discrete logic of the MTC/A boards. This allows for the additional functionality of different gain paths which saturate at 1000, 3600, and 10000 hits. Furthermore, the CPLD can be modified at a later date if desired. There is a benefit from the reduced dead time between events, down from 180 ns for MTC/A to 30-50 ns for MTC/A+ [121].

The analogue measurement board (AMB) was used for SNO to make measurements of the high gain ESUM trigger signal (a linear sum of all PMT pulses, shaped to a Gaussian profile with 120 ns width). The board makes an 8-bit measurement of the signal peak, integral and derivative [122]. The CAEN digitiser, which will replace the AMB for SNO+, stores a 12-bit digital copy with 250 MHz frequency of up to eight trigger traces (the high gain ESUM being just one) [123].

3.7 Cover Gas

As discussed in Section 2.7, long-lived radon daughters are a background to SNO+ physics. The level of radon in the SNOLAB laboratory air is 6×10^7 atoms/m³ [124], resulting in an activity level of approximately 130 Bq/m³ [84].

The target radon activity for SNO+ is below 5000 decays per year in the AV, corresponding to 5.5 atoms/m³. This necessitates a factor of $\sim 10^7$ reduction relative to the laboratory air, towards which the AV neck is only able to provide a factor of 50-100 reduction [124].

SNO used N₂ gas boiled off a liquid nitrogen dewar flowing through the volume above the D₂O to reduce radon ingress from the laboratory air. This was known as the “cover gas” system. However, the reduction in radon ingress by the cover gas only needed to be a factor of 10³ [124]. There was a further issue that pressure fluctuations can reduce the effectiveness of the system. The SNO cover gas is therefore not sufficient

for SNO+ and has been upgraded.

SNO+ will use a sealed system of three 240 L radon tight, flexing buffer bags filled with high purity nitrogen gas. The pressure of the gas can be adjusted to compensate for the ambient pressure in the mine. The system has been demonstrated to meet the radon reduction target [124].

3.8 Universal Interface

An interface with the AV is required such that water and scintillator can flow in and out of piping, from and to the processing plants, while also maintaining the purity requirements of the experiment. This is known as the “universal interface” (UI) because of its many other purposes [125, 126]. This author was involved with the installation and leak testing of the UI [127, 128].

A radon-tight seal is maintained between the UI and the AV using two concentric O-rings. Sufficient torque is applied to the connecting bolts such that the O-rings form a seal and the volume between them is flushed with nitrogen gas. The UI interfaces with the cover gas so that nitrogen gas covers the water or LAB in a sealed system.

The UI also interfaces with the calibration hardware. There is a glove box for human handling of the laserball and radioactive sources, as well as an umbilical retrieval mechanism so that they can be raised and lowered into the detector.

Sensors are installed in the UI for monitoring the level of the water or scintillator. Three independent systems will be used. One of which will be a simple level switch, and the others are likely to be a capacitive level sensor and an ultra-sonic sensor.

The UI also holds the four neck PMTs. These will register hits earlier in time than the other PMTs if an event occurs in the neck and can therefore be used to identify neck events.

The system is built in conjunction with a sliding floor to prevent light entering the cavity, enable a worker to interact safely with the UI and allow for AV movement. This will also be used to measure motion of the AV with respect to the deck.

3.9 Summary

Much work has gone into the refurbishment of the SNO detector to become SNO+. It will be ready to begin the water phase of the experiment in the coming months, followed by the scintillator phase a few months later. The Te-loaded phase is expected to begin in 2017.

Construction of the scintillator plant has been completed. It has been successfully helium leak checked, as well as undergone citric acid passivation and high-purity cleaning. It is now going through the commissioning process. The upper section of the UI is

ready to be installed and will allow deployment of sources into the water and scintillator to calibrate the detector.

The ELLIE system has been installed and PMTs repaired on the upper PSUP and the level below the equator. The levels above the equator remain to be installed, which will be done as the water level rises during the filling process. Final improvements to the electronics will also be performed before completion of the water-fill process and the final phase of electronics commissioning finished once the detector is full.

Chapter 4

Energy Reconstruction

The SNO+ detector was designed to measure physics at a broad range of energies. Different processes at different energies must therefore be distinguishable. For example, in the Te loaded scintillator phase of the experiment the $0\nu\beta\beta$ process must be distinguishable from the $2\nu\beta\beta$ process. In the water phase of the experiment, for the nucleon decay analysis presented in this thesis, the energy of the nucleon decay signal must be distinguishable from the various backgrounds' energies. The number of hits observed by the detector is expected to approximately scale with the energy of an event. This is, however, complicated by various detector effects. For example, photons may be attenuated, scattered, or reflected, and in scintillator may be absorbed and re-emitted. The position of the event in the detector does not elicit a uniform response, neither does direction, especially in the water phase. The detector itself is not uniform, for instance at the AV neck, and the PMTs perform differently. The tools for estimating the energy of an event must therefore take these factors into account in order to best estimate the energy of an event.

Two energy estimators, Prompt Lookup (EPL) and Response Processor (RSP), were implemented by the author which account for detector effects to different extents. Prompt Lookup uses Monte Carlo (MC) simulations to create a lookup table to estimate the relative efficiency of the detector based on the position and direction of an event. RSP models the optical path of photons produced in an event to estimate the probability that individual PMTs will register a hit. Comparisons of their performance to existing estimators are given.

4.1 SNO+ Energy Response

The following section outlines all the processes that affect the energy response of the detector for the light water phase of the experiment. Using these processes a model can be formulated which predicts the number of PMTs that will register a hit for an event with a particular energy and vertex.

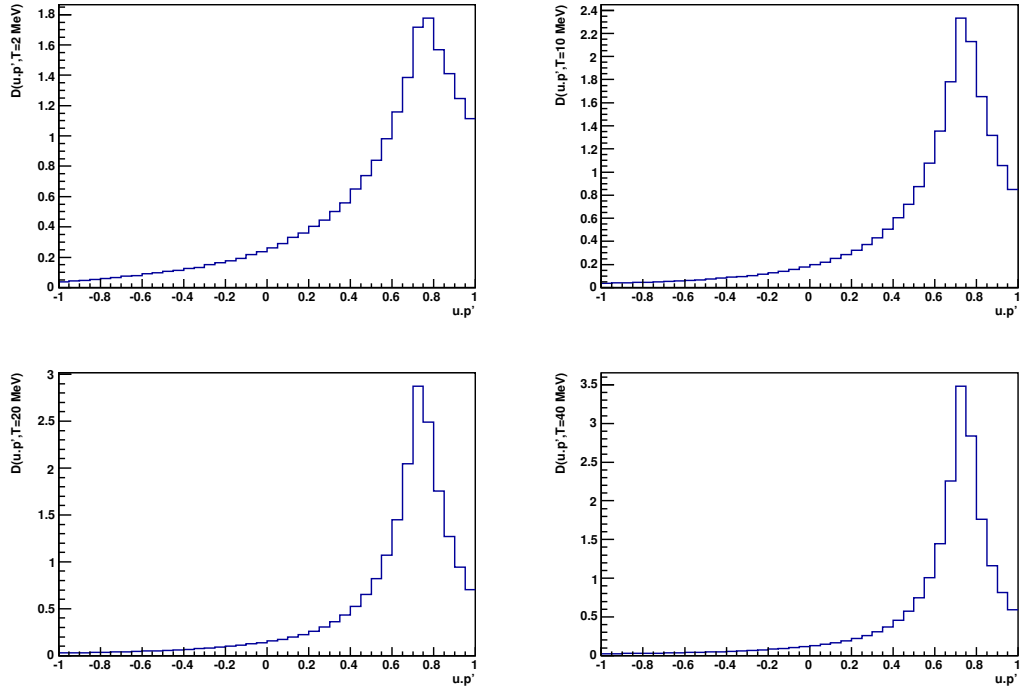


Figure 4.1: The normalised Cherenkov angular distribution at energies (top left) 2 MeV, (top right) 10 MeV, (bottom left) 20 MeV, (bottom right) 40 MeV, where $u \cdot p'$ is the angle Cherenkov photons are emitted relative to the electron direction of travel.

4.1.1 Cherenkov Radiation

As is described in Section 1.5.3, as an electron travels through water faster than the speed of light, a cone of Cherenkov photons is emitted at an angle of

$$\cos \theta_c = \frac{1}{n\beta} \quad (4.1)$$

relative to the direction of the electron. The distribution of Cherenkov photons would be a delta function at this angle, except for multiple scattering of the electron. Figure 4.1 shows the angular distribution of Cherenkov photons, D , for a selection of different energy electrons. This shows that the distribution becomes more peaked as the electrons increase in energy because there is less high-angle scattering.

The number of photons emitted will depend on the energy lost by the electron before crossing the Cherenkov threshold. The yield of photons with wavelength, λ , produced by an electron with energy, T , can be found by integrating Equation 1.34 over the distance travelled above threshold,

$$Y(\lambda, T) = \frac{dN}{d\lambda} = \frac{2\pi\alpha}{\lambda^2} \int_{n\beta > 1} \left[1 - \left(\frac{1}{n\beta} \right)^2 \right] dx. \quad (4.2)$$

The distance travelled above threshold increases approximately linearly with kinetic energy and so the Cherenkov yield is a function of T .

4.1.2 Attenuation and Scattering

Photons are attenuated (or “absorbed”) and scattered as they travel through their respective mediums. The further the distance travelled, and the shorter the attenuation or scattering length, the greater the probability of a photon experiencing either of these processes. The function, α , which characterises these effects,

$$\alpha(\vec{r}, \vec{p}_i, \lambda) = \alpha_{\text{att}}(\vec{r}, \vec{p}_i, \lambda) \alpha_{\text{scat}}(\vec{r}, \vec{p}_i), \quad (4.3)$$

has been decomposed into an attenuation function, α_{att} , and a scattering function, α_{scat} , where \vec{r} is the photon creation position and \vec{p}_i is the PMT position. The function gives the probability that a photon is not attenuated and remains in the prompt window.

The attenuation function is given by the following equation,

$$\alpha_{\text{att}}(\vec{r}, \vec{p}_i, \lambda) = \exp \left(\sum_{m=1}^3 -\frac{d_m(\vec{r}, \vec{p}_i)}{a_m(\lambda)} \right), \quad (4.4)$$

where $m = 1, 2, 3$ represent the inner H₂O, acrylic, and outer H₂O materials that the photons travel through as they propagate outwards from the inner AV. The function d_m is the distance the photon travels through material m , and a_m is the optical attenuation length in material m .

The optical attenuation length for light water as a function of λ is currently from SNO optics fits [129], although may be updated when the SNO+ detector is calibrated. The optical attenuation length for acrylic was determined from *ex-situ* measurements of the acrylic performed for the SNO experiment [129]. Figure 4.2 shows the absorption lengths for light water and acrylic. A flat spectrum is used above 450 nm for acrylic, which is close to transparent given its width.

While attenuated photons are extinguished and therefore cannot arrive at a PMT, a scattered photon may still arrive at a PMT. Cherenkov emission is a prompt process and applying a cut on PMT hits outside a prompt window helps determine if a photon took a direct path to the PMT. Scattering reduces the probability of a photon arriving within the prompt window.

Types of scattering considered to be relevant for the SNO experiment [130] were Rayleigh scattering, Mie scattering, and scattering off particulates. Rayleigh scattering is considered to be the main effect. Mie scattering is not included in the model because it is mostly forward peaked. Scattering off particulate matter in the water however is omnidirectional and therefore indistinguishable from Rayleigh scattering. A scale factor may be applied to the Rayleigh scattering calculation based on optical calibrations performed for SNO+. A scale factor of 1.0 is currently used because of the high purity of the water.

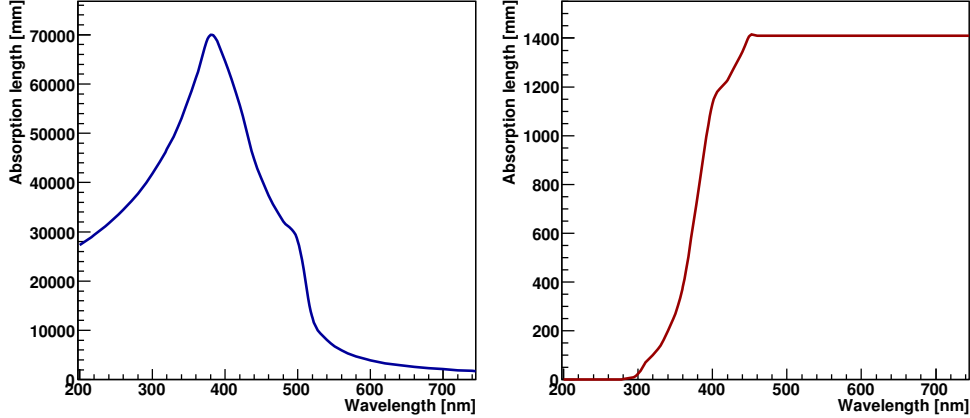


Figure 4.2: Absorption lengths for light water (left), calculated from an optics fit for SNO, and acrylic (right), determined from *ex-situ* measurements for SNO [129].

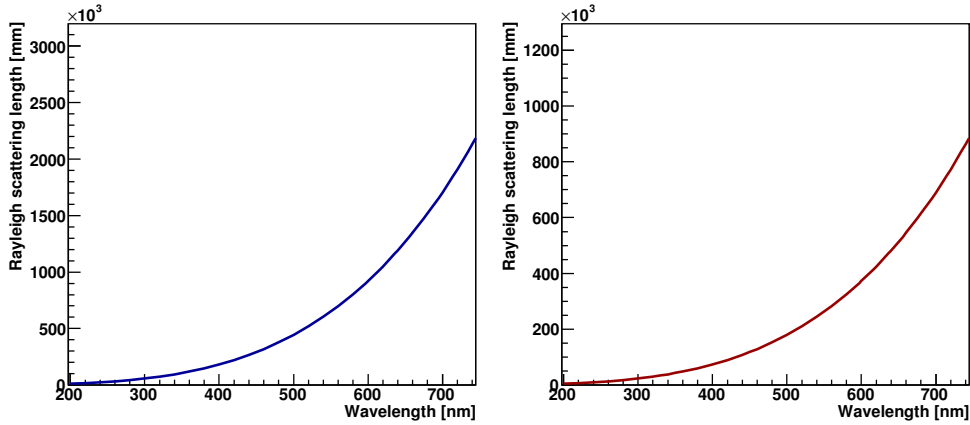


Figure 4.3: Rayleigh scattering lengths for light water (left) and acrylic (right).

The probability per unit length that a photon will be Rayleigh scattered is given by [131],

$$\frac{d\sigma}{dx} = \frac{8\pi^3}{27} \frac{1}{\lambda^4} k_B T \beta_T (n - 1)^2 (n + 2)^2, \quad (4.5)$$

where k_B is the Boltzmann constant, T is the temperature (11°C on average for SNO+), β_T is the isothermal compressibility, and n is the medium's index of refraction. The resulting Rayleigh scattering lengths for water and acrylic are shown in Figure 4.3.

The scattering function is expressed,

$$\alpha_{\text{scat}}(\vec{r}, \vec{p}_i) = 1 - \left(\left(1 - \exp \left(\sum_{m=1}^3 -\frac{d_m(\vec{r}, \vec{p}_i)}{s_m(\lambda)} \right) \right) \eta(\vec{r}, \vec{p}' \cdot \vec{r}) \right) \quad (4.6)$$

where s_m is the scattering length in material m , and η is the probability that a scattered photon will arrive at a PMT outside the prompt window, dependent on event position, \vec{r} , and photon angle relative to the event position vector, $\vec{p}' \cdot \vec{r}$.

Whether or not a scattered photon arrives outside the prompt window depends on the coordinates the scattering occurred at and the subsequent direction, as well as the choice of prompt window. This is very complicated to calculate explicitly, but Monte Carlo simulations may be used to estimate the probability of a scattered photon arriving late based on the photon's creation position and direction.

4.1.3 Fresnel Transmission Probability

The Fresnel transmission probability, F , is the probability of a photon being transmitted through both interfaces of the AV. It is approximated by the following equation,

$$F(\cos \theta_{\text{inner}}) = 0.5 (F_{\parallel}^1 F_{\perp}^2 + F_{\perp}^1 F_{\parallel}^2), \quad (4.7)$$

where $F_{\parallel,\perp}^{1,2}$ are the parallel and perpendicular photon polarisation transmission probabilities for interface 1, light water to acrylic, and interface 2, acrylic to light water. The photon polarisation refers to the angle between its electric field and the plane of the transmission interface. The above equation assumes equal parallel and perpendicular polarisation. The only argument for F is $\cos \theta_{\text{inner}}$, the angle of incidence on the inner surface of the AV, because all other angles, required for the calculation of $F_{\parallel,\perp}^{1,2}$, can be derived from it.

The probability of transmission through interface j for a photon with parallel polarisation is given by,

$$F_{\parallel}^j = \frac{n_{tj} \cos \theta_{tj}}{n_{ij} \cos \theta_{ij}} \left(\frac{2n_{ij} \cos \theta_{ij}}{n_{tj} \cos \theta_{ij} + n_{ij} \cos \theta_{tj}} \right)^2, \quad (4.8)$$

where $j = 1, 2$ refers to the H₂O-acrylic and acrylic-H₂O interfaces respectively. The index of refraction for the incident and transmitted material is denoted $n_{i,t}$ and $\theta_{i,t}$ is the incident and transmitted angle. The geometry involved in the Fresnel transmission calculation is shown in Figure 4.4.

The probability of transmission through interface j for a photon with perpendicular polarisation is given by,

$$F_{\perp}^j = \frac{n_{tj} \cos \theta_{tj}}{n_{ij} \cos \theta_{ij}} \left(\frac{2n_{ij} \cos \theta_{ij}}{n_{ij} \cos \theta_{ij} + n_{tj} \cos \theta_{tj}} \right)^2. \quad (4.9)$$

When light is transmitted from H₂O to acrylic to H₂O again the following equalities in angles and refractive indices can be used:

$$\theta_{i_1} = \theta_{t_2}, \quad (4.10)$$

$$\theta_{t_1} = \theta_{i_2}, \quad (4.11)$$

$$n_{i_1} = n_{t_2}, \quad (4.12)$$

$$n_{t_1} = n_{i_2}. \quad (4.13)$$

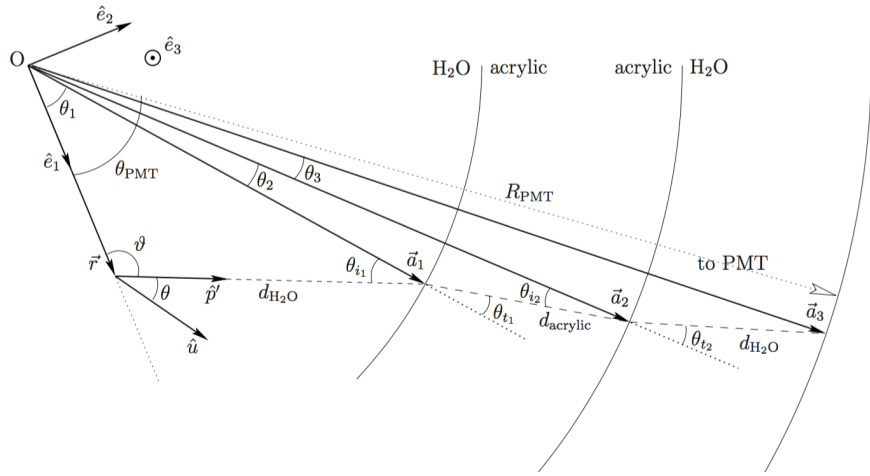


Figure 4.4: The geometry involved in the Fresnel transmission probability calculation, adapted from [131].

4.1.4 PMT Efficiency

The overall efficiency of a PMT channel, ϵ_i , is the probability that a photon incident on a PMT will register as a triggered hit. Here a photon being incident on the PMT means that it has entered the PMT bucket. The photon may take a direct path to the PMT face, or it may be reflected off the concentrator petals. The probability of the photon being reflected onto the PMT face is dependent on the incident angle into the bucket. A photon striking the surface of the PMT may reflect back out of the bucket or be absorbed without liberating a photoelectron. The liberation of a photoelectron is dependent on the incident angle on the PMT, as well as the wavelength of the photon. The different PMTs and electronics channels also have varying efficiencies of registering hits. The PMT efficiency, ϵ_i , can be decomposed into,

$$\epsilon_i(\cos \theta_{\text{PMT}}, \lambda) = \epsilon^{\circ} \epsilon^{\text{qe}}(\lambda) E^{\text{angular}}(\cos \theta_{\text{PMT}}, \lambda) E_i^{\text{relative}}, \quad (4.14)$$

where ϵ° is the average PMT collection efficiency (the probability that a photoelectron will be collected), ϵ^{qe} is the quantum efficiency of a typical PMT at normal incidence, E^{angular} is the angular PMT efficiency for a photon of wavelength λ with angle of incidence θ_{PMT} , and E_i^{relative} is a combination of the relative optical and electronic efficiencies of the i^{th} channel.

The PMT collection efficiency parameter, ϵ° , represents the overall probability that a photoelectron liberated from the photocathode will trigger a PMT. This single parameter is then adjusted relatively by the other PMT specific functions.

The quantum efficiency of the PMTs, ϵ^{qe} , is the probability that a photon of wavelength λ at normal incidence on the PMT will cause a photoelectron to be liberated from the photocathode into the vacuum envelope of the PMT [131, 132]. The measured quantum efficiency [133] is shown in Figure 4.5.

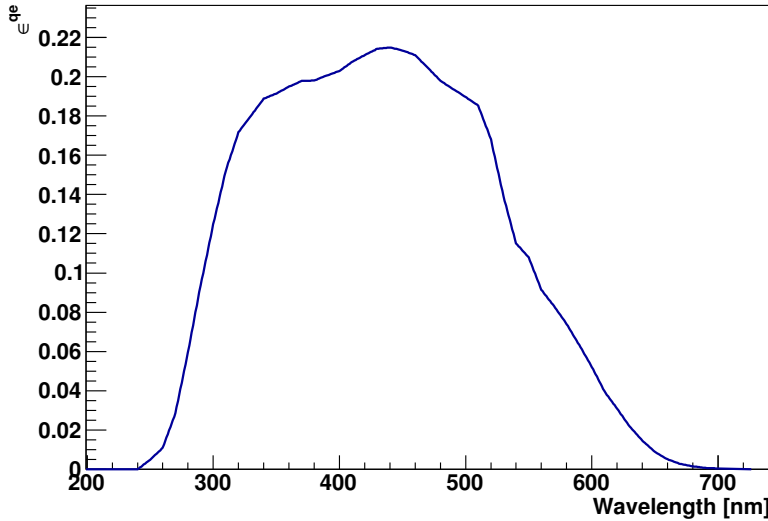


Figure 4.5: The quantum efficiency of the PMTs, defined as the probability of a photo-electron being liberated from the photocathode.

The angular dependence function, E^{angular} , adjusts the response of the PMT for the angle of incidence on the PMT relative to normal incidence.

The results of the optical calibrations give an overall PMT efficiency, E_i^{relative} , for the discriminator triggering and being read out by the electronics, which is calculated as [131],

$$E_i^{\text{relative}} = \frac{n_i}{\bar{n}}, \quad (4.15)$$

where n_i is the trigger rate of the i^{th} PMT (also known as “occupancy”) and \bar{n} is the mean trigger rate of all PMTs for a run. Regular calibrations will be performed to monitor the relative efficiencies.

To date, in this author’s implementation, the relative channel efficiencies have been fixed at one. This is because optical calibrations of the PMTs have not yet been performed, but once they have been these should be incorporated into the model.

4.1.5 Response Model

Incorporating the aforementioned effects on the response of the SNO+ detector, the following response model can be written for the number, N_i , of Cherenkov photons expected to result in a photoelectron triggering the i^{th} PMT,

$$N_i = \int d\lambda Y(\lambda, T) \int_{S_i} D(\vec{r}, \hat{u}, \vec{p}_i, T) F(\vec{r}, \vec{p}_i) \times \alpha(\vec{r}, \vec{p}_i, \lambda) \epsilon_i(\vec{r}, \hat{u}, \vec{p}_i, \hat{n}_i, \lambda) d\Omega, \quad (4.16)$$

where Y is the yield and D is the angular distribution of Cherenkov photons described in Section 4.1.1, F is the probability of transmission through both surfaces of the acrylic,

α is the reduction in prompt light due to absorption and scattering, and ϵ_i is the joint PMT and electronics channel efficiency that a photon striking the PMT will trigger it. The photons are of wavelength, λ , produced by an event of position, \vec{r} , direction, \hat{u} , and kinetic energy, T . The position and normal vector of the PMT are denoted \vec{p}_i and \hat{n}_i , with position vectors given with respect to the centre of the detector.

Only one trigger is recorded per PMT, regardless of the number of photoelectrons triggering them. A correction function, M , must therefore be used to adjust the expected number of photoelectrons triggering the i^{th} PMT for the probability that more than one photoelectron will trigger the PMT. The form of function M is discussed in Section 4.3.2.1. Summing across all PMTs then obtains the total triggered channels,

$$N_{\text{hits}} = \sum_{i=1}^{N_{\text{PMTs}}} N_i M(N_i). \quad (4.17)$$

4.2 Prompt Lookup Method

The Prompt Lookup estimator convolves the various factors affecting the detector energy response described in Section 4.1 using Monte Carlo simulations at different event positions and directions to estimate the event energy.

It works by finding the number of hits within the prompt time window (N_{prompt}), then scales the prompt hits to what would be expected had the event occurred at the centre of the detector ($N_{\text{prompt}}^{\text{scaled}}$). The scaled prompt hits are then mapped to the effective energy of an event, that of a single electron, (T_{eff}). Prompt hits were used to exclude hits caused by reflections or scattering, so that MC simulations are simpler and more reliable. This also improves the sensitivity of the method to event direction.

To scale N_{prompt} to $N_{\text{prompt}}^{\text{scaled}}$, and to map $N_{\text{prompt}}^{\text{scaled}}$ to T_{eff} , MC simulations were performed to create lookup tables. The method was intended to improve upon previous methods, such as: Simple which performed a linear scaling of the observed hits (N_{hits}); and Lookup which used lookup tables based on N_{hits} , radial position, and energy. Lookup was the default estimator used for SNO+. None of the available methods used direction, information available for a water-filled detector.

4.2.1 The scaling factor

The scaling factor, which scales the prompt hits of the event to what would be expected had the event occurred at the centre of the detector, is calculated for light water and scintillator filled AV scenarios as described in the following sections.

PMT hits were considered to be prompt if their time residuals were within a prompt window. The time residual is calculated as,

$$t_{\text{res}} = t_{\text{PMT}} - t_{\text{transit}} - t_{\text{event}}, \quad (4.18)$$

where t_{PMT} is the time the PMT triggers (adjusted for the time between a photon arriving at a PMT and a hit being registered), t_{transit} is the theoretical transit time for a photon taking an undisturbed path from the event vertex to the PMT, and t_{event} is the event time. The theoretical transit time is calculated using the group velocities and distances travelled through the different propagation mediums. Different prompt windows were chosen depending on the material filling the AV.

The scaling factor is further adjusted by the number of working PMTs for the run, compared to the number calculated at the time the estimator was created. This adjustment assumes that the non-operational PMTs are uniformly distributed throughout the detector and will not perform well if a particular region of PMTs are non-operational, for example if a crate was turned off.

4.2.1.1 Light water

In light water the scaling factor is calculated for the event radius, $|\vec{r}|$, and dot product of the event direction and position, $\hat{u} \cdot \vec{r}$. This accounts for the proximity of the event to the AV and the distances that photons have to travel to reach the PMTs, but does not incorporate asymmetries in the detector related to the exact position of the event, for example proximity to the AV neck.

To calculate the scaling factor, isotropic 5 MeV electron events were simulated at radial intervals of 200 mm from the centre of the detector up to 8000 mm. The N_{prompt} values for each radial position and $\hat{u} \cdot \vec{r}$ bin were divided by the central N_{prompt} .

In light water hits were considered to be prompt if their time residuals were between -10 ns and 8 ns. Figure 4.6 is a plot of the time residuals for events filling the detector and shows a peak in events between this prompt window.

The top plot of Figure 4.7 is a graphical representation of the scaling factor used by the Prompt Lookup estimator, while the bottom is a zoomed in version up to 6000 mm radius to show detail inside the acrylic vessel. They show that events close to the AV pointing outwards register the most prompt hits, whilst events for which photons have further to travel and are more susceptible to attenuation and scattering register fewer prompt hits. Events very close to the AV experience higher levels of internal reflection.

4.2.1.2 Scintillator

In scintillator the scaling factor is calculated for the event radius, $|\vec{r}|$, and $\cos \theta$, where θ is the angle to the z -axis in polar coordinates. The direction of the event is no longer appropriate because light is isotropic in scintillator. The method accounts for the proximity of the event to the AV and to the AV neck.

To calculate the scaling factor, isotropic 2.5 MeV electron events were simulated at radial intervals of 200 mm from the centre of the detector up to 8000 mm. The N_{prompt} values for each radial position and $\hat{u} \cdot \vec{r}$ bin were divided by the central N_{prompt} .

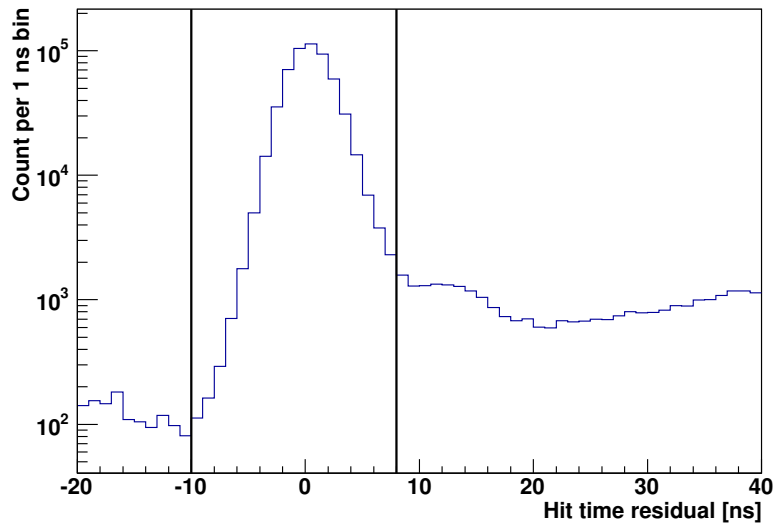


Figure 4.6: A plot of the time residuals in light water.

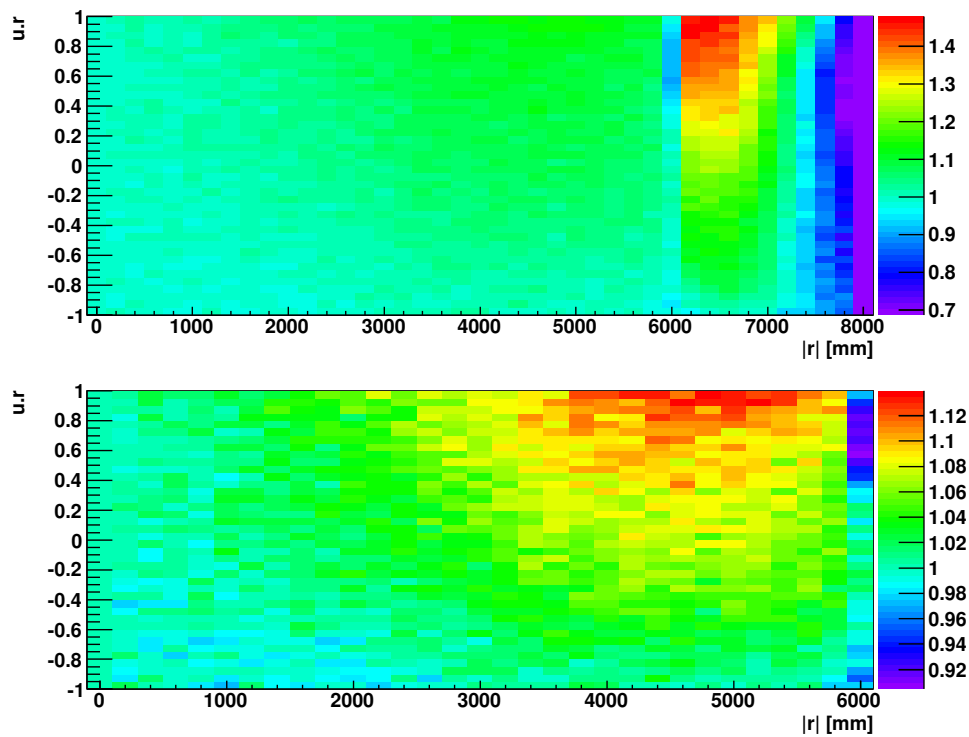


Figure 4.7: (top) A plot of the scaling factor used in the Prompt Lookup estimator for a light water filled AV. (bottom) A zoomed in version up to 6000 mm to show detail inside the AV.

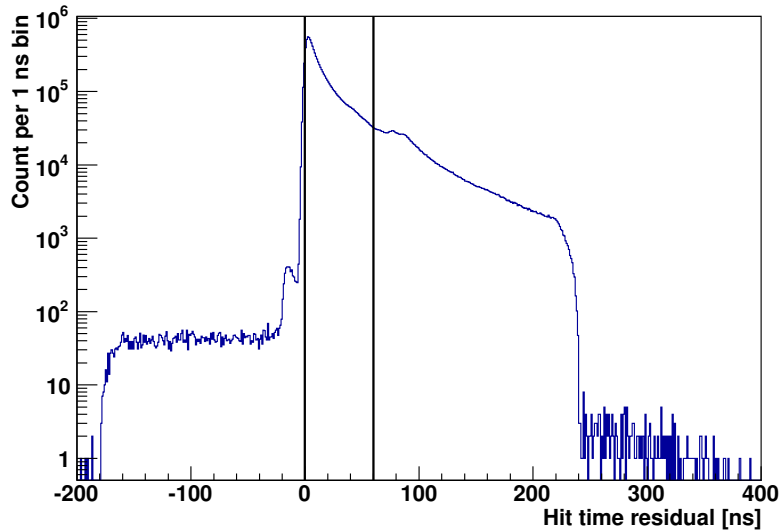


Figure 4.8: A plot of the time residuals in scintillator.

In scintillator hits were considered to be prompt if their time residuals were between 0 ns and 60 ns. Figure 4.8 is a plot of the time residuals, and shows a slower drop in time residuals greater than 0 ns because of the absorption and re-emission of photons on their way to the PMTs.

The top plot of Figure 4.9 shows the scaling factor used by the Prompt Lookup estimator, while the bottom is a zoomed in version up to 5000 mm radius to show detail inside the acrylic vessel. Events close to the AV neck register the fewest prompt hits, due to the lack of PMT coverage. Events closer to the AV than the detector centre, particularly lower on the z -axis, register the most hits. The extremes of the scaling factor are lower in scintillator than in water because there is less attenuation.

4.2.2 Prompt hits to energy map

The prompt hits to energy map is used to convert the scaled prompt hits, $N_{\text{prompt}}^{\text{scaled}}$, to the energy of an event caused by a single electron, T_{eff} , created at the centre of the detector.

4.2.2.1 Light water

To calculate the map for water, isotropic electrons created at the centre of the detector were simulated with energies from 3 MeV to 40 MeV. The mean number of prompt hits was then calculated for each energy.

Below 3 MeV the number of prompt hits is interpolated using a cubic spline method down to 0 at 0.26 MeV, the threshold at which Cherenkov radiation can be emitted in water. Energies below 3 MeV have not been simulated because the number of PMT

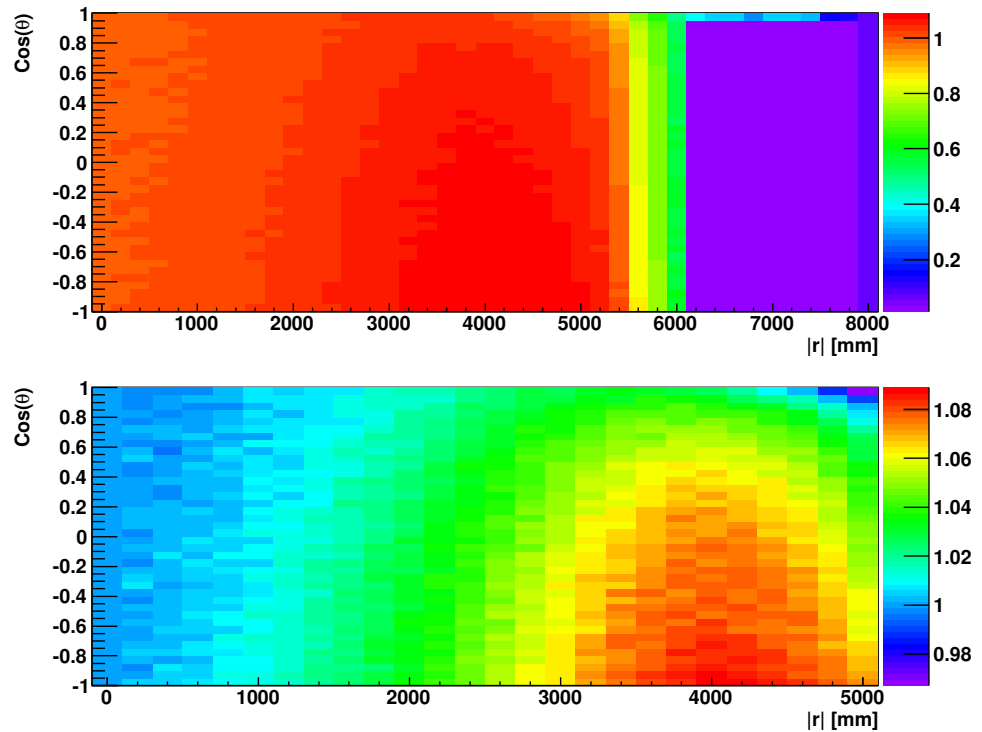


Figure 4.9: (top) A plot of the scaling factor used in the Prompt Lookup estimator for a scintillator filled AV. (bottom) A zoomed in version up to 5000 mm to show detail inside the AV.

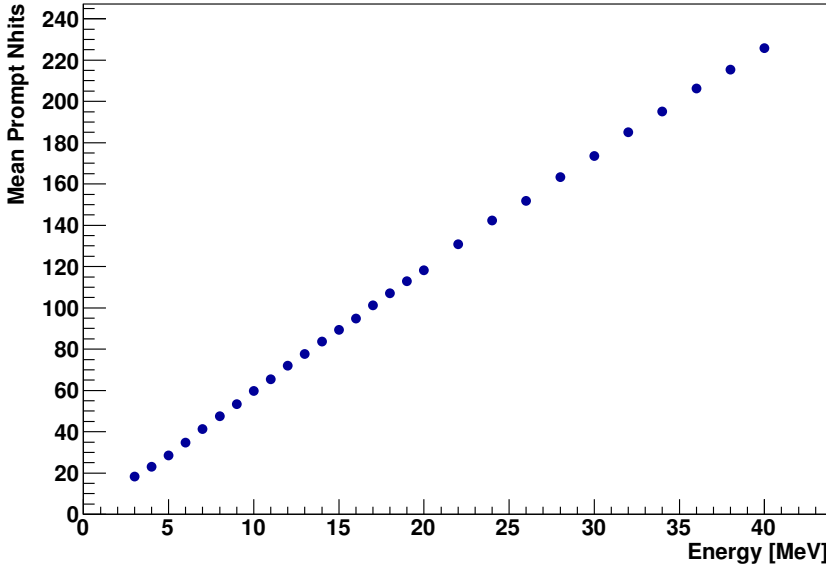


Figure 4.10: A plot of the prompt hits to T_{eff} map for single electrons created at the centre of the detector with a light water filled AV.

hits are so few. Consequently part of the approximately Gaussian N_{hits} distribution will be below the threshold number of hits required to trigger an event. This results in a bias for the mean towards higher prompt hits. This bias also affects how well the cubic spline method interpolates down to 0.26 MeV. Figure 4.10 shows the mean prompt hits to energy map.

4.2.2.2 Scintillator

To calculate the map for scintillator, isotropic electrons created at the centre of the detector were simulated with energies from 1 MeV to 20 MeV. The mean number of prompt hits was then calculated for each energy.

Below 1 MeV the number of prompt hits is interpolated using a cubic spline method down to 0 at 0 MeV. Figure 4.11 is a plot of the mean prompt hits to energy map. The relationship is non-linear because, as the energy increases, multiple photons are triggering the same PMTs.

4.2.3 Comments

Directional information was incorporated into the Prompt Lookup estimator to improve accuracy in the water phase. The method selects PMT hits caused by prompt light because the Monte Carlo is simpler and more reliable, ignoring the effects of scattering and reflections.

The exclusion of late light, however, removes some event information. The performance of the estimator will therefore be affected by scattering over the path length of

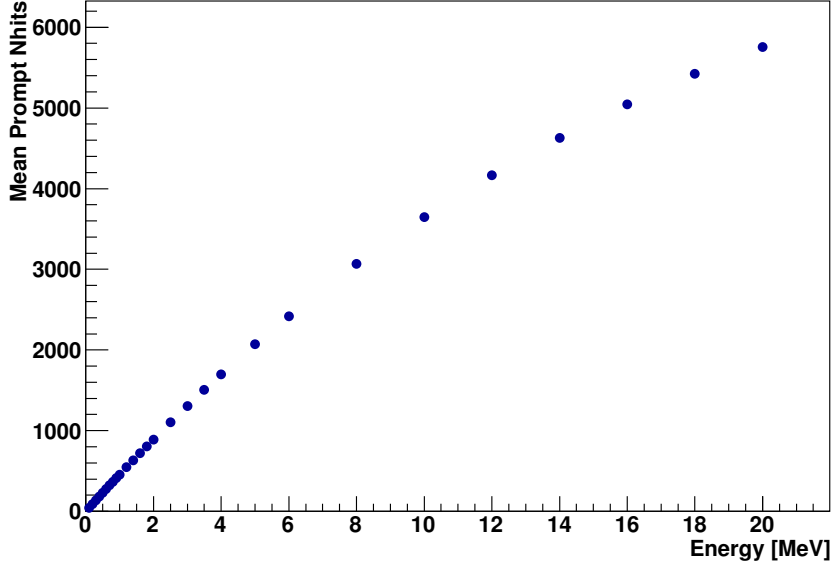


Figure 4.11: A plot of the prompt hits to T_{eff} map for single electrons created at the centre of the detector with a scintillator filled AV.

the photons, and the amount of reflection off the AV. For a future modification, Prompt Lookup could perhaps also use a late light scale factor and map, and transition between prompt and late based on event position and direction.

4.3 RSP Method

The “Original RSP” algorithm [134] had a similar methodology to Prompt Lookup, although a different implementation. The noise corrected number of PMT hits within a prompt window, N_{eff} , was adjusted to what would be expected had the event occurred at the centre of the detector. This adjusted N_{eff} was then scaled based on the ratio of the total number of PMTs, N_{PMTs} , to those that were working for the run the event was in, N_{working} . The equation for the corrected number of hits is,

$$N_{\text{cor}} = N_{\text{eff}} \frac{R^{\text{centre}}}{R} \frac{N_{\text{PMTs}}}{N_{\text{working}}}, \quad (4.19)$$

where R is the optical response of the detector. A map was created from N_{cor} to T_{eff} by performing Monte Carlo simulations of mono-energetic electrons.

The optical response function, R , was calculated based on the event position and direction. The function considered 70% of the detector, around the direction vector of the event, and segmented this portion into 100 angular bins. Most of the Cherenkov light is emitted within this region. The response was then calculated for a PMT at the centre of each bin. This method assumes a perfectly symmetrical detector and that the PMTs perform identically. It does not account for asymmetries in the detector

geometry, such as the AV neck or inactive PMTs, or for the differing efficiencies of individual PMTs.

The deficiencies with the “Original RSP” estimator motivated the development of a new “RSP” for SNO [131], which used a more precise optical model. The RSP estimator modelled the optical path of photons produced in an event, with a particular position and direction, to estimate the probability that each PMT will register a hit. In this way RSP takes into account detector asymmetries and the differing response characteristics of individual PMTs.

Details of this author’s implementation of “SNO+ RSP” are outlined in the following sections. In short the method uses an optical response function, R_i , to obtain an estimate of the probability that a photon produced during an event of a particular position, direction and energy will be registered as a hit by the i^{th} PMT. Then using an energy calibration function, \mathcal{F}_E , which maps electron kinetic energy, T_e , to an estimate of the mean number of Cherenkov photons produced, N_γ , the number of photons hitting each PMT is obtained. A sum across all PMTs yields the predicted number of PMT hits, $N_{\text{predicted}}$, which is compared to the actual number of triggered PMTs within a prompt window, N_{eff} , to adjust N_γ accordingly. An energy seed is used for a first guess of the event energy, the method then continues iteratively until the energy converges on the effective energy, T_{eff} .

4.3.1 The Response Function

The optical response function, R_i , which gives the probability that a photon of wavelength, λ , produced by an event of position, \vec{r} , direction, \hat{u} , and kinetic energy, T , will be registered as a hit by the i^{th} PMT is derived from Equation 4.16 and is given by the following equation,

$$R_i(\vec{r}, \hat{u}, \vec{p}_i, \hat{n}_i, \lambda, T) = D(\vec{r}, \hat{u}, \vec{p}_i, T) \Omega_i(\vec{r}, \vec{p}_i, \hat{n}_i) F(\vec{r}, \vec{p}_i) \\ \times \epsilon_i(\vec{r}, \hat{u}, \vec{p}_i, \hat{n}_i, \lambda) \alpha(\vec{r}, \vec{p}_i, \lambda). \quad (4.20)$$

The position and normal vector of the PMT are denoted \vec{p}_i and \hat{n}_i , with position vectors given with respect to the centre of the detector.

The Cherenkov angular distribution function, D , is the probability that a photon will be emitted at a particular angle relative to the event direction, as described in Section 4.3.1.2. The fraction of the solid angle that the collection area of the i^{th} PMT subtends is denoted by the function Ω_i . Further explanation can be found in Section 4.3.1.3. The probability of transmission through both faces of the AV is denoted by function F and is discussed in Section 4.3.1.4. The PMT efficiency function, ϵ_i , combines the quantum efficiency of the PMT with the angular response effect. Further detail is given in Section 4.3.1.5. The attenuation and scattering of photons as they propagate through the detector is represented by function α . A correction is made to the Rayleigh

scattered photons such that photons may scatter but still arrive at a PMT within the prompt window, as shown in Section 4.3.1.6.

The functions above can be simplified if the input parameters are the initial direction of the photon, \hat{p}' , the angle of incidence on the inner surface of the AV, θ_{inner} , and the angle of incidence on the PMT, θ_{PMT} . These parameters may be derived from the photon's creation position, \vec{r} , position of the PMT, \vec{p}_i , and the normal vector of the PMT, \hat{n}_i , as described in [131]. Using these parameter choices the functions then become:

$$D(\vec{r}, \hat{u}, \vec{p}_i, T) \rightarrow D(\hat{u} \cdot \hat{p}', T) \quad (4.21)$$

$$\Omega_i(\vec{r}, \vec{p}_i, \hat{n}_i) \rightarrow \Omega_i(\vec{r}, \hat{p}', \cos \theta_{\text{PMT}}) \quad (4.22)$$

$$F(\vec{r}, \vec{p}_i) \rightarrow F(\cos \theta_{\text{inner}}) \quad (4.23)$$

$$\epsilon_i(\vec{r}, \hat{u}, \vec{p}_i, \hat{n}_i, \lambda) \rightarrow \epsilon_i(\cos \theta_{\text{PMT}}, \lambda) \quad (4.24)$$

4.3.1.1 Light Path

The RSP method makes use of the Light Path Calculator tool [135] to calculate the new arguments for the response function, R_i , described above in Section 4.3.1. The tool also calculates the distances travelled by the photons in the different mediums, as well as the Fresnel transmission probability and solid angle subtended by the PMTs.

This implementation of SNO+ RSP uses a straight line calculation, rather than considering the refraction of photons as they enter and exit the AV. The impact of refraction from light water, to acrylic, back to light water was not considered a significant enough effect to warrant the additional computational cost of recalculating the light path for each PMT and sampled wavelength. The method could be changed to use the refracted path in a future implementation should the additional computational cost be considered acceptable.

The geometric derivations of the parameter transformations will not be described (further detail can be found in references [135, 130, 131]), but the calculations for the solid angle and Fresnel transmission probabilities will be discussed in sections 4.3.1.3 and 4.3.1.4 respectively.

4.3.1.2 Cherenkov Angular Distribution

The Cherenkov angular distribution function, D , used by RSP [131] fitted an exponential function with the parameters related to the electron energy, T_e . SNO+ RSP uses a lookup table for the normalised Cherenkov angular distribution for different energies, binned by $\hat{u} \cdot \hat{p}'$ value. The lookup table was then interpolated using a cubic spline method to obtain an estimate of the value for the event energy, T_{eff} , and photon angle, $\hat{u} \cdot \hat{p}'$. This lookup table is shown in Figure 4.12.

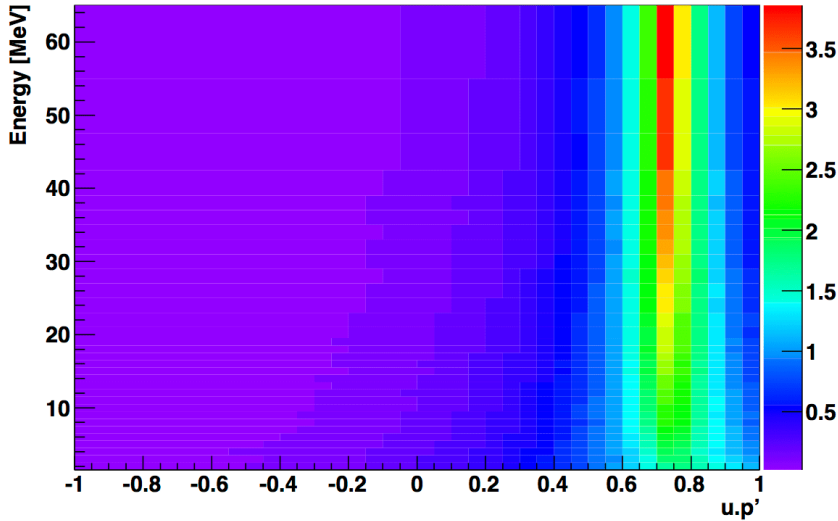


Figure 4.12: The Cherenkov angular distribution function, $D(\hat{u} \cdot \hat{p}', T)$, where $u \cdot p'$ is the angle Cherenkov photons are emitted relative to the electron direction of travel.

Figure 4.13 shows the distribution of total Cherenkov photons produced during an 8 MeV electron event. The distribution is approximately Gaussian with a mean of ≈ 3100 photons and a standard deviation $\approx 8\%$. This will be a significant factor in the resolution of the reconstructed energy.

4.3.1.3 Solid Angle

The solid angle of a PMT is the area it subtends, projected onto a unit sphere around the event position. To calculate this, four points are defined along the perimeter of the PMT face and used to specify an ellipse. This ellipse is then first projected onto the inner surface of the AV, to account for the effect the refractive indices have on the solid angle. In the case of a straight line path the ellipse proportions will not change. Two angles, α and β , are defined with respect to the major and minor axes of the projected ellipse, respectively, and are used to calculate the solid angle, Ω , on the unit sphere [136, 130]. The solid angle calculation is,

$$\Omega \simeq \pi \times \frac{\alpha\beta}{4} \quad (4.25)$$

where angles α and β are small. The geometry involved in the calculation is shown in Figure 4.14.

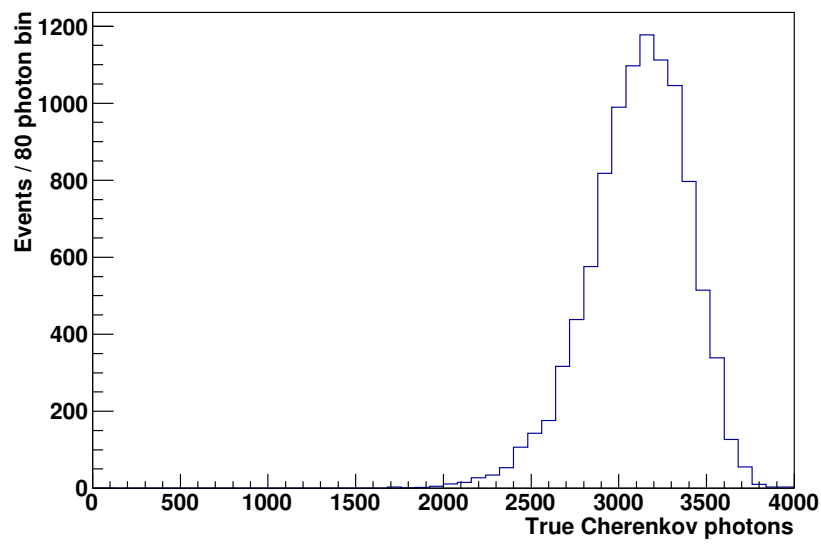


Figure 4.13: The total number of Cherenkov photons created during 8 MeV electron events.

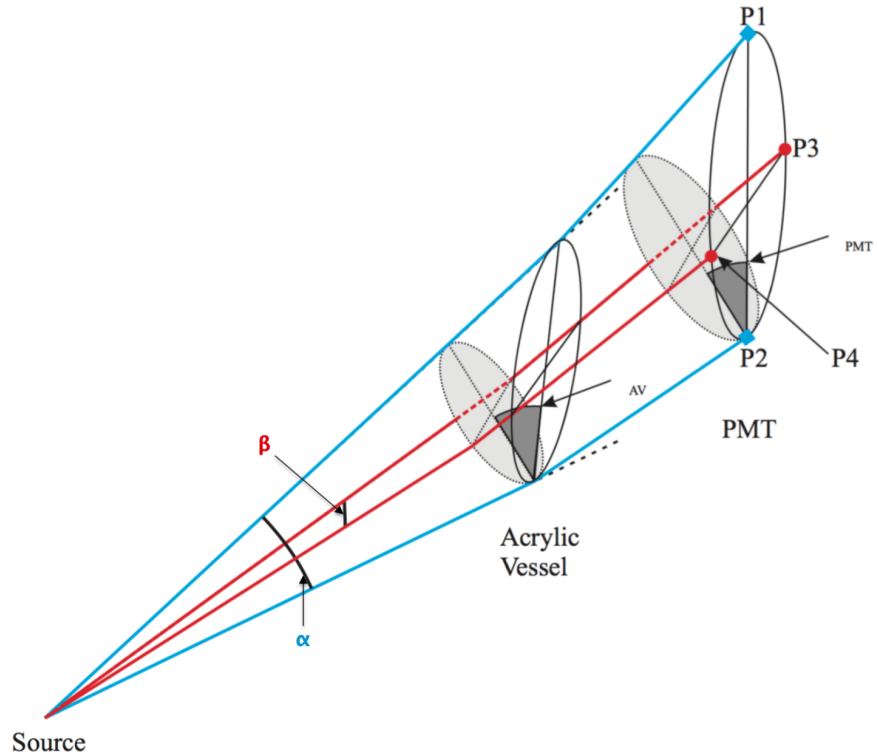


Figure 4.14: The geometry involved in the solid angle calculation, adapted from [130].

4.3.1.4 Fresnel Transmission Probability

Using a straight line path for photon transport the following simplification is made to the transmission calculations described in Section 4.1.3:

$$\theta_{i_1} = \theta_{t_1} = \theta_{i_2} = \theta_{t_2}. \quad (4.26)$$

This results in a constant transmission probability dependent only on the refractive indices. As this scales the predicted Cherenkov photons by the same amount, regardless of the event vertex, Fresnel transmission does not affect the SNO+ RSP estimation. Transmission is close enough to 1, however, that this is considered a reasonable approximation.

4.3.1.5 PMT Efficiency

The angular dependence function, E^{angular} , adjusts the response of the PMT for the angle of incidence on the PMT relative to normal incidence. Up to 42° the angular dependence is obtained from an optics fit to laserball Monte Carlo simulations [136]. Owing to restrictions on possible locations for the laserball, due to the SNO+ geometry, it is not possible to obtain an angular dependence from laserball calibrations much beyond 45° , so the true incident angle of photons on the PMT, from Monte Carlo simulations, were used to extend the angular dependence function to higher angles. The mean of the angular dependence in the range $37.5\text{--}42.5^\circ$ for the optics fit and the MC simulations was calculated and used to scale the Monte Carlo, to transition from the optics fit to MC from 42.5° upwards. Figure 4.15 shows E^{angular} as well as the optics fit. The angular dependence is wavelength dependent due to the wavelength dependence of the probability of reflection off the PMT concentrator. SNO+ RSP will use calibration data as it becomes available rather than the fit to laserball Monte Carlo simulations presented here.

4.3.1.6 Attenuation and Scattering

As described in Section 4.1.2 the loss of photons due to attenuation is given by the following equation,

$$\alpha_{\text{att}}(\vec{r}, \vec{p}_i, \lambda) = \exp \left(\sum_{m=1}^3 -\frac{d_m(\vec{r}, \vec{p}_i)}{a_m(\lambda)} \right), \quad (4.27)$$

where $m = 1, 2, 3$ represent the inner H₂O, acrylic, and outer H₂O materials that the photons travel through as they propagate outwards from the inner AV. The function d_m is the distance the photon travels through material m , and a_m is the optical attenuation length in material m . The distances travelled, d_m , are obtained from the light path calculator.

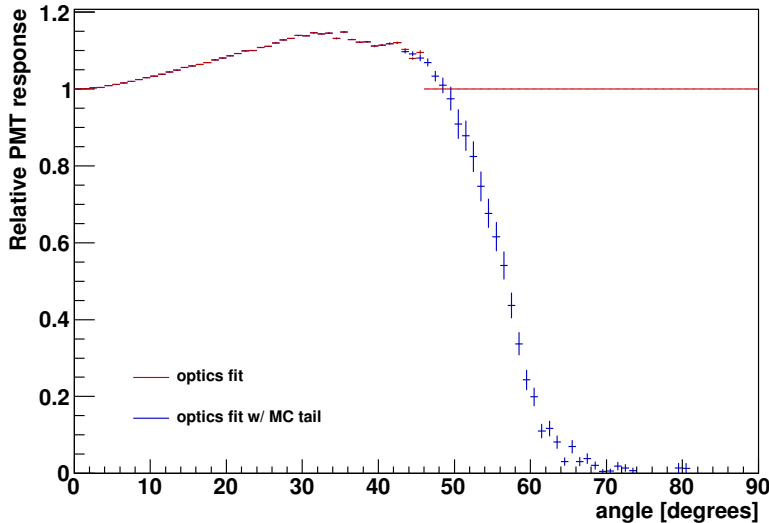


Figure 4.15: The angular dependence function, E^{angular} , from an optics fit up to 42.5° with a tail from Monte Carlo simulations at higher angles.

The function to scale the energy response due to the reduction in photons arriving within the prompt window because of scattering is expressed,

$$\alpha_{\text{scat}}(\vec{r}, \vec{p}_i) = 1 - \left(\left(1 - \exp \left(\sum_{m=1}^3 -\frac{d_m(\vec{r}, \vec{p}_i)}{s_m(\lambda)} \right) \right) \eta(\vec{r}, \hat{p}' \cdot \vec{r}) \right) \quad (4.28)$$

where s_m is the scattering length in material m , and η is the probability that a scattered photon will arrive at a PMT outside the prompt window.

The function, η , was implemented as a lookup table, which can be seen in Figure 4.16. The lookup table was calculated from Monte Carlo simulations. It can be seen that for photons that scatter en route to a PMT, those that are created close to the AV and directed outwards are more likely to be detected within the prompt window than photons created close to the AV and directed inwards which have further to travel. The late arriving Rayleigh scattered photon correction function implemented for SNO [131] had a different distribution, but the version presented here is thought to be an improvement.

4.3.1.7 Summary of the SNO+ RSP Detector Response

Figure 4.17 contains plots of the response function for 5 MeV electrons simulated along the x-, y-, and z-axes up to a radius of 6 m. It can be seen that the response has a very similar distribution to the Prompt Lookup scale factor of Figure 4.7. Events for which Cherenkov photons have the least distance to travel have the highest detector response and those with the furthest to travel have the lowest response. An exception is when events are closest to the AV and pointing outwards, for which there are fewer PMTs to

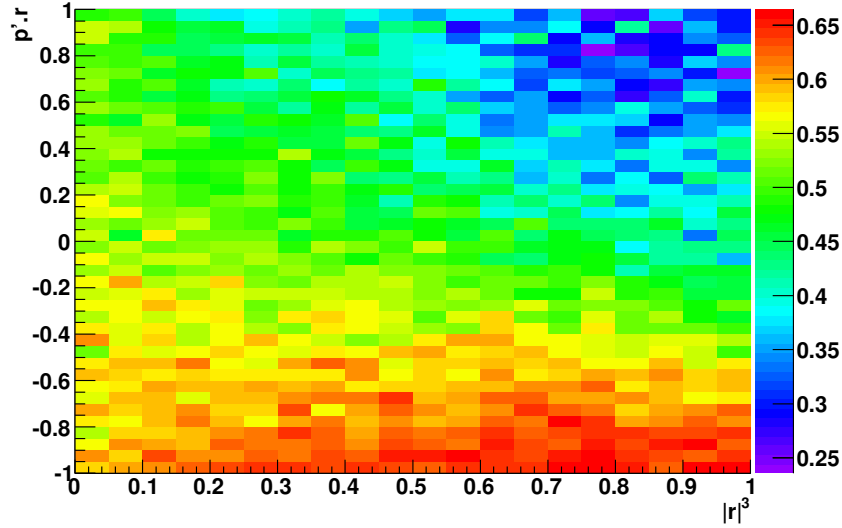


Figure 4.16: The function $\eta(\vec{r}, \hat{p}' \cdot \vec{r})$ for the probability that a Rayleigh scattered photon will not arrive within the prompt window, where $|\vec{r}|^3$ is the radius-cubed and $\hat{p}' \cdot \vec{r}$ is the photon angle relative to the position vector.

register hit. This effect is especially pronounced for events simulated along the z-axis which have a low response when directed towards the AV neck.

4.3.2 The RSP Algorithm

The RSP algorithm requires reconstructed event position and direction information from other methods. SNO+ RSP is also seeded by another energy estimator, Prompt Lookup. The method only runs if the reconstructed event position is within the AV, beyond which the response function and multi-photon correction (see Section 4.3.2.1) are less representative of the detector response.

An initial estimate of the number of Cherenkov photons emitted, N_γ , is obtained from the energy seed, T_e , and an energy calibration function,

$$\mathcal{F}_E^{-1}: T_e \rightarrow N_\gamma, \quad (4.29)$$

using SNO nomenclature. Details on how this mapping was created are given in Section 4.3.2.2.

An iterative convergence loop of the energy estimate begins with a calculation of the expected number of photoelectrons triggering the i^{th} PMT,

$$N_i = N_\gamma \frac{\sum_\lambda R_i(\vec{r}, \hat{u}, \vec{p}_i, \hat{n}_i, \lambda, T) \frac{1}{\lambda^2}}{\sum_\lambda \frac{1}{\lambda^2}}, \quad (4.30)$$

where R_i is the response function outlined in Section 4.3.1. The response is summed over λ between 220 and 710 nm at 10 nm intervals. An inverse square weighting is applied to reflect the wavelength spectra of Cherenkov light given in Equation 1.34.

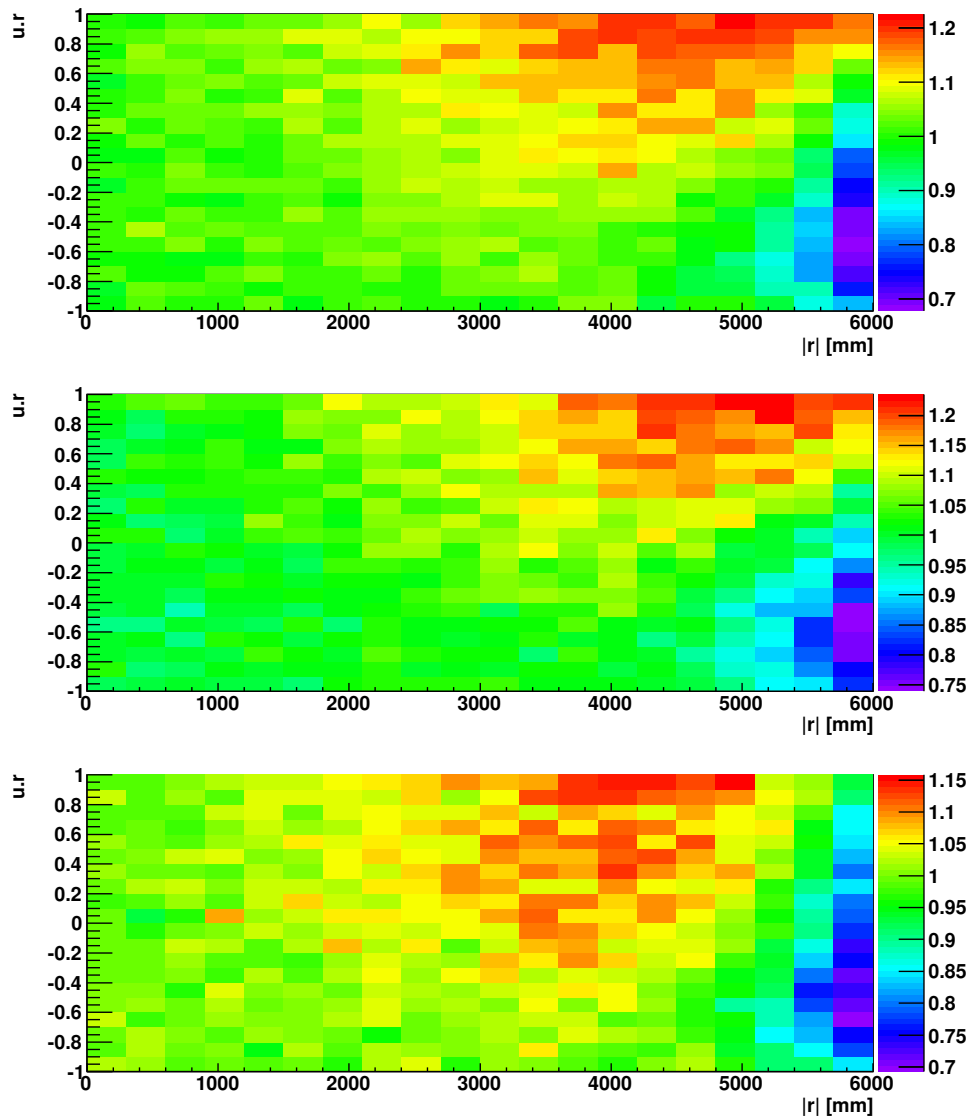


Figure 4.17: The response function for 5 MeV electrons simulated along the x-axis (top), y-axis (middle), and z-axis (bottom).

Decomposing the response function, the calculation in Equation 4.30 can be optimised,

$$N_i = N_\gamma D \Omega_i F \frac{\sum_\lambda \epsilon_i \alpha \frac{1}{\lambda^2}}{\sum_\lambda \frac{1}{\lambda^2}}. \quad (4.31)$$

The wavelength and energy independent functions, solid angle and Fresnel transmission, can be precalculated and called here. The Cherenkov angular distribution value must be calculated within the convergence loop, however only the wavelength dependent functions, PMT efficiency and attenuation, must be calculated with wavelength weighting.

The total number of hits predicted by RSP is calculated by summing across all active PMT channels, and adjusting the number of predicted photoelectrons triggering the PMTs for the probability that more than one photoelectron will trigger the PMT,

$$N_{\text{predicted}} = \sum_i^{N_{\text{active}}} N_i M(N_i), \quad (4.32)$$

where M is the multi-photoelectron correction function, and N_{active} is the number of active PMTs. The form of function M is discussed in Section 4.3.2.1.

The predicted number of PMT hits is then compared to the effective number of hits, N_{eff} , to adjust the predicted number Cherenkov photons emitted during the event. The effective hits, N_{eff} , is the noise corrected number of prompt hits observed during the event,

$$N_{\text{eff}} = N_{\text{prompt}} - R_{\text{noise}} \cdot 18 \text{ ns} \cdot N_{\text{active}}, \quad (4.33)$$

where N_{prompt} is the number of prompt hits observed during the 18 ns prompt window, and R_{noise} is the rate of noise for an individual PMT.

The estimate for the number of Cherenkov photons emitted during the event is adjusted as follows,

$$N_\gamma \rightarrow \frac{N_{\text{eff}}}{N_{\text{predicted}}} N_\gamma. \quad (4.34)$$

The next iteration of event energy, T_{eff} , is then obtained from the adjusted Cherenkov photons, N_γ using the energy calibration function \mathcal{F}_E . The RSP algorithm loops back to the calculation of Equation 4.30 until there is sufficient agreement between N_{eff} and $N_{\text{predicted}}$, or a maximum number of iterations is reached. Once agreement is found between N_{eff} and $N_{\text{predicted}}$, the final estimate of N_γ and T_{eff} are stored.

4.3.2.1 Multi-photoelectron Correction

Only one trigger is recorded per PMT, regardless of the number of photoelectrons triggering them. A correction function must, therefore, be used to adjust the expected number of photoelectrons triggering the i^{th} PMT for the probability that more than one photoelectron will trigger the PMT.

The multi-photoelectron correction used here [137] assumes a Poisson distribution for the number of photons emitted in the direction of the PMT. The correction function is given by,

$$M(N_i) = \frac{1 - e^{-N_i}}{N_i}, \quad (4.35)$$

where N_i is the expected number of photoelectrons triggering the i^{th} PMT, calculated from Equation 4.30.

This was shown to be an inaccurate approximation [138] as it assumes the proportion of photons emitted in any given direction is known. The Cherenkov angular distribution shown in Figure 4.12 was calculated by averaging over many events. For a single event Cherenkov photons will be emitted as a delta function at the Cherenkov angle, then scatter and emit Cherenkov photons in a cone around a different direction, and so on until the electron energy is below the Cherenkov threshold. This will have a different angular distribution to the approximation used. Consequently the number of photons triggering some PMTs will be overestimated, and others underestimated. This will, however, be a good approximation for scintillator.

4.3.2.2 Energy Calibration Function

The energy calibration function maps electron energy, T_e to the estimate of the number of Cherenkov photons emitted, N_γ . The strictly increasing inverse is calculated,

$$\mathcal{F}_E^{-1}: T_e \rightarrow N_\gamma, \quad (4.36)$$

from which the calibration function,

$$\mathcal{F}_E: N_\gamma \rightarrow T_e, \quad (4.37)$$

can be derived.

Mono-energetic single electron events were simulated. The RSP algorithm was then run for each event, but the true electron kinetic energy was used wherever an energy was required. An initial estimate was provided for the number of Cherenkov photons, N_γ . Once N_γ converges the value was then outputted.

A distribution of the predicted Cherenkov photons, N_γ , can then be obtained. See Figure 4.18a for the distribution for 8 MeV electrons. The distribution has a mean of ≈ 1918 and a standard deviation of $\approx 17\%$, approximately double the standard deviation of the true Cherenkov photon distribution of Figure 4.13. The difference between the peaks of Figures 4.13 and 4.18a is because of inaccuracies in the absolute efficiencies used by the detector response model. This makes no practical difference to the output of the method because it is adjusted for by the calibration function.

The mean value of the N_γ distribution was used as the mapping to the true kinetic energy, T_e , for each simulated energy, as shown in Figure 4.18b. A complete list of

Electron energies [MeV]								
2	3	4	5	6	7	8	9	
10	11	12	13	14	15	16	17	
18	19	20	22	24	26	28	30	
32	34	36	38	40				

Table 4.1: Electron energies, T_e , used to calculate the Cherenkov angular distribution function, D , and the mapping for the energy calibration function \mathcal{F}_E .

all simulated energies used to create the map is shown in Table 4.1. The mapping was interpolated between energies, and down to 0.26 MeV (the Cherenkov threshold in water) from the lowest energy simulated (2 MeV).

4.3.3 Comments

The RSP energy estimator is an improvement on Prompt Lookup because it uses a more precise optical model. The model takes into account detector asymmetries such as the AV neck, or a section of the detector not working because of a card or crate fault. It also incorporates the differing response characteristics of individual PMTs. It adjusts the energy response accordingly on a run-by-run basis. Prompt Lookup is incapable of accounting for these detector effects.

RSP is a work in progress, as some response characteristics can only be incorporated with calibration data that is not yet available. The relative channel efficiencies are currently set to 1, and the wavelength dependent angular response is implemented using the results of an optics fit from MC simulations of the laserball at 420 nm.

If it was considered desirable the multi-photoelectron correction can be improved to account for the Cherenkov distribution being more peaked at certain angles for individual events, rather than the averaged approximation used. A refracted path could be implemented if the computational cost could be improved, or reasonable approximations made. This would enable the Fresnel transmission probability to be accounted for, although this would represent a very marginal improvement in resolution. Implementing any of the aforementioned changes requires the recalculation of the energy calibration function.

The SNO+ RSP algorithm has been implemented for the water phase only, however it could be extended for scintillator. The straight line photon path approximation would no longer be appropriate because transmission from scintillator to acrylic to H₂O has a more significant refraction effect. Fresnel transmission would therefore be included. A strict cut must be placed on prompt light so that the effect of absorption and re-emission would be minimal. Only wavelengths for which the scintillator is transparent would therefore arrive within the prompt window. The 1/ λ^2 wavelength distribution would not be appropriate, and instead the scintillator emission spectrum should be

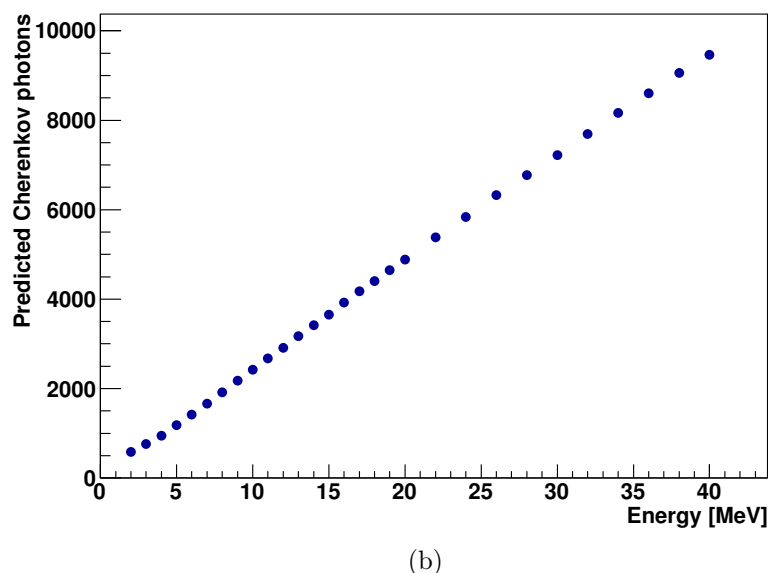
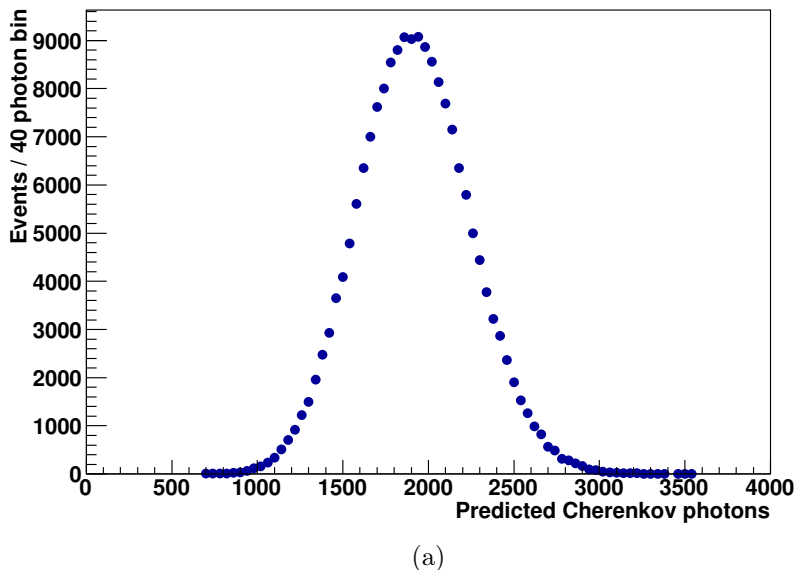


Figure 4.18: (a) The number of Cherenkov photons emitted during 8 MeV electron events predicted by RSP. (b) The map of mean Cherenkov photons to energy, T_e , used for the calibration function.

used. The angular emission distribution would also be flat for isotropic light.

4.4 Estimator performance

4.4.1 Light water

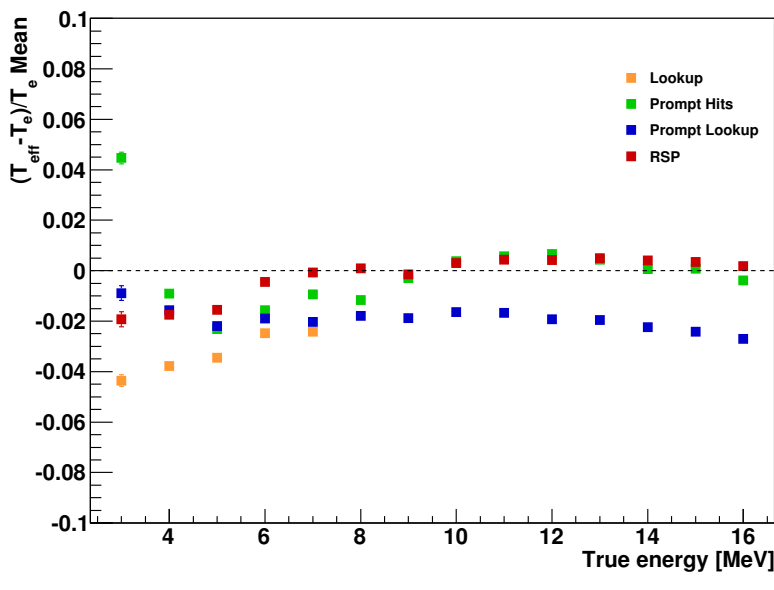
The estimation errors for different energy estimators available for a light water filled detector, with events evenly distributed throughout the AV up to 5.5 m, are shown in Figure 4.19a. The estimators demonstrated are Lookup (the previous default used by SNO+ for the water phase), Prompt Lookup, RSP, and a simple single-value scaling of prompt hits to energy (referred to here as ‘‘Prompt Hits’’). This demonstrates the change in estimation error as a result of the additional information utilised by the other estimators. Electrons were simulated at various energies and the mean of the estimation error, calculated as,

$$\frac{T_{\text{eff}} - T_e}{T_e}, \quad (4.38)$$

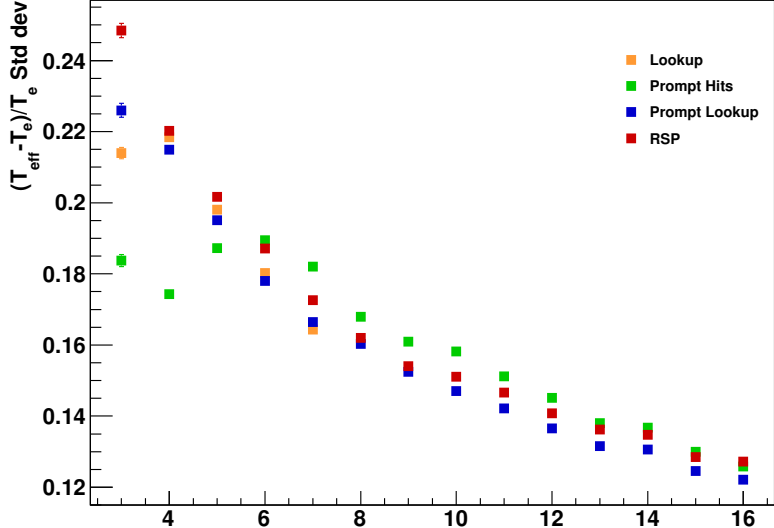
where $T_{\text{eff},e}$ is the reconstructed and true electron energy respectively, is compared to the true energy. It can be seen that the mean RSP energy most closely matches the true energy from 5 MeV upwards. The reconstructed energy has an offset below 5 MeV, possibly due to variances in the performance of the position and direction reconstruction algorithms at lower energies or event selection bias (lower probability of triggering the detector for low energy events). Prompt Lookup has a consistent negative offset, due to position and direction reconstruction effects. The Prompt Hits estimator has a large positive offset at 3 MeV due to a selection bias of higher hit events triggering the detector. At higher energies mean T_{eff} closely matches T_e . Lookup performs so poorly because it has not been recalibrated as the Monte Carlo has developed; it diverges from 8 MeV because the estimator is not calibrated for sufficiently high energies and so these points are not shown.

The resolution is the standard deviation of the estimation error and is shown in Figure 4.19b for events evenly distributed throughout the detector up to 5.5 m. Prompt Hits has the poorest resolution owing to not incorporating position and direction information, except at low energies because it is only able to reconstruct at discrete energies. Prompt Lookup and RSP have similar resolutions as they both include similar information, although Prompt Lookup is marginally smaller.

Figures 4.20a and 4.21a are similar plots to Figure 4.19a but for events at radii 2 m and 5 m respectively. It can be seen that Prompt Lookup is less effective at large radii, variations in the scaling factor are greater at higher radii so the position and direction reconstruction accuracy is more significant. Direction is also less important for events closer to the centre of the detector. RSP is shown to be less effective at small radii. As discussed, the predicted Cherenkov photons to energy map is calculated using events filling the AV which are mostly at higher radii. Likewise Prompt Hits was calibrated



(a)



(b)

Figure 4.19: A summary of the mean estimation errors (a) and resolutions (b) of different energy estimators for electron events, evenly distributed throughout a light water filled AV up to 5.5 m, at different energies.

with events distributed up to 5.5 m, with most events at higher radii, so it performs better at 5 m than 2 m.

The corresponding resolutions for the different estimators are demonstrated in Figures 4.20b and 4.21b for events at radii 2 m and 5 m respectively. At 5 m the resolution profiles are very similar to events filling the AV up to 5.5 m. At 2 m Prompt Lookup has the best resolution.

Figure 4.22a shows the trends for the mean reconstructed energy error at different radii. The estimation error is binned by radius-cubed, r^3 , so that the bins represent equal volumes. RSP and Prompt Lookup both have a bias as the radius increases. This may be due to position and direction reconstruction effects. The RSP bias may also be due to the single wavelength distribution used for the PMT angular response. Prompt Hits has a strong radial bias as the distance photons travel is not accounted for. The vertical dashed line represents a cut-off of 5.5 m. This was the choice of fiducial volume for SNO, although that has yet to be decided for SNO+. The choice is mostly due to the reduction of backgrounds, but it can be seen that the reconstruction algorithms perform beyond this choice. All energy estimators have a negative shift in estimation error for the bin closest to the AV because of the increased effect of reflections.

The corresponding resolutions for the different estimators at different r^3 regions are demonstrated in Figure 4.22b. Prompt Hits consistently has the worst resolution, but applying an adjustment for position and direction effects as for Prompt Lookup provides the best resolution. RSP does not have a resolution as good as Prompt Lookup across the r^3 spectrum because of inaccuracies in the detector response model. Lookup has a radial resolution bias because it does not account for event direction, which affects events close to the AV more than events at the centre of the detector.

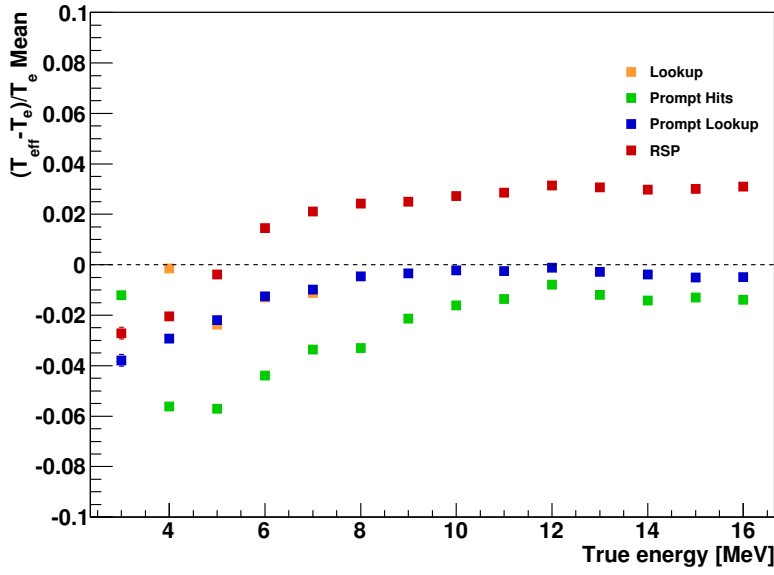
Figure 4.23 shows the distribution of energy estimation errors for the Lookup estimator for electron simulations throughout the AV at energies 4, 7, 10, and 13 MeV. It can be seen that at higher energies the distribution becomes asymmetric because the method has not been calibrated for higher energies.

The performance of the Prompt Hits estimator at the same energies and event position distribution is shown in Figure 4.24. The distributions are spiky because of the discrete energy values that the estimator may return.

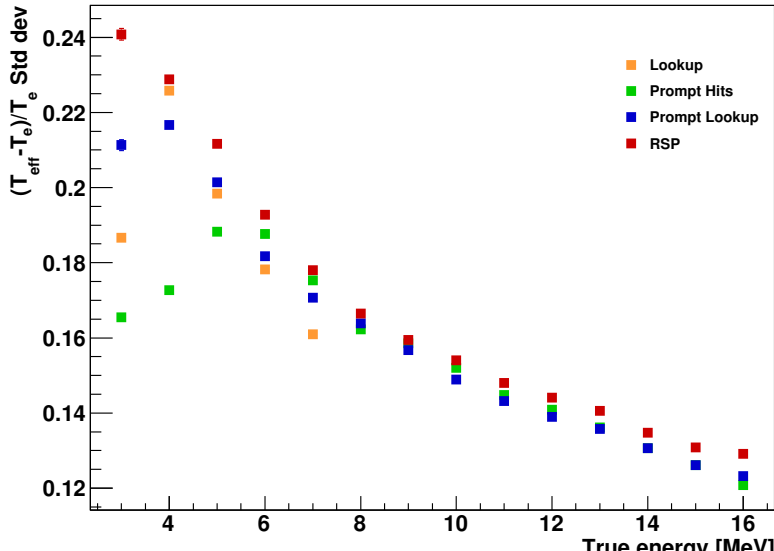
Figures 4.25 and 4.26 are identical plots for Prompt Lookup and RSP. It appears that the distribution of events is more symmetric for RSP.

4.4.2 Scintillator

The mean estimation errors for different energy estimators available for a scintillator filled detector, with events evenly distributed throughout the AV up to 3.5 m, are shown in Figure 4.27a. The estimators demonstrated are Functional (the current default used by SNO+ for the water phase), Prompt Hits, and Prompt Lookup. Electrons were

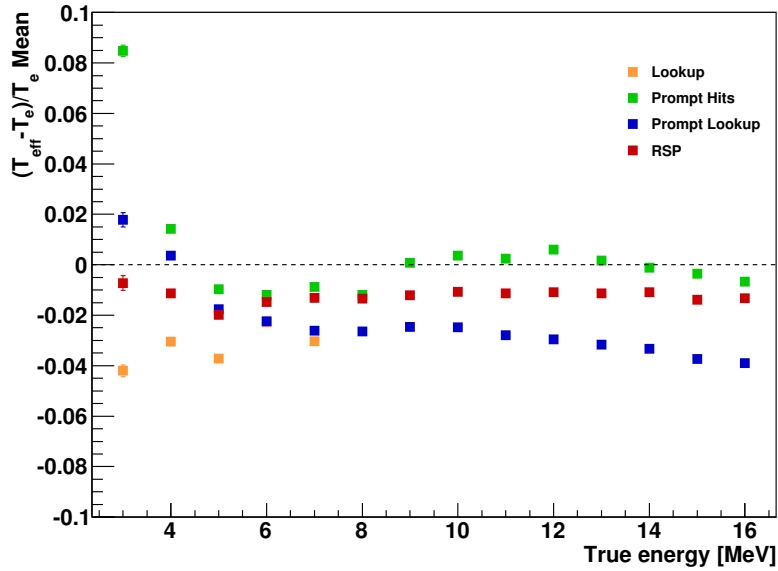


(a)

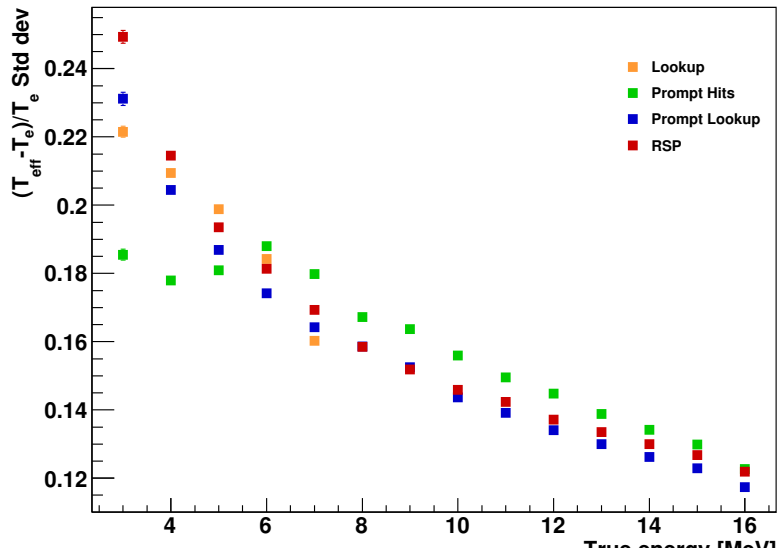


(b)

Figure 4.20: A summary of the mean estimation errors (a) and resolutions (b) of different energy estimators for events at 2 m radius in a light water filled AV across energies.

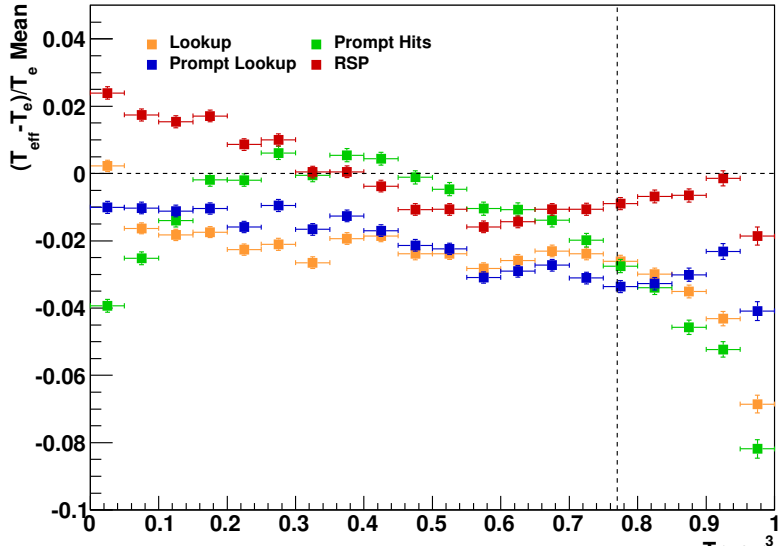


(a)

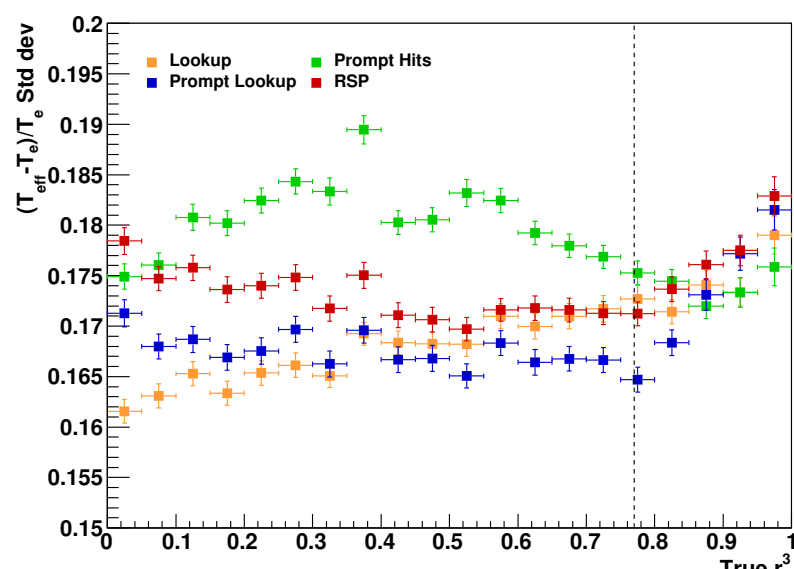


(b)

Figure 4.21: A summary of the mean estimation errors (a) and resolutions (b) of different energy estimators for events at 5 m radius in a light water filled AV across energies.



(a)



(b)

Figure 4.22: A summary of the mean estimation errors (a) and resolutions (b) of different energy estimators for 7 MeV electron events at different radii-cubed, r^3 , with a light water filled AV. The dashed vertical line represents a fiducial volume of 5.5 m and the radius 3 ranges from the centre of the detector (0.0) to the inner surface of the AV (1.0).

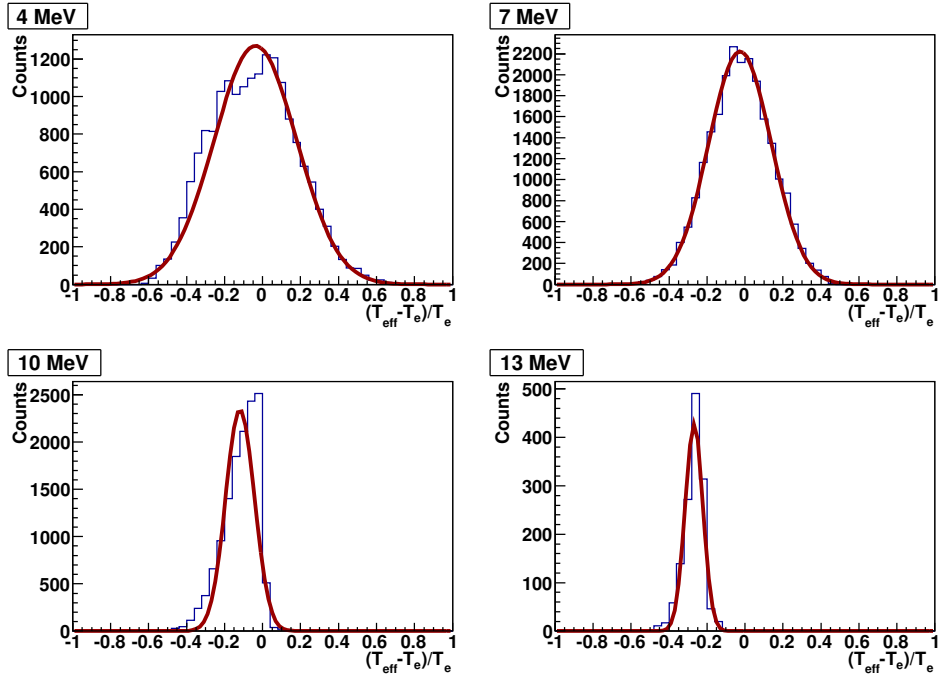


Figure 4.23: A Gaussian fit to the estimation error for the Lookup estimator (the previous default for the SNO+ water phase) at 4, 7, 10, and 13 MeV for electron events filling the AV.

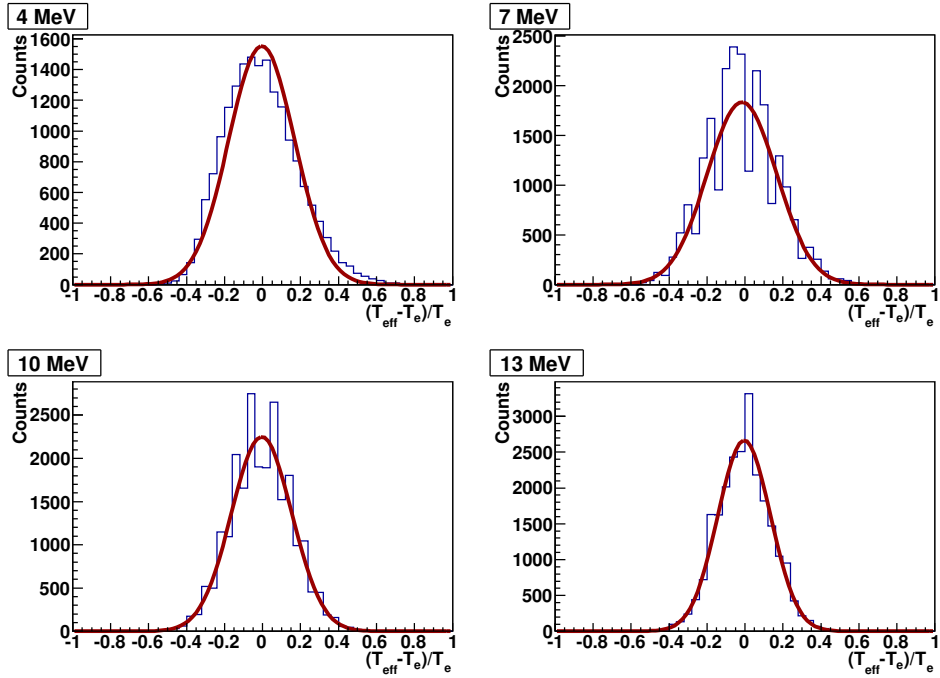


Figure 4.24: A Gaussian fit to the estimation error for Prompt Hits, a simple method that uses a single value scaling of prompt hits to energy, at 4, 7, 10, and 13 MeV for electron events filling the AV.

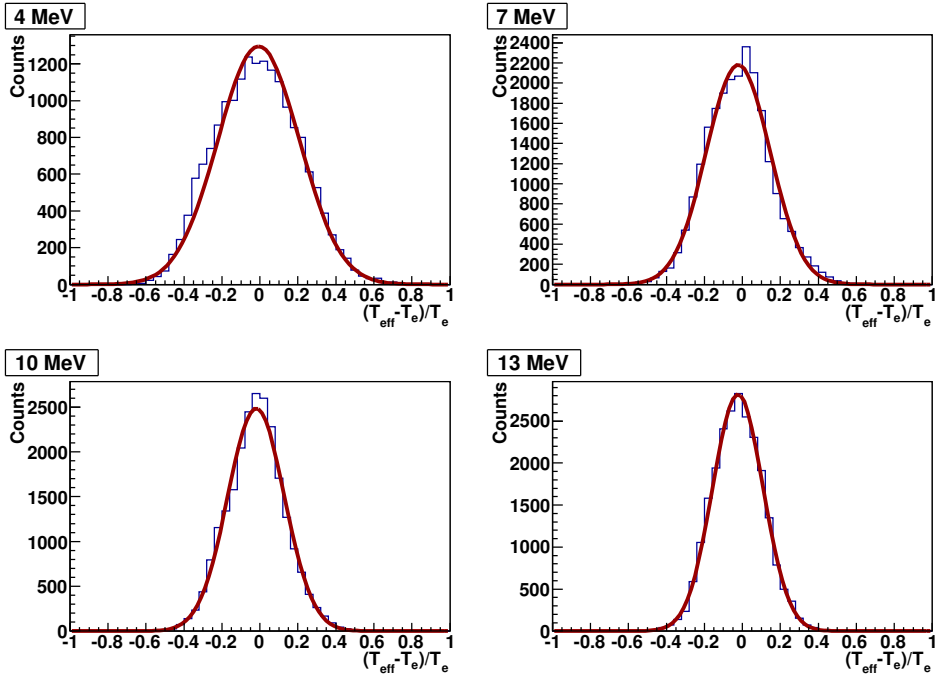


Figure 4.25: A Gaussian fit to the estimation error for the Prompt Lookup estimator at 4, 7, 10, and 13 MeV for electron events filling the AV.

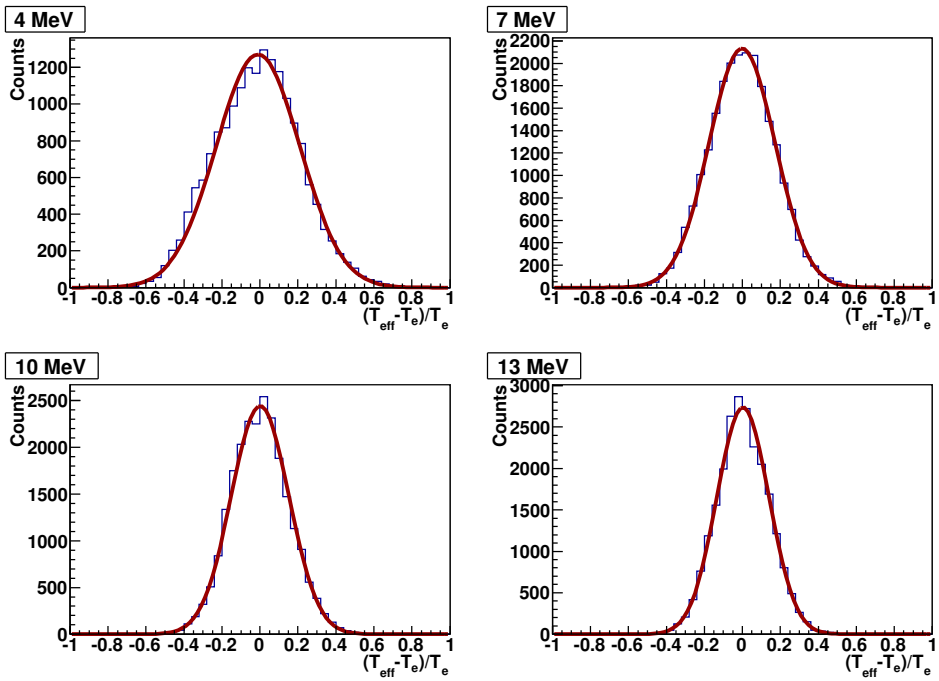


Figure 4.26: A Gaussian fit to the estimation error for the RSP estimator (the new default for the SNO+ water phase) at 4, 7, 10, and 13 MeV for electron events filling the AV.

simulated at various energies and the mean of the estimation error is compared to the true energy. It can be seen that the mean reconstructed value for each approximates the true energy to varying degrees of accuracy. The mean Functional energy error has a consistent offset because it has not been recalibrated after changes to the Monte Carlo, but has a similar shape to Prompt Lookup. Prompt Lookup is the best performing estimator. Prompt Hits, which was calibrated on 2.5 MeV electrons has a positive offset below 2.5 MeV, and a negative offset above, because of the non-linear detector response to different energies due to the multi-photon effect.

The resolutions for these estimators for the same events are shown in Figure 4.27b. Prompt Hits has the poorest resolution below approximately 2.5 MeV and the best resolution above. Prompt Lookup and Functional, which use similar event information, have similar resolutions across the energy spectrum.

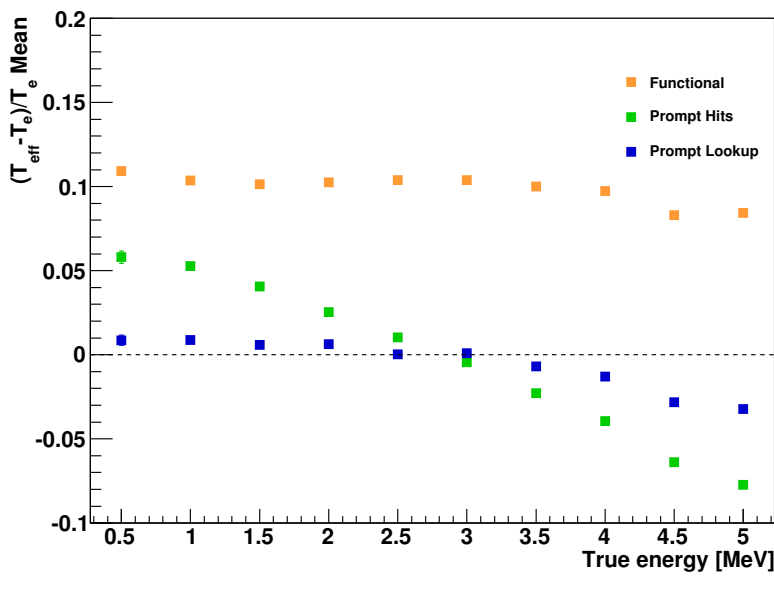
Figure 4.28a shows the trends for the mean reconstructed energy error at different radii-cubed. Again Functional has an offset because it has not been recently calibrated, but appears to have the least radial dependence. Both Prompt Lookup and Functional have positive offsets at higher r^3 values, especially so for Prompt Lookup. The Prompt Hits estimator has a negative offset at higher radii. This is because photons created close to the AV which point inwards will experience more absorption and reemission, so are less likely to trigger PMTs within the prompt window. A fiducial volume of 3.5 m is represented by the vertical dashed line. Within the fiducial volume Functional has the flattest distribution and Prompt Lookup slightly less so. Prompt Hits has the most radially dependent distribution. The fiducial volume radius of 3.5 m is the current proposition for SNO+, chosen to reduce backgrounds, but it can be seen that if it was relaxed the energy estimators continue to perform well at higher radii.

The corresponding resolutions for the different estimators at different r^3 values are demonstrated in Figure 4.28b. Up to 0.7 the resolutions are all similar, with Prompt Lookup marginally the best. Prompt Hits consistently has the highest resolution.

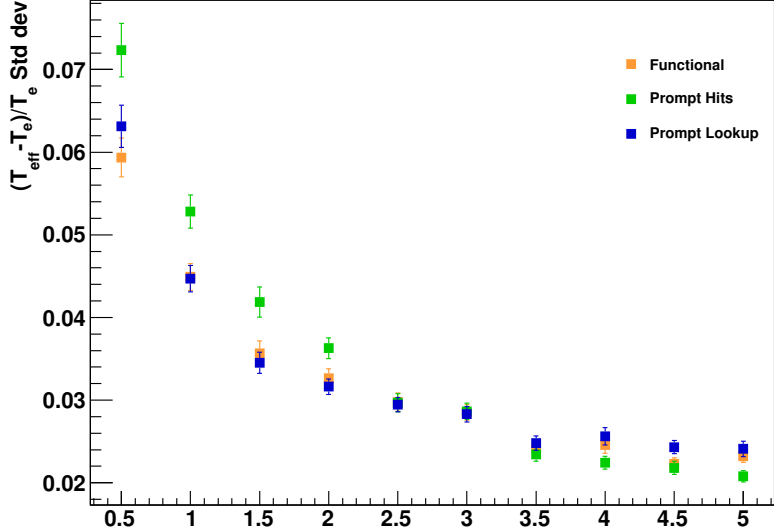
Figure 4.29 shows the distribution of energy estimation error for the Functional estimator for electron simulations evenly distributed up to 3.5 m at energies 1, 2, 3, and 4 MeV. The consistent offset shown in Figure 4.27a can be seen. The performance of the Prompt Hits estimator at the same energies and event position distribution is shown in Figure 4.30. The distribution is spiky at 1 MeV because of the discrete energy values that the estimator may return. At higher energies the discrete energies are less evident. Figure 4.31 is an identical plot for Prompt Lookup. The mean of the estimation error distribution is closest to zero.

4.5 Summary

This chapter has explained the motivation for the development of energy estimators for the water phase, which will be employed for the nucleon decay analysis presented in this

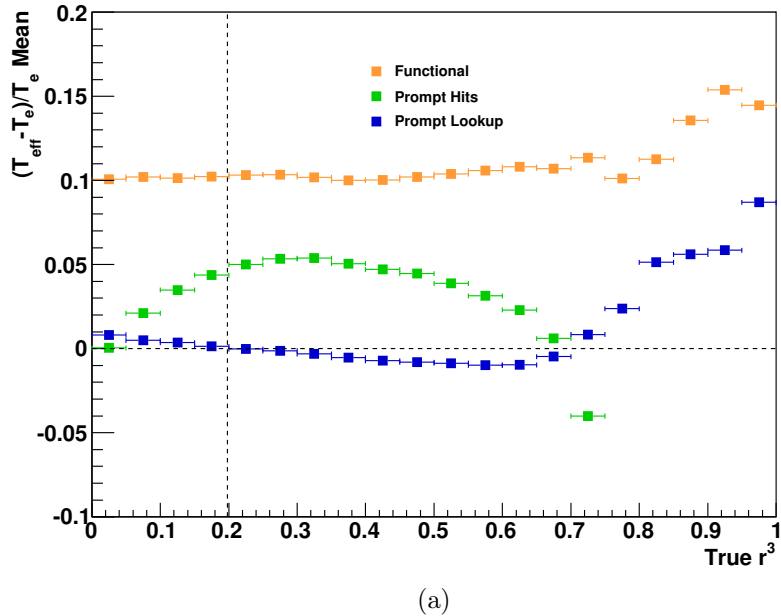


(a)

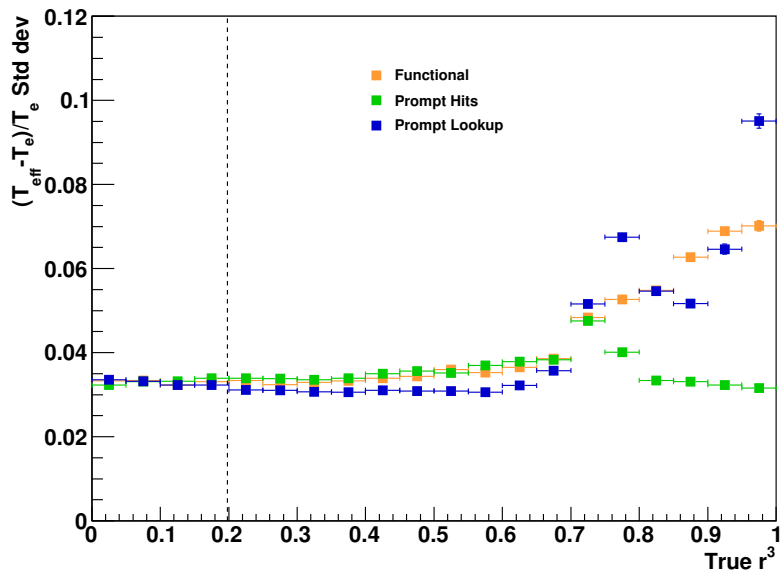


(b)

Figure 4.27: A summary of the mean estimation errors (a) and resolutions (b) of different energy estimators for electron events, evenly distributed throughout a liquid scintillator filled AV up to 3.5 m, at different energies.



(a)



(b)

Figure 4.28: A summary of the mean estimation errors (a) and resolutions (b) of different energy estimators for 2 MeV electron events at different radii-cubed, r^3 , with a liquid scintillator filled AV. The dashed vertical line represents a fiducial volume of 3.5 m, and the radius³ values range from the centre of the detector (0.0) to the inner surface of the AV (1.0).

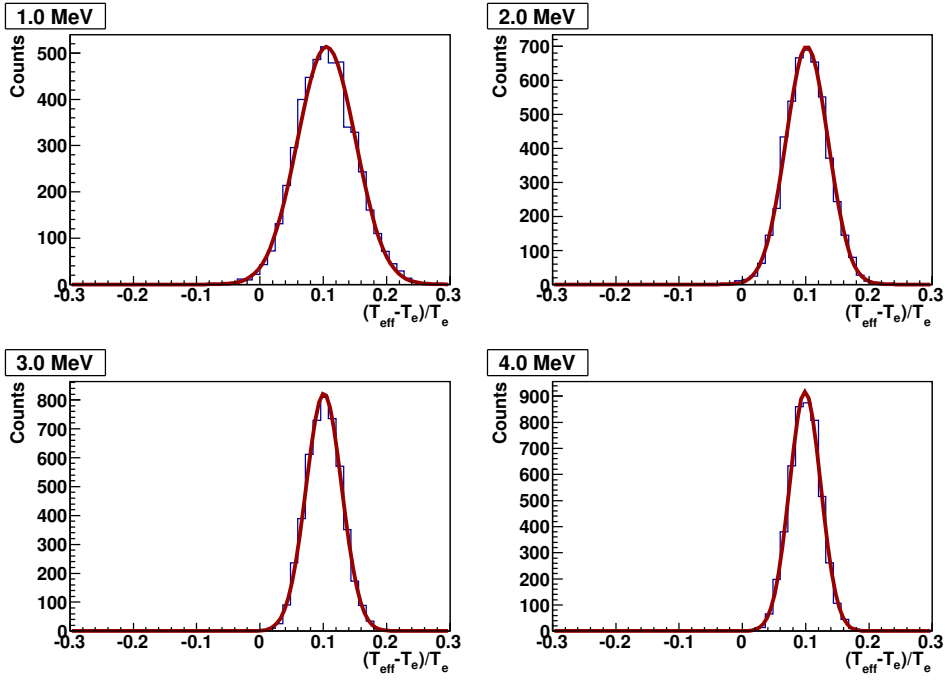


Figure 4.29: A Gaussian fit to the estimation error for the Functional estimator (the default for the SNO+ scintillator phase) at 1, 2, 3, and 4 MeV for electron events within the 3.5 m radius fiducial volume of a scintillator filled AV.

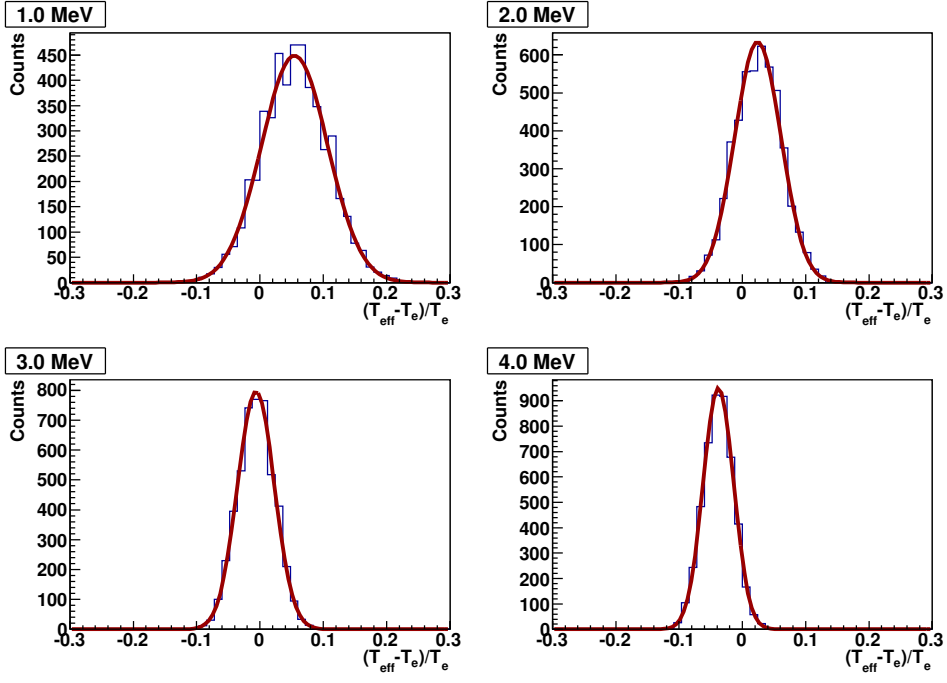


Figure 4.30: A Gaussian fit to the estimation error for Prompt Hits, a simple method that uses a single value scaling of prompt hits to energy, at 1, 2, 3, and 4 MeV for electron events within the 3.5 m radius fiducial volume of a scintillator filled AV.

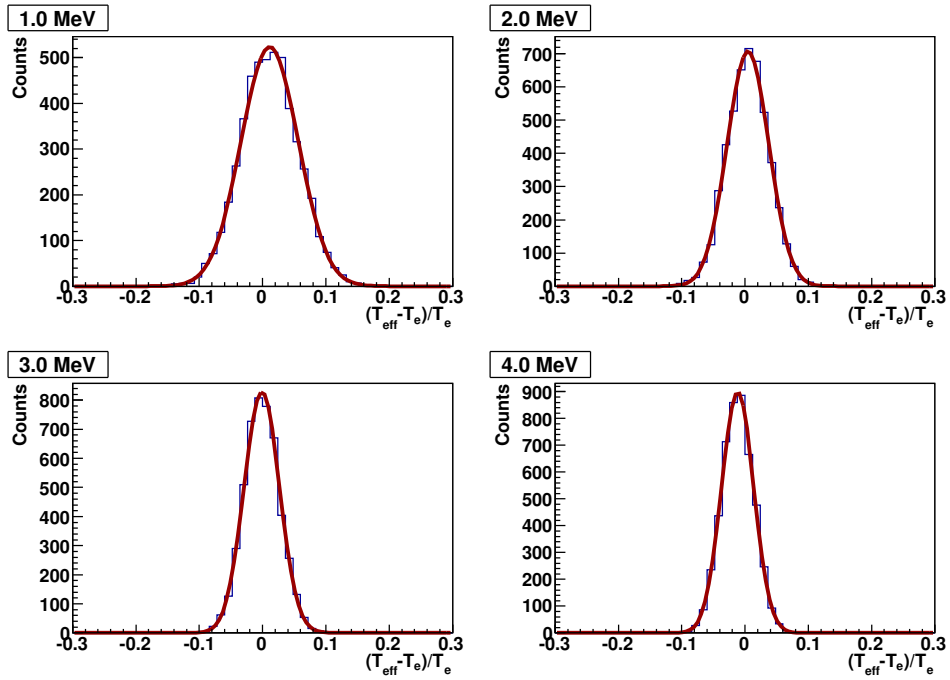


Figure 4.31: A Gaussian fit to the estimation error for the Prompt Lookup estimator at 1, 2, 3, and 4 MeV for electron events within the 3.5 m radius fiducial volume of a scintillator filled AV.

thesis. Existing estimators were created with the scintillator phase in mind so did not take event direction into account, information available due to the Cherenkov nature of light created in water. Two estimators are discussed, Prompt Lookup and RSP, which both use directional information as well as PMT hits within a prompt window. Only prompt hits are considered because the Monte Carlo is more reliable.

While Prompt Lookup scales the reconstructed energy by the number of working PMTs, it does not take into account where in the detector these PMTs are located. This will particularly affect the directional Cherenkov events if a large section of the detector is not working.

There are many other factors not taken into account by this estimator, for example events directed at the neck. This motivated the development of the RSP estimator which calculated the expected number of photoelectrons triggering each PMT, taking into account effects such as the Cherenkov angular distribution, the PMT solid angle, number of working PMTs, transmission/attenuation, and PMT efficiency.

Lookup (the previous default for SNO+), Prompt Lookup, and RSP are compared to the results of a simple single-value scaling of prompt hits to energy method, referred to here as “Prompt Hits”. This demonstrates the improvement in estimation error and resolution as a result of the additional information utilised by the other estimators.

In water, Prompt Hits has a relatively large radial bias in estimation error due to the

absorption of photons crossing the AV. The radial bias is reduced for Prompt Lookup, which accounts for the event position, but not as much as for Prompt Lookup and RSP which account for the event direction. Across all radii within a fiducial volume of 5.5 m Prompt Hits has the worst resolution. Prompt Lookup has a consistently smaller resolution than RSP, so the response model is not as accurate as Monte Carlo simulations.

Estimation errors and resolutions are not shown beyond the AV. Prompt Lookup will continue to work beyond the AV with varying degrees of accuracy, however the model implemented for RSP does not consider event vertices beyond the AV.

For a scintillator filled detector Prompt Lookup and Functional perform very similarly, although Functional has not been recalibrated after Monte Carlo developments.

There are still future developments necessary for RSP as the experiment progresses. Some characteristics of the detector response can only be implemented with calibration data that is not yet available, namely the relative channel efficiencies and the wavelength dependent angular response.

The RSP algorithm has only been implemented for the water phase, but could be adapted for a scintillator filled detector. Various aspects of the response function would need to be altered, such as the wavelength emission spectrum, the angular distribution, and a refracted path would need to be implemented.

Chapter 5

Instrumental Backgrounds

When the SNO detector turned on in 1999 a significantly greater number of events were observed than expected across the N_{hits} spectrum. Figure 5.1 shows that, across the solar neutrino spectrum, the observed N_{hits} was approximately two orders of magnitude greater than MC predictions.

The cause of this discrepancy was the SNO detector’s large instrumental background. These are backgrounds caused by the detector itself, for reasons other than radioactive decays. The main causes of instrumental backgrounds are thought to be electronic breakdown, static discharge, and electronic pick-up. The most common instrumental background observed by SNO was when a PMT operating under high-voltage emitted light into the detector, events known as “flashers”. A description of the probable cause and event signature for flashers follows in Section 5.1.1.

Because SNO+ is a refurbishment of the SNO detector, using the same PMTs and much of the same electronics, SNO+ expects to observe similar issues with instrumental backgrounds. The N_{hits} spectrum of instrumental backgrounds affecting scintillator phase physics will, however, be different to the water phase. In all phases of the experiment, instrumental backgrounds must be almost completely removed. The process for doing so is known as “data cleaning”. Data cleaning relies on the different instrumental background events having different characteristics to physics events, so a selection of event “cuts” can be made to remove them from the data set. Data cleaning must remove background events whilst also accepting as much signal as possible. The fraction of signal that is lost as a result of data cleaning is known as signal “sacrifice”. The fraction of the remaining data set, after data cleaning, that are residual instrumental background events is known as signal “contamination”.

The suite of cuts developed for SNO was very effective at removing instrumental backgrounds. Most of these cuts may be used by SNO+, and naturally are anticipated to be effective during the water phase. However, the most effective cut used for SNO, the AMB cut, will not be available for SNO+. This cut used outputs from the analogue measurement board (AMB), examining the peak and integral of the total PMT charge

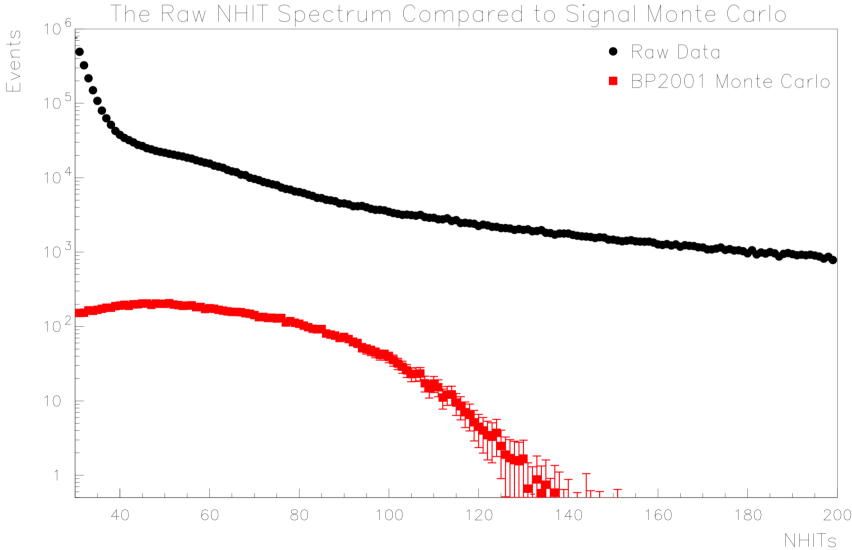


Figure 5.1: Comparison of the raw N_{hits} spectrum for SNO neutrino data set compared to predicted spectrum from Monte Carlo simulations of the BP2001 solar model (assuming no oscillations) [122].

trigger signal, and was particularly effective at removing flasher events for SNO. The AMB board has been upgraded to the CAEN digitiser, which outputs a digital copy of the waveforms of the DAQ trigger signals (see Section 2.3). Cuts based on the CAEN output are yet to be developed as they require data to do so.

It is not known how effective these cuts will be at removing instrumental backgrounds during the scintillator phase. Indeed, some of these cuts will no longer be appropriate, namely those targeting events which do not match the time profile and physical location of PMT hits expected for water Cherenkov events. In scintillator different event profiles are expected. Furthermore, flashers will have a different signature in the scintillator phase, so cuts developed for the water phase may be less effective. New flasher cuts may need to be developed; to do so it would be useful to know what flashers will look like in scintillator. This has motivated the development of a flasher generator in the MC simulations.

This chapter outlines the causes of instrumental backgrounds, and how they were removed by the cuts developed for SNO. As no data is yet available, the sacrifice of the cuts in water and scintillator is estimated using Monte Carlo simulations. It is then described how the flasher generator was developed, and used to estimate signal contamination due to flashers in the water and scintillator phases.

5.1 Causes of Instrumental Backgrounds

The main causes of instrumental backgrounds are from electronic pick-up, cross-talk, or photons being emitted into the detector, either by internal or external sources. An overview is provided here, but for detailed descriptions of each source see [122, 139].

5.1.1 Flashers

The dominant class of instrumental backgrounds are events called “flashers”, when a PMT operating under high voltage breaks down and emits light into the detector, which occur continuously in working PMTs. Approximately 50 flashers are expected per hour. This rate could be reduced by lowering the PMT voltage, but at a cost to the gain of the PMTs.

Flashers are thought to be caused by static discharge in the dynode stack, although it is unknown for certain. Flashers span a broad N_{hits} spectrum, ranging from tens of hits to hundreds. They therefore cross the energy spectrum for both water and scintillator phase physics.

The signature of a typical flasher is usually characterised by a high charge flashing PMT. The charge value for the tube is usually *railed*, meaning that the number of bits used to record the charge has reached a maximum (4095 counts). However, sometimes for especially high charges the counter resets to the beginning and records a very low charge, known as a *negative rail*.

The high charge of the flashing PMT causes the surrounding electronics channels to trigger due to crosstalk. Typically channels on the same paddle board will trigger, although the triggered channels can also cross paddle cards if the pick-up occurs in the PMT cables.

Photons from the flashing tube then cross the detector and trigger PMTs on the opposite side. These hits occur later in the event window than the flashing PMT. The concentration of hits on the far side of detector is caused by the collimation of photons by the PMT and concentrator that they are emitted out of. They typically have an elliptical shape, thought to be caused by shadowing internal to the PMT, perhaps the dynode stack.

A visualisation of a typical flasher with the SNO+ event viewer is shown in Figure 5.2. The top left window is a geodesic map of the PSUP. The coloured points are the PMT hits; points on the front face of the sphere (from the viewer’s perspective) are filled in, and are hollow on the rear face. The distribution of PMT hit times is shown by the multicoloured histogram. The times here are uncalibrated TACs, as described in Section 2.3, so high TACs correspond to early times. The colour of each PMT elsewhere in the viewer matches its entry in the histogram. The top right window represents a two dimensional projection of the PSUP. It is clear to see the grouping of PMTs on one

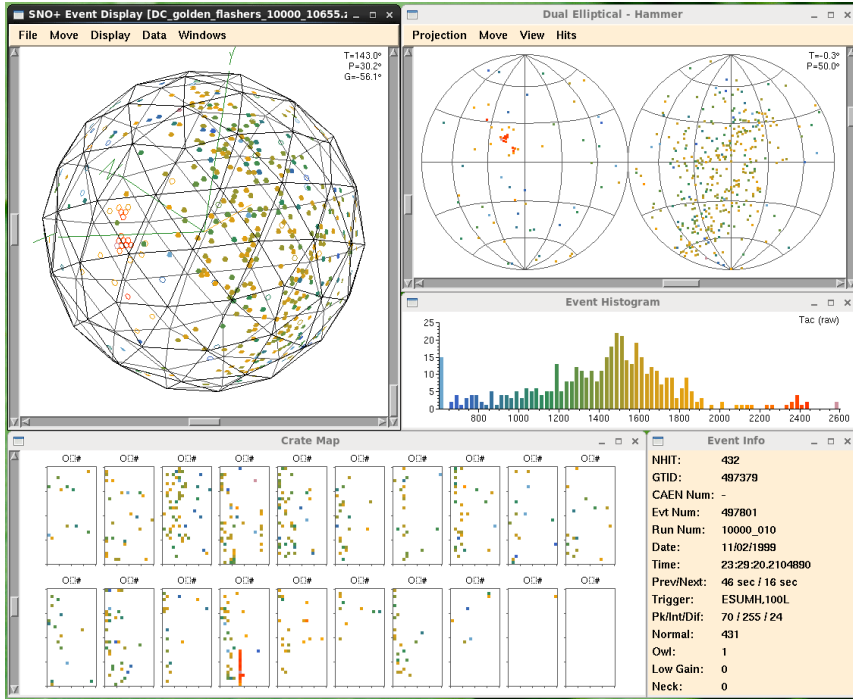


Figure 5.2: A visualisation of a typical flasher from SNO with the SNO+ event viewer. The histogram is of uncalibrated hit times defines the colours in the other windows.

side of the detector, later in time relative to the cluster around a flashing tube. The bottom left window shows the hits in electronics space. Each box represents one of the 19 electronics crates, and each crate’s 16 slots are represented as columns. Here the cluster of hits on a single slot, due to crosstalk, can be seen. The bottom right window summarises the event information, including the number of PMT hits.

5.1.2 Other causes

Other causes of instrumental background include electronic “pick-up”, when external influences on the electronics cause channels to trigger. This can be caused by human activity near to the electronics, but may also be caused by temperature or humidity levels. During pick-up events most tubes on several different crates will fire. The PMT waveforms caused by pick-up tend to be bipolar, so the integrated charge QHL will fluctuate around zero.

Events caused by breakdown in the high-voltage connectors, where the PMTs meet their respective cables, are known as “wet-end breakdown” (WEB). Although initially a major concern for SNO, the rate was dramatically reduced by regassing the light water surrounding the PMTs with nitrogen. Consequently WEB events are not anticipated to be a large problem for SNO+.

Background events that have much the same event signature as flashers, but without photons triggering PMTs on the opposite side to the flashing tube, are called “shark

fins”. The cause is unknown, but they may be flashers with the light prevented from escaping. The events are called shark fins because of the shape of the ESUM trigger signal. The shark fin rate is high, approximately 2.3 Hz, so pile-up with signal events may cause sacrifice. Contamination, however, will be less of a problem in scintillator because shark fins by nature are low N_{hits} events.

“Rings of fire” and “slots of fire” were events in which the channels at the edge of the crate triggered, or most channels on one or two slots in a crate triggered, respectively. A modification to the backplane was installed for SNO which significantly reduced their rates.

A very large event, such as a muon or a flasher, can create a large amount of late light which can spill over into the following event window, causing a “retrigger”. Other causes of retriggers include pick-up from triggering channels, or PMT after-pulsing, when a PMT triggers again possibly due to the liberation of a positive ion in the PMT.

A class of events caused by photon production in the AV neck are known as “neck events”. The cause of these events is unknown, but may be due to static discharge. The neck is a complex region where acrylic interfaces with the inner AV material, water and the cover gas. Acrylic is a good insulator, which may allow static charge to build up. Photons created during these events are collimated by the neck, causing PMTs at the bottom of the PSUP to trigger. There are PMTs located in the neck specifically intended to identify these events.

Events with a flat time distribution are known to be instrumental backgrounds because they have a broader spectrum than Cherenkov events. They are called “flat TAC” events. Flat TACs are emitted repeatedly by PMTs when they die.

“Leslie” events, named after first person to study these events, occur at a lower rate than other instrumental backgrounds. It is not known how the light causing these events is produced, but the events reconstruct at the AV and are isotropic. Leslie events have a large N_{hits} range which suggests they are not caused by radioactive decays.

Finally, “orphans”, although not technically an instrumental background can result in events that are not from a physics process, or pervert other events. Orphans are PMT bundles that the DAQ system does not correctly combine with the rest of the PMTs in an event. They are usually collected into their own event, or on some rare occasions built into the wrong event, potentially resulting in a PMT recording more than one hit.

5.2 Pre-reconstruction cuts

Instrumental background cuts made without event reconstruction information, otherwise known as data cleaning cuts, are the first level of data analysis to remove instrumental backgrounds. The data cleaning cuts tag events as passing or failing each cut so they can be excluded from the data set.

The event properties used to identify backgrounds include:

- **PMT hit times**

Cherenkov light is prompt so has a narrow time distribution. Events with broader time distributions may therefore be identified as background. Naturally this only applies to the water phase, although the inverse property may be investigated for scintillator. The hit times for specific PMTs may also be used, such as removing flashers whose flashing tube occurs early in the time window.

- **Inter-event timing**

Some instrumental backgrounds are known to occur in bursts, which is not the case for physics events such as solar neutrinos, double beta-decay, or nucleon decay. Consequently a cut may be used to remove a burst of consecutive events. However, care must be taken not to remove supernovae or events with coincidence decays such as anti-neutrinos.

- **PMT charges**

Flashing PMTs will record very high charges, whereas noise triggered tubes such as pick-up or cross-talk will result in zero integrated charges.

- **Event geometry**

The geometry of PMT hits in both physical and electronics space may be used to identify backgrounds. Flashers, for example, will have a geometry distinct from Cherenkov events. Particular patterns of hits in electronics space are also identifiable as instrumental background.

- **Veto tubes**

Events due to light created outside the PSUP will cause outward looking (OWL) PMTs to trigger. There are also PMTs in the AV neck, intended to trigger during a neck event. Hits on these PMTs may be used to veto events.

An overview of the SNO data cleaning cuts relevant for SNO+ is provided here, but for a more detailed description of each cut see [122].

5.2.1 Crate Isotropy

The crate isotropy cut was developed to remove events caused by noise hits on adjacent channels, such as pick-up events, rings of fire, and slots of fire. It does this by looking for an uneven distribution of hits in electronics space.

First the cut checks whether most hits come from a single crate, and if so are most hits on that crate on two adjacent slots. If the fraction of hits on a single crate is above 0.7, and the fraction of those hits on two adjacent cards is above 0.8, then the event fails the cut.

This cut will not perform well if the noise hits occur in coincidence with radioactive decays as this will dilute the fraction of noise hits. Crate isotropy will be effective in both water and scintillator phases as it identifies hit distributions in electronics space.

5.2.2 Flasher Geometry Cut

The flasher geometry cut was designed to identify flasher events. As described previously, the signature of a typical flasher is characterised by a high charge tube that induces cross-talk hits on nearby channels. Light then travels across the detector and hits are registered on the other side.

Sometimes, however, the flashing tube is missing from the event. This could be because the hit has been orphaned, cut off from the beginning of the event, or the PMT could be under high voltage but the channel not recording data. For this reason the flasher geometry cut looks for a difference in time and space between hits in the cross-talk cluster and the rest of the event.

First the algorithm must identify a cluster of four or more hits near each other, either physically on the PSUP or in electronics space. In physical space the four hits must be within 1 m of each other. The average difference, in distance and time, for each identified cluster to the rest of the hit PMTs is then calculated. This will be very large for flashers, but small for Cherenkov hits as clusters should be localised to the high hit density region. A cut is made if the cluster of hits is sufficiently far away, and before, the other hits.

5.2.3 Neck Cut

The neck cut was created to identify events occurring in the neck. These events typically recorded many hits by the veto PMTs in the neck, or one of these tubes would have a high charge. These hits would also have an earlier time than the average for hits in the bottom hemisphere of the detector. A cut was made on the time difference.

5.2.4 Junk Cut

The junk cut was developed to remove orphan events in which a PMT bundle has been built into the wrong event. Any event which has a channel with more than one hit is tagged, as this is not theoretically possible for the SNO electronics and indicates a DAQ failure.

5.2.5 Q Cluster

Q Cluster tags flashers, shark fins, and wet-end breakdowns. All of these events have a very high, often railed, PMT charge. This hit is then surrounded in electronics space by cross-talk hits.

The algorithm identifies anomalously high charge tubes and then searches for hits in the adjacent channels. As the pick-up can occur in the PMT cables, the algorithm looks for hits regardless of which slot or paddle card it corresponds to. Four or more hits in a window of five adjacent channels is required to tag the event.

5.2.6 Q v T

The Q v T cut tags flashers which have a high charge in the flashing tube. It does this by looking for PMT charges which are sufficiently above the mean charge for the event. Events with naturally high charges, for instance muons, shouldn't fail this cut as they will have a naturally high mean charge.

The highest charge tube meeting this requirement is identified, and is further required to occur sufficiently early in the event. The tube time is compared to the median hit time, allowing for movement of hit times within the event time window. Events with the highest charge PMT meeting these conditions are tagged as instrumental background.

5.2.7 Q v Nhit

The Q v Nhit cut removes noise events including pick-up, rings of fire, and slots of fire. During physics events, PMTs should trigger because photoelectrons have been liberated in the PMT photocathode, and therefore have an associated charge.

The waveforms for noise triggered channels tends to be bipolar, so integrated over a long enough time the charge should fluctuate around zero. The mean QHL charge should therefore be distinguishable for physics events and noise.

The Q v Nhit algorithm ignores any PMT charges that are at least 100 counts below the pedestal value (charge value recorded by the channel without any PMT signal), and are therefore unphysical. The highest 10% of charges are also ignored so as not to remove background events in coincidence with low energy Cherenkov events, or data taking runs for which there are calibration issues. An upper limit is chosen for the mean QHL charge value of the remaining tubes, R_Q , such that the sacrifice is low.

5.2.8 ITC Time Spread

The In Time Channel (ITC) Time Spread cut removes flat TACs, events caused by continuously emitted photons.

PMT hits caused by Cherenkov photons should occur in a relatively small fraction of the event window. Scintillation light will have a broader time spectrum, but most PMT hits should still occur within a smaller fraction of the event window than flat TAC hits (see Figure 4.8). The ITC cut may therefore be effective in both water and scintillator phases.

ITC slides a fixed time window across the hit times, and finds the maximum number of hits within it. The ITC ratio was then calculated as the fraction of hits inside the window compared to the total number of hits. A window of 93 ns was chosen for SNO, the same as the NHIT100 trigger coincidence time, and a cut was made if the ITC ratio was below 0.6.

The ITC Time Spread cut will also remove bimodal hit time distributions, therefore removing coincidence events and pile-up.

5.2.9 Fitterless Timespread

Fitterless Timespread (FTS) also removes events with too broad a time distribution for a Cherenkov event. These events include flat TAC events or flashers. Due to the large background from flashers a concern would be that some events cannot be identified by a flashing tube or cross-talk cluster, known as “blind flashers”. As the FTS cut is based on the time distribution, it is also effective at tagging blind flashers.

The FTS algorithm calculates the time difference between all pairs of PMT hits, provided they are sufficiently close in the detector (less than 3 m) and the time difference is below 25 ns to try to consider in-time light rather than reflections or noise. Provided there are at least 15 PMT pairs meeting these criteria a cut is made for events with a median time difference greater than 6.8 ns.

As this cut was developed to remove events that are distinctly not Cherenkov, it is not anticipated that the cut will perform well for the scintillator phase. This cut will only be applied for water phase physics analyses.

5.2.10 CAEN cuts

The analogue measurement board (AMB) cut was the most powerful data cleaning cut for SNO. It was particularly effective at removing flashers, as well as some ability to remove pickup events. The cut was based on the output of the AMB board, which made measurements of the ESUMHi trigger signal (a linear sum of all PMT pulses, shaped to Gaussian profile with a 120 ns width).

The AMB cut used the ratios of the signal peak and integral compared to total N_{hits} to identify background events. The ratios were plotted for ^{16}N calibration events, a cut could then be made on events which were further than 3.7σ from the mean of these distributions. Flashers tended to rail the AMB measurement and so could easily be distinguished.

As part of the refurbishment process for SNO+, the AMB has been upgraded to a CAEN digitiser which outputs a digital copy of the waveforms of the DAQ trigger signals, e.g. ESUM, NHIT100 etc (see Section 2.3). This will provide more measurement possibilities than AMB and should therefore be at least as effective. Cuts based on the CAEN output are currently under development, but require event data.

5.3 Post-reconstruction cuts

Post-reconstruction cuts, also known as “higher level” cuts use the reconstructed event vertex to calculate cut parameters which will discriminate between signal and background. The threshold for these cut parameters are chosen for optimal signal acceptance, whilst also effectively removing backgrounds. Two higher level cuts that were employed by SNO, and are used for the water phase physics analysis presented in this thesis, are described here.

5.3.1 Isotropy

An event isotropy parameter, based on the angles of hit PMTs to the event vertex, can be used to identify Cherenkov events [140]. The angles that may be used to construct such an isotropy parameters are shown in Figure 5.3 [141]. The subtended angle, θ_{ij} , is the angle between PMT hits i and j from reconstructed vertex, and angle θ_i is the angle between PMT hit i and the reconstructed event direction from the reconstructed vertex. The separation parameters were then defined,

$$\beta_l = \frac{2}{N(N-1)} \left[\sum_{i=1}^{N-1} \sum_{j=i+1}^N P_l(\cos \theta_{ij}) \right], \quad (5.1)$$

where P_l is a Legendre polynomial and only prompt hits have been considered. The combination of these parameters providing the best separation between electrons and neutrons in the SNO salt D₂O phase was found to be from $\beta_{14} = \beta_1 + 4\beta_4$ [141]. Different parameters may provide better separation for instrumental backgrounds.

Figure 5.4 compares the β_{14} parameter for the various expected neutrino signals for SNO. It can be seen that cutting events with $\beta_{14} > 0.9$ will sacrifice a negligible amount of signal. If necessary, however, to further reduce instrumental backgrounds, a more aggressive cut of $\beta_{14} > 0.8$ may be made which retains over 99% of the signal.

The isotropy cut was developed to remove events that do not share the anisotropic nature of Cherenkov light. This cut will not therefore perform well for the scintillator phase and will only be applied for water phase physics analyses.

5.3.2 ITR

A cut based on the ratio of N_{prompt} to N_{hits} may also be used to distinguish Cherenkov and non-Cherenkov events. For SNO this was known as the in-time ratio (ITR) cut [122].

Figure 5.5 shows the ITR distributions calculated for SNO for flasher and neck type instrumental backgrounds, calibration data, and post-instrumental background cut neutrino data. Cutting events with $\text{ITR} < 0.55$ is very effective at removing flasher and neck instrumental background events, while cutting a very small amount of physics signal.

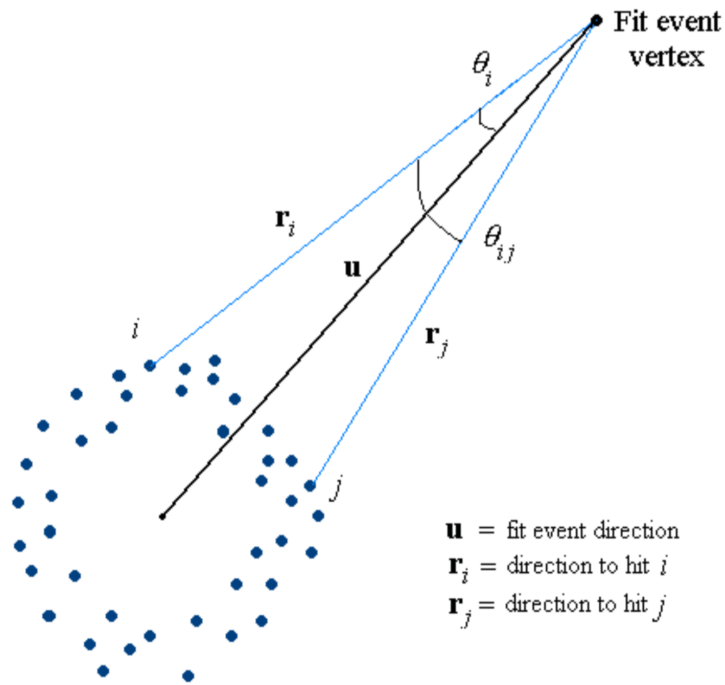


Figure 5.3: Diagram of the angles used to calculate the isotropy parameter, β_{14} [141].

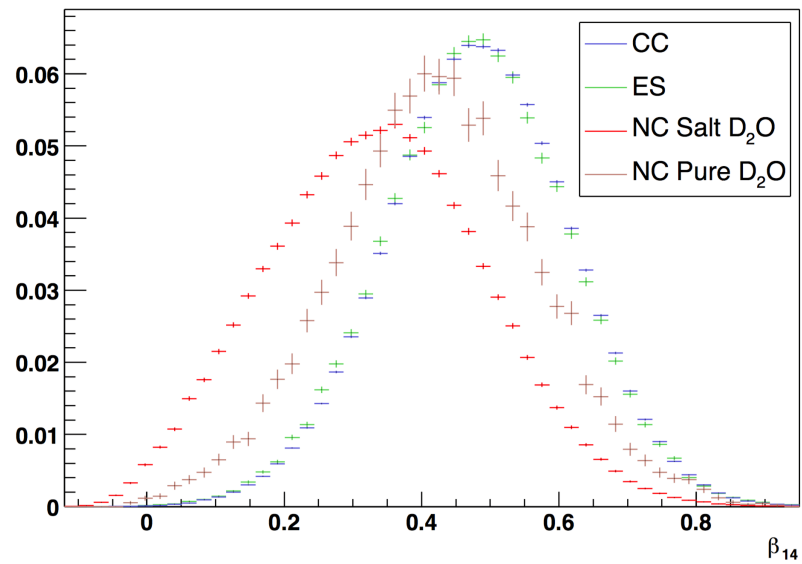


Figure 5.4: Normalised β_{14} distributions for the expected neutrino signals of the SNO experiment [141].

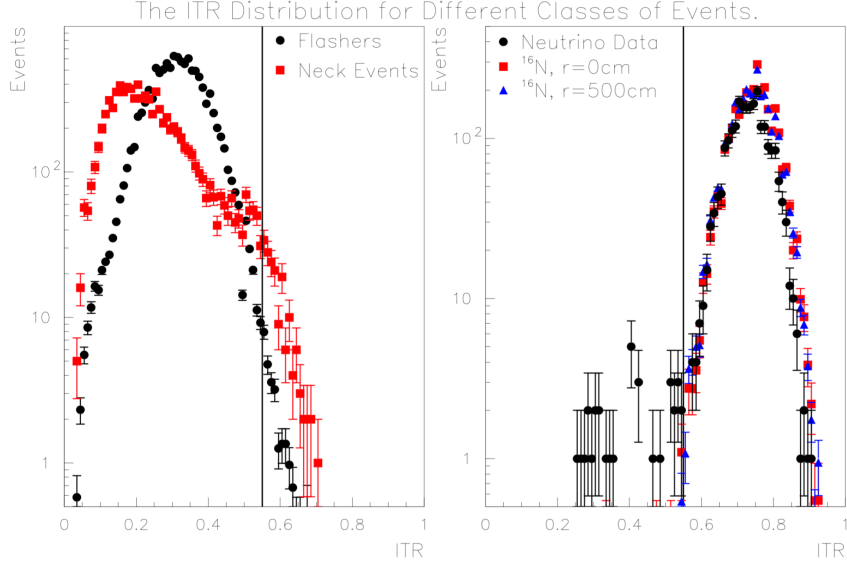


Figure 5.5: The ITR distributions calculated for SNO for flasher and neck type instrumental backgrounds, calibration data, and post-instrumental background cut neutrino data [122].

The ITR cut was developed to remove events with a broader time distribution than that of Cherenkov light. This is the case for scintillator event time profiles, so this cut will be inappropriate for the scintillator phase. An inverse version of this cut may be used, however, to remove events with short time profiles, although it is unclear which events this will remove.

5.4 Sacrifice

Applying instrumental background cuts was shown to be effective at removing instrumental backgrounds for SNO [122]. However they may also have the unintended consequence of removing physics events from the data. The fraction of physics events that fail an instrumental background cut is known as the cut ‘‘sacrifice’’. This section outlines the sacrifice of each instrumental background and higher level cut when applied to simulations of electron events.

No cross-talk or pickup has been simulated, which would be anticipated at some level when taking real data, so the sacrifice presented here is an underestimate. Furthermore, the validity of the analysis presented here is reliant on the accuracy of the PMT charge model. This study must therefore be repeated using calibration data (¹⁶N, laserball etc.) as it becomes available.

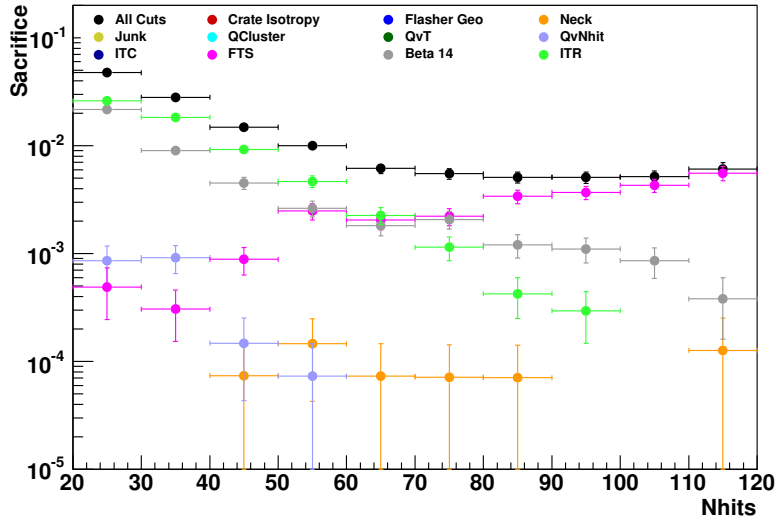


Figure 5.6: Comparison of the sacrifice for the instrumental background cuts in light water across the N_{hits} spectrum.

5.4.1 Light water

To estimate signal sacrifice during the water phase, electron events were simulated at random positions and directions throughout the acrylic vessel. Different energies were simulated, from 1.0 MeV to 16.0 MeV in 1.0 MeV increments, with 10,000 events simulated at each energy.

The data cleaning cuts were applied to the simulated events and the sacrifice was plotted against N_{hits} , energy, radius, direction, and isotropy. It could then be demonstrated whether or not there is a bias to the sacrifice across any of those variables. This is important to understand, particularly any energy bias, to reduce the systematic error on the measured spectrum.

The fractional sacrifice, from $N_{\text{hits}} = 20$ to $N_{\text{hits}} = 120$, is shown in Figure 5.6. Of the data cleaning cuts only FTS, Neck, and Q v Nhit have an effect. Most data cleaning sacrifice is due to FTS, except at low N_{hits} where Q v Nhit dominates. The FTS sacrifice increases as N_{hits} increases. Up to $N_{\text{hits}} = 120$ each data cleaning cut has below 1% sacrifice, which is the target level. At low N_{hits} the higher level cuts have greater than 1% sacrifice and dominate the sacrifice spectrum. Their sacrifice decreases as N_{hits} increases, because scattering decreases for higher energy events. The total sacrifice for all cuts is below 1% above 60 N_{hits} .

The fractional sacrifice across the energy spectrum, 2-16 MeV, is shown in Figure 5.7. Above 8 MeV the sacrifice is flat, although as the energy decreases below 8 MeV the sacrifice increases beyond 1%. Following from the sacrifice as a function of N_{hits} , shown in Figure 5.6, the sacrifice from the higher level cuts is above 1% below 5 MeV,

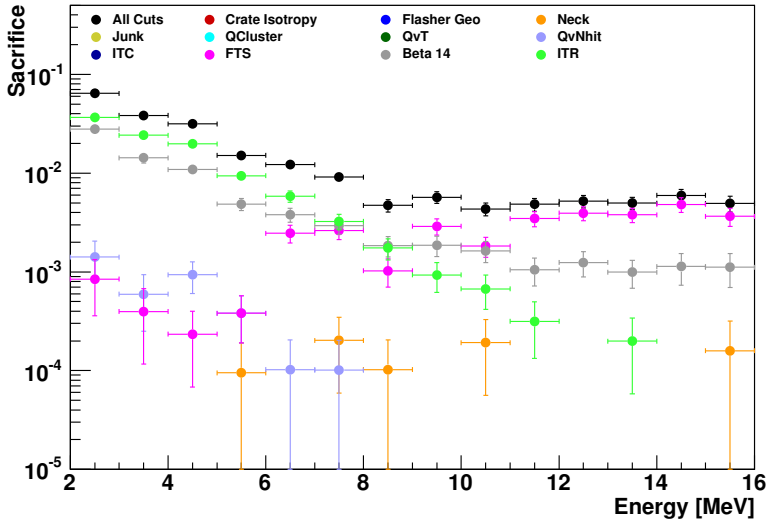


Figure 5.7: Comparison of the sacrifice for the instrumental background cuts in light water across the energy spectrum.

whereas the pre-reconstruction data cleaning cuts have below 1% sacrifice across the spectrum.

The fractional sacrifice across the fiducial volume radius is shown in Figure 5.8. The total sacrifice, including both higher level and data cleaning cuts, is flat across the radial spectrum, demonstrating that there is no radial bias. It can be seen that, averaged across all energies, the sacrifice is approximately 1% or less. The data cleaning cut sacrifices are significantly below 1%.

The fractional sacrifice across $\hat{u} \cdot \vec{r}$ direction values is shown in Figure 5.9. Higher $\hat{u} \cdot \vec{r}$ values point out of the detector, while lower values point inwards. Inward pointing events have a higher sacrifice from the ITR cut. This is because they experience more scattering over the longer path length, and therefore more PMT hits are outside the prompt window. There is no notable bias for the other cuts.

The fractional sacrifice across β_{14} isotropy parameter values is shown in Figure 5.10. Above $\beta_{14} = 0.9$, the most isotropic events, there is 100% sacrifice from the β_{14} isotropy cut as this is the cut threshold. There is also a higher sacrifice due to the ITR cut above $\beta_{14} = 0.9$. For $\beta_{14} < 0.9$ there is no notable bias.

It has been demonstrated that the sacrifice from the data cleaning cuts is not a function of radius, direction or isotropy. However as N_{hits} , and correspondingly energy, increase there is a higher sacrifice from data cleaning cuts.

The higher level cuts are the dominant cause of sacrifice. Overall they are within the 1% level, but for lower N_{hits} , energy, and $\hat{u} \cdot \vec{r}$ values are over this target. This is because of the increased scattering for low energy events and those with longer path

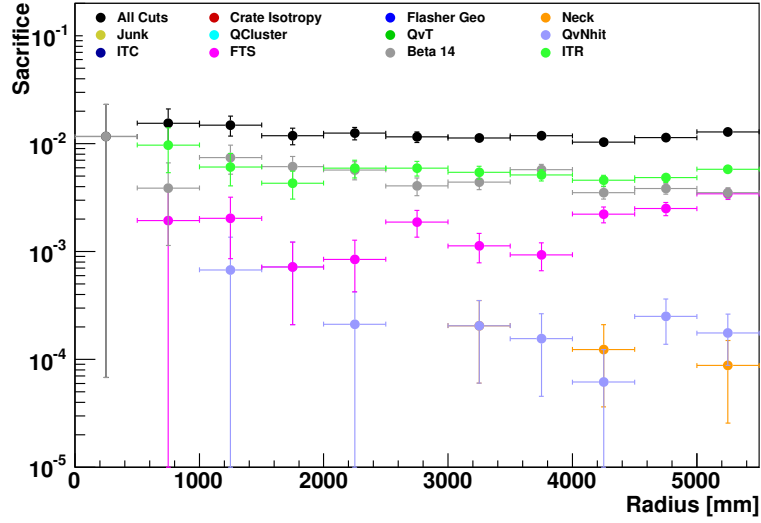


Figure 5.8: Comparison of the sacrifice for the instrumental background cuts in light water at different radii.

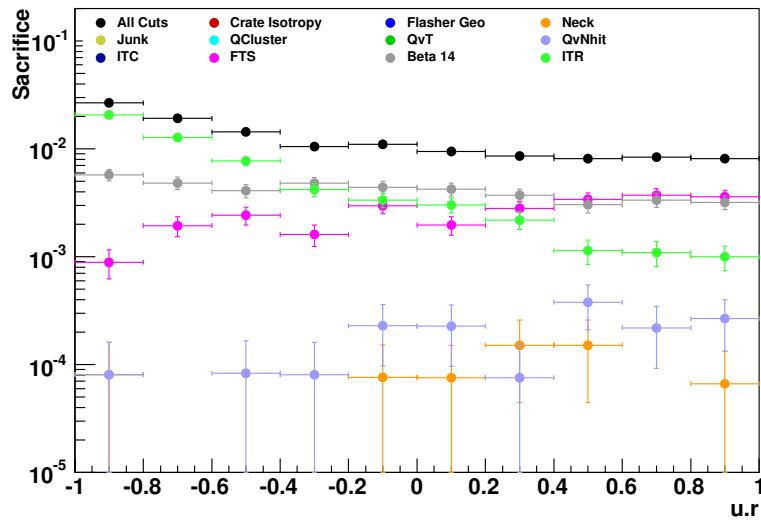


Figure 5.9: Comparison of the sacrifice for the instrumental background cuts in light water at different $\hat{u} \cdot \vec{r}$ values.

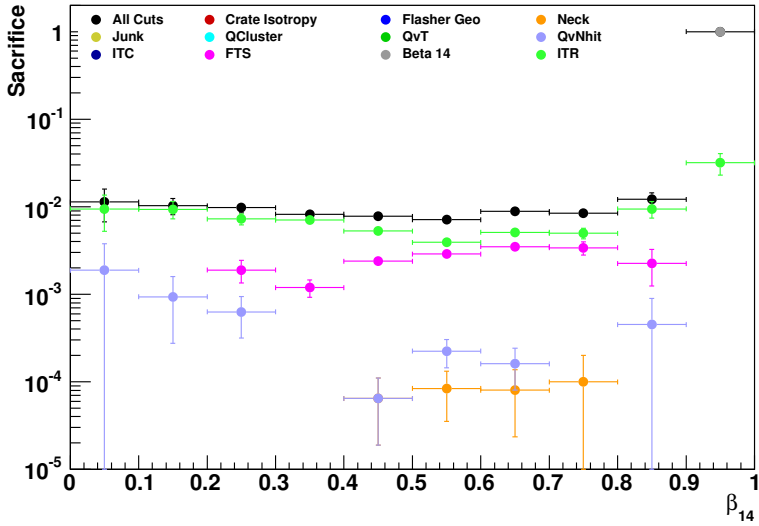


Figure 5.10: Comparison of the sacrifice for the instrumental background cuts in light water for different β_{14} isotropy parameter values.

lengths.

5.4.2 Liquid scintillator

To estimate signal sacrifice during the scintillator phase, electron energies from 0.1 MeV to 6.0 MeV were simulated in 0.1 MeV increments, with 1,000 events simulated at each energy. The sacrifice was plotted for different N_{hits} , energy, and radial values; direction and isotropy are not appropriate for scintillator. The higher level isotropy and ITR cuts were designed for Cherenkov events and are therefore not included here. The FTS cut is included in the plots for completeness, but as it was designed to cut events that are not Cherenkov-like it is the dominant source of sacrifice. It will therefore not be employed for the scintillator phase and is not discussed here further.

The fractional sacrifice, up to 3000 N_{hits} , is shown in Figure 5.11. Of the data cleaning cuts only the neck and flasher geometry cuts have an effect. Their sacrifice is under 0.1% per 300 N_{hits} bin, far below the target sacrifice level. The flasher geometry cut removes lower N_{hits} events than the neck cut, but there is a very small sample of cut events to determine if this is a persistent effect.

The fractional sacrifice across the energy spectrum, 0-6 MeV, is shown in Figure 5.12. As with the N_{hits} plot there is very low sacrifice, and no notable energy bias. The fractional sacrifice across the fiducial volume radius is shown in Figure 5.13. Most of the sacrificed events were outside the fiducial volume, further demonstrating that there is negligible sacrifice from data cleaning cuts in scintillator. Unlike for events in water there is no sacrifice from the Q v Nhit cut. This may be because the higher number of

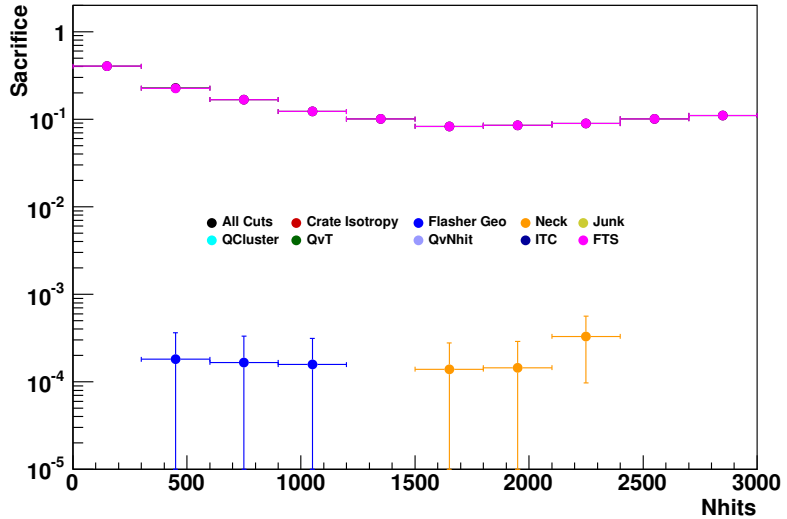


Figure 5.11: Comparison of the sacrifice for the instrumental background cuts in LAB-PPO across the N_{hit} spectrum.

N_{hits} reduces the probability of an anomalously high charge to N_{hits} ratio.

As the sacrifice is so low, with so few simulated physics events being cut, it cannot be said whether there is a bias to the sacrifice as a function of N_{hits} , energy or radius, but it makes no practical difference. That the sacrifice is very low does not imply that the cuts will work well in scintillator. Some cuts may prove to be ineffective as instrumental backgrounds involving undesired photons in the detector will have different signatures due to the material change.

5.5 Developing a Flasher Generator

The instrumental background cuts were developed for SNO with heavy water as the material inside the AV. The cuts are therefore likely to work similarly with light water due to the similar optical properties. The same cannot be said for liquid scintillator; photons are emitted isotropically, with a broader time profile. This effect, as well as the absorption and re-emission of photons, results in a broader PMT hit time distribution. Data cleaning cuts were also designed to work for a different N_{hits} regime than is appropriate for scintillator.

The flasher geometry cut for example will not observe a distance as high between cluster around the flashing tube and the rest of the hits. The Q v T cut will also be applied to different tube hit times. The cuts may therefore not remove a sufficient amount of instrumental background, which may necessitate the development of new cuts. Cuts based on electronics space, however, should continue to work well.

Flashers are the dominant source of instrumental background, and involve the trans-

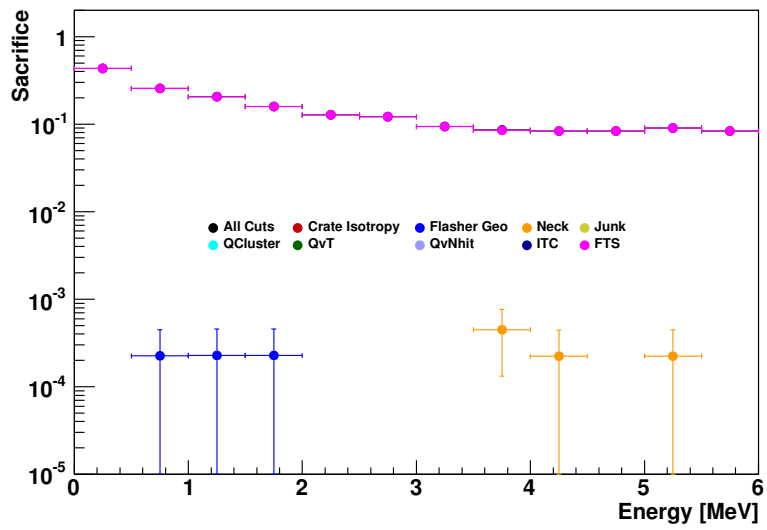


Figure 5.12: Comparison of the sacrifice for the instrumental background cuts in LAB-PPO across the energy spectrum.

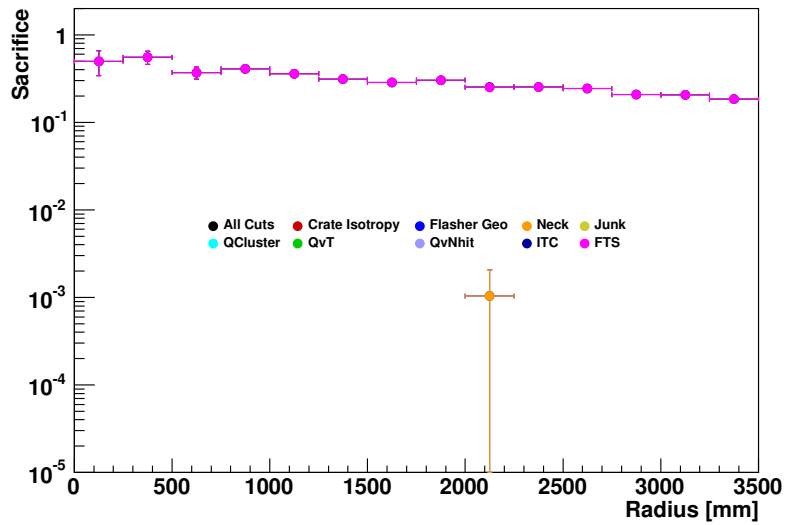


Figure 5.13: Comparison of the sacrifice for the instrumental background cuts in LAB-PPO at different radii.

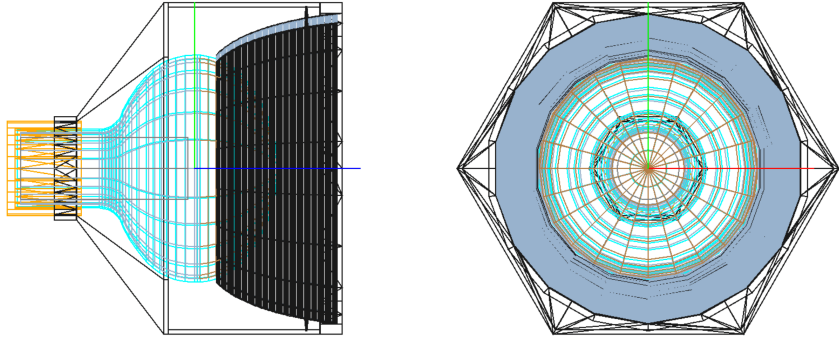


Figure 5.14: A visualisation of the SNO+ PMT geometry from the side (left) and top (right) [142].

mission of photons in the detector. It is therefore desirable to know what flashers will look like in liquid scintillator. To understand the requirements for new cut development it is also important to know what residual instrumental background remains in the sample of physics events after applying the data cleaning cuts. This is known as the signal “contamination”. To answer these questions a Monte Carlo flasher generator has been developed by the author.

Flashers couldn't be simulated for the SNO experiment because the PMT internal geometry and the trigger system was not sufficiently simulated. A more detailed geometry has been constructed for the SNO+ Monte Carlo [142], as well as improvements to the electronics simulations, including a charge model. The shape of the SNO r1408 Hamamatsu PMTs and concentrators were measured and a visualisation of the resultant geometrical construction can be seen in Figure 5.14. The transmission of photons through the PMT photocathode, glass and vacuum materials can now be simulated. The dynode stack is simulated as a solid cylindrical volume.

The flasher generator simulates photons emitted from the rear of the PMT, beside the dynode stack. Photons were assigned random forward directions (out of the PMT) so that any collimation was due to the PMT but with reduced simulation time due to fewer photons bouncing around inside the PMT. Simulating a large number of photons inside a PMT creates a very high, or railed, charge. The photon collimation due to the PMT and concentrator creates a grouping of PMTs on the far side of the detector later in time. To replicate the cluster of hits around the flashing PMT a simple cross-talk model was implemented. The model looks for the highest charge tube and triggers up to five PMTs on either side on the same slot, provided channels are available to be triggered. The charge of the PMTs in the cross-talk cluster was set to zero integrated charge.

Flashers do not have instantaneous photon emission, so the generator was created such that the photons could be released according to a specified time distribution. This

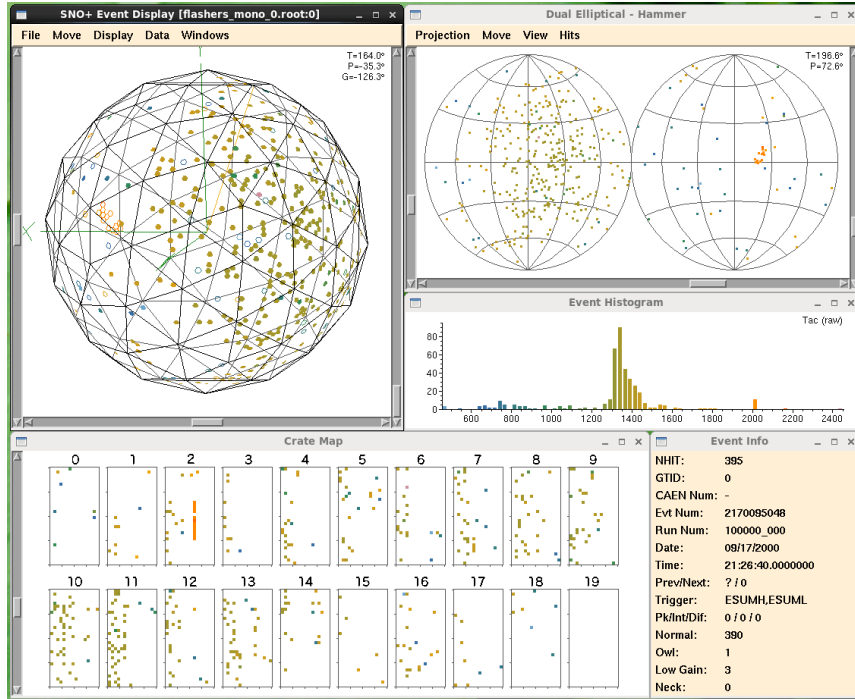


Figure 5.15: Flasher simulation of 500 nm instantaneously emitted photons in heavy water.

time distribution can be tuned using the event information of flashers observed by SNO.

It is not known what wavelength spectrum flashers have. The generator was created to have the options of simulating mono-energetic photons, photons with the blackbody spectrum at a specified temperature, a flat spectrum from 200 to 800 nm, the helium emission spectrum supposing flashers are caused by helium ingress into the PMTs, or the wavelength spectrum of a 490 nm wavelength LED used by the optical calibration system.

Figure 5.15 shows the result of using the flasher generator with heavy water to provide the best comparison with the real flasher of Figure 5.2. Mono-energetic photons of 500 nm with no time spread were simulated, showing that real flashers do not have instantaneous photon emission. The cluster of hits early in time due to cross-talk can be seen in crate 2 of the electronics crate map. The group of hits on far side of detector can be seen on the geodesic sphere and the flat map projection. There is a similar collimation to that which was seen for flashers in SNO, although the elliptical shape is not visible, possibly due to inaccuracies in the positioning of the flasher vertex and the internal geometry of the PMTs. Overall there is a good likeness to real SNO flashers, justifying the simulation method.

The optical response of light water is shown in Figure 5.16. The optical coefficients

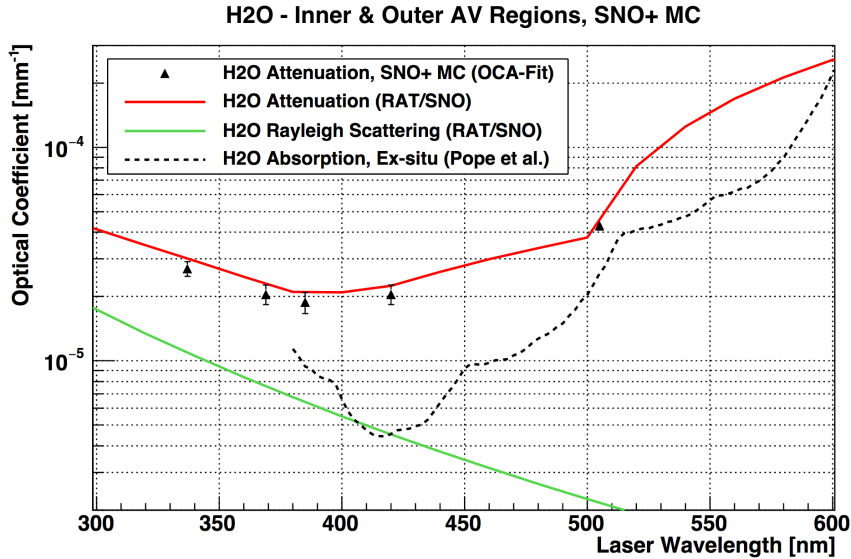


Figure 5.16: Optical attenuation coefficients for the light water regions. Values used in the RAT MC simulations are shown and compared to fitted attenuation coefficients from MC laserball simulations [143].

presented refer to the probability of a photon not being attenuated or scattered,

$$\exp(-(d_{\text{inner AV}}\alpha_{\text{inner AV}} + d_{\text{AV}}\alpha_{\text{AV}} + d_{\text{outer H}_2\text{O}}\alpha_{\text{outer H}_2\text{O}})), \quad (5.2)$$

where d is the photon path distance and α is the optical coefficient. Above 500 nm the attenuation rises steeply, and scattering is highest for lower wavelengths. The optical response of acrylic is shown in Figure 5.17, demonstrating that there is very high attenuation at lower wavelengths. Therefore, despite the relatively short distance photons travel through acrylic, at low wavelengths the acrylic attenuation is significant.

The exact wavelengths of photons created by flashers is not known. The optical response plots, however, suggest that a significant number of them must be in the range 300-500 nm as beyond these values the photons would be attenuated. Figure 5.18 shows a flasher event simulated in light water with 500 nm photons. The outcome is very similar in appearance to the heavy water flasher shown in Figure 5.15.

The wavelengths of photons emitted by flashers in water will determine the attenuation, and therefore the number of photons that must be emitted for a particular number of PMT hits, but the scattering has less of an effect so the events will look similar. The wavelength distribution of photons emitted by flashers in scintillator however could be much more important. Figure 5.19 shows the optical response of LAB-PPO. At 500 nm the scintillator is relatively transparent to photons, whereas at 350 nm the photons will be quickly absorbed by the PPO and re-emitted until they are at a high enough wavelength not to be absorbed. The photons are emitted isotropically by the scintillator so flashers at lower wavelengths will look much less like a flasher created in water than a

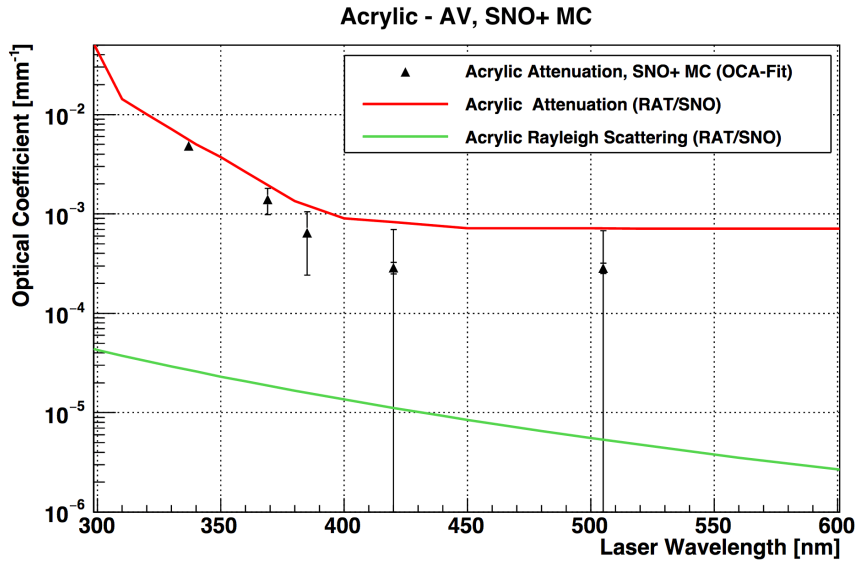


Figure 5.17: Optical attenuation coefficients for the acrylic region. Values used in the RAT MC simulations are shown and compared to fitted attenuation coefficients from MC laserball simulations [143].

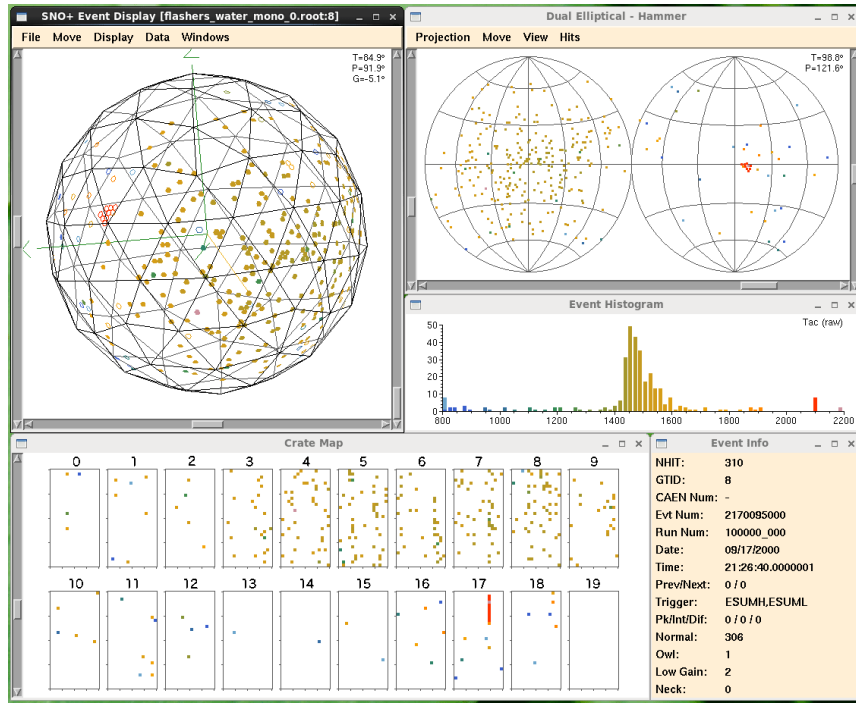


Figure 5.18: Flasher simulation of 500 nm instantaneously emitted photons in light water.

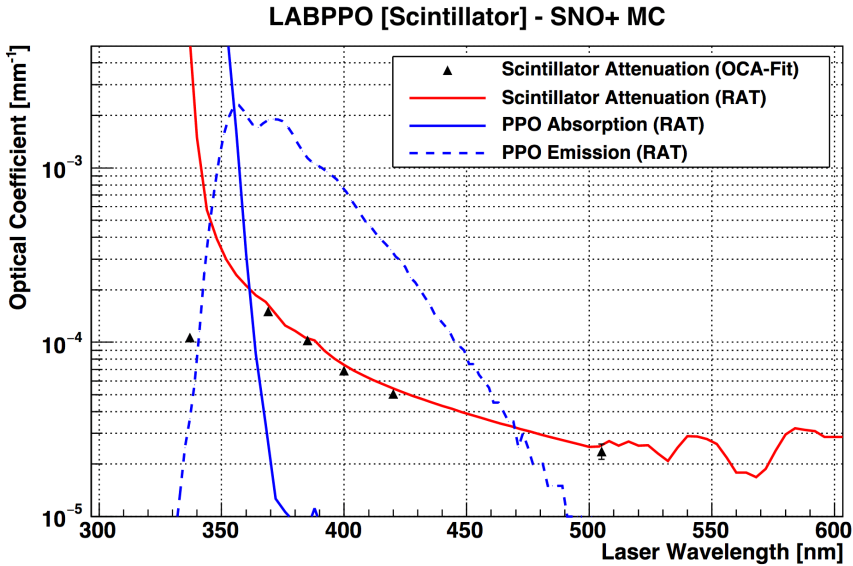


Figure 5.19: Optical attenuation coefficients for LAB-PPO scintillator. Values used in the RAT MC simulations are shown and compared to fitted attenuation coefficients from MC laserball simulations [143].

500 nm flasher.

Figure 5.20 shows a flasher simulated in scintillator with wavelength of 500 nm. There is some scattering, but the event retains much of the signature of a flasher in water. The similarity to water events is because of the transparency of scintillator to photons at 500 nm. Existing instrumental background cuts may therefore still be effective at removing flashers at this wavelength.

A flasher simulated in scintillator with a wavelength of 350 nm is shown in Figure 5.21. It can be seen that the photons have been rapidly absorbed by the LAB-PPO and re-emitted. This results in a grouping of hits on the near side of the detector around the flashing PMT. Existing instrumental background cuts are therefore less likely to be effective at removing flashers at this wavelength. For example, the threshold for the flasher geometry cut on the average distance of events from a flashing tube is unlikely to be met. The same number of photons were emitted as for the 500 nm case, indicating that the number of PMT hits is lower. This is due to the increased optical attenuation and probability of more than one photon triggering the same PMT.

To estimate how many flashers will be expected to pass the instrumental background cuts, and therefore be a background to physics analyses in the scintillator phase, it is necessary to know how many flashers are to be expected. To do this SNO data in the D₂O salt phase was analysed to find the total number of events tagged by any of the cuts designed to identify flashers. The cuts identifying flashers are Q v T, AMB, FTS, Q cluster, and the flasher geometry cut. A further condition was placed that none of these events could also be tagged by any of the cuts looking for events that were not

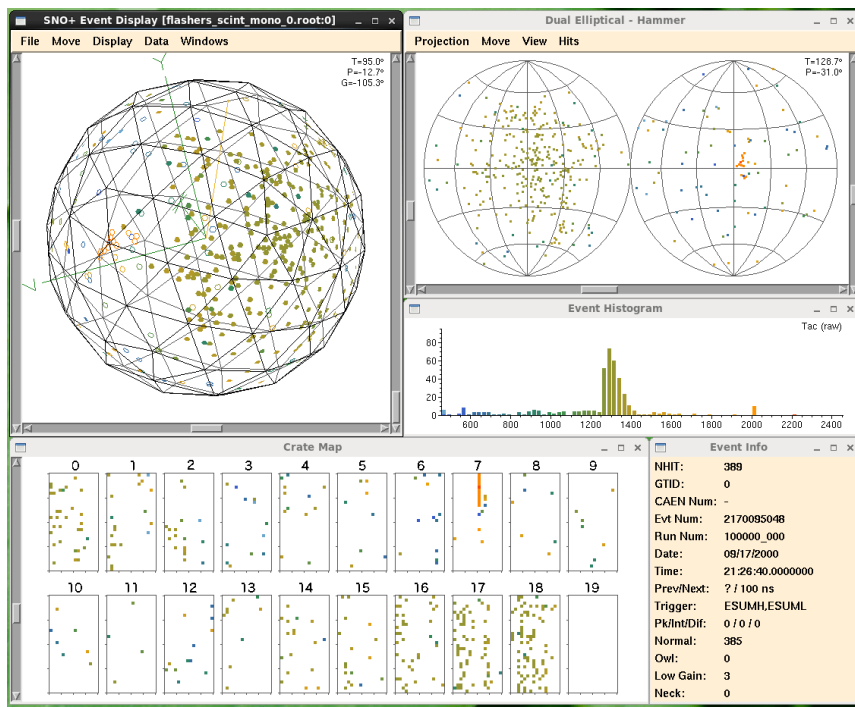


Figure 5.20: Flasher simulation of 500 nm instantaneously emitted photons in LAB-PPO scintillator.

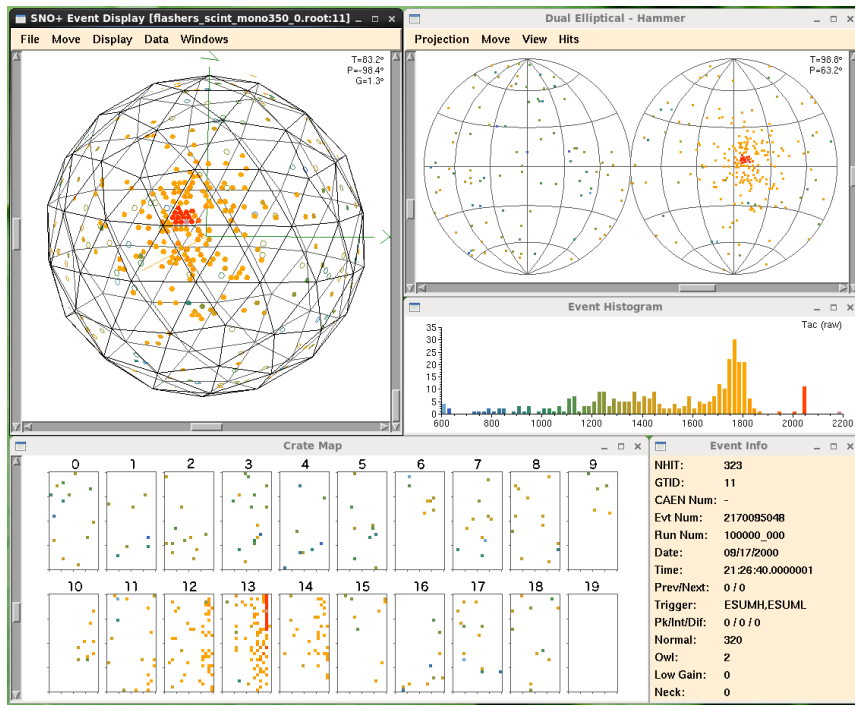


Figure 5.21: Flasher simulation of 350 nm instantaneously emitted photons in LAB-PPO scintillator.

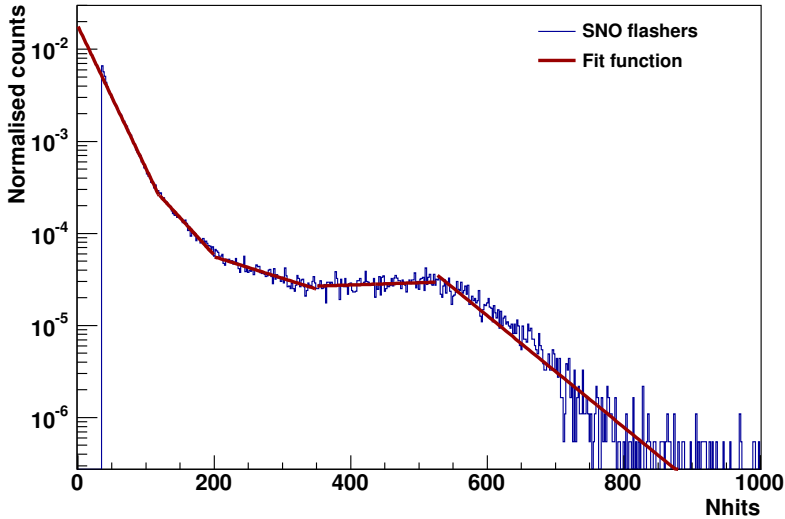


Figure 5.22: N_{hits} distribution of flashers in the SNO D₂O salt phase fitted piecewise.

flashers. The events excluded from the set were those identified as retriggers or muons, or tagged by the Q v Nhit, crate isotropy, OWL, or neck cut. This resulted in the distribution of N_{hits} shown in Figure 5.22. It can be seen that the numbers of events expected decreases by several orders of magnitude as the N_{hits} increase to the hundreds of hits expected for the scintillator phase. A function that was fitted piecewise to this distribution is shown alongside. The distribution was split into segments that appeared as approximately straight lines on a log scale. An exponential function could then be fitted to each piece of the distribution.

The flasher generator can then randomly sample the event N_{hits} from this distribution in order to replicate the distribution of SNO flashers. The flasher generator then needs to specify how many photons to simulate according to the desired N_{hits} . A function was therefore calculated to define number of photons necessary for a given N_{hits} value. As demonstrated earlier, the number of photons is wavelength dependent, so the function must be different depending on the wavelength distribution. Figure 5.23 shows the average number of N_{hits} produced for different numbers of photons simulated for different wavelength spectrums. The solid lines represent functions fitted to these graphs, which could be inverted to find the number of photons necessary for the desired N_{hits} . Of the wavelength spectrum options 500 nm requires the fewest photons for the same number of hits, followed by 350 nm. The detector has a lower response to the other wavelength distributions, because they extend beyond the 350-500 nm range where there is higher attenuation and lower PMT quantum efficiency.

To test that this method replicates the SNO flasher distribution, flasher events were simulated with heavy water. Figure 5.24 shows the N_{hits} distributions of events

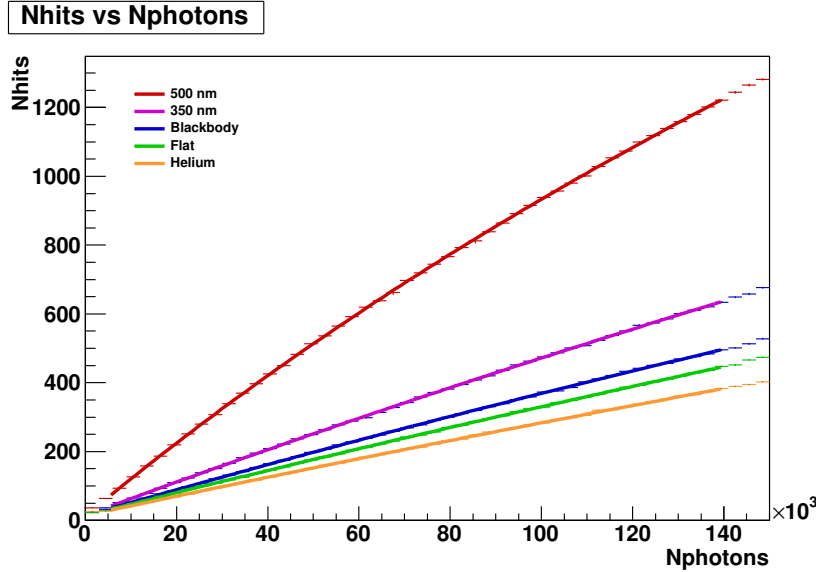


Figure 5.23: The average number of N_{hits} produced for different numbers of photons simulated for different wavelength spectrums. The solid lines represent functions fitted to these graphs.

identified as flashers by SNO overlaid with the distribution of flashers simulated in heavy water. It can be seen that the distribution has been closely replicated.

Simulating the distribution of flashers observed by SNO with the SNO+ Monte Carlo will provide an estimate of the number of flashers passing the background cuts and therefore acting as a background to physics analyses in the scintillator and water phases.

5.6 Contamination from flashers

To set accurate systematic errors, SNO+ must know what residual instrumental background remains after applying cuts. Those events which fall inside the ROI will act as a background to physics analyses. Different instrumental background events will act as a background for water and scintillator phase physics due to the different N_{hits} expected. The residual instrumental background inside the signal ROI is known as the signal contamination. To estimate the contamination due to flashers the SNO distribution of flashers has been replicated, as described above, in both light water and scintillator. The contamination plots that follow are scaled to one year of data taking.

The flashers simulated for this analysis have instantaneous photon emission, whereas in reality flashers have a broader emission profile. The FTS and ITR cuts, which are effective flasher removal cuts, will therefore be less effective. The following analysis also does not include a CAEN cut, another cut which is expected to be effective at flasher removal. The contamination values shown in the following analysis will therefore be an

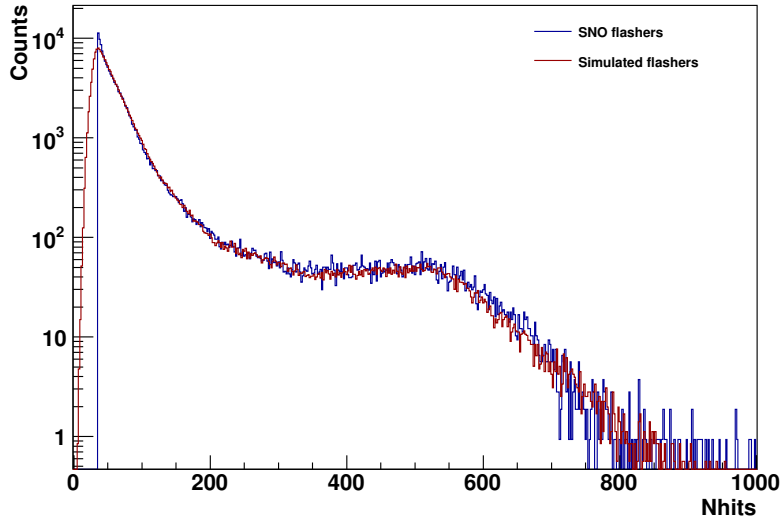


Figure 5.24: Distribution of events identified as flashers by SNO compared to events simulated by the flasher generator with heavy water in the AV.

overestimate.

5.6.1 Light water

Figure 5.25 shows the N_{hits} distribution expected in light water for flashers of 500 nm photons. It can be seen how each level of cuts reduces the expected number of events. After all cuts have been applied the flashers are at most 60 N_{hits} .

The energy spectrum of the 500 nm flashers is shown in Figure 5.26. The number of events before cuts decreases from 3 MeV upwards. This results in fewer flashers passing all cuts at higher energies. The total number of flashers expected to pass all cuts in the energy range 5.5-10 MeV is 6.7 per year.

The spectrum of the reconstructed radial magnitude of 500 nm flashers, shown in Figure 5.27, demonstrates that the fiducial volume cut is effective because most flashers reconstruct at higher radii.

Figure 5.28 shows the N_{hits} distribution expected in light water for flashers of 350 nm photons. After all cuts have been applied the flashers are at most 100 N_{hits} .

The energy spectrum of the 350 nm flashers is shown in Figure 5.29. The total number of flashers expected to pass all cuts across the energy range 5.5-10 MeV is 27.4 per year, significantly greater than for the 500 nm flashers. The main cause is because a greater portion of events are reconstructing below 10 MeV.

The spectrum of the reconstructed radial magnitude of 350 nm flashers is shown in Figure 5.30. More events are reconstructing closer to the centre of the detector, reducing the effectiveness of the fiducial volume cut and affecting the energy reconstruction, but

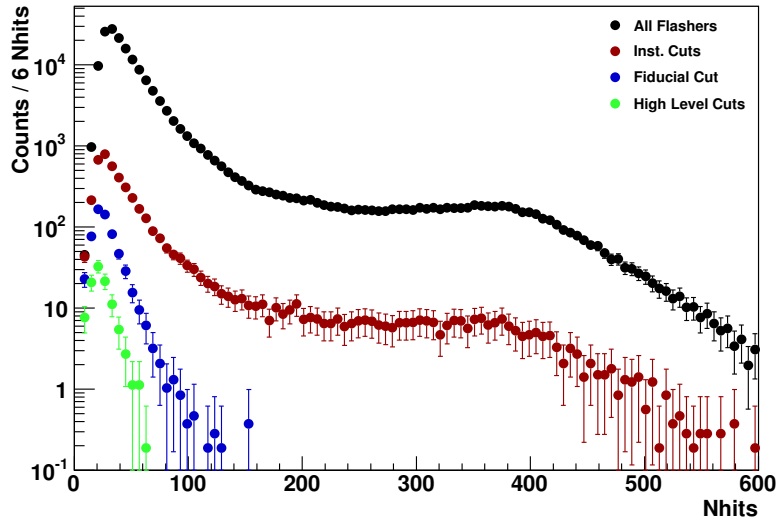


Figure 5.25: N_{hits} distribution of 500 nm flashers, simulated in light water, expected after each level of cuts for one year of data taking.

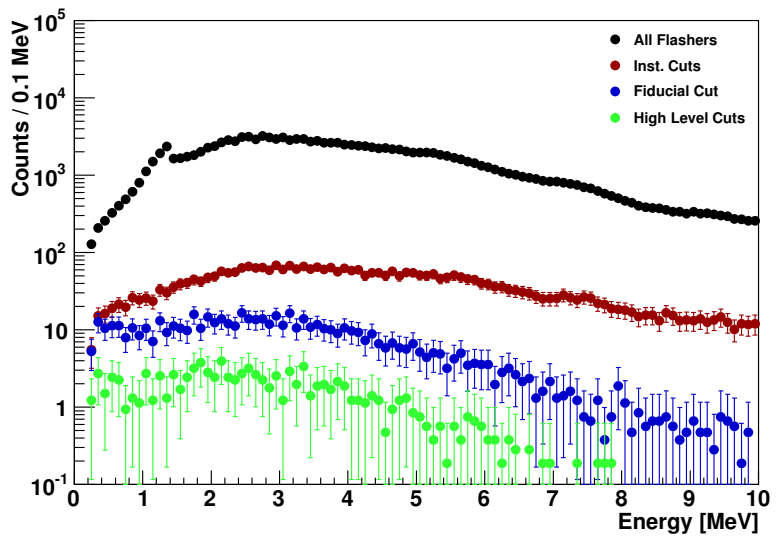


Figure 5.26: Energy distribution of 500 nm flashers, simulated in light water, expected after each level of cuts for one year of data taking.

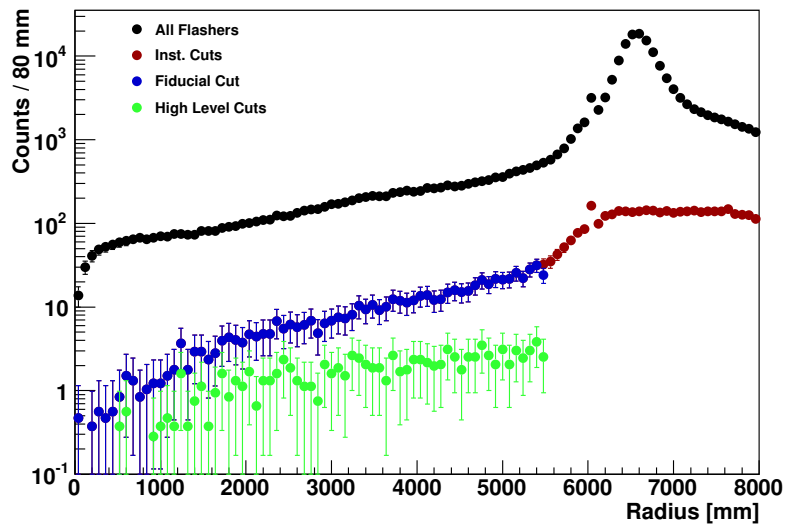


Figure 5.27: Radial distribution of 500 nm flashers, simulated in light water, expected after each level of cuts for one year of data taking.

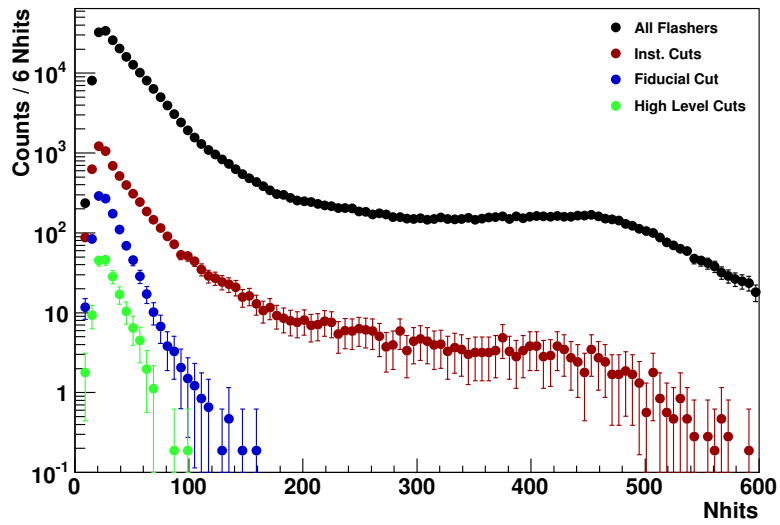


Figure 5.28: N_{hits} distribution of 350 nm flashers, simulated in light water, expected after each level of cuts for one year of data taking.

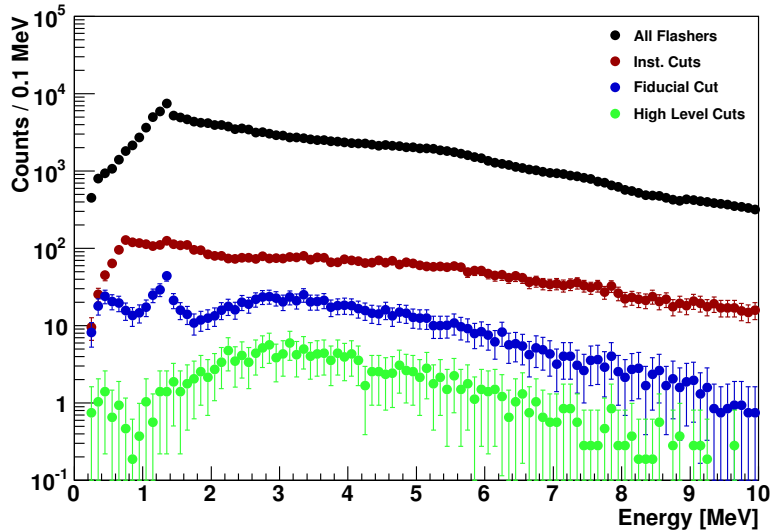


Figure 5.29: Energy distribution of 350 nm flashers, simulated in light water, expected after each level of cuts for one year of data taking.

improving the effectiveness of the ITR cut.

A blackbody emission spectrum at temperature 6000 K is a sensible estimation for the wavelength distribution of photons emitted by a spark in the dynode stack. This is close to the temperature of the Sun's surface and has a peak at ~ 500 nm, a wavelength for which the cuts are known to be effective (as they were for SNO). It also contains a component of other wavelengths so a good balance between the two wavelengths presented.

Figure 5.31 shows the N_{hits} distribution expected in light water for flashers of blackbody photons. After all cuts have been applied the flashers are at most approximately 80 N_{hits} , between the maximum for 500 nm and 350 nm photons.

The energy spectrum of the blackbody flashers is shown in Figure 5.32. The total number of flashers expected to pass all cuts across the energy range 5.5-10 MeV is 10.5 per year, between the expectation for the 350 and 500 nm flashers. More events are reconstructing below 10 MeV than for 500 nm flashers, and the cuts are less effective.

The spectrum of the reconstructed radial magnitude of blackbody flashers is shown in Figure 5.33. More events are reconstructing closer to the centre of the detector than for 500 nm, but fewer than 350 nm.

5.6.2 Scintillator

Similar SNO flasher distribution plots for SNO+ were replicated with LAB-PPO scintillator filling the AV, except that higher level cuts were not applied. The isotropy and ITR cuts employed for light water were designed for Cherenkov events and so not

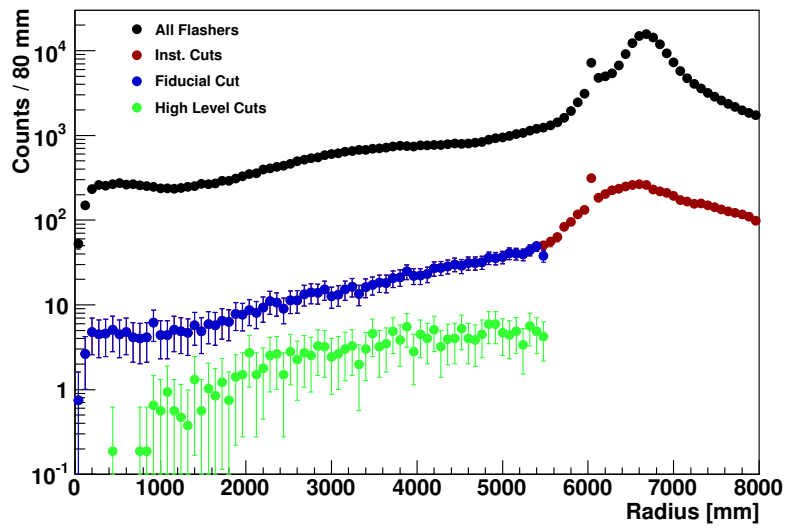


Figure 5.30: Radial distribution of 350 nm flashers, simulated in light water, expected after each level of cuts for one year of data taking.

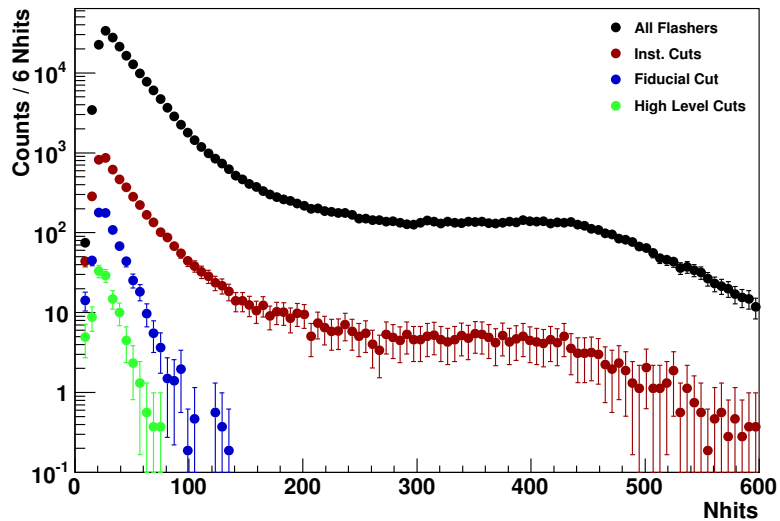


Figure 5.31: N_{hits} distribution of blackbody spectrum (6000 K) flashers, simulated in light water, expected after each level of cuts for one year of data taking.

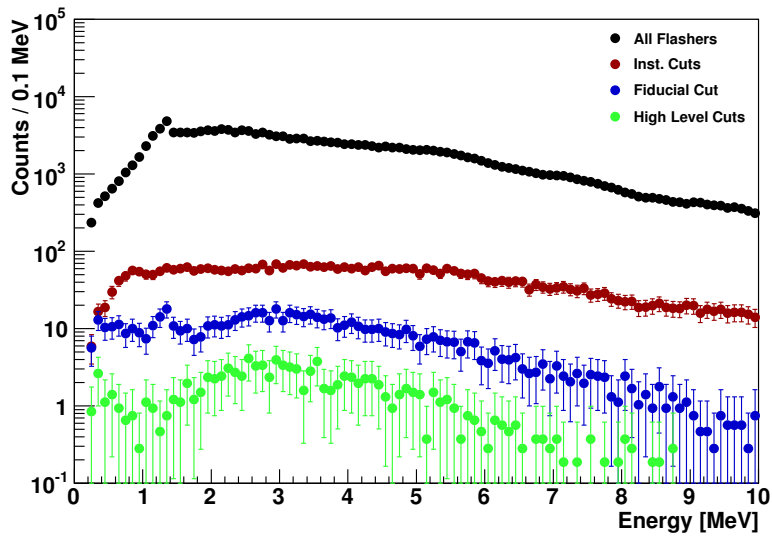


Figure 5.32: Energy distribution of blackbody spectrum (6000 K) flashers, simulated in light water, expected after each level of cuts for one year of data taking.

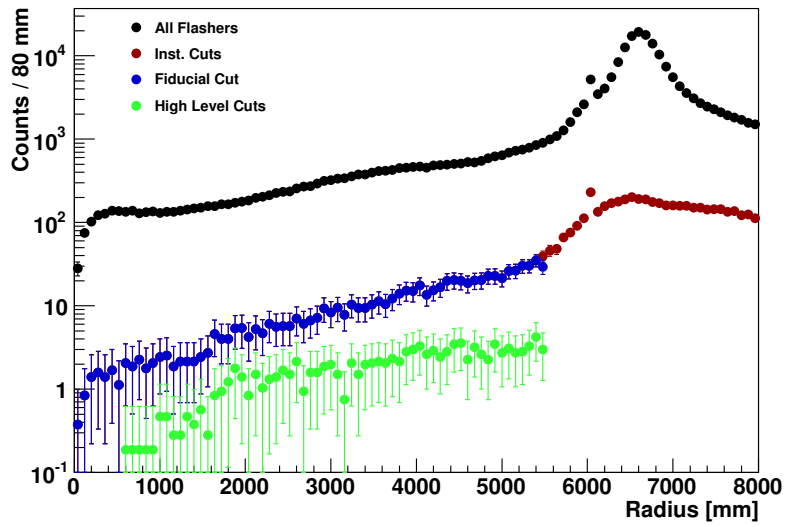


Figure 5.33: Radial distribution of blackbody spectrum (6000 K) flashers, simulated in light water, expected after each level of cuts for one year of data taking.

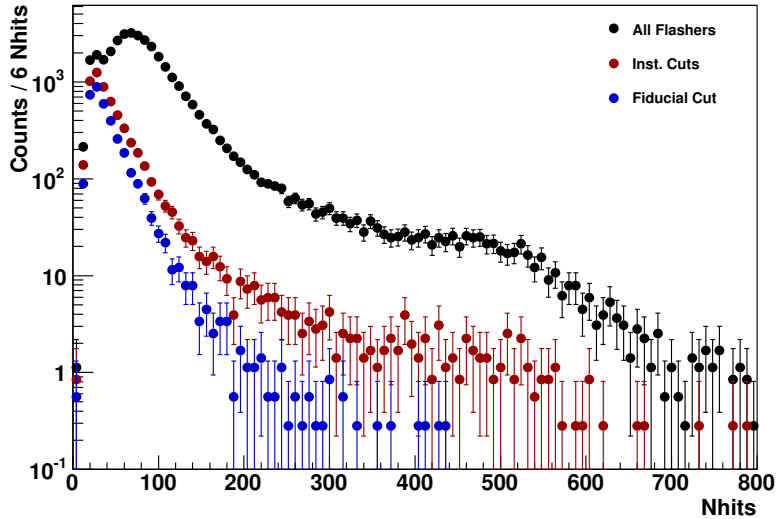


Figure 5.34: N_{hits} distribution of 500 nm flashers, simulated in LAB-PPO, expected after each level of cuts for one year of data taking.

appropriate.

Figure 5.34 shows the N_{hits} distribution expected in scintillator for flashers of 500 nm photons. It can be seen how each level of cuts reduces the expected number of events. After all cuts have been applied the flashers are at most approximately 450 N_{hits} , although there are low statistics at this N_{hits} level.

The energy spectrum of the 500 nm flashers is shown in Figure 5.35. The counts per bin decreases exponentially from 0.2 MeV upwards, resulting in fewer flashers passing all cuts at higher energies. There are no instrumental backgrounds passing the cuts above 0.8 MeV, much lower than the ROI for $0\nu\beta\beta$ decay. Therefore there would be no contamination to the $0\nu\beta\beta$ decay signal from 500 nm flashers. The exponential decrease in flashers as PMT hits increases results in very few events in the signal ROI, which are removed by the instrumental background and fiducial volume cuts.

The spectrum of the reconstructed radius for 500 nm flashers is shown in Figure 5.36. It can be seen that all events reconstruct inside the AV. The absorption and isotropic emission of photons by the scintillator results in the position reconstruction algorithm producing a false result. The peak for the reconstructed radius is approximately 4 m and the fiducial volume cut, reduced to 3.5 m in scintillator, removes all remaining events.

Figure 5.37 shows the N_{hits} distribution expected in scintillator for flashers of 350 nm photons. There are fewer events at higher N_{hits} because of the increased optical attenuation and increased probability of the multi-photon effect. After all cuts have been applied the flashers are at most approximately 50 N_{hits} , significantly lower than for

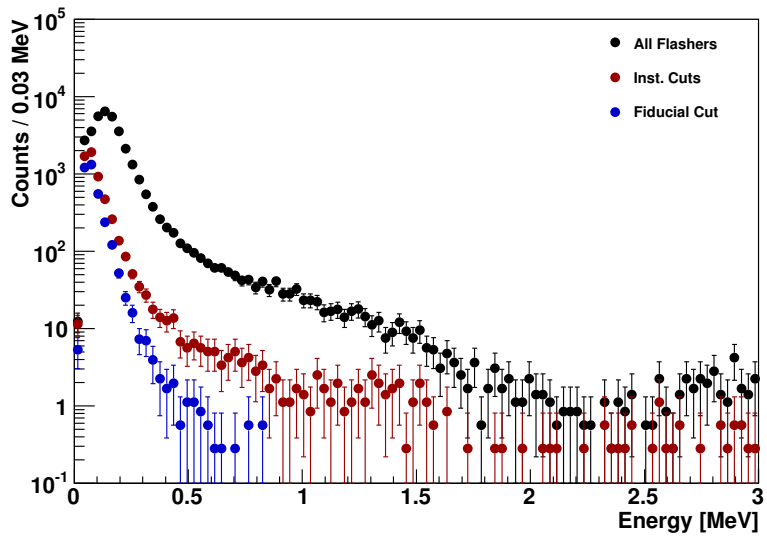


Figure 5.35: Energy distribution of 500 nm flashers, simulated in LAB-PPO, expected after each level of cuts for one year of data taking.

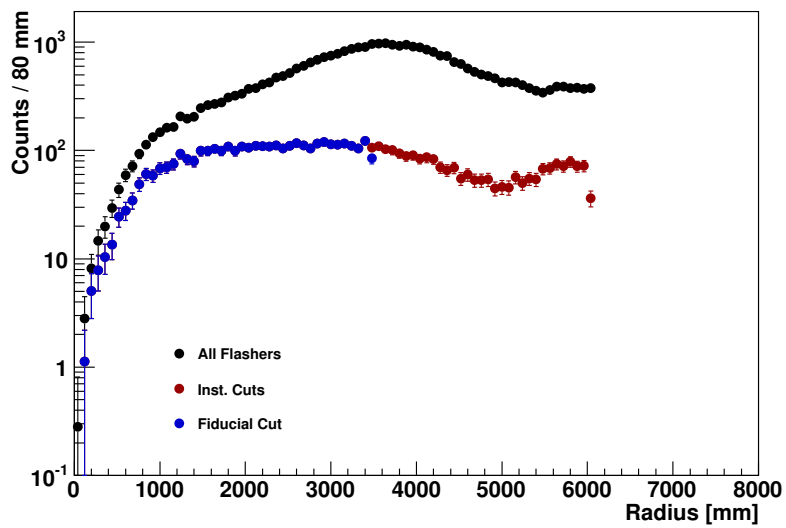


Figure 5.36: Radial distribution of 500 nm flashers, simulated in LAB-PPO, expected after each level of cuts for one year of data taking.

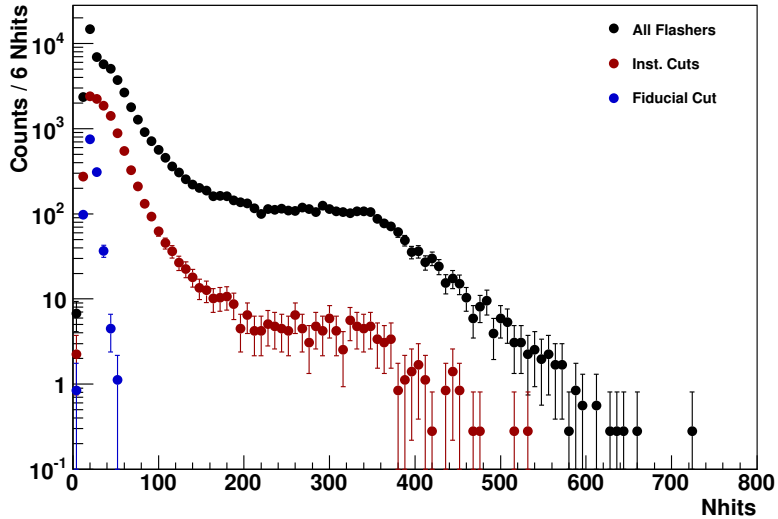


Figure 5.37: N_{hits} distribution of 350 nm flashers, simulated in LAB-PPO, expected after each level of cuts for one year of data taking.

500 nm photons.

The energy spectrum of the 350 nm flashers is shown in Figure 5.38. The peak in events towards 3 MeV before the fiducial volume cut, not reflected in the N_{hits} distribution, is due to the effect on the energy reconstruction algorithm of events reconstructed close to the AV. There are no instrumental backgrounds passing the cuts above approximately 0.1 MeV, lower than for the 500 nm flashers.

The spectrum of the reconstructed radius of 350 nm flashers is shown in Figure 5.39. The rapid absorption and isotropic re-emission of photons has resulted in most events reconstructing close to the AV. This results in a very effective fiducial volume cut, which removes all remaining instrumental background events.

Figure 5.40 shows the N_{hits} distribution expected in scintillator for flashers of photons from the blackbody emission spectrum at temperature 6000 K. After all cuts have been applied the flashers are at most approximately 400 N_{hits} , although there are very few events above 300 N_{hits} .

The energy spectrum of the blackbody flashers is shown in Figure 5.41. More events reconstruct at higher energies than for 500 nm flashers, but without the bimodal distribution of 350 nm flashers. There are no instrumental backgrounds passing the cuts above approximately 0.75 MeV, slightly lower than for the 500 nm flashers.

The spectrum of the reconstructed radius of blackbody flashers is shown in Figure 5.42. There is a bimodal distribution with a peak close to the AV and another close to 3 m, which is sufficient to remove all remaining flasher events.

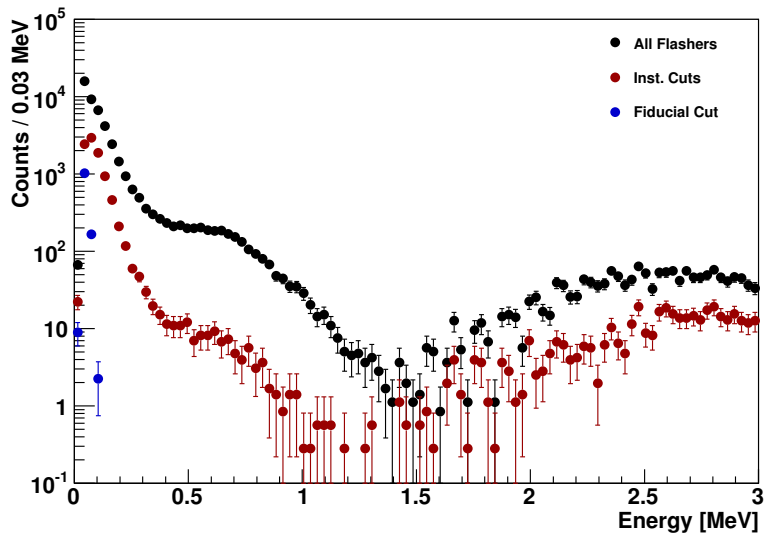


Figure 5.38: Energy distribution of 350 nm flashers, simulated in LAB-PPO, expected after each level of cuts for one year of data taking.

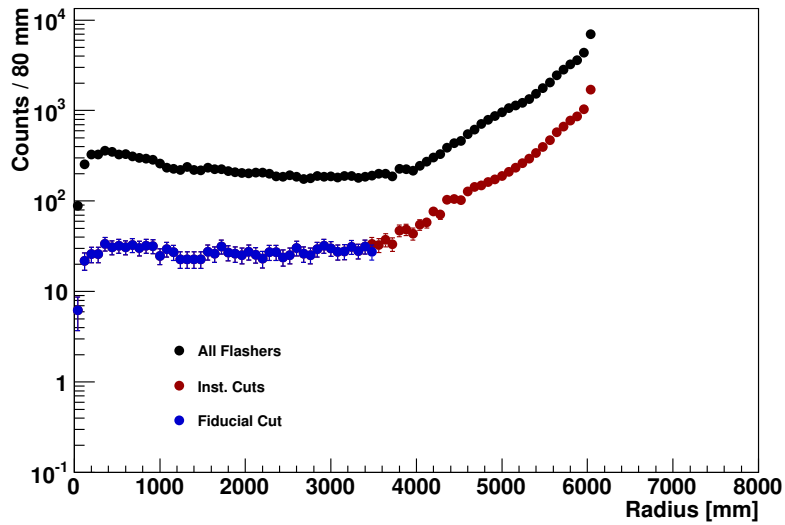


Figure 5.39: Radial distribution of 350 nm flashers, simulated in LAB-PPO, expected after each level of cuts for one year of data taking.

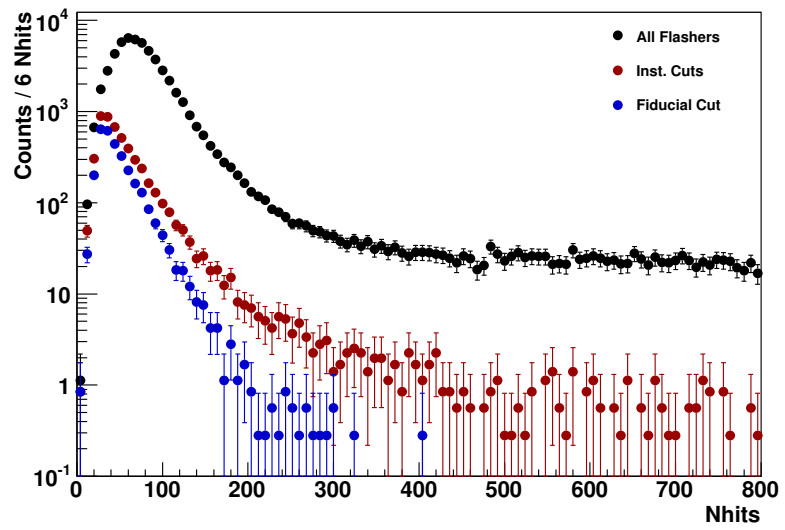


Figure 5.40: N_{hits} distribution of blackbody spectrum (6000 K) flashers, simulated in LAB-PPO, expected after each level of cuts for one year of data taking.

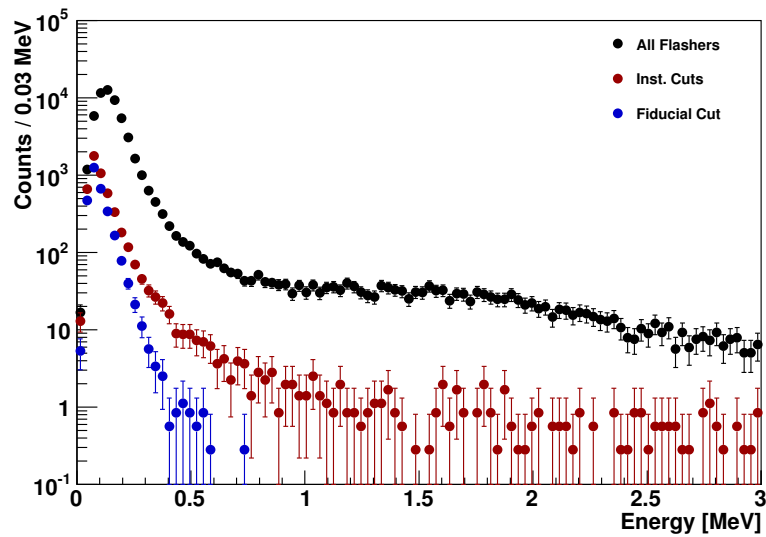


Figure 5.41: Energy distribution of blackbody spectrum (6000 K) flashers, simulated in LAB-PPO, expected after each level of cuts for one year of data taking.

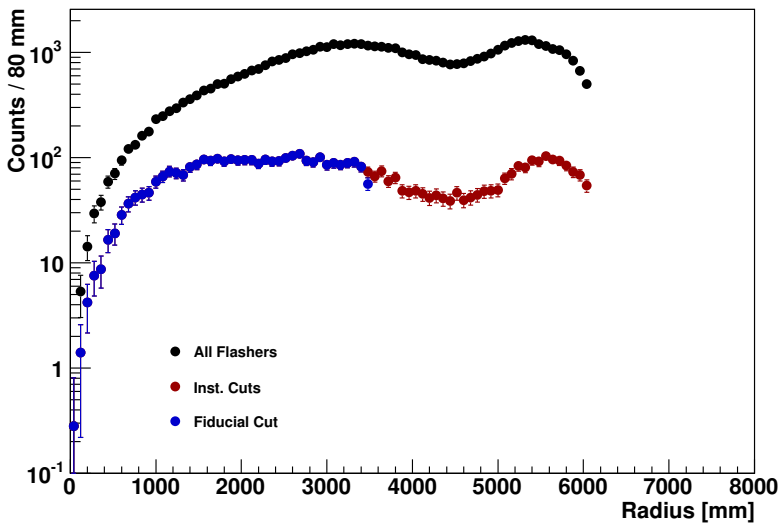


Figure 5.42: Radial distribution of blackbody spectrum (6000 K) flashers, simulated in LAB-PPO, expected after each level of cuts for one year of data taking.

5.6.3 Summary

With light water filling the AV there is little difference between the effectiveness of instrumental background cuts at different wavelengths. The fiducial volume cut is slightly less effective for 350 nm flashers because of the effect of increased scattering on position reconstruction. Of the scenarios presented here, 350 nm flashers are the worst case, because they result in more events reconstructing below 10 MeV and the cuts are less effective. Table 5.1 is a summary of the events removed by each level of cut, including the efficiencies of individual instrumental background cuts.

For an AV filled with LAB-PPO the instrumental background cuts are least effective at removing 350 nm flashers because of their different signature to water flashers. The fiducial volume cut, however, is much more effective. Photons are quickly absorbed and re-emitted on the near side of the vessel relative to the flashing PMT resulting in events reconstructing close to the AV. Conversely to water, of the scenarios presented, 350 nm flashers is the best case, although none of the scenarios results in any contamination of the $0\nu\beta\beta$ ROI. Table 5.2 is a summary of the events removed by each level of cuts.

A blackbody emission spectrum is a sensible estimate for the photons produced by flashers. The temperature chosen here is 6000 K which has a peak at ~ 500 nm but contains photons across the wavelength spectrum and is therefore a compromise between the other scenarios. Table 5.3 lists the expected contamination values over a year of data taking, and shows that the number of blackbody flashers reconstructing within the given energy ranges is between the 350 nm and 500 nm flashers for water and zero for LAB-PPO.

	500 nm		350 nm		Blackbody	
	Events	% Cut	Events	% Cut	Events	% Cut
All Flashers	30978.2	-	35798.5	-	36298.7	-
Inst. Cuts	1055.9	96.6	1385.5	96.1	1295.8	96.4
<i>Crate Isotropy</i>		0.0		0.0		0.0
<i>Flasher Geo</i>		96.4		95.9		96.3
<i>QCluster</i>		53.2		53.4		53.2
<i>QvT</i>		48.2		48.0		48.1
<i>QvNhit</i>		0.0		0.0		0.0
<i>ITC</i>		0.0		0.0		0.0
<i>FTS</i>		0.0		0.0		0.0
Fiducial Cut	65.8	93.8	169.7	87.8	105.0	91.9
High Level Cuts	6.7	89.7	27.4	83.8	10.5	90.0

Table 5.1: Numbers of events remaining after each level of cut for simulated flashers in light water over a period of one year. The efficiencies of individual instrumental background cuts are also shown. The energy of events is in the range 5.5 to 10 MeV and the blackbody spectrum temperature is 6000 K.

	500 nm		350 nm		Blackbody	
	Events	% Cut	Events	% Cut	Events	% Cut
All Flashers	67.2	-	1501.4	-	676.6	-
Inst. Cuts	9.6	85.8	372.6	75.2	25.0	96.3
<i>Crate Isotropy</i>		1.7		36.8		5.6
<i>Flasher Geo</i>		77.8		1.4		90.9
<i>QCluster</i>		46.9		50.3		56.3
<i>QvT</i>		32.6		0.1		41.7
<i>QvNhit</i>		0.4		0.1		4.2
<i>ITC</i>		0.4		0.1		4.2
Fiducial Cut	0.0	100.0	0.0	100.0	0.0	100.0

Table 5.2: Numbers of events remaining after each level of cut for simulated flashers in LAB-PPO scintillator over a period of one year. The efficiencies of individual instrumental background cuts are also shown. The energy of events is in the range 2.1 to 3 MeV and the blackbody spectrum temperature is 6000 K.

Wavelength dist.	Contamination	
	Water	Scintillator
500 nm	6.7 ± 0.8	0.0 ± 0.0
350 nm	27.4 ± 1.6	0.0 ± 0.0
Blackbody	10.5 ± 1.0	0.0 ± 0.0

Table 5.3: The contamination from simulated flashers in light water and LAB-PPO scintillator over a period of one year after all cuts have been applied. The energy of events is in the range 5.5 to 10 MeV for light water, 2.1 to 3 MeV for LAB-PPO, and the blackbody spectrum temperature is 6000 K.

The quoted numbers of events passing all cuts for both water and scintillator phases do not include a CAEN cut, which is expected to be an effective flasher removal cut. The flashers simulated for this analysis also have instantaneous photon emission so the FTS and ITR cuts, which are also effective flasher removal cuts will be less effective. The contamination in the water phase is therefore an overestimate. For the same reasons the numbers of flashers passing all cuts in the scintillator phase is also an overestimate. However, they are all in the relatively low end of the energy spectrum and therefore not a background for $0\nu\beta\beta$ decay.

Chapter 6

Nucleon Decay

The Standard Model (SM) is a very successful theory and has survived considerable experimental testing. However, the SM is known to be an incomplete theory, for instance it does not explain the mass of the neutrino. Investigating forbidden decay channels may provide further insight into new physics.

The SM conserves $B - L$ (baryon–lepton number). Baryon number is an “accidental” symmetry in the SM due to the pattern of particles and renormalisation [144]. If B conservation holds, because the proton is the lightest baryon it must therefore be stable. The Sakharov conditions (see Section 1.7.2), however, require baryon number violation to explain the matter-antimatter asymmetry in the universe.

Many Beyond the Standard Model (BSM) theories predict the existence of both baryon and lepton (L) number violating processes, while conserving $B - L$. Lepton number violation is necessary for Majorana neutrinos and the observation of $0\nu\beta\beta$ decay. The violation of baryon and lepton numbers implies that protons and neutrons could decay with leptonic products, which is an expected signature of such a theory.

One category of B and L violating theories are Grand Unified Theories (GUTs) [145]. GUTs aim to unify the electroweak and strong interactions, and many involve a symmetry between baryons and leptons. Baryon and lepton number violating processes, however, are suppressed by powers of the grand unification scale. Supersymmetry (SUSY) or Universal Extra Dimensions (UEDs) may also cause baryon and lepton number violation, with suppression at the TeV scale rather than the higher GUT scale.

The observance of nucleon decay would be a valuable test for BSM physics. However it is an extremely rare process and no experimental evidence has been observed to date.

6.1 Possible decay modes

The “Minimal $SU(5)$ ” model [146] is the simplest possible GUT, meaning that it is the smallest simple gauge group than can contain $SU(3) \times SU(2) \times U(1)$. It is referred to as “minimal” because it contains the smallest possible Higgs sector [147]. The model predicts the proton lifetime to be $10^{28.5} - 10^{31.5}$ years, via the decay channel $p \rightarrow e^+ \pi^0$.

However, a proton lifetime in this range has been excluded by the IMB experiment [148], which set a limit of 5.5×10^{32} years at 90% CL, and subsequently Super-K [149] which set an improved limit of 1.29×10^{34} years.

Other models predict longer nucleon lifetimes, such as the left-right symmetric $SO(10)$ [150]. Symmetry breaking of $SO(10)$ results in a variety of different proton lifetimes depending upon which group the symmetry breaking goes through. Through the $SU(4)$ group [151], the mode of decay is $p \rightarrow e^+ \pi^0$ with a predicted proton lifetime of $2 \times 10^{32 \pm 2}$ years. Most of this lifetime range has been ruled out by Super-K.

Supersymmetry models result in proton decay through modes other than the $p \rightarrow e^+ \pi^0$ decay described above. The most prominent SUSY candidates are also the $SU(5)$ and $SO(10)$ groups, for which the dominant decay mode is $p \rightarrow \bar{\nu} K^+$ [147]. For this mode, minimal SUSY $SU(5)$ has proton lifetime less than 2.9×10^{30} years and is ruled out by the limit reported by Super-K of 5.9×10^{33} years at 90% CL [152]. SUSY $SO(10)$ has a predicted proton lifetime in the same channel ranging between 1.4×10^{32} to 2.2×10^{34} years [147, 153] which has therefore yet to be excluded.

There are many more exotic models that also exist predicting proton decay to $e^+ \pi^0$ and $\bar{\nu} K^+$ (for example [154]) within the reach of current and next generation experiments. There are also many more decay channels that can be explored, including the decay of neutrons [155].

Hyper-Kamiokande (Hyper-K) is a next generation underground water Cherenkov detector proposed for the Kamioka mine in Japan [156]. It will have a fiducial mass of 0.56 million tons, be surrounded by 99,000 PMTs, and act as a far detector to the off-axis J-PARC neutrino beam. Hyper-K will also try to observe signatures from nucleon decays. Water Cherenkov detectors are the best technique, taking mass and cost into account, to search for proton decays to $e^+ \pi^0$ and $\mu^+ \pi^0$. Over 10 years of data taking Hyper-K is sensitive to the $e^+ \pi^0$ signature at greater than 10^{35} years at 90% confidence level (CL) (see Figure 6.1).

Another next generation long baseline neutrino oscillation experiment is Deep Underground Neutrino Experiment (DUNE) [157]. DUNE will use the world's highest intensity neutrino beam (1.2 MW), on-axis, from the Long-Baseline Neutrino Facility (LBNF) hosted by Fermilab. A 40 kton liquid argon time-projection chamber (LArTPC) will be located at the Sanford Underground Research Facility 1300 km away and act as a far detector. LArTPC technology is especially effective for detecting kaon modes, such as $K^+ \bar{\nu}$, because of the improved reconstruction and high identification efficiency for the decay products. DUNE is sensitive to kaon decay mode signatures at greater than 10^{35} years at 90% CL (see Figure 6.1).

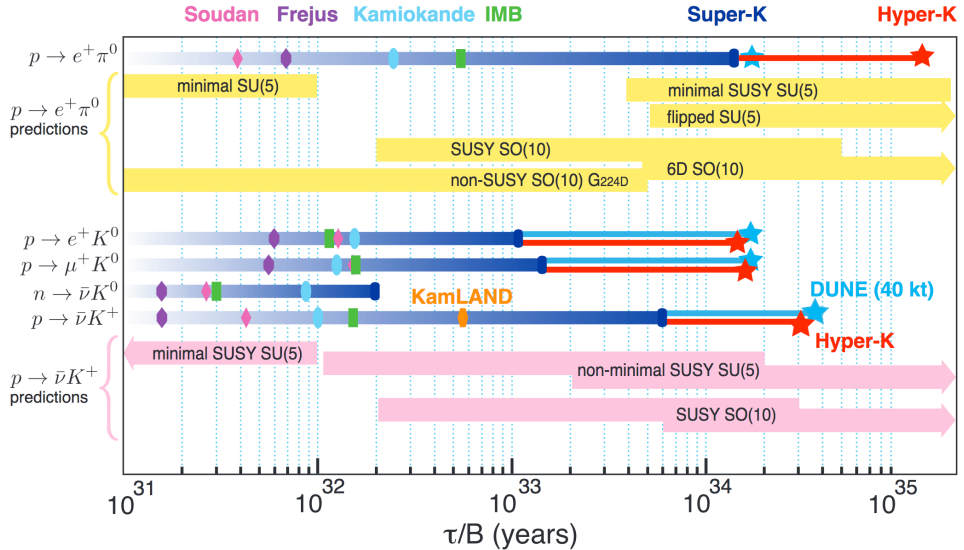


Figure 6.1: Nucleon decay lifetime limits from existing experiments and the next generation DUNE and Hyper-K experiments at 90% CL. The ranges predicted by various Grand Unified Theories are shown for comparison [157].

6.2 Invisible decay modes

There are some models which predict dominant “invisible” decay modes, in which the particles produced deposit very little or no energy in the detector, for instance the 6-D UED model developed by Mohapatra and Perez-Lorenzana [158].

This model predicts the decay of protons and neutrons with three lepton final states, for instance $n \rightarrow \nu\bar{\nu}\bar{\nu}$, $n \rightarrow \pi^0\nu\bar{\nu}\bar{\nu}$, $n \rightarrow \pi^+e^-\bar{\nu}\bar{\nu}$, and $p \rightarrow \pi^+\nu\bar{\nu}\bar{\nu}$. The decay to three neutrinos is more probable than the four-body decays. An alternative model for invisible mode nucleon decay could involve scale-invariant “unparticles” such as $n \rightarrow O_{\mathcal{U}}^s$ [159], although there are many other possibilities.

The Particle Data Group [26] lists 70 possible modes of nucleon or di-nucleon decay which conserve charge, energy-momentum and angular momentum. Limits of over 10^{30} years have been set for the lifetimes of most of these decays, although the poorest limits are currently for invisible decay modes. SNO+ is uniquely sensitive to invisible decay modes, the reasons for which will be elaborated on shortly, and will be able to set a new limit for nucleon lifetime. Searching for invisible channels also provides a model independent test for nucleon decay. It is therefore well motivated for SNO+ to study nucleon decay through this mode.

Although the decay products are unobserved by detectors, invisible modes are detectable. The residual nucleus, which will have a hole in a previously occupied shell, de-excites providing a detectable signature.

In 2004 the SNO experiment set a limit on the decay of protons and neutrons

Decay mode	Daughter (decay, $T_{1/2}$, and Q)	Branching ratio %
(n1) $^{11}\text{C}^*(\text{n})$	$^{10}\text{C}_{\text{gs}}(\beta^+; 19.3 \text{ s}, 3.65 \text{ MeV})$	3.0
(n2) $^{11}\text{C}^*(\text{n}, \gamma)$	$^{10}\text{C}_{\text{gs}}(\beta^+; 19.3 \text{ s}, 3.65 \text{ MeV})$	2.8
(nn1) $^{10}\text{C}^*(\text{n})$	$^9\text{C}(\beta^+; 0.127 \text{ s}, 16.5 \text{ MeV})$	6.2
(nn2) $^{10}\text{C}^*(\text{n}, \text{p})$	$^8\text{B}(\beta^+ \alpha; 0.77 \text{ s}, 18 \text{ MeV})$	6.0

Table 6.1: Branching ratios and experimental signatures of the decay modes for neutrons from the $s_{1/2}$ -state of ^{12}C in the KamLAND experiment [144].

decaying via an invisible mode. The disappearance of a nucleon in a ^{16}O atom would result in either a $^{15}\text{O}^*$ or a $^{15}\text{N}^*$ atom which then de-excites to ground state, emitting a 6-7 MeV γ approximately 45% of the time.

The dominant background for this signature was from NC solar neutrino-neutron scattering on the deuterium nuclei. Free neutrons are produced, which then capture on deuterium nuclei, producing a tritium nuclei and a 6.25 MeV γ . At 90% CL SNO set a limit on the decay of protons, $\tau_p > 2.1 \times 10^{29}$ years, and the decay of neutrons, $\tau_n > 1.9 \times 10^{29}$ years [160].

In 2006 the KamLAND experiment improved on this limit for neutron decay as well as setting a limit for di-neutron decay [144]. For single neutron decay, two de-excitation modes were observable. The first decay mode, in which an $^{11}\text{C}^*$ nucleus emits a neutron, has a 3.0% branching ratio. The capture of the neutron on hydrogen results in a 2.2 MeV γ emission, and subsequently there is a spatially coincident β^+ decay of ^{10}C with a half-life of 19.3 s and Q-value of 3.65 MeV. The second decay mode has a 2.8% branching ratio, and is different in that the $^{11}\text{C}^*$ nucleus emits a γ with the neutron before β^+ decaying.

For double neutron decay, two de-excitation modes are also observable with branching ratios 6.2% and 6.0%. These modes similarly have a prompt signal from the neutron capture, and then the decay of a daughter nucleus. See table 6.4 for further details.

KamLAND has two notable disadvantages to SNO. Firstly, observable signals for neutron decays in ^{12}C have a total branching ratio close to eight times less than for ^{16}O . Secondly, although KamLAND has a similar size fiducial volume to SNO, as scintillator is less dense than water there are fewer candidate nucleons. Nonetheless, without the NC background, KamLAND was able to set a bound a factor of three greater than SNO ($\tau_n > 5.8 \times 10^{29}$ years). A bound of $\tau_{nn} > 1.4 \times 10^{30}$ years was set for di-neutron decay.

Prior to the SNO and KamLAND experiments, Kamiokande [161] reported a limit of $\tau_n > 4.9 \times 10^{26}$ years on invisible mode neutron decay. Due to higher cosmogenics and a lower water purity than SNO, Kamiokande suffered from huge backgrounds below 7.5 MeV and was only able to measure nucleon decay signatures above this energy. Consequently Kamiokande could not measure the same gamma emissions from the de-

excitation of $p_{3/2}$ holes that SNO could measure, and was restricted to higher, less probable branches up to 10 MeV. Kamiokande was also able to measure the background free ~ 20 -40 MeV gammas from the de-excitation of $s_{1/2}$ hole states, however these were much less probable. Consequently Kamiokande's limit was superseded by the aforementioned experiments.

SNO+ will be able to set a limit for invisible mode nucleon decay better than all previous experiments. There will be no sensitivity to neutrons in the nucleon decay signal region because SNO+ will make the measurement during its light water phase, rather than the heavy water measurement made by SNO. This leaves ^8B solar neutrinos as the dominant background, which can be reduced using a direction cut. Also, as mentioned above, because the total branching ratio of visible signals is superior for oxygen to carbon SNO+ will set a better limit than KamLAND, or perhaps make a discovery.

6.3 Expected signal

In a nuclear shell model ^{16}O has four nucleons on Fermi surface shell, $p_{1/2}$, eight nucleons on the inner shell, $p_{3/2}$, and four nucleons on the deep shell, $s_{1/2}$. If a valence proton or neutron on shell $p_{1/2}$ decays, a ^{15}N or ^{15}O nucleus, respectively, is created in its ground state. If a nucleon decays leaving a hole on shell $p_{3/2}$ below the nucleon emission threshold, then it de-excites by emitting a gamma. A nucleon on shell $s_{1/2}$ decays leaving a hole with sufficient energy for the nucleon to de-excite by emitting a proton or neutron. The residual nucleus then de-excites to ground state energy by emitting γ s. Escaping nucleons may also collide with other nucleons before escaping, resulting in many different hole states, which de-excite statistically to different nuclei [162]. See Figure 6.2 for a diagram of the different de-excitation modes for the decay of a proton from a ^{16}O nucleus.

If a proton decays from a ^{16}O nucleus and a $^{15}\text{N}^*$ nucleus is produced, then it de-excites by emitting γ s (and in some circumstances protons and neutron). The de-excitations have branching ratios of 41% for producing a 6.32 MeV γ , 3% for a 9.93 MeV γ , 2% for a 7.03 MeV γ , and 2% for a 7.01 MeV γ . The energies and branching ratios for all observable proton decay modes are shown in Table 6.2.

A neutron decaying from a ^{16}O nucleus produces a $^{15}\text{O}^*$ nucleus, which de-excites producing a 6.18 MeV γ with branching ratio 44%, or a 7.03 MeV γ with branching ratio 2% [162]. The energies and branching ratios for all observable neutron decay modes are shown in Table 6.3.

With a mass of 904 tonnes of H_2O in the detector, 88.9% of which is from oxygen atoms, there are 8.04×10^8 g of oxygen. The natural abundance of ^{16}O is 99.76%, leading to 5.01×10^7 moles of ^{16}O , or 3.02×10^{31} ^{16}O atoms. Consequently there are 2.41×10^{32} protons, and the same number of neutrons. Given the limit set by SNO

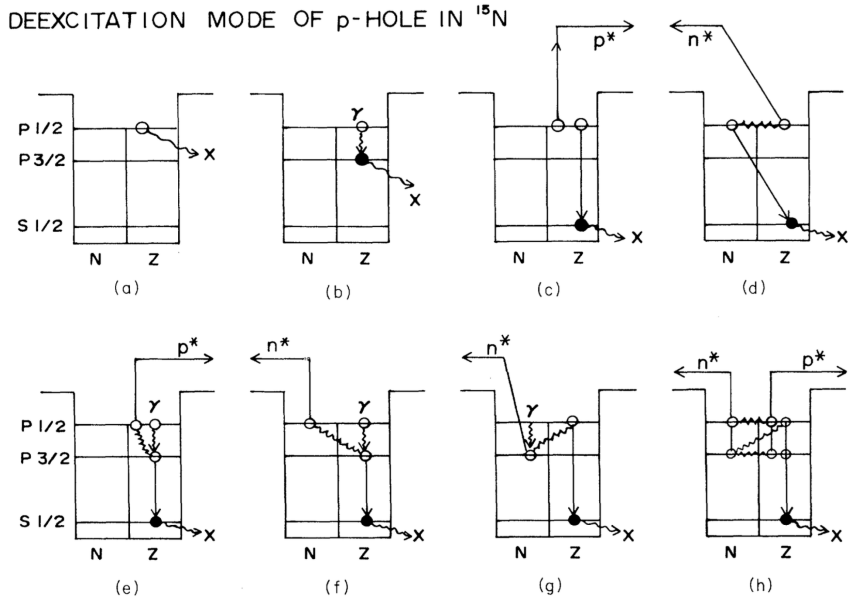


Figure 6.2: Different modes of de-excitation created by a proton decay ($p \rightarrow x$) in ^{16}O . N and Z are the neutron and proton shells, respectively, p^* and n^* are emitted protons and neutrons [162].

Proton decay modes			
E_γ	E_p	E_n	B
6.32	0	0	0.41
9.93	0	0	0.03
0	0.5	0	0.03
0	0	~ 20	0.02
7.03	0	~ 13	0.02
0	1.6	~ 11	0.01
0	~ 21	0	0.02
7.01	~ 14	0	0.02
0	~ 11	~ 2	0.03

Table 6.2: The simulated proton decay modes. E_γ , E_p , and E_n are kinetic energies for the de-exciting γ -ray, proton, and neutron, respectively, in units of MeV. B is the branching ratio for the decay mode [162].

Neutron decay modes			
E_γ	E_p	E_n	B
6.18	0	0	0.44
0	~24	0	0.02
7.03	~17	0	0.02
0	~14.5	0	0.01
0	0	~18	0.02
0	2.0	~11.5	0.02

Table 6.3: The simulated neutron decay modes. E_γ , E_p , and E_n are kinetic energies for the de-exciting γ -ray, proton, and neutron, respectively, in units of MeV. B is the branching ratio for the decay mode [162].

for invisible mode proton decay, $\tau_p > 2.1 \times 10^{29}$ years, and the limit set by KamLAND for invisible mode neutron decay, $\tau_n > 5.8 \times 10^{29}$ years, SNO+ should expect at most 795 proton decays and 288 neutron decays per year. These events have been simulated and are shown in Figure 6.3. Due to the branching ratios of observable signatures and the fiducial volume cut, SNO+ expects to observe at most 447 proton decays and 173 neutron decays per year. In the 5.5-10 MeV range, where backgrounds are lower (see Section 6.4), at most 191 proton decays and 61 neutron decays per year are expected.

6.4 Backgrounds

Backgrounds that need to be considered for an invisible mode nucleon decay study, during the water phase of SNO+, are: internal and external radioactive decays; solar neutrino interactions; anti-neutrino interactions from nearby nuclear reactors; and instrumental backgrounds. The following sections detail the calculations for the expected background rates from each source.

Internal Backgrounds

The radioactive background from the internal H₂O is caused by the Uranium 238 (²³⁸U) and Thorium 232 (²³²Th) chains (see Chapter 2.7 for details).

The half-life of ²³⁸U is 4.47×10^9 years and decays 100% of the time to Bismuth 214 (²¹⁴Bi), which occurs toward the end of the decay chain. ²¹⁴Bi is a short lived isotope (half-life 19.9 minutes) and decays 99.979% of the time via $\beta\gamma$ emission with a Q-value of 3.27 MeV. ²¹⁴Bi is the main concern of the ²³⁸U chain due to the distance the high energy gammas can travel [163]. The alternative α -decay, and the subsequent β -decay of ²¹⁰Tl with 5.48 MeV Q-value are not simulated because the number of events is approximately four orders of magnitude lower.

The half-life of ²³²Th is 1.4×10^{10} years and decays approximately 36% of the time to Thallium 208 (²⁰⁸Tl), which occurs toward the end of the decay chain. ²⁰⁸Tl is a

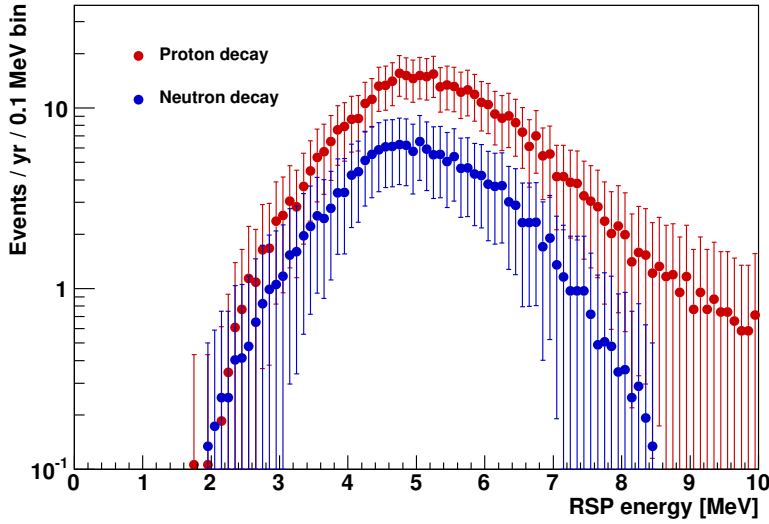


Figure 6.3: Maximum possible energy spectra for invisible mode proton and neutron decay in one year at the current limits set by SNO and KamLAND respectively with a fiducial volume cut applied.

short lived isotope (half-life 3 minutes) and decays via β -decay to a 2.614 MeV excited state of ^{208}Pb which de-excites to its ground state by emission of a 2.614 MeV γ . ^{208}Tl has a Q-value of 5.00 MeV and produces other lower energy gammas and betas up to a maximum of 1.8 MeV [90] but the 2.614 MeV gamma is the main concern due to the distance it can travel.

It is assumed here that the radio-purity levels for internal H_2O will be equivalent to the target levels of the Te-loaded liquid scintillator (see Table 2.2). That gives a purity of $3.5 \times 10^{-14} \text{ g } ^{238}\text{U}/\text{g H}_2\text{O}$ and $3.5 \times 10^{-15} \text{ g } ^{232}\text{Th}/\text{g H}_2\text{O}$.

There are 904 tonnes of H_2O inside the AV, so there are: 1.33×10^{-7} moles or 8.00×10^{16} atoms of ^{238}U ; and 1.36×10^{-8} moles or 8.21×10^{15} atoms of ^{232}Th .

This results in 1.24×10^7 decays/year from ^{214}Bi and 1.46×10^5 decays/year from ^{208}Tl . Simulations show that SNO+ expects to observe 9.55×10^4 of the ^{214}Bi decays/year and 1.02×10^4 of the ^{208}Tl decays/year within the fiducial volume. The results of these simulations are shown in Figure 6.4. In the 5.5-10 MeV range 0.0 ^{214}Bi decays/year and 1.7 ^{208}Tl decays/year are expected.

6.4.1 External Backgrounds

External backgrounds are expected from the internal calibration ropes, the hold-down ropes, hold-up ropes, water shielding, the acrylic vessel as well as dust on its inner and outer surface, and the PMTs. The internal calibration ropes, and acrylic vessel dust layers have not been simulated because of the very low number of events, and neither

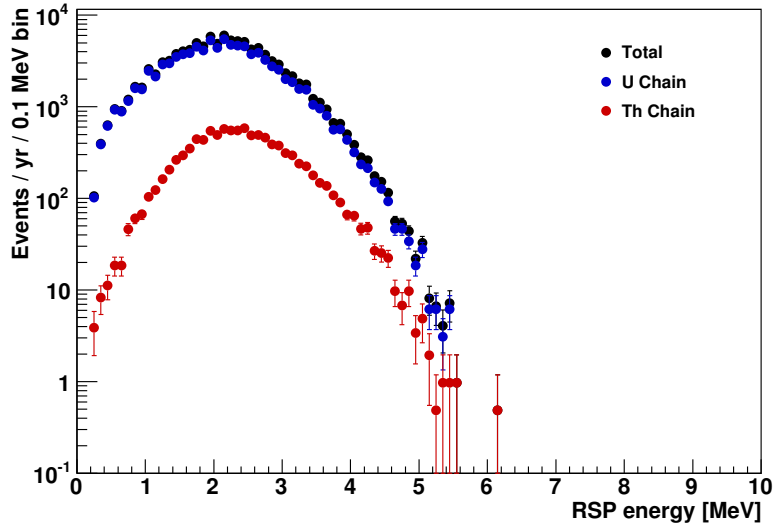


Figure 6.4: Expected energy spectrum from the ^{238}U and ^{232}Th decay chains within the internal H_2O over one year and with a fiducial volume cut applied.

have any isotopes other than ^{214}Bi or ^{208}Tl . The majority of external backgrounds will be excluded by setting the radius of the fiducial volume to 5.5 m.

6.4.1.1 Acrylic Vessel, Hold-down Ropes, and Hold-up Ropes

The acrylic vessel has a mass of 32.53 tonnes and a purity of $1.0 \times 10^{-12} \text{ g } ^{238}\text{U}/\text{g}$ and $1.0 \times 10^{-12} \text{ g } ^{232}\text{Th}/\text{g}$ [164]. This results in 1.28×10^7 decays/year from ^{214}Bi and 1.50×10^6 decays/year from ^{208}Tl .

The hold-down rope net is made from 222.09 kg of Tensylon. Measurements made with the underground germanium detector resulted in radioactivity estimates of $0.58 \pm 0.40 \text{ Bq/kg}$ of ^{214}Bi and $0.33 \pm 0.15 \text{ Bq/kg}$ of ^{208}Tl [163]. The corresponding purity levels are $4.7 \times 10^{-11} \text{ g } ^{238}\text{U}/\text{g}$ and $2.27 \times 10^{-10} \text{ g } ^{232}\text{Th}/\text{g}$. This results in 4.06×10^6 decays/year from ^{214}Bi and 2.32×10^6 decays/year from ^{208}Tl .

The hold-up ropes are made from 45.7 kg of Tensylon [165]. Assuming the same radioactivity levels as the hold-down ropes gives 8.34×10^5 decays/year from ^{214}Bi and 4.78×10^5 decays/year from ^{208}Tl .

Simulations show that SNO+ expects to observe 1.19×10^4 ^{214}Bi decays/year and 1.66×10^4 ^{208}Tl decays/year from the AV, hold-down ropes, and hold-up ropes within the fiducial volume. The results of these simulations are shown in Figure 6.5. In the 5.5-10 MeV range 0.0 ^{214}Bi decays/year and 1.2 ^{208}Tl decays/year are expected.

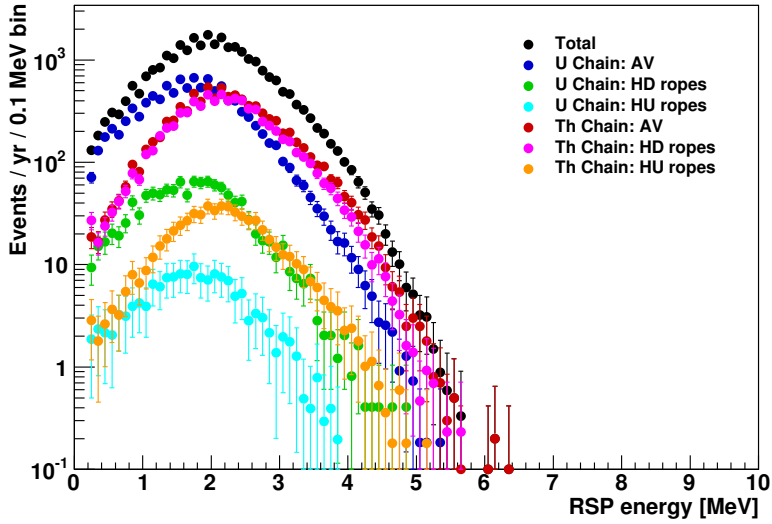


Figure 6.5: Expected energy spectrum from the ^{238}U and ^{232}Th decay chains within the AV, hold-down ropes, and hold-up ropes over one year and with a fiducial volume cut applied.

6.4.1.2 Water Shielding and PMTs

The number of events expected in the water shielding were calculated [165] assuming radio-purity levels measured during the salt phase of SNO [166]. The radio-purity may be improved as there have since been upgrades to the water purification system; this is therefore a conservative estimate.

The water shielding has a mass of 1634 tonnes and a purity of $2.06 \times 10^{-13} \text{ g } ^{238}\text{U/g H}_2\text{O}$ and $5.2 \times 10^{-14} \text{ g } ^{232}\text{Th/g H}_2\text{O}$. This results in 1.32×10^8 decays/year of ^{214}Bi and 3.92×10^6 decays/year of ^{208}Tl .

The 9456 PMTs of SNO+ contain $100 \mu\text{g/PMT}$ of ^{238}U and $100 \mu\text{g/PMT}$ of ^{232}Th . This results in 3.7×10^{11} ^{214}Bi decays/year from the ^{238}U chain and 4.4×10^{10} ^{208}Tl decays/year from the ^{232}Th chain.

The probability that the high energy γ s will travel far enough into the detector, or that these events will mis-reconstruct inside a fiducial volume of 5.5 m, is very low and it is impractical to simulate enough events to get an accurate understanding of how often this occurs. It has therefore been decided in this analysis to use the calibrations calculated for SNO in these regions [167]. The energy spectrum ($E > 4.5 \text{ MeV}$) of the water shielding $\beta\gamma$ background is approximated by a Gaussian with $\mu = 1.416 \text{ MeV}$ and $\sigma = 0.960 \text{ MeV}$. The energy spectrum ($E > 4.5 \text{ MeV}$) of the PMT $\beta\gamma$ background is approximated by a Gaussian with $\mu = 3.441 \text{ MeV}$ and $\sigma = 0.4617 \text{ MeV}$. The number of events in the Cherenkov tail background ($E > 5.5 \text{ MeV}, R < 5500 \text{ mm}$) was estimated to be $2.8_{-2.8}^{+3.9}$ from the water shielding, and $16.0_{-7.2}^{+10.5}$ from the PMTs over a live-time

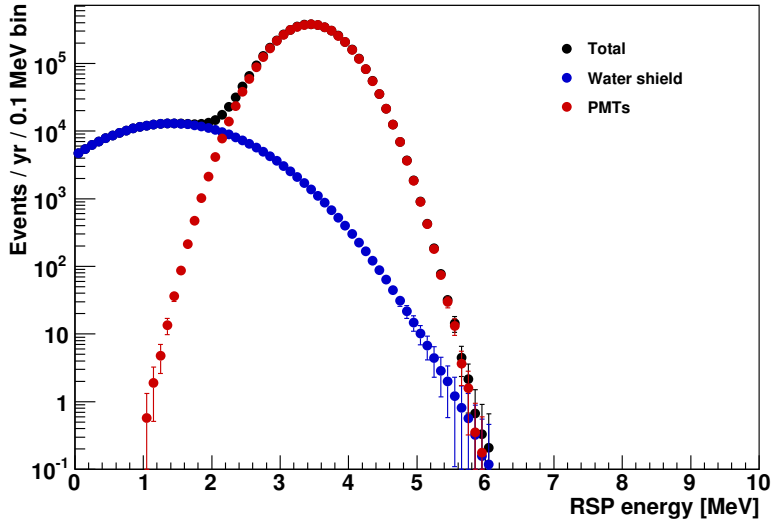


Figure 6.6: Expected energy spectrum from the ^{238}U and ^{232}Th decay chains within the external H_2O and PMTs over one year and with a fiducial volume cut applied.

of 306.39 days. Figure 6.6 shows the background energy spectra from the PMTs and water shielding extrapolated down to 0 MeV for 1 year.

6.4.2 Solar Neutrinos

Solar ^8B and hep neutrinos contribute to the neutrino flux in the ROI of invisible mode nucleon decay. The ^8B neutrino flux is approximately three orders of magnitude greater than the hep neutrino flux, however, and therefore the only component of solar neutrino flux simulated for this analysis.

The currently preferred Standard Solar Model, BS05(OP) [168], predicts a ^8B solar neutrino flux of $5.69 \times 10^6 \text{ cm}^{-2} \text{ s}^{-1}$ [32]. The SNO+ Monte Carlo simulation software combines this with a normalisation of the table of the ^8B neutrino spectrum provided by Winter et al. [169] to obtain the expected flux across energies.

The elastic-scattering neutrino cross-section is approximated by Bahcall et al. [170] to be

$$\sigma(q) = \text{constant} \times \left(\frac{q}{10 \text{ MeV}} \right) \times 10^{-44} \text{ cm}^2, \quad (6.1)$$

where the constant is 9.2 for ν_e scattering and 1.6 for ν_μ scattering. The elastic-scattering cross-section is multiplied by the ^8B neutrino spectrum to give a rate of 9.93×10^{-30} interactions per year per target electron. There are approximately 3.02×10^{32} electrons in the detector, resulting in 3.0×10^3 interactions per year assuming no neutrino oscillations. Simulations show that SNO+ would expect to observe 1.22×10^3 of these interactions within the fiducial volume. The ^8B solar neutrino flux was simulated for both electron neutrinos and oscillated muon neutrinos.

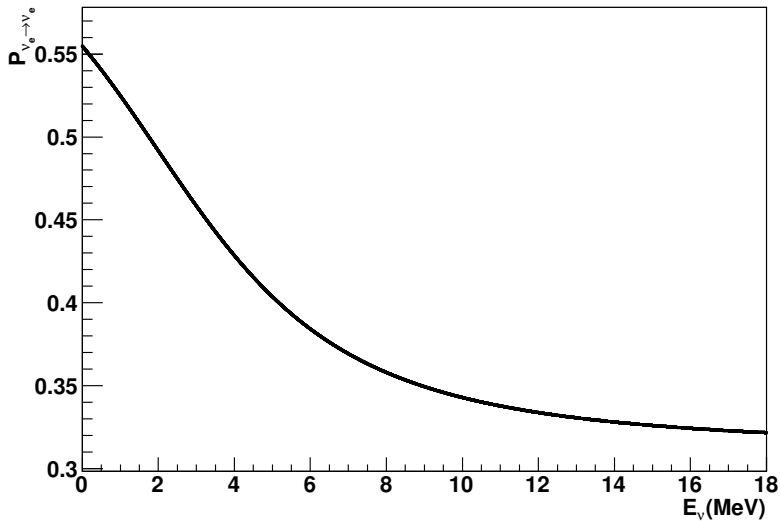


Figure 6.7: The survival probability of ${}^8\text{B}$ neutrinos at the surface of the Sun as a function of energy for the BS05(OP) solar model using a three-flavour adiabatic approximation. The oscillation parameters used were $\tan^2(\theta_{12}) = 0.469$, $\Delta m_{12}^2 = 7.9 \times 10^{-5} \text{ eV}^2$, $\sin^2(\theta_{13}) = 0.01$, and $\Delta m_{13}^2 = 2.46 \times 10^{-3} \text{ eV}^2$ [171].

Oscillations, including matter effects, were applied using a three-flavour adiabatic approximation with higher order corrections [171]. The survival probability used is shown in Figure 6.7, which was calculated for ${}^8\text{B}$ neutrinos without matter effects in Earth. The curve would have a different shape for neutrinos produced by different reactions due to the production region in the Sun. The curve would also have a different shape if Earth matter effects were included; incorporating matter effects for the average distance travelled through Earth over the live-time would improve the oscillation accuracy. After applying neutrino oscillations the number of interactions observed drops to 566 interactions per year, 249 of which are within the 5.5-10 MeV range.

The solar neutrino background may be significantly reduced by applying a cut on events with $\cos \theta > 0.8$ relative to the solar neutrino direction, with a corresponding loss of 10% for all other backgrounds as well as any signal. This is more than compensated for by the $\approx 80\%$ reduction in solar neutrino background. After applying a direction cut 48 events are expected in the 5.5-10 MeV range. Figure 6.8 shows the energy spectrum expected from simulations of ${}^8\text{B}$ solar neutrinos, before and after applying oscillations and a direction cut.

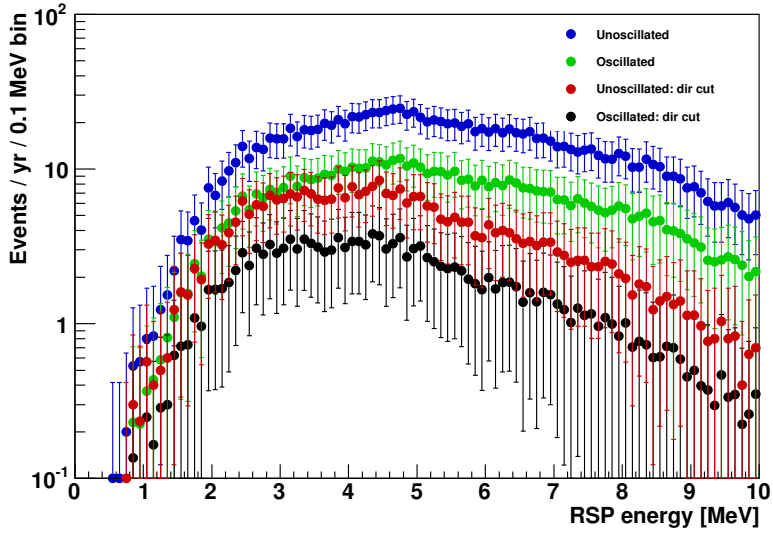


Figure 6.8: Expected energy spectrum from the ${}^8\text{B}$ solar neutrinos over one year with a fiducial volume cut applied. The spectrum is shown before and after applying neutrino oscillations and a direction cut.

6.4.3 Reactor Anti-Neutrinos

Anti-neutrinos with an energy above the threshold of 1.8 MeV cause charged current interactions with the protons in the water, producing positrons and neutrons,

$$\bar{\nu}_e + p \rightarrow e^+ + n. \quad (6.2)$$

The signal for these reactor anti-neutrino interactions comprises a prompt part from the positron and a delayed part from neutron capture (resulting in the emission of a 2.2 MeV gamma) [172]. Double events are therefore typical for anti-neutrinos. It may be possible to tag reactor neutrino events using this double event signature, although difficult because of low numbers of PMT hits and high backgrounds in the energy spectrum [172]. This analysis assumes no tagging of reactor anti-neutrinos.

The reactor anti-neutrino background was estimated with a flux of 3.0×10^5 per cm^2 per second above threshold [173]. This figure was then normalised using the flux spectrum given by C. Bemporad et al. [33].

The total cross-section for inverse beta-decay is [174]

$$\sigma_{tot} = 0.0952 \times \left(\frac{E_e p_e}{1 \text{ MeV}^2} \right) \times 10^{-42} \text{ cm}^2, \quad (6.3)$$

where $E_e = E_{\bar{\nu}} - (M_n - M_p)$ is the positron energy, $p_e = \sqrt{E_e^2 - m_e^2}$ is the positron momentum, $E_{\bar{\nu}}$ is the anti-neutrino energy, and the neutron, proton and electron masses are M_n , M_p and m_e respectively. This cross-section was convolved with the anti-neutrino flux to give a rate of approximately 9.23×10^{-38} interactions per proton per second.

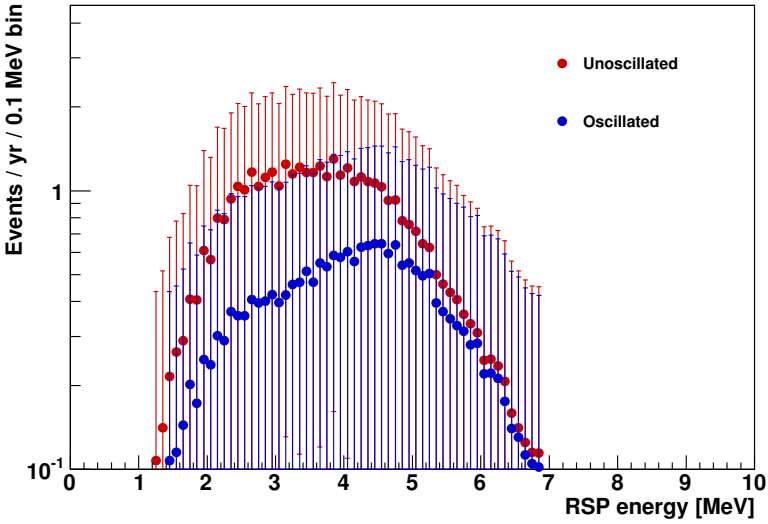


Figure 6.9: Expected energy spectrum from the reactor neutrinos over one year with a fiducial volume cut applied. The spectrum is shown before and after applying neutrino oscillations.

Interactions with the oxygen atoms can be neglected due to Pauli-blocking. There are 6.05×10^{31} protons from the hydrogen atoms inside the water-filled detector, resulting in 176 anti-neutrino interactions each year, assuming no neutrino oscillations. This figure is comparable to the 180 events per 10^{32} protons per year calculated independently for SNO+ [175]. Simulations show that SNO+ would expect to observe 41 of these interactions within the fiducial volume.

Neutrino oscillations were applied using a Monte Carlo processor which randomly applies oscillations using the two-flavour scenario. The ν_e survival probability in the two flavour scenario is,

$$P_{\nu_e \rightarrow \nu_e} = 1 - \sin^2(2\theta) \sin^2 \left(\frac{1.267^3 \Delta m^2 L}{E_\nu} \right), \quad (6.4)$$

and the oscillation parameters used were $\sin^2(2\theta) = 0.861$ and $\Delta m^2 = 7.59 \times 10^{-5} \text{ eV}^2$. Baseline, L , units are km and neutrino energy, E_ν , units are MeV. The processor randomly selects which reactor the neutrino came from based on the expected flux, and sets the baseline accordingly. In this analysis just the closest reactor, Bruce, with a baseline of 240.2 km was used. This reduces the number of neutrino interactions within the fiducial volume to 22 interactions per year. In the 5.5-10 MeV range 3.5 interactions are expected per year. Figure 6.9 shows the energy spectrum expected from simulations of reactor neutrinos, before and after applying oscillations.

6.4.4 Instrumental background

Instrumental backgrounds are events caused by the detector and its read-out system, not from radioactive decays; see Chapter 5 for details. The dominant source of instrumental background is from events known as “flashers”. Flashers are hypothesised to be caused by photons emitted from PMTs operating under high voltage, perhaps due to a spark in the dynode stack. See Section 5.1.1 for details.

Flashers were excluded from SNO analyses using a suite of cuts targeting their event signature. Events in the SNO data set, identified as flashers by these cuts, could be used to obtain an N_{hit} distribution for flasher-type instrumental backgrounds. This distribution could then be simulated using the flasher generator (see Section 5.5), and instrumental background cuts applied, to estimate the number of flasher events that will act as a background to an invisible mode nucleon decay signal (see Section 5.6). The same instrumental background cuts are applied to the radiative backgrounds and simulated nucleon decay signal. See Section 5.4 for the estimated loss of physics signatures as a result of applying these instrumental cuts.

Figure 5.32 shows the energy spectrum for flasher-type instrumental background assuming photons are emitted with a 6000 K blackbody spectrum. There are 105.0 background events expected above 5.5 MeV within a fiducial volume of 5.5 m. Higher level cuts designed to identify physics events, such as event isotropy or hit time cuts, have not been applied at this stage.

An event isotropy classifier which calculates a parameter β_{14} , based on the angles of hit PMTs to the event vertex, can be used to identify Cherenkov events (see Section 5.3.1). Figure 6.10 compares the β_{14} parameter for nucleon decay events to simulated flashers. It can be seen that cutting events with $\beta_{14} > 0.9$ reduces instrumental backgrounds by $\approx 52\%$, while retaining 99% of the nucleon decay signal.

A cut based on the ratio of N_{prompt} to N_{hits} may also be used to distinguish radiative and non-radiative events. For SNO this was known as the In-Time Ratio (ITR) cut (see Section 5.3.2). Figure 6.11 compares the ITR parameter for nucleon decay events to simulated flashers. Cutting events with $\text{ITR} < 0.55$ reduces instrumental backgrounds by a further $\approx 27\%$, while retaining 99% of the nucleon decay signal.

Even with the event isotropy and ITR cuts, 10.5 flasher instrumental background events will still be present in the 5.5–10 MeV energy window. The AMB cut was particularly effective at removing flasher events for SNO, however the AMB board is no longer in place for SNO+. It has been upgraded to the CAEN digitiser which outputs a digital copy of the waveforms of the DAQ trigger signals (see Section 2.3). Cuts based on the CAEN output are currently under development.

Flashers were simulated for this analysis with instantaneous photon emission, rather than a time spread. Consequently, cuts designed to remove events that do not have the prompt signature of Cherenkov events, such as FTS and ITR, will be less effective. This

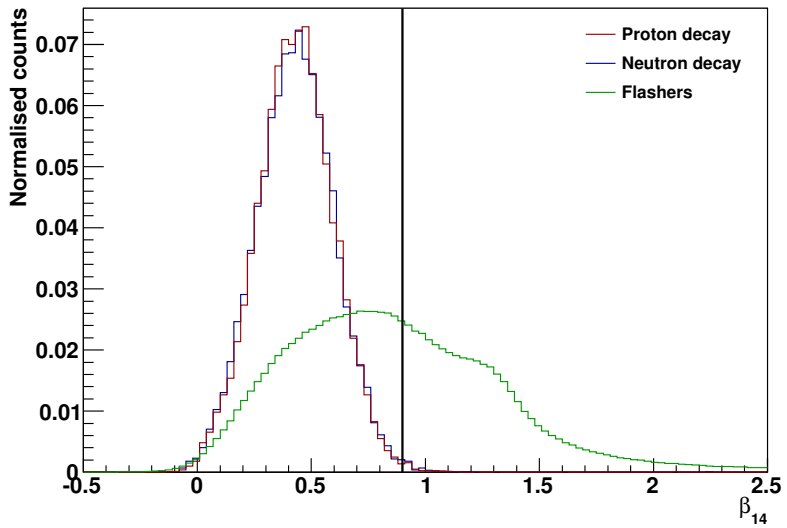


Figure 6.10: Comparison of isotropy parameter β_{14} for simulated nucleon decay signal and flasher instrumental backgrounds. A cut will be made on $\beta_{14} > 0.9$ which is demonstrated by the black line.

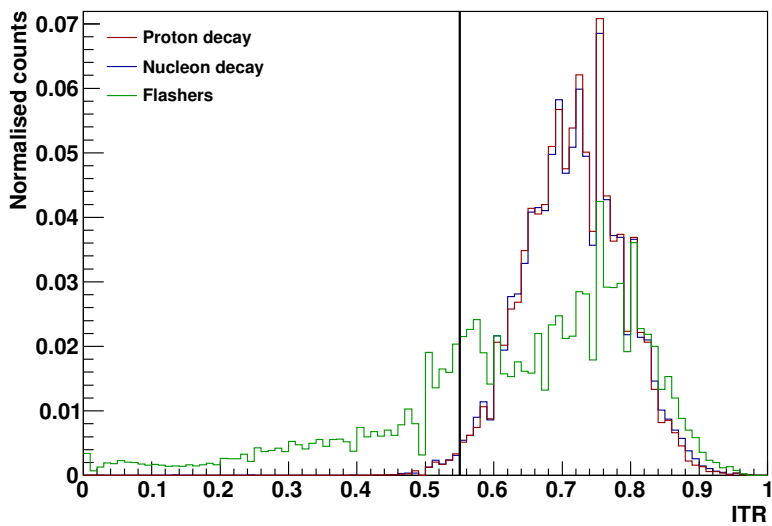


Figure 6.11: Comparison of the in-time ratio (ITR) for simulated nucleon decay signal and flasher instrumental backgrounds. A cut will be made on $ITR < 0.55$ which is demonstrated by the black line.

calculation of the instrumental background is therefore an overestimate. For comparison, SNO estimated a contamination of ≤ 3 events at 95% confidence level upper limit over a live-time of 306.39 days [176].

6.4.5 Summary

The simulated internal and external backgrounds are summarised in Table 6.4. Neither the internal calibration ropes, nor the acrylic vessel dust layers, have been simulated because the expected number of events is relatively low compared to other sources. For the same reason only isotopes ^{214}Bi and ^{208}Tl have been simulated.

Solar neutrino interactions, anti-neutrino interactions from nearby nuclear reactors, and instrumental backgrounds not removed by instrumental cuts are all backgrounds in the ROI of invisible mode nucleon decay.

The solar neutrino background may be significantly reduced by applying a cut on events with $\cos \theta > 0.8$ relative to the solar neutrino direction, with a corresponding loss of 10% for all other backgrounds as well as any signal. This is more than compensated for by the $\approx 80\%$ reduction in solar neutrino background.

Some instrumental backgrounds passing data cleaning cuts and a fiducial volume cut of 5.5 m reconstruct within the ROI of invisible mode nucleon decay. These are reduced by applying higher level cuts, which further has the effect of cutting events which mis-reconstruct because timing residuals are less likely to be within the prompt window. In the future also using cuts developed for CAEN traces will further reduce their contamination. The flasher instrumental background contamination shown here is an overestimate because they are not simulated with a time spread, so cuts designed to remove non-prompt events are less effective.

Given the limit set by SNO for invisible mode proton decay, $\tau_p > 2.1 \times 10^{29}$ years, and the limit set by KamLAND for invisible mode neutron decay, $\tau_n > 5.8 \times 10^{29}$ years, SNO+ should expect at most 795 proton decays and 288 neutron decays to occur per year. These events have been simulated and the observable decays are shown in Figures 6.12-6.13 for comparison with the expected backgrounds. Energies were estimated with the RSP algorithm and scenarios both with and without the direction cut are shown; it can be seen that there is greater signal detection potential with a direction cut.

The expected backgrounds per year from 5.0, 5.5, and 6.0 MeV up to 10.0 MeV are shown in Table 6.5. The efficiencies for detecting invisible mode proton or neutron events are also shown; these are the fraction of simulated events that trigger the detector and are reconstructed within the relevant energy windows. The figures quoted are with the direction cut. For comparison, the equivalent values using the Prompt Lookup method to estimate event energy are shown in Table 6.6.

Source	Mass	Isotope	Activity	Decays/year
Internal water	904 t	^{214}Bi	$3.5 \times 10^{-14} \text{ g}^{238}\text{U/g}$	1.24×10^7
		^{208}Tl	$3.5 \times 10^{-15} \text{ g}^{232}\text{Th/g}$	1.46×10^5
Hold-down ropes	222.09 kg	^{214}Bi	$4.7 \times 10^{-11} \text{ g}^{238}\text{U/g}$	4.06×10^6
		^{208}Tl	$2.27 \times 10^{-10} \text{ g}^{232}\text{Th/g}$	2.32×10^6
Hold-up ropes	45.7 kg	^{214}Bi	$4.7 \times 10^{-11} \text{ g}^{238}\text{U/g}$	8.34×10^5
		^{208}Tl	$2.27 \times 10^{-10} \text{ g}^{232}\text{Th/g}$	4.78×10^5
Water shielding	1634 t	^{214}Bi	$2.06 \times 10^{-13} \text{ g}^{238}\text{U/g}$	1.32×10^8
		^{208}Tl	$5.2 \times 10^{-14} \text{ g}^{232}\text{Th/g}$	3.92×10^6
Acrylic vessel	32.53 t	^{214}Bi	$1.0 \times 10^{-12} \text{ g}^{238}\text{U/g}$	1.28×10^7
		^{208}Tl	$1.0 \times 10^{-12} \text{ g}^{232}\text{Th/g}$	1.5×10^6
PMTs	9456 units	^{214}Bi	$1.0 \times 10^{-4} \text{ g}^{238}\text{U/PMT}$	3.7×10^{11}
		^{208}Tl	$1.0 \times 10^{-4} \text{ g}^{232}\text{Th/PMT}$	4.4×10^{10}

Table 6.4: Summary of expected radioactive backgrounds for invisible mode nucleon decay [165].

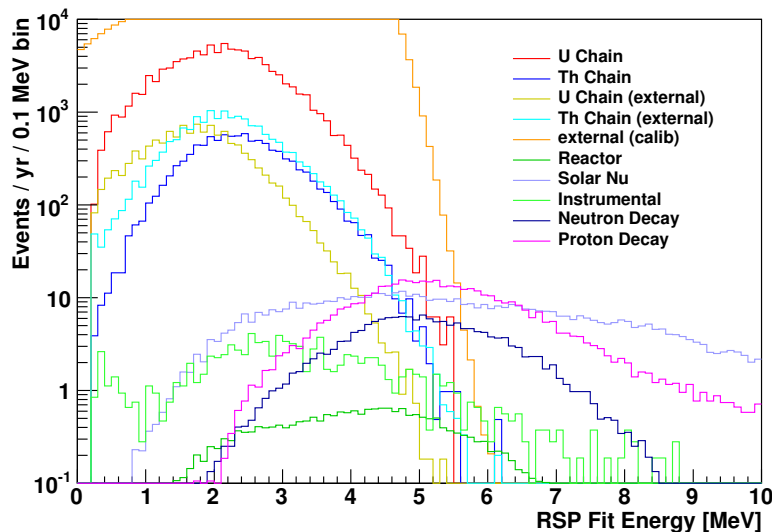


Figure 6.12: Expected water-phase energy spectrum in the region of invisible mode nucleon decay, reconstructed using the RSP method, plotted at the current experimental limit. Backgrounds in the energy range are solar neutrinos, reactor anti-neutrinos, and radioactive decays from the uranium and thorium chains.

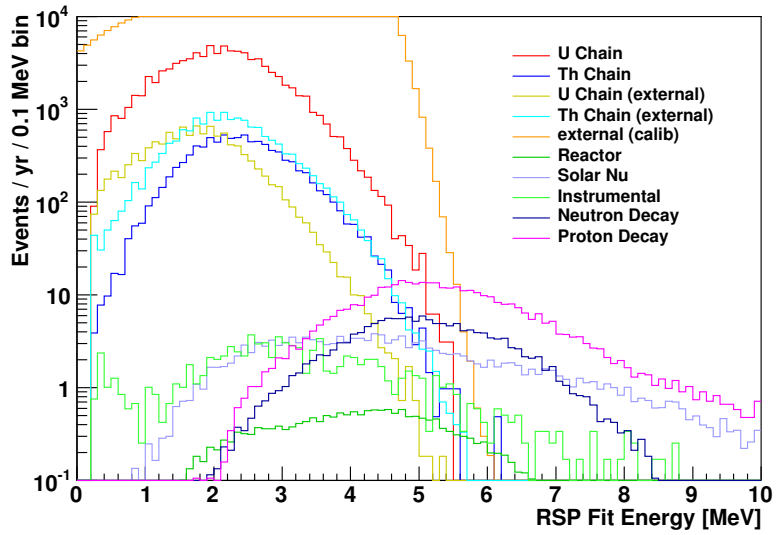


Figure 6.13: Expected water-phase energy spectrum in the region of invisible mode nucleon decay, reconstructed using the RSP method. A direction cut has been applied to reduce the solar neutrino background.

Energy window (MeV)	5.0-10.0	5.5-10.0	6.0-10.0
^{214}Bi internal	46.5 ± 12.0	0.0 ± 0.0	0.0 ± 0.0
^{214}Bi AV	0.5 ± 0.3	0.0 ± 0.0	0.0 ± 0.0
^{214}Bi hdropes	0.0 ± 0.0	0.0 ± 0.0	0.0 ± 0.0
^{214}Bi huropes	0.0 ± 0.0	0.0 ± 0.0	0.0 ± 0.0
^{208}Tl internal	9.7 ± 2.2	1.5 ± 0.8	0.5 ± 0.5
^{208}Tl AV	6.5 ± 0.8	0.8 ± 0.3	0.3 ± 0.2
^{208}Tl hdropes	2.1 ± 0.7	0.2 ± 0.2	0.0 ± 0.0
^{208}Tl huropes	0.2 ± 0.1	0.0 ± 0.0	0.0 ± 0.0
External water	26.5 ± 0.3	3.0 ± 0.1	0.2 ± 0.0
External PMT	1462.0 ± 7.6	17.2 ± 0.8	0.1 ± 0.1
Reactor	5.2 ± 0.1	3.1 ± 0.1	1.7 ± 0.0
Solar	61.0 ± 0.9	48.0 ± 0.8	38.0 ± 0.7
Instrumental	14.5 ± 1.1	9.4 ± 0.9	6.6 ± 0.7
Total	1634.8 ± 14.5	83.2 ± 1.7	47.5 ± 1.2
Efficiency (proton)	0.179 ± 0.002	0.130 ± 0.002	0.089 ± 0.001
Efficiency (neutron)	0.061 ± 0.001	0.041 ± 0.001	0.026 ± 0.000

Table 6.5: Expected backgrounds per year from 5.0, 5.5, and 6.0 MeV up to 10.0 MeV, and the efficiencies for detecting invisible mode proton or neutron decays. The figures quoted are determined using the RSP energy estimator and with a direction cut of $\cos \theta > 0.8$ relative to the solar neutrino direction.

Energy window (MeV)	5.0-10.0	5.5-10.0	6.0-10.0
^{214}Bi internal	46.5 ± 12.0	0.0 ± 0.0	0.0 ± 0.0
^{214}Bi AV	1.6 ± 0.5	0.0 ± 0.0	0.0 ± 0.0
^{214}Bi hdropes	0.4 ± 0.4	0.0 ± 0.0	0.0 ± 0.0
^{214}Bi huropes	0.0 ± 0.0	0.0 ± 0.0	0.0 ± 0.0
^{208}Tl internal	9.2 ± 2.1	1.5 ± 0.8	0.5 ± 0.5
^{208}Tl AV	9.6 ± 1.0	1.2 ± 0.3	0.3 ± 0.2
^{208}Tl hdropes	3.0 ± 0.8	0.2 ± 0.2	0.0 ± 0.0
^{208}Tl huropes	0.3 ± 0.1	0.0 ± 0.0	0.0 ± 0.0
External water	26.5 ± 0.3	3.0 ± 0.1	0.2 ± 0.0
External PMT	1462.0 ± 7.6	17.2 ± 0.8	0.1 ± 0.1
Reactor	5.3 ± 0.1	3.0 ± 0.1	1.5 ± 0.0
Solar	61.9 ± 0.9	47.5 ± 0.8	36.4 ± 0.7
Instrumental	14.5 ± 1.1	9.4 ± 0.9	6.6 ± 0.7
Total	1641.0 ± 14.5	83.0 ± 1.7	45.6 ± 1.2
Efficiency (proton)	0.182 ± 0.002	0.127 ± 0.002	0.081 ± 0.001
Efficiency (neutron)	0.062 ± 0.001	0.040 ± 0.001	0.022 ± 0.000

Table 6.6: Expected backgrounds per year from 5.0, 5.5, and 6.0 MeV up to 10.0 MeV, and the efficiencies for detecting invisible mode proton or neutron decays. The figures quoted are determined using the Prompt Lookup energy estimator and with a direction cut of $\cos \theta > 0.8$ relative to the solar neutrino direction.

6.5 Limit setting

6.5.1 Simple Poisson method

Under the assumption that no signal peak is observed, SNO+ will set a limit on the lifetimes of protons and neutrons under an invisible mode decay hypothesis. The following analysis uses a Poisson method [177, 178] to determine the limit setting potential.

The probability of observing n counts within an energy window is given by the Poisson distribution, with mean $\mu + b$,

$$P(n|\mu) = \frac{(\mu + b)^n e^{-(\mu+b)}}{n!}, \quad (6.5)$$

where μ and b are the expected signal and background respectively. The probability density for μ , which is an unknown quantity, is given by,

$$g(\mu) = N \frac{(\mu + b)^n e^{-(\mu+b)}}{n!}, \quad (6.6)$$

where N is a normalisation constant such that,

$$\int_0^\infty g(\mu) d\mu = 1. \quad (6.7)$$

Assuming no peak is seen in the signal region ($b \cong n$) an upper bound for the number

of observed signal events, S_α , with CL α can be expressed by,

$$\alpha = \int_0^{S_\alpha} g(\mu) d\mu = 1, \quad (6.8)$$

where $\mu \in [0, S_\alpha]$. That is to say with probability α the number of signal events observed is less than S_α , which is found in this analysis by numerically solving Equation 6.8. The desired confidence level for this analysis is 90% ($\alpha = 0.9$). As data is not currently available a mean upper limit, $\overline{S_{90\%}}$, is calculated for different observed events, n ,

$$\overline{S_{90\%}} = \sum_n S_{90\%}(n, b) P(n, b). \quad (6.9)$$

The corresponding upper bound on the rate of gammas emitted into the detector from invisible mode decays is given by [90],

$$R < \frac{\overline{S_{90\%}}}{\epsilon f_T}, \quad (6.10)$$

where ϵ is the efficiency of detecting the gamma ray within the energy window, and f_T is the live-time as a fraction of a year.

A bound can then be set for the lifetime, τ , of invisible mode decays using the equation [90],

$$\tau > \frac{N_{\text{nuc}}}{R}. \quad (6.11)$$

where N_{nuc} is the number of nucleons.

For the calculations of the limits given in Table 6.7 the live-time was estimated to be three months, and, as calculated in Section 6.3 the number of nucleons, N_{nuc} , is 2.41×10^{32} . RSP was used to estimate the energy, and the limits are not presented for the energy window 5.0-10.0 MeV as the expected background rate is prohibitively high. For comparison, Table 6.8 shows the limits calculated with the Prompt Lookup method used to estimate event energy. For the 5.5-10.0 MeV energy window there is less than 4% difference in the lifetime lower bound, and less than 10% for the 6.0-10.0 MeV energy window.

After three months of running SNO+ can expect to set a lower limit of 1.4×10^{30} years for the lifetime of the proton, and 1.2×10^{30} years for the neutron, to decay via an invisible mode. These lifetimes assume an RSP estimated event energy window of 5.5 to 10.0 MeV, that a cut has been made on event direction relative to the solar neutrino direction, instrumental background cuts have been applied, as well as event isotropy and ITR cuts. It is further assumed that no signal has been observed. These limits represent a factor of 6.6 improvement over the current best limit set by SNO for invisible mode proton decay, and a factor of 2.1 improvement over the limit set by KamLAND for the neutron.

Energy window (MeV)	5.5-10.0	6.0-10.0
Background	20.8	11.9
$S_{90\%}$	9.4	7.5
R_p	174.5	203.6
R_n	198.6	256.2
τ_p (10^{29} yr)	13.8	11.8
τ_n (10^{29} yr)	12.1	9.4

Table 6.7: Lower bounds for the lifetimes of invisible mode proton, p , and neutron, n , decays (at 90% CL) set by the simple Poisson method for energy windows of 5.5 and 6.0 to 10.0 MeV, using the RSP energy estimation algorithm. Also shown are the expected backgrounds and the upper bounds on the number of signal events, $S_{90\%}$, after three months of running, and the corresponding nucleon decay rates, $R_{p,n}$. Quoted values are with a direction cut applied to reduce the solar neutrino background and isotropy and instrumental cuts to reduce instrumental backgrounds.

Energy window (MeV)	5.5-10.0	6.0-10.0
Background	20.7	11.4
$S_{90\%}$	9.4	7.1
R_p	178.6	212.7
R_n	206.1	280.3
τ_p (10^{29} yr)	13.5	11.3
τ_n (10^{29} yr)	11.7	8.6

Table 6.8: Lower bounds for the lifetimes of invisible mode proton, p , and neutron, n , decays (at 90% CL) set by the simple Poisson method for energy windows of 5.5 and 6.0 to 10.0 MeV, using the Prompt Lookup energy estimation algorithm. Also shown are the expected backgrounds and the upper bounds on the number of signal events, $S_{90\%}$, after three months of running, and the corresponding nucleon decay rates, $R_{p,n}$. Quoted values are with a direction cut applied to reduce the solar neutrino background and isotropy and instrumental cuts to reduce instrumental backgrounds.

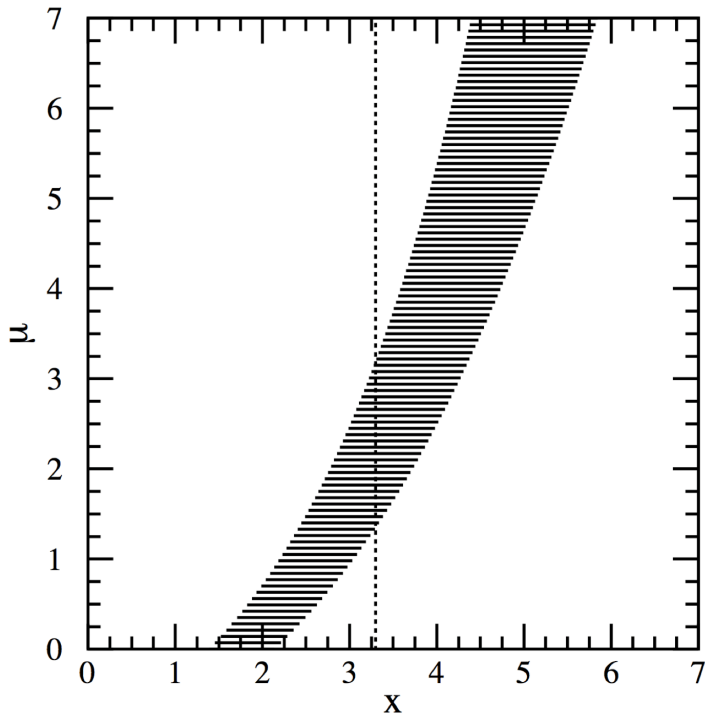


Figure 6.14: A generic confidence belt construction. For each signal mean, μ a horizontal acceptance interval $[x_1, x_2]$ is constructed such that $P(x \in [x_1, x_2]|\mu) = \alpha$. An experiment that measures x_0 (dashed line) can define a confidence interval $[\mu_1, \mu_2]$ as all the μ values with an acceptance interval including x_0 [179].

An alternative method that can be used if a signal peak is observed constructs a confidence belt using central confidence intervals, i.e.

$$P(\mu < \mu_1) = P(\mu > \mu_2) = (1 - \alpha)/2. \quad (6.12)$$

This is done by using Neyman's construction [179] in which first confidence intervals in n , with probability α , are calculated for each possible value of μ . Given an observation of n_0 events, all μ values that have n_0 in their confidence intervals then go into the confidence interval for n_0 . Figure 6.14 shows how such a confidence belt is constructed, where measured value $x \equiv n$. This method also provides a subtly different way of calculating the upper limit in the event that no signal peak is observed by using upper confidence limits instead of central confidence intervals, i.e.

$$P(\mu > \mu_2) = 1 - \alpha. \quad (6.13)$$

A difficulty with the aforementioned methods is the need to decide whether to use upper confidence limits or central confidence intervals. This is a human choice influenced by data that requires *a priori* knowledge of the outcome. If the wrong decision is made this may result in under-coverage i.e. not providing the required confidence level. There is a further problem for the observation of low numbers of

events as the resulting confidence interval can be the empty set. Consequently it would not be the recommendation of this author to use this method for nucleon decay analysis.

6.5.2 Feldman-Cousins method

The Feldman-Cousins technique [179] solves the previously mentioned issues with the simple Poisson method. It provides a way of constructing a confidence interval that is not influenced by human decision and has no issues with under-coverage.

In this instance the method is also applied for a Poisson process, with probability, $P(n|\mu)$, of observing total events, n , given a signal with mean μ , which is expressed by Equation 6.5.

As for the belt construction technique demonstrated by Figure 6.14, for each μ value a confidence interval is calculated in n . To do this for a given value of μ , a ratio, R , is calculated for each integer value of n ,

$$R = \frac{P(n|\mu)}{P(n|\mu_{\text{best}})}, \quad (6.14)$$

where μ_{best} is the non-negative value of μ which maximises $P(n|\mu)$.

The technique then ranks the R values in decreasing order of size. Values of n are added to the confidence region, starting with the highest rank, until the desired confidence level is reached, i.e. $n \in [n_1, n_2]$ such that

$$\alpha < \sum_{n=n_1}^{n=n_2} P(n|\mu). \quad (6.15)$$

This guarantees over-coverage which is an unavoidable feature of the method. In the case of this analysis, the acceptance regions were calculated by computer for all values of μ in the range $[0, 500]$ in 0.005 interval steps. This gives 0.01 level precision.

An experiment observing n_0 events selects all values of μ whose acceptance region includes n_0 to define a confidence belt, $\mu \in [\mu_1, \mu_2]$. An example confidence belt construction is shown in Figure 6.15. For small values of n the confidence belt sets an upper limit and, as n increases, a non-zero lower limit is introduced. Thus, the technique avoids the need to choose a confidence interval type, required by the simple Poisson method.

The mean upper limit, $\overline{\mu}_2$, is calculated for different observed events, n ,

$$\overline{\mu}_2 = \sum_n^{\mu_1=0} \mu_2(n, b) P(n, b), \quad (6.16)$$

assuming that the lower limit, μ_1 is found to be zero. With a mean upper limit determined, the method then proceeds as for simple Poisson using Equations 6.10 and 6.11 (where $\overline{\mu}_2 \equiv \overline{S}_{90\%}$) to obtain a lower limit on the lifetime, τ , for invisible mode proton and neutron decays. If a non-zero lower limit, μ_1 , was returned by the Feldman-Cousins technique then there is evidence for nucleon decay at the α confidence level.

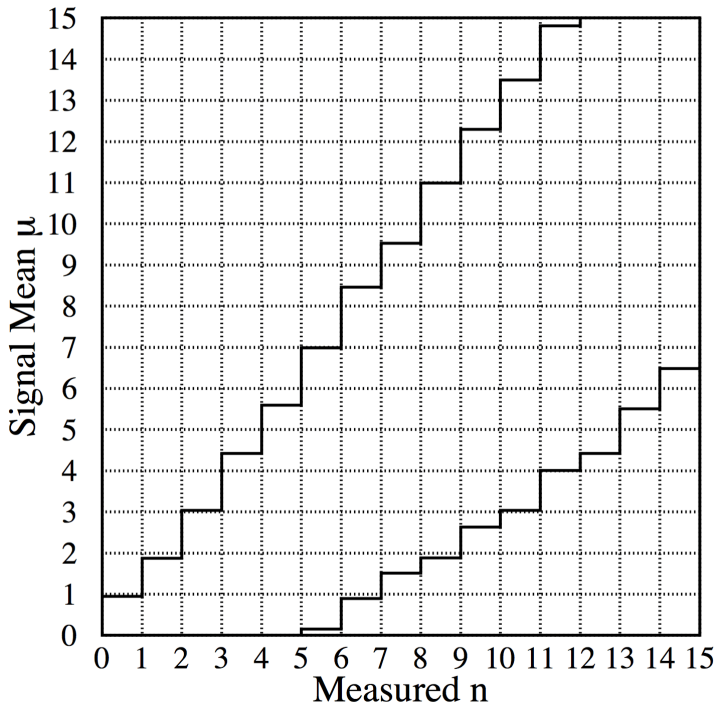
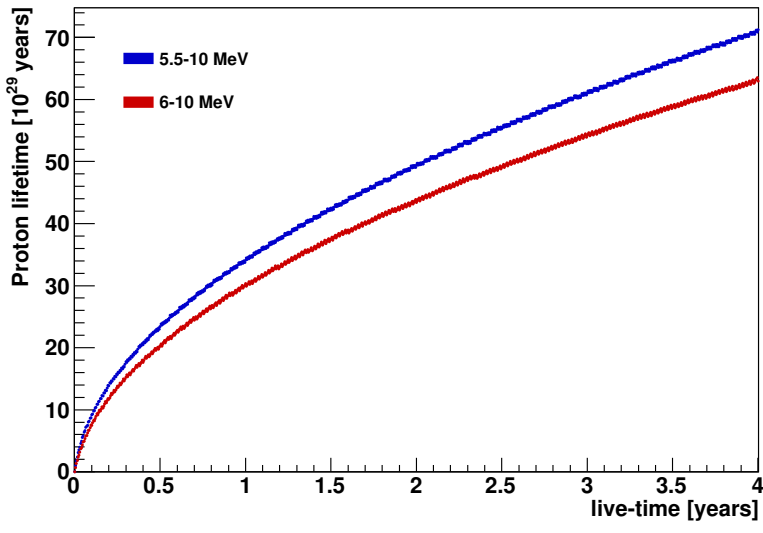


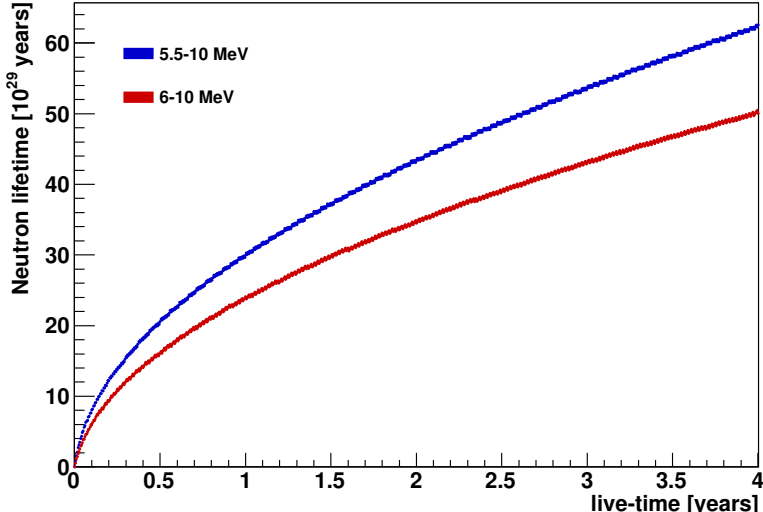
Figure 6.15: Example confidence belt using the Feldman-Cousins ordering principle [179].

The lower bound on the lifetime that may be set by SNO+ at different live-times is shown in Figure 6.16a for proton decay and Figure 6.16b for neutron decay. RSP has been used to estimate the energy. The lower limits are compared for the energy ranges 5.5-10 MeV and 6-10 MeV, showing that a better limit can be set by using the 5.5-10 MeV range. For comparison, Figure 6.17 shows the limit that may be set using the Prompt Lookup method to estimate event energy.

Table 6.9 shows the lower limits that may be set by SNO+ for the lifetimes of protons and neutrons to undergo invisible mode decay assuming a live-time of three months. Compared to the simple Poisson method, there is a decrease in the upper limit, $\overline{S}_{90\%}$, which becomes less conservative. Correspondingly there is an increase in the resultant lower bound on proton lifetime to 1.6×10^{30} years, and 1.4×10^{30} years for the neutron, to decay via an invisible mode. These lifetimes assume an RSP estimated event energy window of 5.5 to 10.0 MeV, that a cut has been made on event direction relative to the solar neutrino direction, instrumental background cuts have been applied, as well as event isotropy and ITR cuts. It is further assumed that no signal has been observed. These limits represent a factor of 7.5 improvement over the current best limit set by SNO for invisible mode proton decay, and a factor of 2.4 improvement over the limit set by KamLAND for the neutron. For comparison, Table 6.10 shows the limits calculated with the Prompt Lookup method used to estimate event energy. For the 5.5-10.0 MeV

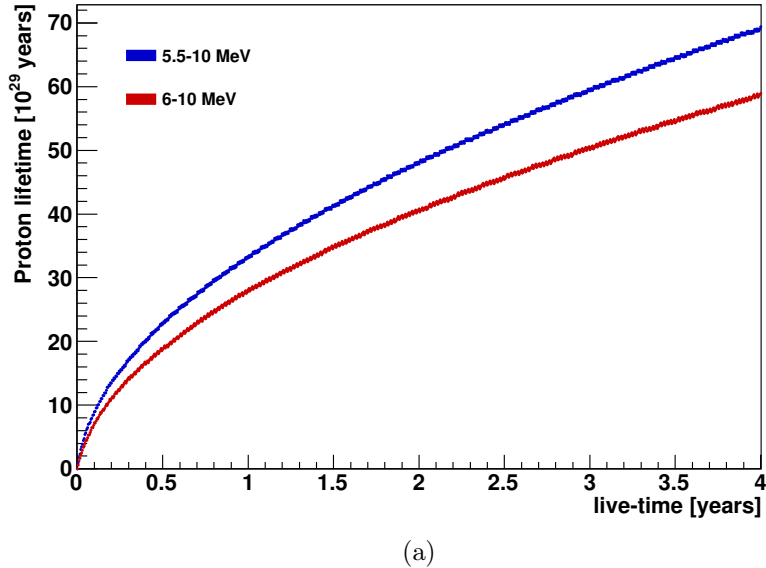


(a)

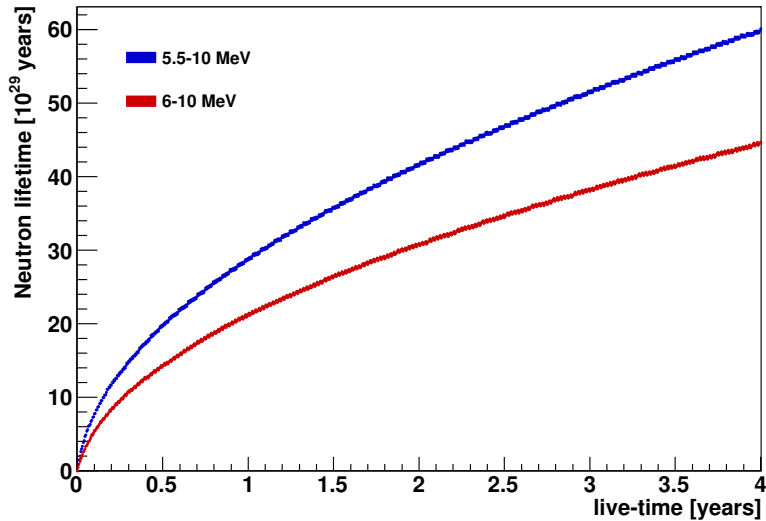


(b)

Figure 6.16: Lower bounds for the lifetimes of invisible mode proton (a) and neutron (b) decays (at 90% CL) vs live-time set by the Feldman-Cousins method for energy windows of 5.5 and 6.0 to 10.0 MeV, using the RSP energy reconstruction algorithm. Calculations include a direction cut to reduce the solar neutrino background and isotropy and instrumental cuts to reduce instrumental backgrounds.



(a)



(b)

Figure 6.17: Lower bounds for the lifetimes of invisible mode proton (a) and neutron (b) decays (at 90% CL) vs live-time set by the Feldman-Cousins method for energy windows of 5.5 and 6.0 to 10.0 MeV, using the Prompt Lookup energy reconstruction algorithm. Calculations include a direction cut to reduce the solar neutrino background and isotropy and instrumental cuts to reduce instrumental backgrounds.

Energy window (MeV)	5.5-10.0	6.0-10.0
Background	20.8	11.9
$S_{90\%}$	8.3	6.4
R_p	153.9	174.2
R_n	175.1	219.2
$\tau_p (10^{29} \text{ yr})$	15.7	13.8
$\tau_n (10^{29} \text{ yr})$	13.8	11.0

Table 6.9: Lower bounds for the lifetimes of invisible mode proton, p , and neutron, n , decays (at 90% CL) set by the Feldman-Cousins method for energy windows of 5.5 and 6 to 10 MeV, using the RSP energy reconstruction algorithm. Also shown are the expected backgrounds and the upper bounds on the number of signal events, $S_{90\%}$, after three months of running, and the corresponding nucleon decay rates, $R_{p,n}$. Quoted values are with a direction cut applied to reduce the solar neutrino background and isotropy and instrumental cuts to reduce instrumental backgrounds.

energy window there is less than 5% difference in the lifetime lower bound, and less than 16% for the 6.0-10.0 MeV energy window.

The upper limit has been calculated here using all background events expected for the live-time across the whole of the energy region (5.5-10 or 6-10 MeV). For computational reasons this becomes more problematic as the background level increases. The solution to this is to bin by energy. Each energy bin, i , is then also described by a Poisson process with an observation, n_i , and background, b_i . The average upper limit is then used, which is calculated by

$$\langle \mu_2 \rangle = \sum_i \mu_2(n_i, b_i) P(n_i, b_i). \quad (6.17)$$

6.5.3 Profile Likelihood method

The simple Poisson and Feldman-Cousins methods described in the above sections assume the expected background is known with complete certainty. Consequently they do not account for systematic errors.

Systematic errors can be incorporated using a method known as the “Profile Likelihood” [180], which reduces a multi-dimentional likelihood function to a function that only depends on one parameter. A large-sample approximation to the likelihood ratio test ($\ln \mathcal{L} + \frac{1}{2}$ method) is then used to extract confidence intervals by finding points where the $-2 \log$ -likelihood function increases by a factor defined by the required confidence level. This method is known to have under-coverage in certain circumstances.

The likelihood function is defined by assuming a Poisson distribution for the signal and a normal distribution for the background to incorporate the systematic error. The

Energy window (MeV)	5.5-10.0	6.0-10.0
Background	20.7	11.4
$S_{90\%}$	8.3	6.5
R_p	158.3	193.0
R_n	182.7	254.3
$\tau_p (10^{29} \text{ yr})$	15.2	12.5
$\tau_n (10^{29} \text{ yr})$	13.2	9.5

Table 6.10: Lower bounds for the lifetimes of invisible mode proton, p , and neutron, n , decays (at 90% CL) set by the Feldman-Cousins method for energy windows of 5.5 and 6 to 10 MeV, using the Prompt Lookup energy reconstruction algorithm. Also shown are the expected backgrounds and the upper bounds on the number of signal events, $S_{90\%}$, after three months of running, and the corresponding nucleon decay rates, $R_{p,n}$. Quoted values are with a direction cut applied to reduce the solar neutrino background and isotropy and instrumental cuts to reduce instrumental backgrounds.

likelihood function is then given by,

$$L(\mu, b|x, y) = \frac{(\mu + b)^x}{x!} e^{-(\mu+b)} \cdot \frac{1}{\sqrt{2\sigma_b \pi}} e^{-\frac{(y-b)^2}{2\sigma_b^2}}, \quad (6.18)$$

and the profile likelihood function is given by,

$$\lambda(\mu|x, y) = \frac{L(\mu, \hat{b}(\mu)|x, y)}{L(\hat{\mu}, \hat{b}|x, y)} \quad (6.19)$$

where $\hat{\mu}$ and \hat{b} are found by maximising over μ and b , and $\hat{b}(\mu)$ is found by fixing μ and maximising over b alone. The derivative of the log-likelihood is,

$$\frac{\partial}{\partial b} \log L(\mu, b|x, y) = \frac{x}{\mu + b} - 1 + \frac{(y - b)}{\sigma_b} = 0 \quad (6.20)$$

which can be solved analytically.

A standard statistical result [181] is that $-2 \log \lambda$ has an approximately χ^2 distribution with 1 degree of freedom, which can be used to extract limits. To find the $100(1 - \alpha)\%$ confidence interval, $\mu \in [\mu_1, \mu_2]$, the method starts at the minimum, which is at the usual maximum likelihood estimator, and then moves to the left and right to find points where the function increases by the α percentile of a χ^2 distribution with 1 degree of freedom. The mean upper limit, $\bar{\mu}_2 \equiv \overline{S_{90\%}}$, is determined as in Equation 6.16, and a lower limit on the lifetime, τ , for invisible mode proton and neutron decay is calculated using Equations 6.10 and 6.11.

The systematic error on the background cannot be determined without data. The resultant lower limits that may be set by SNO+ at different live-times are shown in Figure 6.18a for proton decay and Figure 6.18b for neutron decay under the assumption of 5, 10 and 50% error on the background rate scenarios. RSP has been used to estimate

event energy. It can be seen that the higher the systematic error is, the lower the lifetime lower bound is for an equivalent live-time. For a 50% systematic error, increasing the live-time beyond three months does not yield a significant improvement in the lifetime lower bound. For comparison, Figure 6.19 shows the limit that may be set using the Prompt Lookup method to estimate event energy.

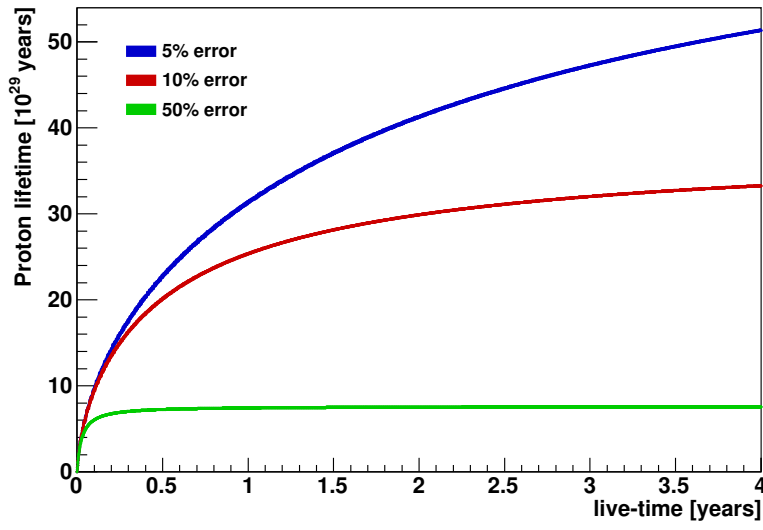
For the constraint on nucleon decay set by SNO, a quadrature sum of statistical and systematic uncertainty for the elastically scattered solar neutrinos during the pure D₂O phase was determined to be 11% [160]. This is the dominant background for the limit that will be set by SNO+, and so an uncertainty of 10% will be assumed in calculations henceforth.

Table 6.11 shows the lower limit for invisible mode proton and neutron decay that may be set by SNO+ assuming a live-time of three months and an energy window of 5.5-10 MeV. For a 10% systematic error the method results in a lower bound of 1.5×10^{30} years for the lifetime of the proton, and 1.3×10^{30} years for the neutron, to decay via an invisible mode, lower than the limits set by the Feldman-Cousins technique. These lifetimes assume an RSP estimated event energy window of 5.5 to 10.0 MeV, that a cut has been made on event direction relative to the solar neutrino direction, instrumental background cuts have been applied, as well as event isotropy and ITR cuts. It is further assumed that no signal has been observed. These limits represent a factor of 7.1 improvement over the current best limit set by SNO for invisible mode proton decay, and a factor of 2.3 improvement over the limit set by KamLAND for the neutron. For comparison, Table 6.12 shows the limits calculated with the Prompt Lookup method used to estimate event energy. There is less than 3% difference in the lifetime lower bound for proton decay and less than 5% for neutron decay assuming a systematic error of 10%.

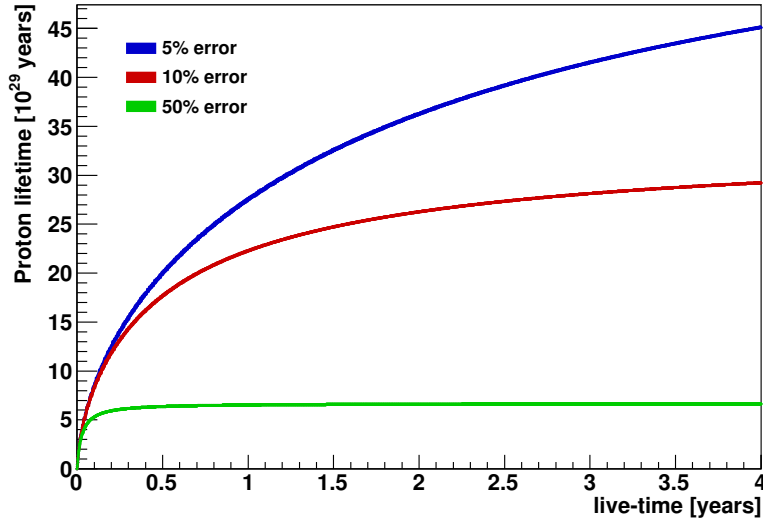
6.6 Summary

Prior to the deployment of liquid scintillator in the SNO+ detector, the acrylic vessel will be filled with light water. This “water fill” period is expected to last at least three months and will enable the detector to be calibrated as well as physics analyses. One such study could be to set a new limit on the lifetime of the proton and neutron to decay via “invisible” modes, in which very little or no energy is deposited in the detector by decay products. These decay modes have some of the lowest limits on nucleon lifetime and enable a model independent search for nucleon decay.

SNO+ has greater sensitivity to this measurement than previous experiments and should be able to set a new limit, or perhaps make a discovery. The use of light water means that SNO+ will not experience the NC background of SNO and has a superior branching ratio of visible signal to KamLAND. SNO+ also has a significantly lower background than Kamiokande.

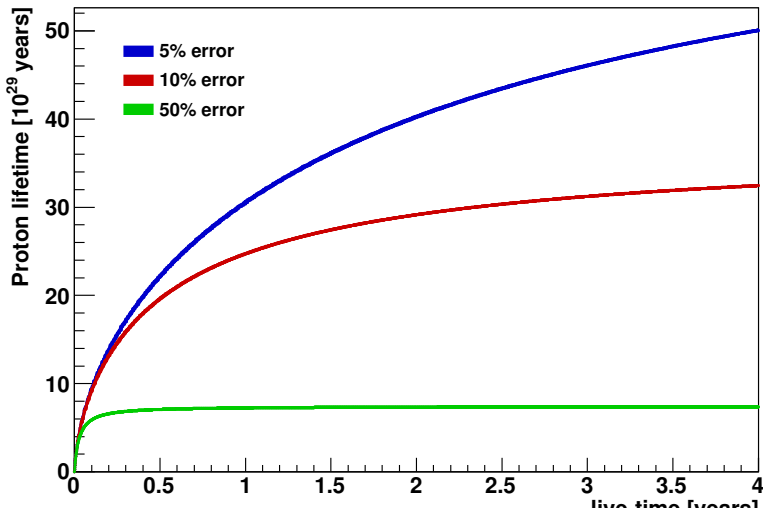


(a)

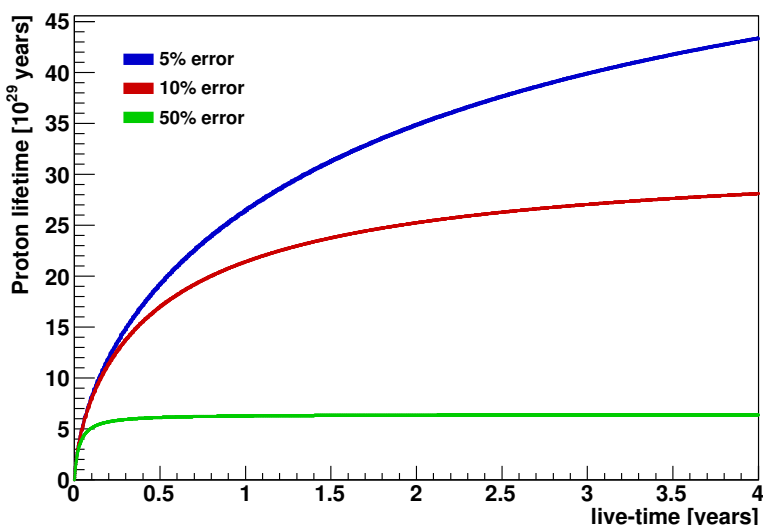


(b)

Figure 6.18: Lower bounds for the lifetimes of invisible mode proton (a) and neutron (b) decays (at 90% CL) vs live-time set by the Profile Likelihood method for an energy window of 5.5 to 10 MeV, using the RSP energy reconstruction algorithm. Calculations include a direction cut to reduce the solar neutrino background and isotropy and instrumental cuts to reduce instrumental backgrounds.



(a)



(b)

Figure 6.19: Lower bounds for the lifetimes of invisible mode proton (a) and neutron (b) decays (at 90% CL) vs live-time set by the Profile Likelihood method for an energy window of 5.5 to 10 MeV, using the Prompt Lookup energy reconstruction algorithm. Calculations include a direction cut to reduce the solar neutrino background and isotropy and instrumental cuts to reduce instrumental backgrounds.

Sys Error (%)	5	10	50
Background	20.8	20.8	20.8
$S_{90\%}$	8.0	8.7	18.8
R_p	148.9	160.8	348.5
R_n	169.5	183.0	396.8
τ_p (10^{29} yr)	16.2	15.0	6.9
τ_n (10^{29} yr)	14.2	13.2	6.1

Table 6.11: Lower bounds for the lifetimes of invisible mode proton, p , and neutron, n , decays (at 90% CL) set by the Profile Likelihood method for energy windows of 5.5 and 6.0 to 10.0 MeV, using the RSP energy reconstruction algorithm. Also shown are the expected backgrounds and the upper bounds on the number of signal events, $S_{90\%}$, after three months of running, and the corresponding nucleon decay rates, $R_{p,n}$. Quoted values are with a direction cut applied to reduce the solar neutrino background and isotropy and instrumental cuts to reduce instrumental backgrounds.

Sys Error (%)	5	10	50
Background	20.7	20.7	20.7
$S_{90\%}$	8.1	8.7	18.8
R_p	153.2	165.3	357.4
R_n	176.8	190.8	412.6
τ_p (10^{29} yr)	15.7	14.6	6.7
τ_n (10^{29} yr)	13.6	12.6	5.8

Table 6.12: Lower bounds for the lifetimes of invisible mode proton, p , and neutron, n , decays (at 90% CL) set by the Profile Likelihood method for energy windows of 5.5 and 6.0 to 10.0 MeV, using the RSP energy reconstruction algorithm. Also shown are the expected backgrounds and the upper bounds on the number of signal events, $S_{90\%}$, after three months of running, and the corresponding nucleon decay rates, $R_{p,n}$. Quoted values are with a direction cut applied to reduce the solar neutrino background and isotropy and instrumental cuts to reduce instrumental backgrounds.

The analysis in this chapter shows that in three months of operation SNO+ is able to set a limit of 1.5×10^{30} years for the lifetime of the proton, and 1.3×10^{30} years for the neutron, to decay via an invisible mode, assuming an energy window of 5.5-10 MeV. This represents a factor of 7.1 improvement over the current best limit set by SNO for invisible mode proton decay, and a factor of 2.3 improvement over the limit set by KamLAND for the neutron.

This upper limit on the number of nucleon decays was calculated using the Profile Likelihood technique with a systematic error on the background of 10%. This background error was chosen as it is similar to the error determined by SNO for the elastically scattered solar neutrinos during the D₂O phase [160]. Of the techniques described above, this is the method recommended by the author for the analysis of data because it enables the systematic error to be incorporated into the limits set, which was demonstrated to have a potentially large effect depending on the error determined by the analysis of event data.

The estimation for instrumental backgrounds is expected to be reduced in the future with the development of instrumental cuts which utilise the digitised trigger signals. Similar cuts were particularly effective for SNO, but as a result of detector electronics hardware upgrades new (and hopefully improved) cuts will be created. Furthermore, the flashers simulated for the contamination analysis did not include a time spread which would affect the efficiencies of the FTS and ITR cuts. For this reason, the limits presented here are a conservative estimate.

Chapter 7

Conclusions

SNO+ is primarily a liquid scintillator experiment intended to search for $0\nu\beta\beta$ decay of ^{130}Te . However, prior to the deployment of liquid scintillator the AV will be filled with light water. This will be used to calibrate the detector, but is also an opportunity to perform physics analyses. One such study will be to search for nucleon decay, which is the focus of this thesis.

To set the best possible limit on nucleon decay, or perhaps make a discovery, a good energy estimator is necessary. The existing estimators developed for SNO+ did not take direction into account, which is not available for the scintillator phase. In the water phase however, direction reconstruction is possible because of the nature of Cherenkov light.

This thesis outlines a model for the energy response of the detector, given an event vertex, which can be used to estimate event energy. The model calculates the light path between the photon creation point and each PMT. With light water on both sides of the AV the path is approximately a straight line. This light path gives the direction that the photon would need to be travelling to reach the PMT. Cherenkov photons are emitted in a cone, with an angle dependent on the event energy and material's refractive index. In reality, because of scattering of the charged particle, the angle photons are emitted at relative to the direction of travel of the charged particle is not a delta function. An angular distribution was therefore calculated which, combined with the event energy, gives the number of photons travelling in the direction of each PMT. These photons are created with $1/\lambda^2$ wavelength distribution. The number of photons travelling towards each PMT is also decided by the solid angle of the PMT. Photons are then attenuated and scattered over the distances travelled, reducing the number of them reaching the PMTs. The photons reaching PMTs are further reduced by the probability of Fresnel transmission through both faces of the AV. The efficiency of PMTs at detecting these photons is wavelength dependent, with a peak between 300-500 nm. The PMT efficiency also has an angular dependence, due to reflections off the PMT glass and the concentrator.

This motivated the development of two energy estimators, the first of which was Prompt Lookup. This method used a lookup table to scale the number of PMT hits observed to what would be expected at the centre of the detector. The lookup table was created by simulating electrons isotropically at different radii. The adjusted N_{hits} is then mapped to the event energy. There is a further scaling by the number of working PMTs for the run. This assumes that not working PMTs are evenly distributed throughout the detector. This will not work well if particular sections of the detector are not working. For instance if whole slots are not working, or in more extreme circumstances a whole crate.

To solve this issue, and to provide further improvements in estimation accuracy the Energy Response Processor (RSP) method was developed. RSP uses a response function, based on the energy model, to calculate the probability of each PMT registering a hit. Summed across all PMTs this gives an estimate for the number of PMT hits. The event energy, used as a variable, can be adjusted iteratively to match the PMT hits to what was actually observed. This method should be much more accurate as the response is affected by the exact working condition of the detector. RSP and Prompt Lookup were shown to have no energy bias above 6 MeV and have the least radial bias. Compared to other methods RSP is the most symmetric. Issues reconstructing low energies are because of a selection bias for events. RSP has now been adopted as the default estimator for the water phase.

An obstacle for physics analyses is the large instrumental background expected. These are non-radiative events caused by the detector itself. The most common issue is due to “flashers” which are when PMTs operating at high voltage emit photons into the detector. Typically a flasher can be identified by a very high charge tube, with a cluster of hits around it due to cross-talk. There is also a group of PMT hits on the far side of the detector caused by collimation from the PMT and concentrator. These were observed by SNO and, because most of the same electronics are used, are expected for SNO+. Instrumental backgrounds were almost completely removed by SNO using a suite of cuts targeting their distinct properties to physics events. The process of removing instrumental backgrounds is known as “data cleaning”.

Data cleaning cuts must accept as much signal as possible. The events not accepted are known as the signal “sacrifice”. The sacrifice is presented here for electrons simulated in water and scintillator. This demonstrates that the sacrifice is below the 1% target for water. It is expected that for scintillator the FTS cut sacrifice would be too high because it targets events with a broader time distribution than Cherenkov light. This was shown to be true, but otherwise the sacrifice is below the 1% target for other cuts.

The number of instrumental background events that remain in the data set after the cuts is known as “contamination”. The contamination is estimated here by creating a flasher generator which simulates photons emitted from beside the dynode stack, deep

in the PMT base. This was not possible for SNO because the PMT geometry was not simulated to sufficient detail, it was however estimated in a different way. The generator results in events with a similar signature to flashers in water. The wavelength distribution of flashers is not known, but they look similar in water in the 300-500 nm range, with some variation due to scattering. Large differences for different wavelengths are however expected in scintillator. The signature will be close in scintillator at 500 nm because scintillator is transparent at this wavelength. However, at 350 nm photons are quickly absorbed and re-emitted by the scintillator. This results in most hits occurring in a group on the near side of the detector. The different event signatures will affect how well the instrumental background cuts work. The generator was used to simulate the N_{hits} distribution of flashers observed by SNO in light water and scintillator. Assuming a blackbody distribution (temperature 6000 K) for the wavelength of photons there is a contamination of 10.5 events in water from 5.5-10 MeV and no contamination for scintillator in the ROI of $0\nu\beta\beta$. The number of instrumental background events decreases exponentially as the N_{hits} increases. There are more PMT hits per MeV for scintillator, so events passing all cuts have lower energies than the $0\nu\beta\beta$ ROI even though the cuts may be less effective. The contamination reported in the water phase is an overestimate. One of the most effective cuts was based on measurements made by the AMB on the ESUM trigger signal. The AMB has been replaced for SNO+ with a signal digitiser and cuts using its output are under development. The flashers simulated also have instantaneous photon emission, rather than a time spread which real flashers have, so cuts tagging on a broad time distribution will be less effective.

In the water phase the contamination from instrumental backgrounds will be a background to physics analyses, including the nucleon decay analysis presented here. Chapter 6 shows that SNO+ will have a greater sensitivity to “invisible” modes than previous experiments reporting limits. Invisible modes, such as decays to neutrinos, deposit little or no energy in the detector through the decay products. The Profile Likelihood technique shows that SNO+ can set a better limit than SNO because it does not experience the NC background, and has a superior branching ratio of visible signal and lower background to KamLAND. The analysis presented shows that in three months of operation SNO+ will be able to set a limit of 1.5×10^{30} years for the lifetime of the proton, and 1.3×10^{30} years for the neutron, to decay via an invisible mode, assuming a systematic error of 10% on the background rate. This represents a factor of 7.1 improvement over the current best limit set by SNO for invisible mode proton decay, and a factor of 2.3 improvement over the limit set by KamLAND for the neutron.

Bibliography

- [1] A. De Gouvea. *TASI Lectures on Neutrino Physics*. arXiv:hep-ph/0411274. 2004.
- [2] A. Allisy. “Henri Becquerel: The Discovery of Radioactivity”. *Radiat Prot Dosimetry* 68.1 (1996), pp. 3–10.
- [3] J. J. Thomson. “Cathode Rays”. *The Electrician* 39.104 (1897).
- [4] J. Chadwick. “Intensitätsverteilung im magnetischen Spektrum von β -Strahlen von Radium B+C”. *Verhandlungen der Deutschen Physikalischen Gesellschaft* 16 (1914), pp. 383–391.
- [5] C. D. Ellis and W. A. Wooster. “The Average Energy of Disintegration of Radium E”. *Proceedings of the Royal Society* 117.776 (1927).
- [6] L. Meitner and W. Orthmann. “About an Absolute Determination of the Power of the Primary β -Radiation from Radium E”. *Zeitschrift fur Physik* 60 (1930), pp. 143–155.
- [7] G. Gamow. *Constitution of Atomic Nuclei and Radioactivity*. Clarendon Press, 1931.
- [8] J. Chadwick. “Possible Existence of a Neutron”. *Nature* 129.312 (1932).
- [9] E. Fermi. “Attempt of a Theory of β -Radiation”. *Zeitschrift fur Physik* 88 (1934), pp. 161–177.
- [10] C. Cowan et al. “Detection of the Free Neutrino: a Confirmation”. *Science* 124.3212 (1956), pp. 103–104.
- [11] T. D. Lee and C. N. Yang. “Question of Parity Conservation in Weak Interactions”. *Phys. Rev.* 104.254 (1956).
- [12] C. S. Wu et al. “Experimental Test of Parity Conservation in Beta Decay”. *Phys. Rev.* 105.1413 (1957).
- [13] R. P. Feynman and M. Gell-Mann. “Theory of the Fermi Interaction”. *Phys. Rev.* 109.193 (1958).
- [14] E. C. G. Sudarshan and R. E. Marshak. “Chirality Invariance and the Universal Fermi Interaction”. *Phys. Rev.* 109.1860 (1958).
- [15] M. Goldhaber et al. “Helicity of Neutrinos”. *Phys. Rev.* 109.1015 (1958).
- [16] R. Davis. “Attempt to Detect the Antineutrinos from a Nuclear Reactor by the $\text{Cl}^{37}(\bar{\nu}, e^-)\text{A}^{37}$ Reaction”. *Phys. Rev.* 97.766 (1955).
- [17] E. J. Konopinski and H. M. Mahmoud. “The Universal Fermi Interaction”. *Phys. Rev.* 92.1045 (1953).
- [18] J. C. Street and E. C. Stevenson. “New Evidence for the Existence of a Particle of Mass Intermediate Between the Proton and Electron”. *Phys. Rev.* 52 (1937), pp. 1003–1004.

- [19] S. Neddermeyer and C. Anderson. “Note on the Nature of Cosmic-Ray Particles”. *Phys. Rev.* 51 (1937), pp. 884–886.
- [20] C. M. G. Lattes et al. “Observations on the tracks of slow mesons in photographic emulsions”. *Nature* 160.4066 (1947), pp. 453–456.
- [21] G. Danby et al. “Observation of High-Energy Neutrino Reactions and the Existence of Two Kinds of Neutrinos”. *Phys. Rev. Lett.* 9.36 (1962).
- [22] M. L. Perl et al. “Evidence for Anomalous Lepton Production in $e^+ - e^-$ Annihilation”. *Phys. Rev. Lett.* 35 (1975), pp. 1489–1492.
- [23] D. Decamp and A. Finch. “Determination of the number of light neutrino species”. *Phys. Lett. B* 231.4 (1989), pp. 519–529.
- [24] G. D. N. Schramm and M. S. Turner. “Big-bang nucleosynthesis enters the precision era”. *Rev. Mod. Phys.* 70.303 (1998).
- [25] K. Kodama et al. “Observation of tau neutrino interactions”. *Phys. Lett. B*. 504 (2000), pp. 218–224.
- [26] K. Olive et al. “2015 Review of Particle Physics”. *Chin. Phys. C* 38.090001 (2015).
- [27] O. Nackenhorst. “Search for the Standard Model Higgs boson produced in association with $t\bar{t}$ and decaying into $b\bar{b}$ at $\sqrt{s} = 8$ TeV with the ATLAS detector using the Matrix Element Method”. PhD thesis. Georg-August-Universität Göttingen, 2015.
- [28] C. Giunti and C. W. Kim. *Fundamentals of Neutrino Physics and Astrophysics*. Oxford University Press, 2007.
- [29] J. A. Formaggio and G. P. Zeller. “From eV to EeV: Neutrino cross sections across energy scales”. *Rev. Mod. Phys.* 84 (3 Sept. 2012), pp. 1307–1341. DOI: 10.1103/RevModPhys.84.1307.
- [30] C. Spiering. *Towards High-Energy Neutrino Astronomy: A Historical Review*. arXiv:1207.4952v1 [astro-ph.IM].
- [31] S. Boyd. *Neutrino Physics Lecture Notes*. https://www2.warwick.ac.uk/fac/sci/physics/staff/academic/boyd/warwick_week/neutrino_physics/. Accessed: 2016-01-13.
- [32] J. N. Bahcall, A. M. Serenelli, and S. Basu. “New Solar Opacities, Abundances, Helioseismology, and Neutrino Fluxes”. *ApJ* 621 (2005).
- [33] C. Bemporad et al. “Reactor-based Neutrino Oscillation Experiments”. *Rev. Mod. Phys.* 74.297 (2002).
- [34] G. Eder. “Terrestrial Neutrinos”. *Nucl. Phys.* 78 (1966), pp. 657–662.
- [35] P. Lipari. *Introduction to neutrino physics*. <http://cds.cern.ch/record/677618/>. Accessed: 2016-01-18.
- [36] B. Krosigk. “Measurement of proton and α -particle quenching in LAB based scintillators and determination of spectral sensitivities to supernova neutrinos in the SNO+ detector”. PhD thesis. Dresden University, 2015.
- [37] K. Hirata et al. “Observation of a neutrino burst from the supernova SN1987A”. *Phys. Rev. Lett.* 58 (14 Apr. 1987), pp. 1490–1493. DOI: 10.1103/PhysRevLett. 58.1490.

- [38] R. M. Bionta et al. “Observation of a neutrino burst in coincidence with supernova 1987A in the Large Magellanic Cloud”. *Phys. Rev. Lett.* 58 (14 Apr. 1987), pp. 1494–1496. DOI: 10.1103/PhysRevLett.58.1494.
- [39] E. N. Alexeyev et al. “Detection of the neutrino signal from SN 1987A in the LMC using the INR Baksan underground scintillation telescope”. *Physics Letters B* 205.2 (1988), pp. 209–214. ISSN: 0370-2693. DOI: http://dx.doi.org/10.1016/0370-2693(88)91651-6.
- [40] M. Aglietta et al. “On the neutrino burst from SN 1987a detected in the Mt. Blanc LSD experiment”. *Nuclear Physics B - Proceedings Supplements* 3 (1988), pp. 453–462. ISSN: 0920-5632. DOI: http://dx.doi.org/10.1016/0920-5632(88)90196-X.
- [41] K. Bays et al. “Supernova relic neutrino search at Super-Kamiokande”. *Phys. Rev. D* 85 (5 Mar. 2012), p. 052007. DOI: 10.1103/PhysRevD.85.052007.
- [42] E. Waxman and J. Bahcall. “High energy neutrinos from astrophysical sources: An upper bound”. *Phys. Rev. D* 59 (2 Dec. 1998), p. 023002. DOI: 10.1103/PhysRevD.59.023002.
- [43] M. G. Aartsen et al. “Observation of High-Energy Astrophysical Neutrinos in Three Years of IceCube Data”. *Phys. Rev. Lett.* 113 (10 Sept. 2014), p. 101101. DOI: 10.1103/PhysRevLett.113.101101.
- [44] P. Anselmann et al. “Solar neutrinos observed by GALLEX at Gran Sasso.” *Phys. Lett.* B285 (1992), pp. 376–389. DOI: 10.1016/0370-2693(92)91521-A.
- [45] M. Altmann et al. “Complete results for five years of GNO solar neutrino observations”. *Phys. Lett.* B616 (2005), pp. 174–190. DOI: 10.1016/j.physletb.2005.04.068. arXiv: hep-ex/0504037 [hep-ex].
- [46] A. I. Abazov et al. “Search for neutrinos from the Sun using the reaction ${}^{71}\text{Ga}(\nu_e, e^-) {}^{71}\text{Ge}$ ”. *Phys. Rev. Lett.* 67 (24 Dec. 1991), pp. 3332–3335. DOI: 10.1103/PhysRevLett.67.3332.
- [47] P. Adamson et al. “First measurement of muon-neutrino disappearance in NOvA” (2016). arXiv: 1601.05037 [hep-ex].
- [48] R. Acciarri et al. “Long-Baseline Neutrino Facility (LBNE) and Deep Underground Neutrino Experiment (DUNE) Conceptual Design Report Volume 1: The LBNF and DUNE Projects” (2016). arXiv: 1601.05471 [physics.ins-det].
- [49] I. M. Frank and I. Tamm. “Coherent visible radiation of fast electrons passing through matter”. *C. R. Acad. Sci. URSS* 14 (1937), pp. 109–114.
- [50] B. M. Bolotovskii. “Vavilov-Cherenkov radiation: its discovery and application”. *Physics-Uspekhi* 52.11 (2009), p. 1099. URL: http://stacks.iop.org/1063-7869/52/i=11/a=R03.
- [51] Y. Ashie et al. “Measurement of atmospheric neutrino oscillation parameters by Super-Kamiokande I”. *Phys. Rev. D* 71 (11 June 2005), p. 112005. DOI: 10.1103/PhysRevD.71.112005.
- [52] J. Boger et al. “The Sudbury Neutrino Observatory”. *Nuclear Instruments and Methods in Physics Research A* 449 (1–2 2000), pp. 172–207.
- [53] S. Chatrchyan et al. “The CMS experiment at the CERN LHC”. *JINST* 3 (2008), S08004. DOI: 10.1088/1748-0221/3/08/S08004.

- [54] K. Hiraide et al. “Search for charged current coherent pion production on carbon in a few-GeV neutrino beam”. *Phys. Rev. D* 78 (11 Dec. 2008), p. 112004. DOI: 10.1103/PhysRevD.78.112004.
- [55] A. A. Aguilar-Arevalo et al. “The MiniBooNE Detector”. *Nucl. Instrum. Meth.* A599 (2009), pp. 28–46. DOI: 10.1016/j.nima.2008.10.028. arXiv: 0806.4201 [hep-ex].
- [56] T. Araki et al. “Measurement of Neutrino Oscillation with KamLAND: Evidence of Spectral Distortion”. *Phys. Rev. Lett.* 94 (8 Mar. 2005), p. 081801. DOI: 10.1103/PhysRevLett.94.081801.
- [57] M. Aglietta et al. “Experimental study of atmospheric neutrino flux in the NUSEX experiment”. *Europhys. Lett.* 8 (1989), pp. 611–614. DOI: 10.1209/0295-5075/8/7/005.
- [58] C. Berger et al. “Experimental study of muon bundles observed in the Fréjus detector”. *Phys. Rev. D* 40 (7 Oct. 1989), pp. 2163–2171. DOI: 10.1103/PhysRevD.40.2163.
- [59] J. L. Thron. “The Soudan-2 proton decay experiment”. *Nuclear Instruments and Methods in Physics Research Section A: Accelerators, Spectrometers, Detectors and Associated Equipment* 283.3 (1989), pp. 642–645. ISSN: 0168-9002. DOI: http://dx.doi.org/10.1016/0168-9002(89)91432-0.
- [60] M. Calicchio et al. “The macro detector at the Gran Sasso Laboratory”. *Nuclear Instruments and Methods in Physics Research Section A: Accelerators, Spectrometers, Detectors and Associated Equipment* 264.1 (1988), pp. 18–23. ISSN: 0168-9002. DOI: http://dx.doi.org/10.1016/0168-9002(88)91095-9.
- [61] K. Hirata et al. “Experimental Study of the Atmospheric Neutrino Flux”. *Phys. Lett.* B205 (1988), p. 416. DOI: 10.1016/0370-2693(88)91690-5.
- [62] W. Gajewski. “A search for oscillation of atmospheric neutrinos with the IMB detector”. *Nuclear Physics B - Proceedings Supplements* 28.1 (1992), pp. 161–164. ISSN: 0920-5632. DOI: http://dx.doi.org/10.1016/0920-5632(92)90164-N.
- [63] S. Hatakeyama et al. “Measurement of the Flux and Zenith-Angle Distribution of Upward Through-Going Muons in Kamiokande II + III”. *Phys. Rev. Lett.* 81 (10 Sept. 1998), pp. 2016–2019. DOI: 10.1103/PhysRevLett.81.2016.
- [64] V. Castellani et al. “Helioseismology, solar models and neutrino fluxes”. *Nuclear Physics B - Proceedings Supplements* 70.1 (1999), pp. 301–314. ISSN: 0920-5632. DOI: http://dx.doi.org/10.1016/S0920-5632(98)00440-X.
- [65] Q. R. Ahmad et al. “Direct Evidence for Neutrino Flavor Transformation from Neutral-Current Interactions in the Sudbury Neutrino Observatory”. *Phys. Rev. Lett.* 89 (1 2002), p. 011301.
- [66] B. Aharmim et al. “Combined analysis of all three phases of solar neutrino data from the Sudbury Neutrino Observatory”. *Phys. Rev. C* 88 (2 Aug. 2013), p. 025501. DOI: 10.1103/PhysRevC.88.025501.
- [67] K. Eguchi et al. “First Results from KamLAND: Evidence for Reactor Antineutrino Disappearance”. *Phys. Rev. Lett.* 90 (2 Jan. 2003), p. 021802. DOI: 10.1103/PhysRevLett.90.021802.
- [68] L. Wolfenstein. “Neutrino oscillations in matter”. *Phys. Rev. D* 17 (9 1978), pp. 2369–2374.

- [69] B. Kayser. *Neutrino Physics*. <http://www.slac.stanford.edu/econf/C040802/papers/L004.PDF>. Accessed: 2016-01-13.
- [70] C. Giunti and M. Laveder. “Neutrino mixing” (2003). arXiv: hep-ph/0310238 [hep-ph].
- [71] Q. R. Ahmad et al. “Measurement of Day and Night Neutrino Energy Spectra at SNO and Constraints on Neutrino Mixing Parameters”. *Phys. Rev. Lett.* 89 (1 June 2002), p. 011302. doi: 10.1103/PhysRevLett.89.011302.
- [72] J. N. Bahcall and C. Peña-Garay. “A road map to solar neutrino fluxes, neutrino oscillation parameters, and tests for new physics”. *Journal of High Energy Physics* 2003.11 (2003), p. 004. URL: <http://stacks.iop.org/1126-6708/2003/i=11/a=004>.
- [73] D. Perepelitsa. *Sakharov Conditions for Baryogenesis, Columbia University*. [ht tp://phys.columbia.edu/~dvp/dvp-sakharov.pdf](http://phys.columbia.edu/~dvp/dvp-sakharov.pdf). Accessed: 2016-02-12. Nov. 2008.
- [74] K. Assamagan et al. “Upper limit of the muon-neutrino mass and charged-pion mass from momentum analysis of a surface muon beam”. *Phys. Rev. D* 53 (11 1996), pp. 6065–6077.
- [75] R. Barate et al. “Study of fermion pair production in e^+e^- collisions at 130-GeV to 183-GeV”. *Eur. Phys. J.* C12 (2000), pp. 183–207.
- [76] S. Mertens. “Background Processes in the Electrostatic Spectrometers of the KATRIN Experiment”. PhD thesis. Springer Theses, 2014.
- [77] C. Kraus et al. “Final results from phase II of the Mainz neutrino mass search in tritium”. *Eur. Phys. J.* 40.446 (2005).
- [78] V. M. Lobashev et al. “Direct search for mass of neutrino and anomaly in the tritium beta-spectrum”. *Phys. Lett. B*. 460 (1999), pp. 227–235.
- [79] R. G. Hamish Robertson. *KATRIN: an experiment to determine the neutrino mass from the beta decay of tritium*. arXiv:1307.5486v1 [physics.ins-det].
- [80] K. Zuber. *Neutrinoless double beta decay experiments*. arXiv:nucl-ex/0610007v1.
- [81] S. R. Elliott and P. Vogel. “Double beta decay”. *Ann. Rev. Nucl. Part. Sci.* 52 (2002), pp. 115–151. doi: 10.1146/annurev.nucl.52.050102.090641. arXiv: hep-ph/0202264 [hep-ph].
- [82] M. Lindner, A. Merle, and W. Rodejohann. “Improved Limit on θ_{13} and Implications for Neutrino Masses in Neutrino-less Double Beta Decay and Cosmology”. *Phys. Rev. D* 73 (2006), p. 053005. doi: 10.1103/PhysRevD.73.053005. arXiv: hep-ph/0512143 [hep-ph].
- [83] <https://www.snlab.ca/about>. Accessed: 2016-02-18.
- [84] S. Andringa et al. “Current Status and Future Prospects of the SNO+ Experiment”. *Adv. High Energy Phys.* 2016 (2015), p. 6194250. arXiv: 1508.05759 [physics].
- [85] P. G. Jones. “Background rejection for the neutrinoless double-beta decay experiment SNO+”. PhD thesis. Oxford University, 2011.
- [86] R. Knapik. *SNO+ Electronics*. SNO+ Document 733v1. Dec. 2010.
- [87] A. Mastbaum. *Electronics Overview*. SNO+ DocDB 1316v1.

- [88] R. Alves et al. “The calibration system for the photomultiplier array of the SNO+ experiment”. *JINST* 10.03 (2015), P03002. DOI: 10.1088/1748-0221/10/03/P03002. arXiv: 1411.4830 [physics.ins-det].
- [89] S. J. M. Peeters and E. Leming. *Modified laserball: status*. SNO+ DocDB 2623v1.
- [90] I. Coulter. “Modelling and reconstruction of events in SNO+ related to future searches for lepton and baryon number violation”. PhD thesis. University of Oxford, 2013. URL: <http://ethos.bl.uk/OrderDetails.do?uin=uk.bl.ethos.604461>.
- [91] P. G. Jones. *SNO+ PMT Geometry in RAT*. SNO+ DocDB 375v2.
- [92] K. Majumdar. “On the Measurement of Optical Scattering and Studies of Background Rejection in the SNO+ Detector”. PhD thesis. Oxford University, 2015.
- [93] M. Yeh et al. “A new water-based liquid scintillator and potential applications”. *Nucl. Instrum. Meth.* A660 (2011), pp. 51–56. DOI: 10.1016/j.nima.2011.08.040.
- [94] A. J. Wright. “Robust Signal Extraction Methods and Monte Carlo Sensitivity Studies for the Sudbury Neutrino Observatory and SNO+ Experiments”. PhD thesis. Queens U., 2009. URL: <http://www.sno.phy.queensu.ca/sno/publications.html>.
- [95] H. M. O’Keeffe and M. C. Chen. *Expected radioactive backgrounds in the SNO+ experiment*. SNO+ DocDB 507v29.
- [96] C. Arpesella et al. “Direct Measurement of the Be-7 Solar Neutrino Flux with 192 Days of Borexino Data”. *Phys. Rev. Lett.* 101 (2008), p. 091302. DOI: 10.1103/PhysRevLett.101.091302. arXiv: 0805.3843 [astro-ph].
- [97] S. Abe et al. “Production of Radioactive Isotopes through Cosmic Muon Spallation in KamLAND”. *Phys. Rev.* C81 (2010), p. 025807. DOI: 10.1103/PhysRevC.81.025807. arXiv: 0907.0066 [hep-ex].
- [98] S. Hans et al. “Purification of telluric acid for SNO+ neutrinoless double-beta decay search”. *Nucl. Instrum. Meth.* A795 (2015), pp. 132–139. DOI: 10.1016/j.nima.2015.05.045.
- [99] I. Lawson and B. Cleveland. “Low background counting at SNOLAB”. *AIP Conf. Proc.* 1338 (2011), pp. 68–77. DOI: 10.1063/1.3579561.
- [100] B. Aharmim et al. “Electron energy spectra, fluxes, and day-night asymmetries of ${}^8\text{B}$ solar neutrinos from measurements with NaCl dissolved in the heavy-water detector at the Sudbury Neutrino Observatory”. *Phys. Rev. C* 72 (5 Nov. 2005), p. 055502. DOI: 10.1103/PhysRevC.72.055502.
- [101] C. Kraus and S. J. M. Peeters. “The rich neutrino programme of the SNO+ experiment”. *Progress in Particle and Nuclear Physics* 64.2 (2010), pp. 273–277. ISSN: 0146-6410. DOI: <http://dx.doi.org/10.1016/j.ppnp.2009.12.027>.
- [102] E. Guillian. “The Sensitivity of SNO+ to Δm_{12}^2 Using Reactor Anti-neutrino Data” (2008). arXiv: 0809.1649 [hep-ph].
- [103] T. Araki et al. “Experimental investigation of geologically produced antineutrinos with KamLAND”. *Nature* 436.7050 (July 28, 2005), pp. 499–503. URL: <http://dx.doi.org/10.1038/nature03980>.
- [104] P. Antonioli et al. “SNEWS: The Supernova Early Warning System”. *New J. Phys.* 6 (2004), p. 114. DOI: 10.1088/1367-2630/6/1/114. arXiv: astro-ph/0406214 [astro-ph].

- [105] L. Sibley. “SNO+: Physics Program and Status Update.” *AIP Conference Proceedings* 1604 (2014), pp. 449–455. ISSN: 0094243X.
- [106] J. Barea, J. Kotila, and F. Iachello. “Nuclear matrix elements for double- β decay”. *Phys. Rev.* C87.1 (2013), p. 014315. DOI: 10.1103/PhysRevC.87.014315. arXiv: 1301.4203 [nucl-th].
- [107] J. Kotila and F. Iachello. “Phase space factors for double- β decay”. *Phys. Rev.* C85 (2012), p. 034316. DOI: 10.1103/PhysRevC.85.034316. arXiv: 1209.5722 [nucl-th].
- [108] R. Ford. “A scintillator purification plant and fluid handling system for SNO+”. *AIP Conference Proceedings* 1672, 080003 (2015). DOI: <http://dx.doi.org/10.1063/1.4927998>.
- [109] R. Ford et al. “SNO+ Scintillator Purification and Assay”. *AIP Conference Proceedings* 1338.1 (2011), pp. 183–194. DOI: <http://dx.doi.org/10.1063/1.3579580>.
- [110] A. J. Noble et al. *Scientific Review of SNO Water Systems*. SNO+ Document 1870v1. Apr. 1996.
- [111] R. Ford. *Water Systems Status*. SNO+ Document 60v1. Nov. 2007.
- [112] K. Singh. *Pictures taken with camera system and underwater light*. SNO+ Document 2507v1. May 2014.
- [113] J. Maneira et al. *SNO+ Timing Fibres: hardware, installation and routing*. SNO+ Document 501v4. Apr. 2011.
- [114] J. Maneira. *Fibre installation*. SNO+ Document 3560v1. Mar. 2016.
- [115] D. Braid. *Photomultiplier Tube Repairs for the SNO+ Experiment*. SNO+ Document 2571v1. June 2014.
- [116] D. Braid. *PMT Repair Manual*. SNO+ Document 3729v1. May 2016.
- [117] D. Braid. Private communication. June 24, 2016.
- [118] D. Braid and P. Rost. *PMT Repair Update*. SNO+ Document 3568v1. Mar. 2016.
- [119] N. Gagnon. *SNO+ Electronics*. SNO+ Document 410v1. Dec. 2009.
- [120] J. Klein. *SNO+ Electronics*. SNO+ Document 191v1. Aug. 2008.
- [121] A. Mastbaum. *MTC/A+ Users Guide*. SNO+ Document 1976v2. Sept. 2014.
- [122] N. McCauley. “Producing a Background Free Data Set for Measurement of the Charge Current Flux and Day-Night Asymmetry at the Sudbury Neutrino Observatory”. PhD thesis. University of Oxford, 2001.
- [123] A. Mastbaum. *Trigger System Upgrades for the SNO+ Experiment*. SNO+ Document 1410v1. Mar. 2012.
- [124] N. Fatemi-Ghomie. *Cover gas commissioning report*. SNO+ Document 2918v1. Feb. 2015.
- [125] C. Jillings. *Universal Interface*. SNO+ Document 199v1. Aug. 2008.
- [126] C. Jillings. *SNO+ Universal Interface Design Criteria Document*. SNO+ Document 231v1. Apr. 2009.
- [127] J. Walker and C. Jillings. *UI Leakage and Radon Activity*. SNO+ Document 3728v1. June 2013.

- [128] J. Walker and D. Braid. *UI Seal Measurements*. SNO+ Document 2367v2. Mar. 2014.
- [129] S. Grullon. *Optical Properties Task Force Investigative Summary*. SNO+ DocDB 1531v3.
- [130] B. Moffat. “The Optical Calibration of the Sudbury Neutrino Observatory”. PhD thesis. Queen’s U., Kingston, 2001. URL: <http://www.sno.phy.queensu.ca/sno/publications.html>.
- [131] R. F. MacLellan. “The energy calibration for the solar neutrino analysis of all three phases of the Sudbury Neutrino Observatory”. PhD thesis. Queens U., 2009. URL: <http://www.sno.phy.queensu.ca/sno/publications.html>.
- [132] S. D. Biller et al. “Measurements of photomultiplier single photon counting efficiency for the Sudbury Neutrino Observatory”. *Nucl. Instrum. Meth.* A432 (1999), pp. 364–373. doi: 10.1016/S0168-9002(99)00500-8.
- [133] R. Boardman. “The Detection of Čerenkov Radiation from Neutrino Interactions”. PhD thesis. Oxford U., 1992. URL: <http://www.sno.phy.queensu.ca/sno/publications.html>.
- [134] M. G. Boulay. “Direct evidence for weak flavor mixing with the Sudbury Neutrino Observatory”. PhD thesis. Queen’s U., Kingston, 2001. URL: <http://www.sno.phy.queensu.ca/sno/publications.html>.
- [135] R. Stainforth. *LightPathCalculator Documentation*. SNO+ DocDB 1700v8.
- [136] R. Stainforth. “Characterising the Optical Response of the SNO+ Detector”. PhD thesis. Liverpool U., 2016.
- [137] R. Ford. “Calibration of SNO for the Detection of ${}^8\text{B}$ Neutrinos”. PhD thesis. Queen’s U., Kingston, 1998. URL: <http://www.sno.phy.queensu.ca/sno/publications.html>.
- [138] M. Dunford. “Measurement of the ${}^8\text{B}$ solar neutrino energy spectrum at the Sudbury Neutrino Observatory”. PhD thesis. Pennsylvania U., 2006. URL: <http://wwwlib.umi.com/dissertations/fullcit?p3246154>.
- [139] M. Dunford et al. *Updates to Data Cleaning for the Salt Phase Version 1.2*. SNO Internal Document. Feb. 2004.
- [140] G. Beier. *Isotropy Classifier*. SNO+ Document 2835-v2. Mar. 2015.
- [141] J. Dunmore. “The Separation of CC and NC Events in the Sudbury Neutrino Observatory”. PhD thesis. University of Oxford, 2004.
- [142] P. G. Jones. *SNO+ PMT Geometry in RAT*. SNO+ Document 375v2. Jan. 2011.
- [143] R. Stainforth. *Laserball Fits with OCA*. SNO+ Document 3563v3.
- [144] T. Araki et al. “Search for the Invisible Decay of Neutrons with KamLAND”. *Phys. Rev. Lett.* 96 (10 Mar. 2006), p. 101802. doi: 10.1103/PhysRevLett.96.101802.
- [145] H. Georgi and S. L. Glashow. “Unity of All Elementary-Particle Forces”. *Phys. Rev. Lett.* 32 (8 Feb. 1974), pp. 438–441. doi: 10.1103/PhysRevLett.32.438.
- [146] H. Georgi, H. R. Quinn, and S. Weinberg. “Hierarchy of Interactions in Unified Gauge Theories”. *Phys. Rev. Lett.* 33 (7 Aug. 1974), pp. 451–454. doi: 10.1103/PhysRevLett.33.451.

- [147] S. T. Clark. "Searches for proton decay with the Super-Kamiokande detector". PhD thesis. Kansas U., 2007. URL: <http://www-sk.icrr.u-tokyo.ac.jp/sk/pub/index.html#dthesis>.
- [148] R. Becker-Szendy et al. "Search for proton decay into $e^+ + \pi^0$ in the IMB-3 detector". *Phys. Rev. D* 42 (9 Nov. 1990), pp. 2974–2976. DOI: 10.1103/PhysRevD.42.2974.
- [149] H. Nishino et al. "Search for nucleon decay into charged antilepton plus meson in Super-Kamiokande I and II". *Phys. Rev. D* 85 (11 June 2012), p. 112001. DOI: 10.1103/PhysRevD.85.112001.
- [150] H. Fritzsch and P. Minkowski. "Unified interactions of leptons and hadrons". *Annals of Physics* 93.1 (1975), pp. 193–266. ISSN: 0003-4916. DOI: [http://dx.doi.org/10.1016/0003-4916\(75\)90211-0](http://dx.doi.org/10.1016/0003-4916(75)90211-0).
- [151] J. C. Pati and A. Salam. "Lepton number as the fourth "color"". *Phys. Rev. D* 10 (1 July 1974), pp. 275–289. DOI: 10.1103/PhysRevD.10.275.
- [152] K. Abe et al. "Search for proton decay via $p \rightarrow \nu K^+$ using 260 kiloton · year data of Super-Kamiokande". *Phys. Rev. D* 90 (7 Oct. 2014), p. 072005. DOI: 10.1103/PhysRevD.90.072005.
- [153] V. Lucas and S. Raby. "Nucleon decay in a realistic SO(10) SUSY GUT". *Phys. Rev. D* 55 (1997), pp. 6986–7009. DOI: 10.1103/PhysRevD.55.6986. arXiv: hep-ph/9610293 [hep-ph].
- [154] T. Goto and T. Nihei. "Effect of an RRRR dimension 5 operator on proton decay in the minimal SU(5) SUGRA GUT model". *Phys. Rev. D* 59 (11 May 1999), p. 115009. DOI: 10.1103/PhysRevD.59.115009.
- [155] J. C. Pati, A. Salam, and U. Sarkar. " $\Delta B = -\Delta L$, neutron $\rightarrow e^- \pi^+, e^- K^+$, $\mu^- \pi^+$ and $\mu^- K^+$ decay modes in $SU(2)_L \times SU(2)_R \times SU(4)_{\text{col}}$ or $SO(10)$ ". *Physics Letters B* 133.5 (1983), pp. 330–336. ISSN: 0370-2693. DOI: [http://dx.doi.org/10.1016/0370-2693\(83\)90157-0](http://dx.doi.org/10.1016/0370-2693(83)90157-0).
- [156] K. Abe et al. "Letter of Intent: The Hyper-Kamiokande Experiment - Detector Design and Physics Potential" (2011). arXiv: 1109.3262 [hep-ex].
- [157] R. Acciarri et al. "Long-Baseline Neutrino Facility (LBNF) and Deep Underground Neutrino Experiment (DUNE)" (2015). arXiv: 1512.06148.
- [158] R. N. Mohapatra and A. Perez-Lorenzana. "Neutrino mass, proton decay and dark matter in TeV scale universal extra dimension models". *Phys. Rev. D* 67 (2003), p. 075015. DOI: 10.1103/PhysRevD.67.075015. arXiv: hep-ph/0212254 [hep-ph].
- [159] X. He and S. Pakvasa. "Unparticle Induced Baryon Number Violating Nucleon Decays". *Phys. Lett. B* 662 (2008), pp. 259–263. DOI: 10.1016/j.physletb.2008.03.025. arXiv: 0801.0189 [hep-ph].
- [160] S. N. Ahmed et al. "Constraints on nucleon decay via 'invisible' modes from the Sudbury Neutrino Observatory". *Phys. Rev. Lett.* 92 (2004), p. 102004. DOI: 10.1103/PhysRevLett.92.102004. arXiv: hep-ex/0310030 [hep-ex].
- [161] Y. Suzuki et al. "Study of invisible nucleon decay, $n \rightarrow \nu \bar{\nu} \nu$, and a forbidden nuclear transition in the Kamiokande detector". *Physics Letters B* 311.1 (1993), pp. 357–361. ISSN: 0370-2693. DOI: [http://dx.doi.org/10.1016/0370-2693\(93\)90582-3](http://dx.doi.org/10.1016/0370-2693(93)90582-3).

- [162] H. Ejiri. “Nuclear deexcitations of nucleon holes associated with nucleon decays in nuclei”. *Phys. Rev.* C48 (1993), pp. 1442–1444. DOI: 10.1103/PhysRevC.48.1442.
- [163] S. Grullon, S. Asahi, and J. Maneira. *External Background Simulation Studies for Te*. SNO+ Document 1720-v7. July 2013.
- [164] **SNO** Collaboration. “The Sudbury Neutrino Observatory”. *Nuclear Instruments and Methods in Physics Research* A449 (2004), pp. 172–207.
- [165] V. Lozza. *Water backgrounds expected numbers*. SNO+ Document 507-v30. Apr. 2016.
- [166] J. Maneira. *External Backgrounds in SNO+*. SNO+ Document 43. Aug. 2007.
- [167] **SNO** Collaboration. *SNO Preliminary Analysis for Neutral Current Rate Measurement*. SNO Internal Document. Apr. 2002.
- [168] Particle Data Group. *Solar Neutrino Review*. http://pdg.lbl.gov/2006/reviews/solarnu_s067sol.pdf. Accessed: 2015-11-12.
- [169] W. T. Winter and S. J. Freedman. “The ^8B neutrino spectrum”. *Phys. Rev. C* 73 (2006).
- [170] J. N. Bahcall, M. Kamionkowski, and A. Sirlin. “Solar neutrinos: Radiative corrections in neutrino-electron scattering experiments”. *Phys. Rev. D* 51 (1995).
- [171] N. Barros. “Precision Measurement of Neutrino Oscillation Parameters: Combined Three-phase Results of the Sudbury Neutrino Observatory”. PhD thesis. Universidade de Lisboa, 2011.
- [172] K. Singh and S. Andringa. *Reactor Anti-Neutrino Tagging*. SNO+ Document 2181-v1. Oct. 2013.
- [173] S. Andringa. *Anti-neutrino analysis*. SNO+ Document 1377. Mar. 2012.
- [174] P. Vogel and J. F. Beacom. “The angular distribution of the reaction $\bar{\nu}_e + p \rightarrow e^+ + n$ ”. *Phys. Rev. D* 60 (1999).
- [175] S. Andringa. *Study of Reactor Anti-Neutrino Oscillations in SNO+*. SNO+ Document 398. Dec. 2009.
- [176] B. Aharmim et al. “Determination of the ν_e and total ^8B solar neutrino fluxes using the Sudbury Neutrino Observatory Phase I data set”. *Phys. Rev. C* 75 (4 Apr. 2007), p. 045502. DOI: 10.1103/PhysRevC.75.045502.
- [177] O. Helene. “Upper limit of peak area”. *Nuclear Instruments and Methods in Physics Research* 212.1 (1983), pp. 319–322. ISSN: 0167-5087. DOI: [http://dx.doi.org/10.1016/0167-5087\(83\)90709-3](http://dx.doi.org/10.1016/0167-5087(83)90709-3).
- [178] O. Helene. “Determination of the upper limit of a peak area”. *Nucl. Instrum. Meth.* A300 (1991), pp. 132–136. DOI: 10.1016/0168-9002(91)90716-4.
- [179] G. J. Feldman and R. D. Cousins. “Unified approach to the classical statistical analysis of small signals”. *Phys. Rev. D* 57 (7 Apr. 1998), pp. 3873–3889. DOI: 10.1103/PhysRevD.57.3873.
- [180] W. A. Rolke, A. M. López, and J. Conrad. “Limits and confidence intervals in the presence of nuisance parameters”. *Nuclear Instruments and Methods in Physics Research Section A: Accelerators, Spectrometers, Detectors and Associated Equipment* 551.2–3 (2005), pp. 493–503. ISSN: 0168-9002. DOI: <http://dx.doi.org/10.1016/j.nima.2005.05.068>.

- [181] G. Casella and R. L. Berger. *Statistical inference*. Duxbury advanced series. Pacific Grove (Calif.): Brooks Cole, 2002. ISBN: 0-495-39187-5. URL: <http://opac.inria.fr/record=b1134456>.